Final Report Prepared for
NASA Lewis Research Center
under
Grant No. NAG 3-841

THE EFFECTS OF STREAMLINE CURVATURE AND SWIRL ON TURBULENT FLOWS IN CURVED DUCTS

KU-FRL-793-1

by

Chih-Hsiung (Gary) Cheng

and

Dr. Saeed Farokhi

Flight Research Laboratory
The University of Kansas Center for Research, Inc.
Lawrence, Kansas 66045-2969

December 1990

ABSTRACT

A technique for improving the numerical predictions of turbulent flows with the effect of streamline curvature is developed. Separated flows, the flow in a curved duct, and swirling flows are examples of flow fields where streamline curvature plays a dominant role. A comprehensive literature review on the effect of streamline curvature was conducted in the present study. New algebraic formulations for the eddy viscosity μ_t incorporating the k-ε turbulence model are proposed to account for various effects of streamline curvature. The loci of flow reversal of the separated flows over various backward-facing steps are employed to test the capability of the proposed turbulence model in capturing the effect of local curvature. The inclusion of the effect of longitudinal curvature in the proposed turbulence model is validated by predicting the distributions of the static pressure coefficients in an S-bend duct and in 180^{o} turn-around ducts. The proposed turbulence model embedded with transverse curvature modification is substantiated by predicting the decay of the axial velocities in the confined swirling flows. The numerical predictions of different curvature effects by the proposed turbulence models are also reported.

TABLE OF CONTENTS

NOMENCLATURE

a_1, a_2, a_3	Algebraic functions
C_1	Inertial return-to-isotropy constant of the Reynolds stress model
C_2	Forced return-to-isotropy constant of the Reynolds stress model
C_c	Empirical constant
C_{ij}	Convection term of the Reynolds stress equation
C_k	Convection term of the turbulent kinetic energy equation
C_s	Empirical coefficient of the Reynolds stress model
$C_{\varepsilon 1}$	Empirical coefficient of the standard k-ε model
$C^*_{\varepsilon 1}$	Modified empirical coefficient with curvature effect
$C_{\varepsilon 2}$	Empirical coefficient of the standard k-ε model
$C^*_{\varepsilon 2}$	Modified empirical coefficient with curvature effect
C_μ	Empirical coefficient of the standard k-ε model
C^*_μ	Modified empirical coefficient with curvature effect
$C_{\mu 1}...C_{\mu 4}$	Modified empirical coefficients for Reynolds stress tensors
$C_{\mu x}$, $C_{\mu y}$	Modified empirical coefficients for Reynolds stress tensors
D	Pipe diameter
D_{ij}	Diffusion term of the Reynolds stress equation

D_k	Diffusion term of the turbulent kinetic energy equation
D_n	Dean number
e	Turbulent mixing energy
f_ϵ	Algebraic function in equation (2.7)
h	Step height
k	Turbulent kinetic energy
L	Duct length
l	Length scale
l_0	Length scale without curvature effect
n	Normal direction in the streamline (s,n) coordinate; normal distance away from the wall
$\hat{P}$	Instantaneous static pressure
P	Mean static pressure
P_{ij}	Production rate of the Reynolds stress $-\overline{u_i u_j}$
P_k	Pressure strain term of the turbulent kinetic energy
P_r	Production rate of the turbulent kinetic energy
Ps_{ij}	Pressure-strain term of the Reynolds stress equation
p	Fluctuating static pressure
R	Radius of surface curvature; pipe radius
R_c	Radius of curvature along the centerline

Re	Reynolds number
R_f	Flux Richardson number
Ri	Richardson number
Ri_c	Richardson number of rotation
Ri_t	Turbulent Richardson number
R_t	Turbulent Reynolds number
r	Radial direction in the Cylindrical coordinate
S	Swirl number
s	Longitudinal direction in the streamline (s,n) coordinate
U, V, W	Mean velocity components in the streamwise, normal, and circumferential directions respectively
u, v, w	Fluctuating velocity components in the streamwise, normal, and circumferential directions respectively
$\hat{U}_i$	Components of the instantaneous velocity in the direction of X_i
U_i	Components of the mean velocity in the direction of X_i
U_τ	Friction velocity
U_θ	Longitudinal velocity
u_i	Components of the fluctuating velocity in the direction of X_i
$\overline{u_iu_j}$	Components of Reynolds stress tensors
V_t	Turbulence velocity scale
W	Width of a duct

X_i	Space coordinate in tensor notation
x	Streamwise (axial) direction in the Cartesian and Cylindrical coordinates
y	Transverse direction in the Cartesian coordinate; normal distance away from the wall
β	Empirical constant
δ_{ij}	Kronecker delta function
ε	Dissipation rate of the turbulent kinetic energy
ε_{ij}	Dissipation rate of the Reynolds stress $\overline{u_i u_j}$
μ	Coefficient of fluid viscosity
μ_e	Effective viscosity
μ_t	Turbulent (eddy) viscosity
ν	Laminar kinematic viscosity
ν_e	Effective kinematic viscosity
ν_t	Turbulent kinematic viscosity
ϕ	Function defined by equation (3.17)
ϕ_0	Function defined by equation (3.21)
ρ	Density
Σ	Summation
σ_k, σ_ε	Empirical constants of the k-ε model
τ_{ij}	Stress tensors

θ	Circumferential direction in the cylindrical coordinate
ω	Turbulent dissipation rate
ξ, η, ζ	Transformed curvilinear coordinate

Superscript

^	Instantaneous quantities
_	Time-averaged quantities
o	Degree

Subscript

ave	Averaged value
BL	Boundary layer
c	Center line
D	Pipe diameter
d	Downstream
i, j, k, m	Tensor notations
in	Inlet condition
ref	Reference condition
u	Upstream
W	Channel width
θ	Momentum thickness

Abbreviation	
SSME	Space shuttle main engine
STOVL	Short take off and vertical landing
TAD	Turn-around duct

CHAPTER I

INTRODUCTION

The tremendous improvement of computer capabilities in the past few years, including memory and speed, enables accurate numerical predictions of turbulent flows. Due to the closure problem of the governing equations for turbulent flows, numerous turbulence models have been proposed. The eddy-viscosity type of turbulence closure modeling has demonstrated a variety of good numerical predictions both qualitatively and quantitatively. Among them, the k-ε model is the most widely employed isotropic two-equation model. This model has been extensively applied to different turbulent flow problems. However, the standard k-ε model appears to be insufficient in predicting the complex turbulent shear layers, such as flows subjected to curvature and rotation.

Flows with streamline curvature are particularly of interest in engineering due to their frequent presence in real life applications. There are several types of streamline curvature problems which may occur in the flow field. The separated flows would be considered to involve local curvature; flows in curved

ducts can be classified as a longitudinal curvature problem; and swirling flows typify the transverse curvature. The appearance of streamline curvature could change the structure of turbulent flow fields drastically. For example, turbulence intensity is enhanced with the application of concave curvature, while convex curvature inhibits the turbulent mixing. The change of turbulent structure will influence the mean flow field and vice versa. Consequently, any models do not include the effect streamline curvature will fail when streamline curvature occurs.

Modifications to turbulence modeling are therefore necessary to account for the effects of various streamline curvature. The ad hoc change of modeling constants,however, to fit experimental measurements is not desirable, as it lacks physical rationale and generality. A large increase in computing time is not feasible for practical applications either. In the present investigation, new formulations for the eddy viscosity with the effects of different streamline curvature are proposed. Since the transport equations of the Reynolds stresses have a better description of the curvature effects, algebraic forms of the equations, approximated from the Reynolds-stress model, are essential. By extracting the extra strain rate and the main strain rate for the flow fields with different streamline curvature environments, new algebraic expressions for the eddy viscosity are derived from the algebraic Reynolds-stress model. In the

proposed eddy-viscosity formulations, the flux Richardson number R_f plays an important role as it dictates the effects of various streamline curvature on the turbulence structure through the amplification or diminution of the eddy viscosity. Different coordinate systems are employed for various effects of streamline curvature in accordance with geometrical flow characteristics.

The implemented eddy viscosity will be incorporated with the k-ε model to predict the effects of streamline curvature on the turbulent flow field. A Navier-Stokes flow solver embedded with the standard k-ε model is employed. A second-order finite differencing scheme for the temporal and spatial discretizations, incorporating a quasi-damping scheme which is deduced from second-order upwind difference concept, is adopted for the convection terms. The proposed models will be verified by comparing computationally predicted results with turbulent flows subjected to different streamline curvature effects. The examples for model verification are a) the flow over a backward-facing step, b) the flow in a curved duct, and c) swirling flows. The numerical computations are performed on the Cray X-MP supercomputer at NASA-Lewis Research Center.

CHAPTER II

REVIEW OF LITERATURE

During the last two decades, turbulence modeling has become the most productive, controversial, and rapidly improving subject for researchers in the computational fluid dynamics field. It started with simple boundary layer flows on a flat plate, and today numerous successes of the predictions on simple shear layer flows have been reported. However, the numerical computation of complex turbulent flows--such as three-dimensional flows, flows subjected to curvature and rotation, separated flows and shock boundary layer interaction--is still being investigated.

The drastic change of flow characteristics due to the presence of the streamline curvature has been demonstrated by many researchers [1]-[4] based on classical laminar boundary layer theory study. The objective of the present research work is to explore the effects of streamline curvature and swirl on turbulent flows, which effects are much more complicated than their laminar counterparts. A review of literature is therefore conducted in two complementary ways--by 1) examining the experimental works to help

understand the physics of curved flows, and 2) studying and evaluating both the theoretical research and numerical techniques--to implement the turbulence modeling with the inclusion of curvature and swirl effect. The detailed information of the literature review in these two categories, and their summaries, are tabulated in Table A.1 (for experimental work) and Table A.2 (for theoretical and numerical work).

2.1 Experimental Investigations

A variety of experimental investigations have been conducted in the last few decades. **Bradshaw and his co-workers [5]-[10]** conducted a series of experiments on convex surfaces, concave surfaces and curved ducts. They found that the turbulence intensity is reduced by the application of convex curvature which indicates a stabilizing effect, while longitudinal vortices are induced by the application of the concave curvature which has a destabilizing effect that enhances the turbulence mixing. Curved shear layers exhibited non-equilibrium behavior and required different formulation for the stabilizing and destabilizing effects. The rapid response of boundary layers to the presence of the convex curvature, as well as a fairly rapid recovery when the curvature is removed, has been experimentally demonstrated. Hence, Bradshaw et. al. suggested that the effect of convex curvature be modeled in Reynolds-stress

equations, at least partly as dependent on the rapid part of the pressure-strain term in the Reynolds-stress equations. It was further proposed that the apparent mixing length, increased due to the concave curvature, be modeled roughly proportional to the *Richardson number* Ri, which is

$$Ri = \frac{2(U_\theta/R)}{\partial U_\theta / \partial n} \tag{2.1}$$

where R is the radius of curvature, n is the normal distance away from the wall, and U_θ is the longitudinal velocity. It was noted by **Smits, Young and Bradshaw** [7] that the ratio of shear stress to kinetic energy is increased by the concave curvature. The increment of Reynolds stress is caused by the increase in the transverse production term in the Reynolds stress equation as the curvature occurs. Experimental data also revealed that flows recover more rapidly on the convex surface than on the concave surface as the curvature disappears.

Gillis and Johnston [11] demonstrated the characteristics of flat-plate boundary layers recovering from a sustained convex longitudinal curvature. Since the radial pressure gradient acts to destroy the size of the largest eddies, the radius of curvature is proposed to be a scaling parameter. The experimental results exhibited a slow recovery of Reynolds stresses from convex curvature

effect, which is contradictory to Bradshaw's results. This is attributed to the stabilizing effect which permanently attenuates the turbulence length-scale and reduces the effects of the upstream condition. However, the near-wall layers are not influenced very much by the curvature.

Streamline energy spectra for turbulent duct flow with small streamline curvature has been examined by **Hunt and Joubert [12]** in terms of a Townsend-type two-component turbulence model. Their result indicated that the flow was primarily affected by a direct change in turbulent shear stress through a conservative reorientation of the turbulence intensity components.

Ramaprian and Shivaprasad [13] have performed extensive measurements of the surface curvature effects on turbulent energy balance and triple correlations. Turbulent energy production rate is reported to be significantly reduced by convex curvature and confined to a region very close to the wall; however, it is only slightly enhanced by concave curvature. Diffusion of both momentum and turbulent kinetic energy is found to be suppressed by convex curvature and strengthened by concave curvature.

Effects of convex and concave surface curvature with artificially controlled constant pressure were tested by **So and Mellor [14]-[15].** Reported test results are similar for curvature effects with and without adverse pressure gradients. Turbulent energy and its production rate, normalized by U_τ, appear

to be similar to the flat-plate data in the near-wall region; hence, no influence on the flow by surface curvature near the wall is concluded. A coherent structure of Görtler vortices is generated at the onset of concave curvature and then breaks up as flow moves downstream, due to the increase of turbulence level.

Tani [16] performed an experimental test on concave-wall flow. He compared the data with Görtler's small-disturbance theory because longitudinal vortices induced by concave curvature will intensify the growth of disturbances into turbulence in a boundary layer. Measured data reveal a spanwise variation having a definite wave number whether the boundary layer is laminar or turbulent, but the determination of the wave number is unavailable in Tani's paper.

After inspection of individual surface curvature effects, curved duct flows, in which there is a combination of both curvature effects, are examined. First, an experimental study on the development of steady, laminar, incompressible flow in a curved pipe was conducted by **Agrawal, Talbot and Gong [17]**. The data indicate that at the vicinity of the curved pipe inlet, the inviscid axial velocity profile transits from a uniform distribution to a vortex-type distribution.

White [18] also investigated wall shear stress in a coiled pipe with various inlet Reynolds number. The results show that the friction force increases with the Dean number D_n, defined as

$$D_n = R_e\sqrt{\frac{r}{R}} \tag{2.2}$$

with r is the radius of the pipe.

Strong secondary flows are discovered in S-shaped ducts with square cross section by **Taylor, Whitelaw and Yianneskis [19]**. In the first bend, secondary flows are larger in the laminar flow case than in the turbulent flow case due to larger inlet boundary layer thickness in laminar case. Taylor et al. reported that secondary flows reach their maximum values at the exit of the first bend, while the second bend produces the secondary flow effect in the opposite direction.

Humphrey, Whitelaw and Yee [20] reported Laser-Doppler anemometer measurement of the mean velocities and Reynolds stresses in a 90°-bend duct with a square cross section. The locus of maximum velocity in laminar flow is shown to move more rapidly toward the outer wall than that in the turbulent flow. Low turbulence intensity and low level of anisotropy are exhibited at the wall with convex curvature, whereas high turbulence intensity and high level

of anisotropy are introduced at the wall with concave curvature. Some geometry with lower Reynolds number (laminar flow) was tested by **Humphrey, Taylor and Whitelaw [29]**, and it appears that the secondary flow is already established at the entrance plane and persists downstream more than 10 hydraulic diameters.

Turbulent flows in a 180°-bend pipe and in a 45°/45° S-bend pipe were investigated by **Row [21]**. In the 180°-bend pipe, it is indicated that the secondary flows increase to a maximum and then decrease to a steady value. The flow in an S-bend pipe demonstrates that the secondary flows cause a complete interchange of fluids near the wall region and in the central core.

Humphrey and Chang [22] explored the turbulent flow field in a 180°-bend square duct through L.D.V. measurements. According to the experimental result, they concluded that in the downstream straight section to a curved duct, turbulence diffusion and redistribution processes force the flow to erase all memory of the force imbalance acting on the flow in bend. However, a very weak secondary motion persists in the downstream straight section because of differences in the cross-stream gradients of the Reynolds stresses.

Based on the present review, it is found that there are few experimental studies on two-dimensional turbulent flows in S-bend ducts, and the work by **Butz [23]** is one of them. Due to strong secondary flows in S-shaped ducts,

large aspect ratio is required to eliminate the lateral velocity component. Mean velocities and pressure recovery coefficients were measured in Butz's work.

Brinich and Graham [24] investigated the turbulent flow and heat transfer in a two-dimensional 210°-turning curved channel having an aspect ratio of 6, a radius ratio of 0.96, and adiabatic and heated walls; and operating at three different inlet velocities. The results show that at the start of the curved section an abrupt increase in pressure occurred for both the inner and outer walls. This is due to the force required to change the stream direction from rectilinear to curved flow. Another sudden pressure rise appears at 75° station because of a change in the longitudinal vortex development.

2.2 Theoretical and Numerical Methods

Since the early parts of this century, researchers have realized the importance and complications associated with curved flows. Some researchers, such as **Hawthorne [3]** and **Rowe [21]**, have tried to solve the problem through a quasi-inviscid theory. Meanwhile, laminar boundary layer theory incorporated with various techniques was employed more often in the curved flow field: for example, **Tani [16]** used small disturbance theory to examine the instability of the longitudinal vortices; **White [18]** proposed an empirical algebraic solution for the resistance coefficient due to the curvature effect; **Agrawal, Talbot and**

Gong [17] adopted an asymptotic expansion correction (developed by **Singh [25]**) to the governing equations of motion to compare with their experimental measurements; **Stewart, Cebeci and Chang [26]** obtained an approximate algebraic formulation by using a series expansion for three mean velocity components; and a similar expansion technique was employed by **van Dyke [27]**. **Humphrey [28] and his co-workers [29]** tried to use the finite difference method to predict the flow field. Although all the above methods have the advantage of simplicity and less computing time, none of them can capture the characteristics of curved flows very well, especially when the curvature is large. This is mainly because the mechanism of turbulence mixing does not exist in these proposed theories, and hence the amplification and attenuation of turbulence could not interact with mean flow field. In the remaining part of this chapter, we will concentrate on the turbulence modeling and its theoretical development.

Bradshaw [30] performed a very extensive review of streamline curvature effects generated by surface curvature, swirling flows, rotating ducts, and/or spinning pipes. He also provided a method of distinguishing *"simple" shear layers* from *"complex" shear layers*. A simple shear layer is defined as one where the simple shear, $\partial U/\partial y$, is so much larger than any other rates of

strain that the direct effects of the latter on turbulence are negligible. Complex shear layers are recognized as perturbations of simple shear layers by the imposition of extra rates of strain or body forces, or by the interaction with other shear layers. **Bradshaw [30]-[31]** also deduced some characteristic parameters for flows with streamline curvature by drawing an analogy between meteorological flows, such as buoyancy effect, and curved-flow fields, such as radial pressure gradient. He proposed a correction to the apparent mixing length with small curvature effects based on the *Monin-Oboukhov formula*

$$\frac{l}{l_0} = 1 - \beta \, \mathrm{Ri} \tag{2.3}$$

where β is a positive empirical constant of order 10, and l_0 is the length scale for zero curvature flows.

A critical evaluation of various turbulence models performed by **Nallasamy [32]** reveals that the first generation turbulence modeling techniques developed based on simple shear-layer flows can no longer predict complex turbulent flows. **Lakshminarayana [33]** recently conducted a fairly thorough review of turbulence modeling techniques for complex turbulent shear layers, such as flows subjected to curvature and body rotation, separated flows, and vortex flows. The algebraic eddy viscosity and the two-equation models, with

constant value of C_μ, are concluded to be inadequate for the prediction of complex shear layers. Lakshminarayana recommended that a proper expression for C_μ, incorporated with a two-equation model, be used for two-dimensional flows with separation, curvature, or rotation. It is suggested that Reynolds stress models be employed for cases with very severe extra strains, large separation, curvature, or rotation effects, because of the large anisotropy.

In the following review, papers will be summarized based on the sequence of zero-equation (algebraic stress) models, two-equation models, modified two-equation models, and Reynolds stress models.

Hunt and Joubert [12] employed the length-scale model in equation (2.3), proposed by Bradshaw [30], to calculate a two-dimensional curved duct. No detailed comparison between experimental data and numerical prediction was reported.

Towne and his co-workers [34]-[37] computed some curved-duct flows by using a parabolized Navier-Stokes (PNS) solver with a two-layer eddy-viscosity turbulence model embedded in it. In the outer region, the turbulence model of **Cebeci and Smith [38]** is used, while in the inner region either the model of Cebeci and Smith [38] or that of **McDonald and Camarata [39]** is adopted. In spite of less computing time required for the PNS solver, the streamwise marching technique has its own limitation (i.e., viscous flows with

no or small separation), while streamline curvature does include flow separation effect. Numerical predictions of turbulent cases are shown to be less accurate than those of laminar flows because of the failure of the two-layer turbulence model in recovering the effect of extra rate of strain.

The **Baldwin-Lomax** [40] two-layer eddy-viscosity model was tested by **Loeffler, Jr.** [41] by applying it to an S-shaped diffuser. With the **Beam-Warming** [42] implicit scheme embedded, a large separation zone was predicted; but the numerical results were not validated by comparing them with experimental data.

A simple mixing length model, in which the turbulent stress is proportional to the local strain rate of the mean flow, was used by **Anderson** [43] to compute duct flows with streamline curvature and streamline divergence. In the free stream, the length scale is selected to be the duct height, while **van Driest's** [44] model is employed at the near-wall region. Detailed comparisons with measured data are not available in the Ref. [43].

Irwing and Smith [45] modified the Reynolds-stress model proposed by **Launder, Reece and Rodi** [46], with the assumption of local isotropy as well as local equilibrium, and obtained algebraic equations for the Reynolds stresses. The extra Reynolds stress production term is included to calculate the effects

of streamline curvature, according to Irwing and Smith's observation that curvature effects on the Reynolds stresses are quite large.

Gibson [47] introduced an explicit form for the length-scale function, where the influence of the wall on the fluctuating pressure field is modeled to account for the curvature effects. It was suggested in Ref. [47] that curvature effects can be included by the relatively small production terms appearing in each individual Reynolds-stress equation.

An algebraic turbulence velocity scale for flows with curvature was developed by **So [48]**. The approximation was made based on the Reynolds-stress equations, in which the pressure-strain term is modeled by **Mellor and Herring [49]**, with the assumption of local isotropy and local equilibrium. With the aid of two-dimensional boundary layer approximation, the velocity scale is derived to be a function of Richardson number Ri.

Two-equation models probably are the most widely used models for complex turbulent flows. **Chang, Han and Humphrey [50]** applied the standard k-ε model to a 90°-bend duct with square cross section. The discrepancies exhibited the failure of the standard k-ε model to account for large-scale anisotropy in the flow. The standard k-ε model in conjunction with a parabolized scheme was employed both by **Patankar, Pratap and Spalding [51]** and by **Pratap and Spalding [52]** to compute curved ducts and pipes.

Numerical predictions appear to underestimate the strength of secondary flows. Two suggestions were then made to modify the turbulence modeling for complex turbulent flows: 1) solving Reynolds stress equations, and 2) implementing the eddy viscosity based on approximate algebraic Reynolds-stress equations.

Murthy and Lakshminarayana [53] compared the Baldwin-Lomax eddy-viscosity model with the standard k-ε model, in a curved duct, incorporating in both models a space-marching, non-iterative algorithm. Although the standard k-ε model is found to be superior to the eddy-viscosity model, neither model can produce quantitative agreement with the experimental measurements.

A general algebraic expression for C_μ was deduced by **Pourahmadi and Humphrey [54]** to modify the k-ε model to account for curvature effects. A new eddy viscosity was obtained by the combination of Bradshaw's length-scale model in equation (2.3), and a functional C_μ, which can be written as

$$F(\sqrt{C_\mu}) = C_\mu^{3/2} + a_1 C_\mu + a_2 C_\mu^{1/2} + a_3 = 0 \qquad (2.4)$$

where $a_1, a_2, a_3 = a_1, a_2, a_3(P_r/\varepsilon, U_\theta/r, \partial U_i/\partial X_j)$. **Santi [55]** applied both this model and the standard k-ε model to a 180° turn-around duct, with uniform and non-uniform inlet flow conditions, and compared the results. Based on various

computational results, Santi criticized Pourahmadi and Humphrey's model for an error in finding the root of the $F(\sqrt{C_\mu})$ equation (Eq. 2.4) and for additional difficulties which occur in specifying a selection criterion for regions with multiple roots.

Launder, Priddin and Sharma [56] proposed that C_μ^* and $C_{\varepsilon 2}^*$ be functional, and that an extra term be added to the energy dissipation rate (ε) equation to include the effects of curvature. In this model, the modeling constant C_μ^* can be expressed as

$$C_\mu^* = C_\mu \exp\left[\frac{-3.4}{(1 + R_t / 50)^2} \right] \tag{2.5}$$

where R_t is the turbulent Reynolds number, and $C_\mu = 0.09$ is the value of C_μ^* in the absence of the effects of streamline curvature. Another empirical coefficient $C_{\varepsilon 2}^*$ is modified to be proportional to a turbulent Richardson number Ri_t (based on a time scale of the energy-containing eddies) and is defined as

$$C_{\varepsilon 2}^* = C_{\varepsilon 2} [1 - 0.3 \exp\{ -R_t^2 \}] (1 - C_c Ri_t) \tag{2.6}$$

where C_c is a constant with a value of 0.2, and $C_{\varepsilon 2}$ is the modeling constant of the standard k-ε model and equal to 1.92. An additional term appears in the ε-equation which is attributed to the curvature correction on the production term

of the ε-equation instead of the decay part. This model was employed by **Sharma** [57] and provided reasonably good predictions.

Rodi and Scheuerer [58] also compared this model with Gibson's algebraic stress model (Ref. [47]) in calculating the curved shear layers. The discrepancy between numerical and experimental results demonstrated the inadequacy of both models in capturing the curvature effects in general.

An effort to include the anisotropy in the approximate algebraic Reynolds stress equations was conducted by **Galmes and Lakshminarayana** [59] in predicting three-dimensional shear flows over curved rotating bodies. In addition to using the same modified C_μ^* formulation as in equation (2.5), they implemented the production term of the ε equation, based on their analysis, by modifying the empirical coefficient $C_{\varepsilon 1}^*$ to include the rotation effect, as follows:

$$C_{\varepsilon 1}^* = C_{\varepsilon 1} f_\varepsilon = C_{\varepsilon 1} [\ 1 + 0.3 (\ 1 - Ri_c\ ) \exp(\ -R_t^2\ )\ ] \qquad (2.7)$$

where $C_{\varepsilon 1}$ is the modeling constant of the standard k-ε model with a value of 1.44, and Ri_c is the Richardson number of rotation. A rather complicated model was proposed by these authors in which a modified k-ε model, coupled with a set of six algebraic Reynolds-stress equations, needs to be solved simultaneously. In each of the six algebraic equations, the pressure-strain term

as originally proposed by Launder, Reece and Rodi [46] is noted to have been modified by Galmes and Lakshminarayana so as to include the anisotropy and near-wall effects caused by rotation and curvature.

Warfield and Lakshminarayana [60] implemented the algebraic Reynolds stress model proposed by **Rodi [61]**, to modify the Kolmogorov-Prandtl eddy-viscosity relation and produce an anisotropic turbulence model to account for the effect of rotation. Algebraic expressions for a vector form of C_μ, which contains four components ($C_{\mu 1}$, $C_{\mu 2}$, $C_{\mu 3}$, and $C_{\mu 4}$), were derived so that the Reynolds stress tensors are not necessarily aligned with the mean strain tensor. However, the formulations for the C_μ vector are considered to be relatively complicated.

Naot and Rodi [62] obtained the algebraic equations for the vector modeling coefficient C_μ in the k-ε model, composed of $C_{\mu x}$ and $C_{\mu y}$, to consider the anisotropic effect. The algebraic expression was derived from an approximated algebraic Reynolds-stress model by simplifying the Reynolds-stress equation proposed by Launder, Reece and Rodi [46], with the convection and diffusion terms neglected (i.e., in local equilibrium).

A new eddy-viscosity model for swirling flow, representing a type of flow with streamline curvature, was developed by **Kim and Chung [63]**. With an assumption of weakly swirling flows, an expression for eddy viscosity was

derived through Rodi's algebraic stress model [61]. A relatively good agreement was displayed by choosing the modeling constant β equal to 0.25. Nevertheless, according to **Cheng [64]**, some inconsistency was found in Ref. [63], and it is not certain that the success of Kim and Chung's model is attributable to the inclusion of Richardson number or to the ad hoc change of the empirical coefficient C_{μ}^{*}.

Wilcox and Chambers [65] demonstrated the prediction of the streamline curvature effects on turbulent boundary layers by using the e-ω model. It was suggested that the streamline curvature primarily affects the equation of turbulent mixing energy e, while the equation of turbulent dissipation rate ω remains unaffected by the curvature. A curvature correction term was then added to the e-equation to account for the centrifugal effect.

The Reynolds stress model proposed by Launder, Reece and Rodi [46], coupled with modeled energy dissipation (ε) equation, was used by **Gibson and Rodi [66]** to predict a highly curved mixing layer. The Reynolds-stress model developed for plane flow is considered to have the advantage that neither modification to the basic closure hypothesis nor changes in the modeling constants are required to predict strong curvature effects. This method apparently not only is much more complicated and computing intensive but also

requires more modeling approximation for higher order terms. Some qualitative agreements with the measured data were reported.

Hah and Lakshminarayana [67] investigated turbulent wake flows including curvature and rotation effects by using three different turbulence models: 1) standard k-ε model, 2) ε/algebraic-stress model, and 3) ε/Reynolds-stress model. Due to poor representation and inadequacy of the production term of the ε-equation for curved flows, different forms of this term in combination with those three models were tested as well. It seems that the k-ε model with modified production term in the ε equation can predict the streamline curvature effect very well but fails to capture the effect of rotation. It was suggested in Ref. [67] that the ε/Reynolds-stress model or the ε/algebraic Reynolds-stress model be employed to account for the rotation effect.

Lilley [68] demonstrated the turbulent flow prediction results of several different turbulence models, namely mixing length model, k-kl model, Reynolds stress model, and algebraic stress model, in turbulent swirling jets. An analytical formula for the length scale was presented to account for swirling effect. An extra term was introduced in the kl-equation to include the effect of rotation, so that as the swirl number increases, kl will be enhanced. Fairly good

agreement with measured data was shown for the mixing length model and k-kl model.

2.3 Conclusions

Based on the literature survey, the following conclusions may be reached:

1) Streamline curvature in the plane of the mean shear produces considerably large changes in higher-order quantities of the turbulence structure of shear layers: e.g., second order variables--Reynolds stresses, turbulent kinetic energy, etc.

2) Turbulent mixing is inhibited by the presence of convex curvature; hence, the stabilizing effect will attenuate the Reynolds stresses and turbulent kinetic energy.

3) Concave curvature has a destabilizing effect which will not only enhance the turbulence intensity and enlarge the length scale, but also induce the Görtler-type vortex structure, which the extra rates of strain become significant.

4) Streamline curvature effect could be caused by surface curvature, swirling flows, flow separations, or rotation of the whole system; and we consider a turbulent flow field with this effect a complex shear flow.

5) The algebraic eddy-viscosity and the standard two-equation models are not adequate for the prediction of complex shear layers.

6) Although it fails to predict the flows with large extra strains, Bradshaw's buoyancy analogy seems to be the simplest model to calculate the corrected length scale, through a correlation in which a Richardson number is involved to include the effect of streamline curvature.

7) The k-ε model, with the aid of modification of modeling constants (through the algebraic Reynolds-stress equations) or adding new terms in k- and/or ε-equations, appears to be the most plausible approach regarding model complexity and the computing time.

8) The k-ε model, coupled with a set of algebraic Reynolds-stress equations, does have a better coverage of the physical characteristics of extra strains (from the effect of anisotropy); however, it is evident that more computing time and a more complicated modeling procedure are required.

9) Even with a more complicated and time-consuming Reynolds-stress model, better predictions of curvature effects are not guaranteed.

10) In spite of the great number of turbulence models proposed for curved or rotating flows, most will show good predictions in only some particular geometries but will fail predicting others.

11) For engineering applications, modifications to the turbulence modeling, allowing greater simplicity and less computing time, are feasible, desirable, and necessary.

CHAPTER III

THEORETICAL APPROACH

3.1 Governing Equations

The equations of motion for a steady, incompressible, adiabatic flow of a Newtonian fluid are based on the following fundamental conservation laws, and will be expressed in tensor notation for universality [69]. The continuity equation (conservation of mass) is given by

$$\frac{\partial \hat{U}_i}{\partial X_i} = 0 \tag{3.1}$$

The momentum equations, or so-called *Navier-Stokes equations* (conservation of momentum) are written as

$$\rho \hat{U}_j \frac{\partial \hat{U}_i}{\partial X_j} = - \frac{\partial \hat{P}}{\partial X_i} + \frac{\partial \hat{\tau}_{ij}}{\partial X_j} \tag{3.2}$$

where $\hat{U}_i$ represents the three instantaneous velocity components in X_i-coordinate direction, $\hat{P}$ is the instantaneous static pressure, ρ is the density, and the instantaneous stress tensor $\hat{\tau}_{ij}$ is given by

$$\hat{\tau}_{ij} = \mu\left(\frac{\partial \hat{U}_i}{\partial X_j} + \frac{\partial \hat{U}_j}{\partial X_i}\right) \tag{3.3}$$

where μ denotes the coefficient of fluid viscosity.

With the present computer capabilities, we know well the impossibility of solving the instantaneous Navier-Stokes equations for all the detailed fluctuating properties of a turbulent flow and with spatial resolution of finest eddies. Therefore, we can only hope to resolve the time-averaged quantities. By using the *Reynolds' decomposition*, $\hat{U}_i = U_i + u_i$ and $\hat{P} = P + p$, and *time-averaging procedure* [70]-[71], we can obtain the system of governing equations for the time-averaged, steady, incompressible, adiabatic turbulent flow field, which can be written as

$$\frac{\partial U_i}{\partial X_j} = 0 \tag{3.4}$$

$$\rho U_j \frac{\partial U_i}{\partial X_j} = -\frac{\partial P}{\partial X_i} + \frac{\partial}{\partial X_j}\left[\mu\left(\frac{\partial U_i}{\partial X_j} + \frac{\partial U_j}{\partial X_i}\right) - \rho\,\overline{u_i u_j}\right] \tag{3.5}$$

where U_i and P are time-mean parameters, and u_i and p are fluctuating components. We note that excluding the last term, $\rho\overline{u_i u_j}$, in equation (3.5) gives the momentum equations for laminar flows. The term of $-\rho\overline{u_i u_j}$ is found to play

the same role as the simple Newtonian viscous stresses in a laminar flow, hence, the fluctuating term is regarded as *Reynolds stress* or *turbulent stress*. For $i = j$, $-\rho\overline{u_i u_j}$ represents turbulent normal stresses, otherwise, the Reynolds' shear stresses. Since the Reynolds-stress term appears in equation (3.5), additional equations are needed to solve the system of equations. A transport equation for the Reynolds stresses can be derived from equation (3.5) by multiplying it with u_i and taking a time average of the resulting equation [38], [72], i.e.

$$C_{ij} = P_{ij} + Ps_{ij} + D_{ij} - \varepsilon_{ij} \tag{3.6}$$

where

$$C_{ij}\ (\text{convection}) = U_k \frac{\partial \overline{u_i u_j}}{\partial X_k}$$

$$P_{ij}\ (\text{production}) = -\left[\overline{u_i u_k} \frac{\partial U_j}{\partial X_k} + \overline{u_j u_k} \frac{\partial U_i}{\partial X_k} \right]$$

$$Ps_{ij}\ (\text{pressure-strain}) = \overline{\frac{p}{\rho}\left(\frac{\partial u_i}{\partial X_j} + \frac{\partial u_j}{\partial X_i} \right)}$$

$$D_{ij}\ (\text{diffusion}) = -\frac{\partial}{\partial X_k}\left[\overline{u_i u_j u_k} - \nu\frac{\partial \overline{u_i u_j}}{\partial X_k} + \overline{\frac{p}{\rho}(\delta_{jk}u_i + \delta_{ik}u_j)}\right]$$

$$\varepsilon_{ij}\ (\text{dissipation}) = 2\nu\overline{\left(\frac{\partial u_i}{\partial X_k}\frac{\partial u_j}{\partial X_k}\right)}$$

and ν is the coefficient of laminar kinematic viscosity, δ_{jk} and δ_{ik} are the Kronecker delta functions.

For i = j, by defining the *turbulent kinetic energy* as $k = \Sigma\ \overline{u_i u_i}/2$, i.e. summing the normal Reynolds stresses, equation (3.6) becomes the transport equation of turbulent kinetic energy, which is

$$C_k = P_r + P_k + D_k - \varepsilon \tag{3.7}$$

where

$$C_k\ (\text{convecton}) = U_k\frac{\partial k}{\partial X_k}$$

$$P_r\ (\text{production}) = -\overline{u_i u_k}\frac{\partial U_i}{\partial X_k}$$

$$P_k\ (\text{pressure-strain}) = \overline{\frac{p}{\rho}\frac{\partial u_i}{\partial X_k}}$$

$$D_k \text{ (diffusion)} = -\frac{\partial}{\partial X_k}\left[\overline{u_k\left(\frac{u_i u_i}{2}+\frac{p}{\rho}\right)}-\nu\frac{\partial k}{\partial X_k}\right]$$

$$\varepsilon \text{ (dissipation)} = \nu\overline{\frac{\partial u_i}{\partial X_k}\frac{\partial u_i}{\partial X_k}}$$

and the pressure-strain term P_k is usually neglected on the evidence of measured turbulent energy balance [72].

It is obvious that every time we take time-averaging to introduce more equations, the more unknowns (higher-order turbulence quantities) appear in our system of equations. *Turbulence closure modeling* is therefore required to balance the numbers of unknowns and the governing equations.

3.2 Turbulence Modeling

As indicated in equations (3.4) and (3.5), the time-averaged Navier-Stokes formulation has more unknowns than the number of equations. The technique to model the new unknown term ($\rho\overline{u_i u_j}$) to close the system of equations is called turbulence modeling. For the last few decades, numerous turbulence models have been proposed by researchers for various types of flows. Detailed discussions and comparisons of various turbulence models are

described in the review papers by Nallasamy [32] and Lakshminarayana [33]. Despite a great variety of turbulence models which have been proposed, they can be classified into two categories: a) *eddy-viscosity model*, and b) *Reynolds stress model.* The eddy-viscosity models are constructed based on the *Boussinesq's eddy-viscosity concept* which probably is the widest-applied approximation for turbulence modeling, which draws a similarity between Reynolds stress and viscous stress, and is given by

$$-\rho\,\overline{u_i u_j} = \mu_t\left(\frac{\partial U_i}{\partial X_j} + \frac{\partial U_j}{\partial X_i}\right) - \frac{2}{3}\delta_{ij}\rho\,k \tag{3.8}$$

where μ_t is named eddy viscosity or turbulent viscosity. Various methodologies have been employed to evaluate the eddy viscosity μ_t. Based on the number of differential equations, in addition to the time-averaged Navier Stokes equations, used in each technique, the eddy-viscosity models are categorized as *zero-equation (algebraic), one-equation, two-equation, and multi-scale models.* As mentioned in the review of literature and suggested in Ref. [73], the standard k-ε model, a version of two-equation models and proposed by **Launder and Spalding [74]**, will be employed and implemented in the present study to predict the effect of streamline curvature because of its extensive

verification, wide application, and easy modification. A detailed formulation of the k-ε model will be described later on.

In the Reynolds stress models, the Reynolds stress tensors are computed directly by solving the coupled partial differential equations as shown in equation (3.6), in which higher-order terms appear and need to be modeled. It is obvious that the Reynolds stress models require not only more computing time and computer memory because of more differential equations and unknowns, but also more thorough understanding of turbulence physics to model these higher-order terms. However, the Reynolds stress models have the advantage of predicting complex turbulent flows such as flows subjected to separation, rotation and the effect of streamline curvature. Hence, in the present implementation approach, the essence of the Reynolds stress models will be adopted to correct the formulation of the eddy viscosity.

With the aid of Boussinesq's eddy viscosity formulation in equation (3.8), the mean momentum equation, i.e. equation (3.5), may be written as

$$U_j \frac{\partial U_i}{\partial X_j} = -\frac{1}{\rho}\frac{\partial P}{\partial X_i} + \frac{\partial}{\partial X_j}\left[\frac{\mu_e}{\rho}\left(\frac{\partial U_i}{\partial X_j} + \frac{\partial U_j}{\partial X_i}\right)\right] \tag{3.9}$$

and $\mu_e = \mu + \mu_t$ is the effective viscosity. By using dimensional analysis, the eddy viscosity μ_t can be expressed as

$$\mu_t \sim \rho V_t l \tag{3.10}$$

where V_t is the turbulence velocity scale, and l is the turbulence length scale. It was postulated by Prandtl and Kolmogorov and later adopted in the standard k-ε model that

$$l \sim \frac{k^{3/2}}{\varepsilon} \quad , \qquad V_t \sim \sqrt{k} \tag{3.11}$$

which will lead us to obtain

$$\mu_t = \rho C_\mu \frac{k^2}{\varepsilon} \tag{3.12}$$

where C_μ is an empirical coefficient. In equation (3.12), two more unknowns are introduced and will require the solution of two partial differential equations for the turbulent kinetic energy and turbulent dissipation rate. This is why the k-ε model is identified as a two-equation eddy-viscosity model.

In the standard k-ε model, the transport equation for turbulent kinetic energy as shown in equation (3.7) was modeled as

$$C_k = P_r + D_k - \varepsilon \tag{3.13}$$

where

$$C_k = U_k \frac{\partial k}{\partial X_k}$$

$$P_r = \frac{\mu_t}{\rho}\left(\frac{\partial U_i}{\partial X_k} + \frac{\partial U_k}{\partial X_i}\right)\frac{\partial U_i}{\partial X_k}$$

$$D_k = \frac{1}{\rho}\frac{\partial}{\partial X_k}\left(\frac{\mu_t}{\sigma_k}\frac{\partial k}{\partial X_k}\right)$$

and as for the turbulent dissipation rate ε, it is expressed as the dependent variable of a differential conservation equation which is highly empirically modeled and is given by

$$U_k \frac{\partial \varepsilon}{\partial X_k} = \frac{1}{\rho}\frac{\partial}{\partial X_k}\left(\frac{\mu_t}{\sigma_\varepsilon}\frac{\partial \varepsilon}{\partial X_k}\right) + C_{\varepsilon 1}\frac{\varepsilon}{k}\frac{\mu_t}{\rho}\left(\frac{\partial U_i}{\partial X_k} + \frac{\partial U_k}{\partial X_i}\right)\frac{\partial U_i}{\partial X_k} - C_{\varepsilon 2}\frac{\varepsilon^2}{k} \qquad (3.14)$$

which physically represents the convection, diffusion, production and dissipation of the turbulent dissipation rate ε, respectively. In equations (3.12)-(3.14), C_μ, σ_k, σ_ε, $C_{\varepsilon 1}$ and $C_{\varepsilon 2}$ are modeling constants, and some typical values of these constants in the standard k-ε model are recommended by Launder and Spalding [75] in Table 3.1:

Table 3.1 The values of modeling constants in the standard k-ε model

C_μ	σ_k	$C_{\varepsilon 1}$	$C_{\varepsilon 2}$	σ_ε
0.09	1.0	1.44	1.92	1.3

According to equations (3.12)-(3.14), the standard k-ε model apparently does not have the capability to account for the effects of streamline curvature. The modeling constant C_μ in the eddy viscosity formulation, as shown in equation (3.12), is empirically tuned for the simple shear layer. Meanwhile, there is no mechanism in the model which can either amplify the turbulent intensity or eddy viscosity in the presence of concave curvature, or inhibit turbulent mixing with the application of convex curvature. Therefore, the expression for eddy viscosity in the standard k-ε model is considered to be inadequate to account for the streamline curvature effect. It is evident that modifications to the standard k-ε model are necessary to include the curvature effects. However, the ad hoc changes in modeling constants are not desired due to lack of physical explication. The implementation to the formulation of the Reynolds stress should be reasonable and feasible.

3.3 Implementation Approach

It was suggested by Muck, Hoffmann and Bradshaw [5] that the effects of curvature be modeled in the Reynolds-stress equations. Lakshminarayana [33] also indicated that the Reynolds-stress equations can interpret the physical phenomena very well. As a result, the implementation approach will start with the Reynolds-stress equations. Unfortunately, more higher-order unknown turbulent parameters are exhibited in the Reynolds-stress equations. Launder, Reece and Rodi's [46] Reynolds-stress model is therefore adopted because of its well validation and wide application, which is given by

$$C_{ij} = P_{ij} + Ps_{ij} + D_{ij} - \varepsilon_{ij} \tag{3.15}$$

where

$$C_{ij} = U_k \frac{\partial \overline{u_i u_j}}{\partial X_k}$$

$$P_{ij} = -\left[\overline{u_i u_k} \frac{\partial U_j}{\partial X_k} + \overline{u_j u_k} \frac{\partial U_i}{\partial X_k} \right]$$

$$Ps_{ij} = -C_1 \frac{\varepsilon}{k} \left(\overline{u_i u_j} - \delta_{ij} \frac{2}{3} k \right) - C_2 \left(P_{ij} - \delta_{ij} \frac{2}{3} P_r \right)$$

$$D_{ij} = C_s \frac{\partial}{\partial X_k} \frac{k}{\varepsilon} \left[\overline{u_i u_m} \frac{\partial \overline{u_j u_k}}{\partial X_m} + \overline{u_j u_m} \frac{\partial \overline{u_k u_i}}{\partial X_m} + \overline{u_k u_m} \frac{\partial \overline{u_i u_j}}{\partial X_m} \right]$$

$$\varepsilon_{ij} = \frac{2}{3} \delta_{ij} \varepsilon$$

and C_s is an empirical constant with a value of 0.11. The modeling constants C_1 and C_2 are inertial and forced return-to-isotropy constants respectively, where their values will be discussed later on. It should be noted that in this model, a local isotropy is assumed, which will be valid as long as the cross flow (lateral or circumferential velocity) is not very large. Even the system of equations now is closed, solving these six partial differential equations coupled with k- and ε- equations is still not feasible for today's computer and engineering applications.

An approximation of the Reynolds-stress model proposed by Rodi [61] is very physics-explicable and economical-- the net transport of Reynolds stresses $\overline{u_i u_j}$ is proportional to the net transport of turbulent kinetic energy k with a factor of $\overline{u_i u_j}/k$, i.e.

$$C_{ij} - D_{ij} = \frac{\overline{u_i u_j}}{k} (C_k - D_k) \qquad (3.16)$$

In this approximation, it is assumed that $\overline{u_i u_j}/k$ varies but slowly across the flow field. By combining equations (3.13) and (3.15) with equation (3.16), an algebraic expression for $\overline{u_i u_j}$ is obtained as

$$\frac{\overline{u_i u_j}}{k} = \frac{\phi}{\varepsilon}\left[P_{ij} - \frac{2}{3}\delta_{ij}P_r\right] + \frac{2}{3}\delta_{ij} \tag{3.17}$$

where

$$\phi = \frac{1 - C_2}{C_1 - 1 + \dfrac{P_r}{\varepsilon}}$$

This approximation will be invalid only when $\overline{u_i u_j}/k$ change greatly, i.e. D($\overline{u_i u_j}/k$) / Dt is not negligible, so it is not suitable for the near-wall region. Although equation (3.17) is in algebraic form, it is difficult to incorporate with the k-ε model because the six Reynolds stress components are coupled. In order to further simplify this algebraic formulation, the understanding and analysis of flow characteristics are necessary.

There are three kinds of basic streamline curvature: 1) *local curvature* such as separation bubbles and flows over an airfoil, 2) *longitudinal curvature* such as flows through a curved duct, and 3) *lateral curvature* such as swirling

flows. The coordinate system for each flow field is somewhat different, and also both the main strain rate and the extra strain rate vary in each case.

3.3.1 Local curvature

For flows subjected to local curvature, the streamwise direction basically does not change much, for example the flow over an airfoil or the separated flow in a backward-facing step geometry. In this case, the two-dimensional Cartesian coordinate system is selected. The streamwise direction is defined to be along the x-coordinate, i.e. i, j, or k = 1, and the transverse direction will be in y-coordinate as i, j, or k = 2. The velocity components are defined as $U = U_1$, $u = u_1$ in the streamwise direction, and $V = U_2$, $v = u_2$ in the transverse direction respectively. According to Bradshaw [30], the extra rate of strain is $\partial V/\partial x$ besides the main strain rate $\partial U/\partial y$ for the flows with streamline curvature in Cartesian coordinates. By keeping terms associated with these two strain rates, and through some elaborate manipulation, the primary Reynolds shear stress $-\overline{uv}$ is obtained as

$$-\overline{uv} = \frac{k^2}{\varepsilon}\frac{\partial U}{\partial y}\frac{2}{3}\phi\left[1 - R_f - \phi\frac{P_r}{\varepsilon}\frac{R_f^2 + 4R_f + 1}{1 - R_f}\right] \tag{3.18}$$

where the flux Richardson number R_f is

$$R_f = - \frac{\partial V / \partial x}{\partial U / \partial y}$$

The detailed derivation procedure will be described in **Appendix B**. By collaborating with the Boussinesq's eddy-viscosity concept as shown in equation (3.8), an algebraic expression for the eddy viscosity μ_t can be derived as

$$\mu_t = \rho \frac{k^2}{\varepsilon} \frac{2\phi}{3} \left[1 - R_f - \phi \frac{P_r}{\varepsilon} \frac{R_f^2 + 4R_f + 1}{1 - R_f} \right] \tag{3.19}$$

With the flux Richardson number embedded in the eddy-viscosity formulation, streamline curvature can influence the eddy viscosity and so the Reynolds stress directly. It is evident that the flux Richardson number R_f is positive for convex curvature (*stabilizing effect*), and so the eddy viscosity is reduced. On the other hand, concave curvature (*destabilizing effect*) gives a negative R_f and will enlarge the eddy viscosity. This modification is therefore qualitatively consistent with the physics of the problem and conclusions reached from the experimental studies. The effects of streamline curvature vanish as $R_f = 0$, and the eddy viscosity becomes

$$\mu_t = \rho \frac{k^2}{\varepsilon} \frac{2}{3} \phi \left[1 - \phi \frac{P_r}{\varepsilon} \right] \tag{3.20}$$

In order to determine two return-to-isotropy modeling constants, C_1 and C_2, in equation (3.17), the above equation will be matched with the correlation for the eddy viscosity in the standard k-ε model at the free stream condition where there is no curvature effect and the production rate is equal to local dissipation rate, i.e. where local equilibrium prevails, and hence

$$C_\mu = \frac{2}{3} \phi_0 (1 - \phi_0) \tag{3.21}$$

where

$$\phi_0 = \frac{1 - C_2}{C_1}$$

The values of C_1 and C_2 have been determined empirically by several researchers such as Launder, Reece and Rodi [46] ($C_1 = 1.5$, $C_2 = 0.4$), Gibson and Launder [76] ($C_1 = 1.8$, $C_2 = 0.6$), Gibson and Younis [77] ($C_1 = 3$, $C_2 = 0.3$), and Gibson and Launder [78] ($C_1 = 2.2$, $C_2 = 0.55$). Kim and Chung [63] also observed that $1.5 \leq C_1 \leq 1.8$, and $0.5 \leq C_2 \leq 0.8$. However, the variations of C_1 and C_2 are expected not to affect the results substantially, which also will

be demonstrated in the numerical predictions later on. In the present model, C_1 = 1.5 is selected which will yield C_2 = 0.76 from equation (3.21).

3.3.2 Longitudinal curvature

The streamwise direction can change drastically for the flows subjected to longitudinal curvature, for example the flow in an S-bend duct or any curved ducts. Consequently, the two-dimensional Cartesian coordinates may not be suitable in this flow field because the assumption for the extra strain rate is no longer valid. In this case, the approximation procedure will be performed based on a two-dimensional streamline coordinate (s,n) system, where s-coordinate is in streamwise direction as i, j or k = 1, and n-coordinate represents the direction normal to s-coordinate as i, j or k = 2. The velocity components are designated as $U = U_1$ and $u = u_1$ in the streamwise direction, and $V = U_2$ and $v = u_2$ in the normal direction. The term--U/R is known to represent the extra rate of strain in the s-n coordinate system in addition to the main rate of strain $\partial U/\partial n$ (see Ref. [30]). By retaining the terms associated with these two strain rates and following the similar procedure as that in the Cartesian coordinate, the modified eddy viscosity μ_t can be derived as shown in **Appendix C**, and hence

$$\mu_t = \rho \frac{k^2}{\varepsilon} \frac{2\phi}{3} \left[1 - R_f - \phi \frac{P_r}{\varepsilon} \frac{R_f^2 + 4R_f + 1}{1 - R_f} \right] \tag{3.22}$$

where

$$R_f = \frac{2\dfrac{U}{R}}{\left(1 + \dfrac{n}{R}\right)\dfrac{\partial U}{\partial n} + \dfrac{U}{R}}$$

and R is the radius of surface curvature, n is the normal distance away from the wall. For convex curvature, the radius R has the same direction as n, so R is positive; while the radius R is in the opposite direction as n for concave curvature, hence R is negative.

It is interesting to note that equation (3.22) is exactly the same as equation (3.19), except the definition of the flux Richardson number R_f is different. This is very practical for engineering applications which implies no change of formulation for different coordinate systems. It is easy to recognize that the eddy viscosity in equation (3.22) will be diminished for convex curvatures due to the positive radius of surface curvature and flux Richardson number. The increase of the eddy viscosity of course will be introduced with the application of concave curvature because of the negative radius of surface curvature and negative R_f.

3.3.3 Transverse curvature

Transverse curvature occurs when flows have swirl. The cylindrical coordinate system, $X_i = [x, y, \theta]$, will be used with $x = X_1$ in longitudinal (axial) direction, $r = X_2$ in the radial direction, and $\theta = X_3$ in circumferential direction. The symbols $U_i = [U, V, W]$ and $u_i = [u, v, w]$ represent the mean and fluctuating velocity components in the x, r and θ direction respectively. It is to be noted that the additional terms introduced by the swirling component appear not only in the Reynolds-stress productions but also in the Reynolds-stress convections, which was proved by **Johnson [84]**, and **Humphrey and Chang [85]**. The full Reynolds stress equations are complicated, as shown in Appendix D, hence some assumptions are necessary in order to simplify the modified model. Axisymmetric, thin-shear-layer, and weak swirl are therefore assumed for the proposing model, which lead to $\partial/\partial\theta \approx 0$, $\partial/\partial r \gg \partial/\partial x$, and $W/r \ll \partial W/\partial r$. The weak swirl approximation is also consistent with the constraint, isotropic turbulence, of most turbulence models including the k-ε model. The anisotropic effect becomes more important as the swirl increases. With the above assumptions and following the similar derivation procedure of two proposed models, the modified eddy viscosity μ_t can be derived as shown in Appendix D, and hence

$$\mu_t = \rho \frac{k^2}{\varepsilon} \frac{2\phi}{3} \left[1 - \phi \frac{P_r}{\varepsilon} \frac{1 + 2R_f}{1 - R_f} \right] \tag{3.23}$$

where

$$R_f = \frac{2 \frac{W}{r} \frac{\partial W}{\partial r}}{\left(\frac{\partial U}{\partial r} \right)^2 + \left(\frac{\partial W}{\partial r} \right)^2} \tag{3.24}$$

It is evident that the flux Richardson number R_f is positive when the extra rate of strain, $W\partial W/(r\partial r)$, is positive, and so the eddy viscosity μ_t is reduced by this effect, which can be seen from equation (3.23). Whereas, the enhancement of the eddy viscosity μ_t can be achieved by the introduction of the negative flux Richardson number, i.e. the extra rate of strain is negative. Comparing equation (3.23) with equations (3.19) and (3.22), we can easily find even though the eddy viscosity formulations are different, the effects of the extra rate of strains, embedded in the flux Richardson numbers, on the eddy viscosity μ_t are essentially the same.

The computational predictions by these three modified models will be compared with the experimental measurements, and will be further discussed in chapter V (Results and Discussions).

3.3.4 Wall function

As indicated in the literature, [11], [13]-[15]; the near-wall turbulent structure is not significantly affected by the surface curvature. Hence, the standard wall function, suggested by Launder and Spalding [75] and used in TEACH-based program, will be applied in the present research. Detailed description is explained in Ref. [75] and Ref. [79].

CHAPTER IV

NUMERICAL METHOD

4.1 Equation Integration

A two-dimensional and a three dimensional Navier-Stokes flow solvers (FDNS-2D and FDNS-3D) embedded with the k-ε model, developed by **Y.S. Chen [80-82]**, are used to test the proposed model in the present study. The transport equations of the mean flow and turbulence model are transformed into the general curvilinear coordinates (ξ, η, ζ). The system of coupled transformed equations is discretized into a set of linearized algebraic equations. In the discretization process, several techniques are employed to stabilize the numerical integration and maintain the same order of accuracy.

1) A time-centered (Crank-Nicholson) difference scheme is utilized for the temporal discretization.

2) A second-order central difference method plus a damping term are used to manage the convection terms. The damping term could be either fourth order, deduced from second-order upwind differencing scheme, or second order, resulted from first-order

upwind differencing scheme. With the coefficient of the damping term being specified explicitly, the numerical stability of the matrix solver can be enhanced.

3) The diffusion, production and other source terms are discretized with the second-order central differencing scheme to maintain the same numerical accuracy.

The set of discretized linear equations is solved by an alternating direction linear-relaxation method (ADI) with a simplified predictor-corrector algorithm. In this pressure-based predictor-corrector solution procedure, an explicit fourth-order pressure smoothing term is added to the velocity-pressure coupled discrete equation, derived approximately from the discrete continuity and momentum equations, to inhibit the instability in the pressure solution. For each time step, the predictor-corrector loop will be executed iteratively until the conservation of mass is satisfied.

4.2 Grid Generation

Although there will be a variety of flow geometries, orthogonal grids system would be generated to avoid the ill-conditioned matrix caused by large grid skewness. Figure 1 illustrates the grid system for a backward-facing step,

and the mesh system for a 30°-45° S-bend duct is exhibited in Figure 2. Grid packing near the wall and large gradient zones may also be observed in Figures 1 and 2.

CHAPTER V

RESULTS AND DISCUSSIONS

To evaluate the performance of the proposed turbulence model, various curved flows are examined in the present study. According to the previous classification of streamline curvature, numerical computations are performed on different geometries for each type of curvature effects. The numerical predictions and discussions are divided into 1) local curvature, 2) longitudinal curvature, and 3) transverse curvature.

5.1 Local Curvature

A backward-facing step with separation and reattachment provides the geometry for local flow curvature. **Driver and Seegmiller [83]** conducted an experimental investigation on the incompressible turbulent flow over a backward-facing step with an area ratio of 8:9. The grid system is shown in Figure 1 and the detailed information about the test configuration is provided in Figure 3. To study the effect of varying modeling constant values (C_1 and C_2) and the dependence of the cell size on the numerical predictions, two sets

of grid systems (61 x 41 or 111 x 45) along with different values for modeling constants (C_1 = 1.5 or C_1 = 1.8) are tested for the present model.

First, a comparison is made between the present model and the standard k-ε model with C_1 = 1.5 and 61 x 41 grids. The improvement by the present model is discernible from the locus of flow reversal illustrated in Figure 4. The result shows that the flow separation from the step wall generates the effect of convex curvature, which attenuates the eddy viscosity and actually causes the flow to reattach further downstream. Since there is no mechanism in the standard k-ε model to simulate the curvature effect, a predicted convex shear layer exhibits higher viscosity and early reattachment takes place. Figure 5 demonstrates better predictions by the present model on the streamwise velocity profiles.

The more rapid change of the velocities in the recirculation zone predicted by the standard k-ε model indicates the higher energy generated by the larger eddy viscosity. The turbulent kinetic energy profiles shown in Figure 6, indicate the reduction of the turbulent kinetic energy by the convex curvature in the present model. However, both models underpredict the turbulent kinetic energy when the flow is near the reattachment location. This is possibly attributed to the effect of large-scale eddy, which becomes pronounced inside

the recirculation zone; and the current single-time-scale model fails to capture this phenomenon.

The prediction on the Reynolds shear stress $-\rho\overline{uv}$ by the present model, as shown in Figure 7, appears to be reasonably accurate. The success of the prediction of the Reynolds shear stress in the recirculation zone reveals validity of the eddy viscosity formulation. Meanwhile, it is worth noting that the present model costs 755 seconds of Cray X-MP CPU time (for 3122 time iterations) to converge to an accuracy of 5×10^{-4}, while 572 seconds of Cray X-MP CPU time (for 2486 time iterations) are required by the standard k-ε model to converge to the same accuracy. It is encouraging that with all the improvements of the numerical predictions by the present model, only three minutes of Cray X-MP CPU time in addition are introduced. This shows the practicality and feasibility of the current approach for the complex engineering applications involving curvature. The velocity contours, static pressure contours, and velocity vector plots for both the standard k-ε model and the present model are displayed in Figures 8-13.

To demonstrate the insensitivity of the modeling constant C_1 value on computational results, a comparative investigation between $C_1 = 1.5$ and $C_1 = 1.8$ is performed. Figures 14-17 illustrate almost identical results of the flow reversal locations, streamwise velocity profiles, turbulent kinetic energy profiles,

and Reynolds shear stress profiles between the two C_1 values. The above exercise satisfies our previous statement that the performance of the present model is insensitive to a reasonable variation of C_1 value. The remaining computations are performed with the empirical coefficient C_1 specified as 1.5.

By increasing the grid numbers from 61 x 41 to 111 x 45, a better description of not only the change of streamline curvature but also the discrete flow field is expected to be achieved. From Figures 18-21, it appears that the numerical calculations of the locus of flow reversal, streamwise velocity, turbulent kinetic energy, and the Reynolds shear stress profiles are independent of the grid size. With the same accurate results, the medium grids instead of finer grids will be employed to save the computing time.

To achieve further verification of the proposed model with local curvature effect, the numerical prediction on a backward-facing step with an area ratio of 2:3, tested by **Kim, Kline, and Johnston [86]**, is conducted and the computational result is compared with the experimental data. The layout of the backward-facing step is sketched as shown in Figure 22 and will be discretized into an 85 x 51 mesh system. The improvement of the present model, as indicated in Figure 23, is consistent with the result of the previous backward-facing step case. It is evident that the locus of flow reversal, plotted in Figure 23, reveals the superiority of the proposed model over the standard

k-ε model in predicting the larger recirculation zone. This is indicative of the attenuation of the eddy viscosity caused by the effect of convex curvature. The measured reattachment length x_R is 7±1 step heights; and it verifies the prediction of the present model with later reattachment. The variation of x_R is due to the inherent unsteadiness of the flow field.

Figure 24 exhibits better performance of the present model in capturing the streamwise velocity profiles. The reduction of the turbulent kinetic energy by the effect of convex curvature in the recirculation zone is substantiated by the agreement between experimental data and numerical predictions of the present model, which is illustrated in Figure 25. The Reynolds shear stress $-\overline{uv}$ profiles shown in Figure 26 reveal better predictions of the present model. The successful predictions of the turbulent kinetic energy and the Reynolds shear stress by the present model indicates that the proposed formulation for the eddy viscosity is capable of describing the characteristics of the flow separation with curvature effect. Figure 27 also illustrates that the proposed model can predict the wall static pressure coefficients better than the standard k-ε model.

Although the overall predictions of the present model are reasonably successful, there is some discrepancy between experimental results and numerical predictions. The disagreement can be attributed not only to the unsteadiness of the flow field but also to additional turbulence phenomena, such

as large-scale eddy and anisotropy not accounted in our theory. Therefore, it is suggested that further improvement on the proposed model be made by taking into account the physics of the large-scale eddy and anisotropy. This will be explained further in chapter VI--"SUMMARY" of this report. The detailed descriptions of the flow field computed by both the standard k-ε and the present model, such as velocity contours, velocity vectors, and particle traces, are shown in Figures 28-31.

5.2 Longitudinal Curvature

The most typical longitudinal curvature occurs in a flow through a curved duct. An S-bend duct is a more complicated geometry because the second bend of the duct creates an effect opposite to that of the first bend. In this case, if the model can not capture well the effect of curvature in the first-bend section, the error will accumulate in the second bend and cause the collapse of the model. A 30°-45° S-bend duct with an aspect ratio of 5.6, measured by Butz [23], will be tested against the present model. The detailed description of the facility and the inlet flow conditions are shown in Figure 32. An 88 x 51 grid system is constructed, as shown in Figure 2; and the inlet velocity and turbulent intensity profiles are prescribed.

The comparison of static pressure coefficients along the curved wall is illustrated in Figure 33. It seems that in the first bend, both models fail on the upper surface (concave side), but succeed on the lower surface (convex side). In the second bend, the present model does a better job in predicting surface pressure than the standard k-ε model. One might question the success of the predicted results on the upper surface (convex side) in the second bend by the present model. However, as the measured data exhibits some randomness and the present model predicts the exit static pressure relatively well, the numerical prediction of the present model can be considered to be reasonably successful. The discrepancy on the upper surface in the first bend is suspected of being caused by the Görtler-like secondary flows. This occurs at the onset of the concave curvature, where the normal velocity is numerically set equal to zero numerically at the entrance plane. There is no experimental measurement of the normal velocity component at the entrance plane. The error of predicted static pressure on the upper surface (concave side) in the first bend is considered to be the primary source of deviation of the numerical calculation from experimental result on the same surface (convex side) in the second bend.

The longitudinal velocity profiles at the inlet, inflection and exit planes from the experimental results and both computational models are compared in Figures 34-36. The results demonstrate that the proposed turbulence model has

a better agreement with the experimental data than the standard k-ε model. The slight deviations of the longitudinal velocity from the measured data at the inflection and exit planes are attributed to the effect of the small secondary flow. With 88 x 51 grids, the present model converges to 5 x 10^{-4} in 110 seconds of Cray X-MP CPU time with 199 time iterations, while the standard k-ε model consumes 116 seconds with 218 time iterations. It is interesting to note that the present model has improved the numerical predictions without increasing the computing time substantially. The contour plots of x-component velocity, y-component velocity, and static pressure are also shown in Figures 37-39 for both the present and the standard k-ε models.

The 30°-45° S-bend duct does not demonstrate the superiority of the proposed model over the standard k-ε model very well because the surface curvature is relatively small. The centerline radius of curvature is five times the duct width, and hence the effect of streamline curvature does not dominate the flow field significantly. A 2-D curved duct with small radius of curvature (strong curvature), therefore, is required to evaluate the performance of the present model in predicting the development of turbulence structures subjected to strong curvature effect. A 10-by-100 centimeter, 180-degree-turn water tunnel, with a 10 cm centerline radius of curvature, investigated by **Sandborn and Shin [87]**, is employed as the next test case. The configuration of the 180°

turn-around duct (TAD) and inlet conditions are described in Figure 40. The flow field in the 180° turn-around duct with strong curvature, especially, is of great engineering interest due to its resemblance to the flow passage downstream of the turbine in the fuel preburner of the Space Shuttle Main Engine (SSME) as well as STOVL applications. Complex shear layers, regions of separation, high levels of unsteadiness, and three-dimensional structure may occur in this type of flow field. A 141 x 41 orthogonal grid system is constructed for this case, as shown in Figure 41.

The longitudinal velocity profiles in Figure 42 display the similarity between the predictions of the present model and those of the standard k-ε model upstream of the flow separation. However, the results demonstrate the success of the present model and the collapse of the standard k-ε model in capturing the separation bubble on the inner surface (convex curvature) near the 180° turn. Once again, as with its failure to predict the flow in a backward-facing step, the standard k-ε model is inadequate in describing the change of the eddy viscosity (or the length scale) attributed to the effect of streamline curvature. The larger eddy viscosity along the inner surface predicted by the standard k-ε model prevents the occurrence of flow separation; whereas, smaller eddy viscosity computed by the present model, benefiting from curvature correction, enables the natural onset of flow separation. The numerical results

of the present model reveal that flow starts to separate after 170° turn. Figure 43 provides a detailed description about the longitudinal velocity distribution in the separation bubble downstream of 180° turn. The results indicate that the proposed implementation to the standard k-ε model is necessary and proper.

The wall static pressure coefficient C_p is plotted as shown in Figure 44. It is surprising that the standard k-ε model predicts much better than the present model even without predicting flow separation. However, the pressure distribution calculated by the present model does show the signature of flow separation where the static pressure recovery along the inner surface is retarded. That is the location where the predicted static pressure coefficient C_p by the present model starts to deviate from the measured data. Hence, the relative value of the measured static pressure is doubtful. It was later discovered in Ref. [87] that screens were placed at the outlet of the channel, which is about four channel widths downstream of 180° turn, to increase the flow exit resistance such that the water completely filled the channel. However, the screen raised the adverse pressure gradient at the exit and caused the exit static pressure to be larger than it would have been. To support this argument, another 180° turn-around duct will be examined next. Some information about the flow field such as x- and y-component velocity contours, static pressure contour, velocity vectors, and particle traces are shown in Figures 45-49. The

separation bubble can be observed clearly from the plots of the velocity vectors and particle traces.

A further validation will be made by examining a 2-D U-duct investigated by **Monson and Seegmiller [88]**. The geometry of the coordinate system, and the inlet conditions, are illustrated in Figure 50. The ratio of the centerline radius of curvature to the channel width is equal to unity, while a 234 x 101 mesh system is constructed due to longer inlet and exit ducts as well as higher Reynolds number.

The numerical results reveal that both the present and standard k-ε models predict flow separations. Nevertheless, the flow field calculated by the present model is observed to separate earlier (ahead of 180° turn) and reattach later, which is consistent with the experimental measurement. A later flow separation (preceded by 180° turn) and an earlier reattachment are suggested by the standard k-ε model. This is confirmed by the comparison of longitudinal velocity profiles as shown in Figure 51. Nevertheless, the present model seems to under-estimate the thickness of the separation bubble. It is then found in Ref. [88] that the thickness of the separation bubble in the Re = 10^6 case is larger than that in the Re = 10^5 case; while most of the turbulence models, including the present model, predict it differently. From the physical arguments, the Reynolds number trend in experimental results seem to be doubtful.

The distribution of wall static pressure coefficient C_p, plotted in Figure 52, supports the previous argument. The present model has better agreement than the standard k-ε model in predicting the static pressure. Furthermore, the signature of flow separation presented by the proposed model does match the flow characteristic near the exit of 180° turn. However, both models fail to predict the static pressure at the downstream exit plane. It seems that the actual flow separates earlier than the present model, and this causes the present model to predict larger static pressure recovery at the exit. It is apparent from these comparisons that the present model performs a better overall prediction, due to the adjustment to the effect of surface curvature, than the standard k-ε model, especially on the convex surfaces where the attenuation of the eddy viscosity plays an essential role in the occurrence of flow separation. The contour plots of x- and y-component velocities as well as static pressure are illustrated in Figures 53-55, respectively. The plots of velocity vectors and particle traces, as shown in Figures 56-57, indicate an earlier, larger flow separation by the present model and a later, smaller flow separation by the standard k-ε model.

5.3 Transverse Curvature

One representative of the class of flows with transverse curvature is the swirling flow. There are two constraints in selecting the test cases to validate

the proposed model with the effect of transverse curvature. First, the flow must have small swirl number such that the characteristics of the flow is consistent with the assumptions, i.e. weak swirl and isotropic turbulence, made in the present model. Second, confined swirling flows in straight pipes would be employed for the purpose of avoiding the interference from other curvature effects such as surface curvature effect, and also maintaining the axisymmetry of the flow. The numerical computations of the standard k-ε and the present models for the effect of transverse curvature will be conducted in the form of 2-D axisymmetric instead of truly three-dimensional test case.

An experimental study on a confined swirling coaxial jet in a straight pipe with the swirl number equal to 0.21, investigated by **Roback and Johnson [89]**, is therefore chosen to be the test case. A 151 x 45 grid system is built up for this flow geometry, and the schematic of the configuration along with the inlet conditions are illustrated in Figure 58. The inlet velocity profiles and turbulence quantities are specified at 5 mm downstream of the jet nozzle. With such a small swirl number, a vortex breakdown occurs in this flow field because of the combination of axial and radial pressure gradients. The radial pressure gradient is induced by the centrifugal force, while the axial pressure gradient is attributed to both centrifugal force of the swirling flow and the diffusing geometry of the experimental set up, i.e. dump diffuser.

Consequently, the comparison of the mean axial velocity along the centerline, demonstrated in Figure 59, is one indication for the performance of both models. Although both models fail to depict the size of the central recirculation zone, as caused by overpredicting the eddy viscosity, the present model appears as an improvement over the standard k-ε model. The large eddy viscosity computed by both models is suspected to be strongly related to the specification of the length scale at the inlet boundary. The inlet length scale is not available from the experimental results, and is assumed to be one percent of the pipe diameter. The change of the inlet length scale is expected to greatly alter the numerical results; but it is not the main concern in the present study.

A detailed comparison of the mean axial velocities is illustrated in Figure 60. The experimental results show some random scatter, which is partially caused by the non-axisymmetric phenomenon. It is evident that the present model does provide minor improvements over those by the standard k-ε model, but the improvements are insufficient to satisfy the physical characteristics of the flow. In addition to the uncertainty of the inlet length scale, the following reasons may be cited: 1) the additional streamline curvature caused by the central recirculation zone affects the flow field, 2) asymmetric flow, 3) anisotropic turbulence characteristics, and finally, the inadequacy of the current implementation approach for swirling flows. To identify the causes for only a

minor improvement by the present model, another confined swirling flow case will be examined later on.

The mean azimuthal and radial velocity profiles, plotted in Figures 61-62, indicate that the present model predicts better than the standard k-ε model, but the results are relatively similar. A detailed description of the flow field such as the axial and the radial velocity contours, the velocity vectors, and the particle traces are reported in Figures 63-66. The central recirculation zone predicted by the present model is larger than that suggested by the standard k-ε model, and can be clearly observed from the particle trace plot.

The next test case for the transverse curvature effect is the confined swirling flow studied by **Weske and Sturov [90]**. The layout of the test section and the specification of the inlet conditions are exhibited in Figure 67. With the inlet velocity profiles and turbulence quantities prescribed at 3.5 cm downstream of the swirl generator, the inlet swirl number is calculated to be 0.43 and has a distribution of solid body rotation.

The axial velocity profiles are compared in Figure 68 but with the absence of experimental data, because it is not reported in Ref [90]. As shown in Figure 68, almost identical numerical results are predicted by both models. In Figure 69, the comparisons of the circumferential velocities illustrate that the standard k-ε model predicts slightly better than the present model. This is

contrary to the results in the previous swirling flow case. However, both models predict faster mean flow decay of the swirling flow than the experimental results indicate. The present implementation approach to include the effect of transverse curvature (swirling effect) is proved to be inadequate based on the results of two swirling flows. It is believed that the derivation of the eddy viscosity μ_t from the equation of the Reynolds shear stress $\overline{uv}$ is improper. The reason for the deficiency is that the other Reynolds shear stress components, $\overline{uw}$ and $\overline{vw}$, are of the same order of magnitude as the shear stress tensor $\overline{uv}$ in the swirling flows. Therefore, difficulty will be encountered in choosing the Reynolds shear stress component from which the scalar eddy viscosity would be determined. Employment of the scalar eddy viscosity is not considered to be suitable for the flow with swirling effect. Instead, a vector eddy viscosity for each Reynolds shear stress, or calculating each Reynolds stress tensor through algebraic equations, as derived similarly in the present study, is recommended for this type of flow for future studies.

CHAPTER VI

SUMMARY

6.1 Conclusions

The results of the test cases, employed to study the effects of local and longitudinal curvatures, show the success of the proposed eddy viscosity formulation in improving the numerical prediction capability of the standard k-ε model consistently. Moreover, the present model offers the following advantages, namely 1) generality--same formulation for the eddy viscosity in both Cartesian and Streamline coordinates, 2) convenience--the formulation for the eddy viscosity is easy to be adopted into various one- and two-equation models, 3) efficiency--the required computer CPU time by the present model is nearly the same as the standard k-ε model.

In the backward-facing step flows, the present model is indeed capable of dictating the effect of local curvature rendered by flow separation and hence capturing the attenuation of the eddy viscosity. The present model, however, still underpredicts the reattachment point. This problem is attributable to the effects of large-scale eddy and anisotropy in the recirculation zone, especially

the latter one. The flow inside the recirculation zone is basically dominated by a large-scale eddy with low Reynolds number. This is a deficiency of the high-Reynolds-number k-ε model used in this study. It is also known that the anisotropic effect becomes dominant as the flow approaches the wall, thus the effect plays an important role near the reattachment region. Consequently, the proposed model could be significantly improved with the consideration of these two effects.

In the curved-duct flows, the present model demonstrates a good agreement with the measured data. The major success of the present model is to predict the flow separation in curved ducts by accounting for the effect of wall curvature. With the absence of the curvature effect, the standard k-ε model appears to predict the flow without separation or with later and smaller separation zone. However, the discrepancy between the measured data and the numerical results takes place when the present model estimates the size of separation bubbles. As discussed in chapter five, the experimental results are believed to be questionable. Hence, a more detailed and reliable experiment for the 180-degree turn-around duct is required to further validate the present model in predicting the size and location of the separation bubble.

For the flows with swirling effect, the present model does not improve the numerical predictions consistently. In spite of depicting the size of vortex

breakdown in the confined swirling coaxial jets better than the standard k-ε model, the present model overpredicts the eddy viscosity and results in faster decay of the circumferential velocity in the confined swirling pipe flow. The current approach to include the effect of transverse curvature, deducing the scalar eddy viscosity from the equation of the Reynolds shear stress $\overline{uv}$, is thus considered to be improper for the flows subjected to swirling effect. With the dominance of the anisotropic effect in the swirling flows, each Reynolds shear stress term can be of the same order of magnitude and should have its corresponding eddy viscosity formulation, respectively. Therefore, the effect of transverse curvature should be accounted for either by employing a vector form of the eddy viscosity or by solving for each Reynolds stresses directly through approximated algebraic equations. Although, the numerical predictions of the swirling flows by the present model show deficiencies, a qualitative improvement is accomplished, which reveals that the extra rate of strain should be included to account for the effect of transverse curvature. The implementation of transverse curvature is expected to be more complicated than those for the local and longitudinal curvatures due to turbulence anisotropy.

The present model demonstrates improvements to the prediction capability of turbulent flows dominated by local and longitudinal curvatures over the standard k-ε model. The effect of transverse curvature, as in swirling

flows, requires more elaborate formulation of the eddy viscosity and should be included in future work.

6.2 Recommendations for Future Work

1) The present model demonstrates good predictions in the backward-facing step cases, where the effect of local curvature prevails. It is recommended that the anisotropic effect be included, hence the reattachment length can be predicted more precisely.

2) A more extensive experimentation on the 180-degree turn-around duct is required to evaluate the performance of the present model in predicting the separation bubble rendered by the effect of wall curvature (longitudinal curvature).

3) A vector form of the eddy viscosity or solving the algebraic Reynolds stress equations should be employed to account for the effect of transverse curvature (swirling flows). The effect of strong anisotropy will result in the breakdown of the algebraic eddy viscosity approach. The adoption of the extra rate of strain induced by the curvature effect should still be valid, but each components of the vector eddy viscosity should be attained from corresponding Reynolds stresses.

REFERENCES

1. **Rayleigh, L.,** "On the Dynamics of Revolving Fluids," Proceeding Royal Society, A 93, 1916, pp. 148-154.

2. **Taylor, G.I.,** "Distribution of Velocity and Temperature Between Concentric Rotating Cylinders," Proceeding Royal Society, A 151, 1935, pp. 494-512.

3. **Hawthorne, W.R.,** "Secondary Circulation in Fluid Flow," Proceeding Royal Society, A 206, 1951, pp. 374-387.

4. **Squire, H.B. and Winter, K.G.,** " The Secondary Flow in a Cascade Airfoils in a Non-uniform Stream," Journal of Aeronautical Science, Vol. 18, 1951, pp. 271-277.

5. **Muck, K.C., Hoffmann, P.H., and Bradshaw, P.,** "The Effect of Convex Surface Curvature on Turbulent Boundary Layers," Journal of Fluid Mechanics, Vol. 161, 1985, pp. 347-369.

6. **Hoffmann, P.H., Muck, K.C., and Bradshaw, P.,** "The Effect of Concave Surface Curvature on Turbulent Boundary Layers," Journal of Fluid Mechanics, Vol. 161, 1985, pp. 371-403.

7. **Smits, A.J., Young, S.T.B., and Bradshaw, P.,** "The Effect of Short Regions of High Surface Curvature on Turbulent Boundary Layers," Journal of Fluid Mechanics, Vol. 94, 1979, pp. 209-242.

8. **Castro, I.P. and Bradshaw, P.,** "Turbulent Structure of a Highly Curved Mixing Layer," Journal of Fluid Mechanics, Vol. 73, 1976, pp. 265-304.

9. **Meroney, R.N. and Bradshaw, P.,** "Turbulent Boundary-Layer Growth over a Longitudinal Curved Surface," AIAA Journal, Vol. 13, 1975, pp. 1448-1453.

10. **Bansod, P. and Bradshaw, P.,** "The Flow in S-Shaped Ducts," Aeronautical Quarterly, 1972, pp. 131-140.

11. **Gillis, J.C. and Johnston, J.P.,** "Turbulent Boundary-Layer Flow and Structure on a Convex Wall and It's Redevelopment on a Flat Wall", Journal of Fluid Mechanics, Vol. 135, 1983, pp. 123-153.

12. **Hunt, I.A. and Joubert, P.N.,** "Effects of Small Streamline Curvature on Turbulent Duct Flow," Journal of Fluid Mechanics, Vol. 91, 1979, pp. 633-659.

13. **Ramaprian, B.R. and Shivaprasad, B.G.,** "The Structure of Turbulent Boundary Layers along Mildly Curved Surfaces," Journal of Fluid Mechanics, Vol. 85, 1978, pp. 273-303.

14. **So, R.M.C. and Mellor, G.L.,** "Experiment on Convex Curvature Effects in Turbulent Boundary Layers," Journal of Fluid Mechanics, Vol. 60, 1973, pp. 43-62.

15. **So, R.M.C. and Mellor, G.L.,** "Experiment on Turbulent Boundary Layers on a Concave Wall," Aeronautical Quarterly, Feb. 1975, pp. 25-40.

16. **Tani, I.,** "Production of Longitudinal Vortices in the Boundary Layer along a Concave Wall," Journal of Geophysical Research, Vol. 67, No. 8, 1962, pp. 3075-3080.

17. **Agrawal, Y., Talbot, L. and Gong, K.,** "Laser Anemometer Study of Flow Development in Curved Circular Pipes," Journal of Fluid Mechanics, Vol. 85, 1978, pp. 497-518.

18. **White, C.M.,** "Streamline Flow through Curved Pipes," Proceeding Royal Society, A 123, 1929, pp. 645-663.

19. **Taylor, A.M.K.P., Whitelaw, J.H. and Yianneskis, M.,** "Developing Flow in S-Shaped Ducts," NASA CR-3550, 1982.

20. **Humphrey, J.A.C., Whitelaw, J.H. and Yee, G.,** "Turbulent Flow in a Square Duct with Strong Curvature," Journal of Fluid Mechanics, Vol. 103, 1981, pp. 443-463.

21. **Rowe, M.,** "Measurements and Computations of Flow in Pipe Bends," Journal of Fluid Mechanics, Vol. 43, Part 4, 1970, pp. 771-783.

22. **Humphrey, J.A.C. and Chang, S.M.,** "Measurement and Calculation of Developing Turbulent Flow in a U-Bend and Downstream Tangent of Square Cross-Section," Contract Report No. N00014-80-C-0031, Office of Naval Research, Dec. 1981.

23. **Butz, L.A.,** "Turbulent Flow in S-Shaped Ducts," M.S. Thesis, Aeronautics and Astronautics Dept., Purdue University, 1979.

24. **Brinich, P.F. and Graham, R.W.,** "Flow and Heat Transfer in a Curved Channel," NASA TN D-8464, 1977.

25. **Singh, M.P.,** "Entry Flow in a Curved Pipe," Journal of Fluid Mechanics, Vol. 65, Part 3, 1974, pp. 517-539.

26. **Stewartson, K., Cebeci, T. and Chang, K.C.,** "A Boundary-Layer Collision in a Curved Duct," Quarterly Journal of Mechanics and Applied Mathematics, Vol. 33, 1980, pp. 59-75.

27. **van Dyke, M.,** "Extended Stokes Series: Laminar Flow through a Loosely Coiled Pipe," Journal of Fluid Mechanics, Vol. 86, Part 1, 1978, pp. 129-145.

28. **Humphrey, J.A.C.,** "Numerical Calculation of Developing Laminar Flow in Pipes of Arbitrary Curvature Radius," The Canadian Journal of Chemical Engineering, Vol. 56, 1978, pp. 151-164, and pp. 624-626.

29. **Humphrey, J.A.C., Taylor, A.M.K. and Whitelaw, J.H.,** "Laminar Flow in a Square Duct of Strong Curvature," Journal of Fluid Mechanics, Vol. 83, Part 3, 1977, pp. 509-527.

30. **Bradshaw, P.,** "Effects of Streamline Curvature on Turbulent Flow," AGARDograph No. 169, 1973.

31. **Bradshaw, P.,** "The Analogy between Streamline Curvature and Buoyancy in Turbulent Shear Flow," Journal of Fluid Mechanics, Vol. 36, Part 1, 1969, pp. 177-191.

32. **Nallasamy, M.,** "A Critical Evaluation of Various Turbulence Models as Applied to Internal Fluid Flows," NASA TP-2474, 1985.

33. **Lakshminarayana, B.,** "Turbulence Modelling for Complex Flows," AIAA-85-1652, 1985.

34. **Towne, C.E. and Schum, E.F.,** "Application of Computational Fluid Dynamics to Complex Inlet Ducts," NASA TM-87060, 1985, also AIAA-85-1213, 1985.

35. **Towne, C.E. and Hoffman, J.D.,** "Computation of Viscous Flow in Planar and Axisymmetric Ducts by an Implicit Marching Procedure," NASA TM-83567, 1984, also AIAA-84-0256, 1984.

36. **Towne, C.E. and Hoffman, J.D.,** "Implicit Marching Solution of Compressible Viscous Subsonic Flow in Planar and Axisymmetric Ducts," NASA TM-82876, 1982, also Ph.D. Thesis, Purdue University, Dec. 1982.

37. **Vakili, A., Wu, J.M., Hingst, W.R. and Towne, C.E.,** "Comparison of Experimental and Computational Compressible Flow in a S-Duct," AIAA-84-0033, Jan. 1984.

38. **Cebeci, T. and Smith, A.M.O.,** Analysis of Turbulent Boundary Layers, Academic Press, New York, 1974.

39. **McDonald, H. and Camarata, F.J.,** "An Extended Mixing Length Approach for Computing the Turbulent Boundary Layer Development," Computation of Turbulent Boundary Layers- 1968 AFOSR-IFP-Stanford Conference, S.J. Kline, et. al., Editors, Stanford University, 1969, pp. 83-98.

40. **Baldwin, B.S. and Lomax, H.,** "Thin Layer Approximation and Algebraic Model for Separated Turbulent Flow," AIAA-78-257, 1978.

41. **Loeffler, Jr., A.L.,** "A Navier-Stokes Codes for S-Shaped Diffusers- A Review," International Journal for Numerical Methods in Fluids, Vol. 8, No. 4, April 1988, pp. 463-474.

42. **Beam, R.M. and Warming, R.F.,** "An Implicit Factored Scheme for the Compressible Navier-Stokes Equations," AIAA Journal, Vol. 16, No. 4, 1978, pp. 393-402.

43. **Anderson, O.L.,** "Calculation of Internal Viscous Flows in Axisymmetric Ducts at Moderate to High Reynolds Numbers," Computers and Fluids, Vol. 8, 1980, pp. 391-411.

44. **van Driest, E.R.,** "On Turbulent Flow near a Wall," Journal of Aeronautical Science, Vol. 23, 1956, pp. 1007-1011.

45. **Irwing, H.P.A.H. and Smith, P.A.,** "Prediction of the Effect of Streamline Curvature on Turbulence," The Physics of Fluids, Vol. 18, No. 6, June 1975, pp. 624-630.

46. **Launder, B.E., Reece, G.J. and Rodi, W.,** "Progress in the Development of a Reynolds-Stress Turbulence Closure," Journal of Fluid Mechanics, Vol. 68, Part 3, 1975, pp. 537-566.

47. **Gibson, M.M.,** "An Algebraic Stress and Heat-Flux Model for Turbulent Shear Flow with Streamline Curvature," International Journal of Heat, Mass Transfer, Vol. 21, 1978, pp. 1609-1617.

48. **So, R.M.C.,** "A Turbulence Velocity Scale for Curved Shear Flows," Journal of Fluid Mechanics, Vol. 70, Part 1, 1975, pp. 37-57.

49. **Mellor, G.L. and Herring, H.J.,** "A Survey of the Mean Turbulent Field Closure Models," AIAA Journal, Vol. 11, No. 5, 1973, pp. 590-599.

50. **Chang, S.M., Han, T. and Humphrey, J.A.C.,** "Prediction of Case 512," The 1980-1981 AFOSR-HTTM-Stanford Conference on Complex Turbulent Flows, S.J. Kline, et. al., Editors, Stanford University, 1981, Vol. I, pp. 155-160, and Vol. III, pp. 1375-1382.

51. **Patankar, S.V., Pratap, V.S. and Spalding, D.B.,** "Prediction of Turbulent Flow in Curved Pipes," Journal of Fluid Mechanics, Vol. 67, Part 3, 1975, pp. 583-595.

52. **Pratap, V.S. and Spalding, D.B.,** "Numerical Computations of the Flow in Curved Ducts," The Aeronautical Quarterly, Vol. 26, August 1975, pp. 219-228.

53. **Murthy, K.N.S. and Lakshminarayana, B.,** "Computation of Three-Dimensional Viscous Flows Using a Space-Marching Method," Journal of Aircraft, Vol. 22, No. 4, 1985, pp. 311-317.

54. **Pourahmadi, F. and Humphrey, J.A.C.,** "Prediction of Curved Channel Flow with an Extended k-ε Model of Turbulence," AIAA Journal, Vol. 21, No. 10, 1983, pp. 1365-1373.

55. **Santi, L.M.,** "Turbulent Flow Field Predictions in Sharply Curved Turn-Around Ducts," NASA CR-3990, 1986.

56. **Launder, B.E., Priddin, C.H. and Sharma, B.I.,** "The Calculation of Turbulent Boundary Layers on Spinning and Curved Surfaces," Transaction of the ASME, Journal of Fluids Engineering, March 1977, pp. 231-239.

57. **Sharma, B.I.,** "Computation of Flow Past a Rotating Cylinder with an Energy-Dissipation Model of Turbulence," AIAA Journal, Vol. 15, 1977, pp. 271-274.

58. **Rodi, W. and Scheuerer, G.,** "Calculation of Curved Shear Layers with Two-Equation Turbulence Models," Physics of Fluids, Vol. 26, No. 6, 1983, pp. 1422-1436.

59. **Galmes, J.M. and Lakshminarayana, B.,** "Turbulence Modeling for Three-Dimensional Shear Flows over Curved Rotating Bodies," AIAA Journal, Vol. 22, No. 10, 1984, pp. 1420-1428.

60. **Warfield, M.J. and Lakshminarayana, B.,** "Computation of Rotating Turbulent Flow with an Algebraic Reynolds Stress Model," AIAA Journal, Vol. 25, No. 7, 1987, pp. 957-964.

61. **Rodi, W.,** "A New Algebraic Relation for Calculating the Reynolds Stresses," Zeitschrift für Angewandte Mathematik und Mechanik, Vol. 56, 1976, pp. T219-T221.

62. **Naot, D. and Rodi, W.,** "Calculation of Secondary Currents in Channel Flow," Journal of the Hydraulics Division, Proceedings of the ASCE, Vol. 108, No. HY8, August 1982, pp. 948-968.

63. **Kim, K.Y. and Chung, M.K.,** "New Eddy Viscosity Model for Computation of Swirling Turbulent Flows," AIAA Journal, Vol. 25, No. 7, 1987, pp. 1020-1022.

64. **Cheng, G.C.,** "Further Comments on New Eddy Viscosity Model for Computation of Swirling Turbulent Flows," submitted to AIAA Journal, 1990.

65. **Wilcox, D.C. and Chambers, T.L.,** "Streamline Curvature Effects on Turbulent Boundary Layers," AIAA Journal, Vol. 15, No. 4, 1977, pp. 574-580.

66. **Gibson, M.M. and Rodi, W.,** "A Reynolds-Stress Closure Model of Turbulence Applied to the Calculation of a Highly Curved Mixing Layer," Journal of Fluid Mechanics, Vol. 103, 1981, pp. 161-182.

67. **Hah, C. and Lakshminarayana, B.,** "Prediction of Two- and Three-Dimensional Asymmetrical Turbulent Wakes, Including Curvature and Rotation Effects," AIAA Journal, Vol. 18, No. 10, 1980, pp. 1196-1204.

68. **Lilley, D.G.,** "Prediction of Inert Turbulent Swirl Flows," AIAA Journal, Vol. 11, No. 7, 1973, pp. 955-960.

69. **Batchelor, G.K.,** An Introduction to Fluid Dynamics, Cambridge University Press, New York, 1979.

70. **Hinze, J.O.,** Turbulence, Second Edition, McGraw-Hill, New York, 1975.

71. **Schlichting, H.,** Boundary Layer Theory, 7th Edition, Mcgraw-Hill, New York, 1979.

72. **Bradshaw, P., Cebeci, T. and Whitelaw, J.H.,** Engineering Calculation Methods for Turbulent Flow, Academic Press, New York, 1981.

73. **Farokhi, S.,** Private Communication, University of Kansas, Lawrence, 1989.

74. **Launder, B.E. and Spalding, D.B.,** Mathematical Models of Turbulence, Academic Press, London, 1972.

75. **Launder, B.E. and Spalding, D.B.,** "The Numerical Computation of Turbulent Flows," Computer Methods in Applied Mechanics and Engineering, Vol. 3, 1974, pp. 269-289.

76. **Gibson, M.M. and Launder, B.E.,** "Ground Effects on Pressure Fluctuations in the Atmospheric Boundary Layer," Journal of Fluid Mechanics, Vol. 86, 1978, pp. 491-511.

77. **Gibson, M.M. and Younis, B.A.,** "Calculation of Swirling Jets with a Reynolds Stress Closure," Physics of Fluids, Vol. 29, 1986, pp. 38-48.

78. **Gibson, M.M. and Launder, B.E.,** "On the Calculation of Horizontal Turbulent, Free Shear Flows under Gravitational Influence," Transaction of the ASME, Journal of Heat Transfer, Vol. 98, 1976, pp. 81-87.

79. **Cheng G.C.,** "Application of a Two-Equation Turbulence Closure Model to Two-Dimensional Planar and Conical Diffuser Flows," M.S. Thesis, Aerospace Engineering Dept., University of Kansas, Lawrence, KS, 1987.

80. **Chen, Y.S.,** "Compressible and Incompressible Flow Computations with a Pressure Based Method," AIAA Paper 89-0286, AIAA 27th Aerospace Sciences Meeting, Jan. 1989.

81. **Chen, Y.S.,** "3-D Stator-Rotor Interaction of the SSME," AIAA Paper 88-3095, AIAA 24th Joint Propulsion Conference, July 1988.

82. **Chen, Y.S.,** "Viscous Flow Computations Using a Second-Order Upwind Differencing Scheme," AIAA Paper 88-0417, AIAA 26th Aerospace Sciences Meeting, Jan. 1988.

83. **Driver, D.M. and Seegmiller, H. Lee**, "Features of a Reattaching Turbulent Shear Layer in Divergent Channel Flow," AIAA Journal, Vol. 23, No. 2, 1985, pp. 163-171.

84. **Johnson, R.W.**, "Turbulent Convection Flow in a Square Duct with a 180° Bend; an Experimental and Numerical Study," Ph.D. Dissertation, Department of Mechanical Engineering, University of Manchester Institute of Science and Technology, England, Spring 1984.

85. **Humphrey, J.A.C.**, and **Chang, S.M.**, "Turbulent Flow in Passage Around a 180° Bend; an Experimental and Numerical Study," ONR Contract Report No. N00014-80-C-0031, September 1983.

86. **Kim, J., Kline, S.J., and Johnston, J.P.**, "Investigation of a Reattaching Turbulent Shear Layer: Flow over a Backward-Facing Step," Transactions of the ASME, Journal of Fluids Engineering, Vol. 102, Sep. 1980, pp. 302-308; also "Case 0421: Flow over a Backward-Facing Step," The 1980-1981 AFOSR-HTTM-Stanford Conference on Complex Turbulent Flows, S.J. Kline, et. al., Editors, Stanford University, 1981, pp. 275-286 and pp. 885-899.

87. **Sandborn, V.A., and Shin, J.C.**, "Water Flow Measurements in a 180 Degree Turn-Around Duct," Report Prepared under Contract No. NAS8-36354, June 1989.

88. **Monson, D.J., Seegmiller, H.L., McConnaughey, P.K., and Chen, Y.S.**, "Comparison of Experiment with Calculations Using Curvature-Corrected Zero and Two Equation Turbulence Models for a Two-Dimensional U-Duct," AIAA Paper 90-1484, Seattle, Washington, June 1990.

89. **Roback, R., and Johnson, B.V.**, "Mass and Momentum Turbulent Transport Experiments with Confined Swirling Coaxial Jets," NASA CR-168252, Aug. 1983.

90. **Weske, D.R., and Sturov, G.YE.**, "Experimental Study of Turbulent Swirled Flows in a Cylindrical Tube," Fluid Mechanics: Soviet Research, Vol. 3, No. 1, Jan.-Feb. 1974, pp. 77-82.

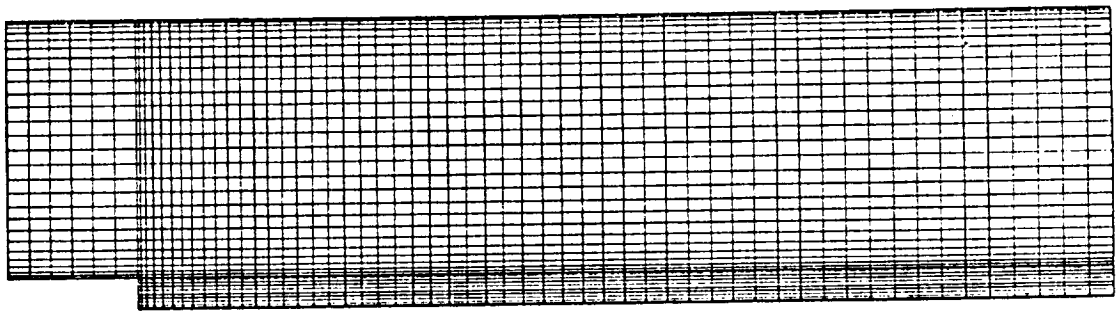

Figure 1 Grid System for a Two-Dimensional Backward-Facing Step Geometry

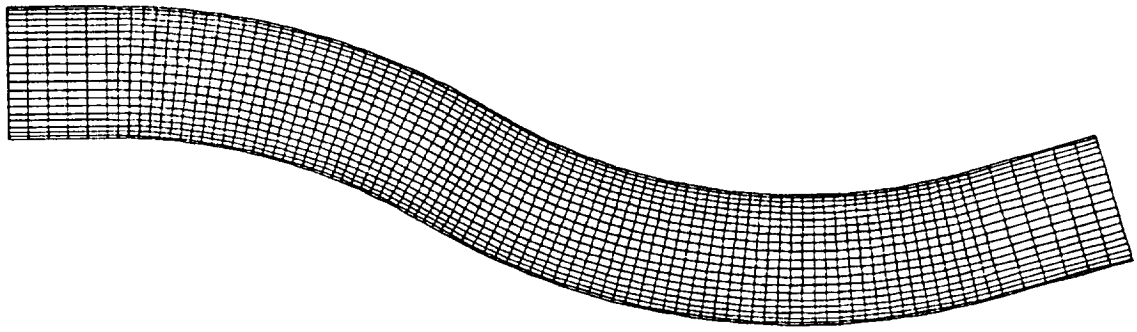

Figure 2 Mesh System for a Two-Dimensional S-Bend Duct Geometry

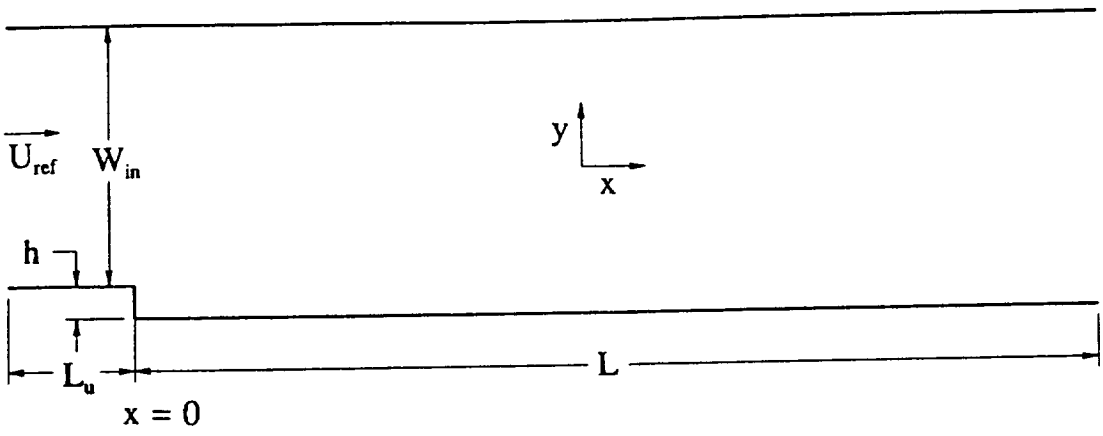

Tunnel Geometry: h = 1.27 cm

W_{in} = 8h

L = 30h

L_u = 4h

aspect ratio = 12

Inlet Conditions: U_{ref} = 44.2 m/sec

M_{ref} = 0.128

δ_{BL} = 1.9 cm

Re_θ = 5000

Figure 3 Backward-Facing Step Flow Experimental Geometry and Inlet Conditions by Driver and Lee Seegmiller [83]

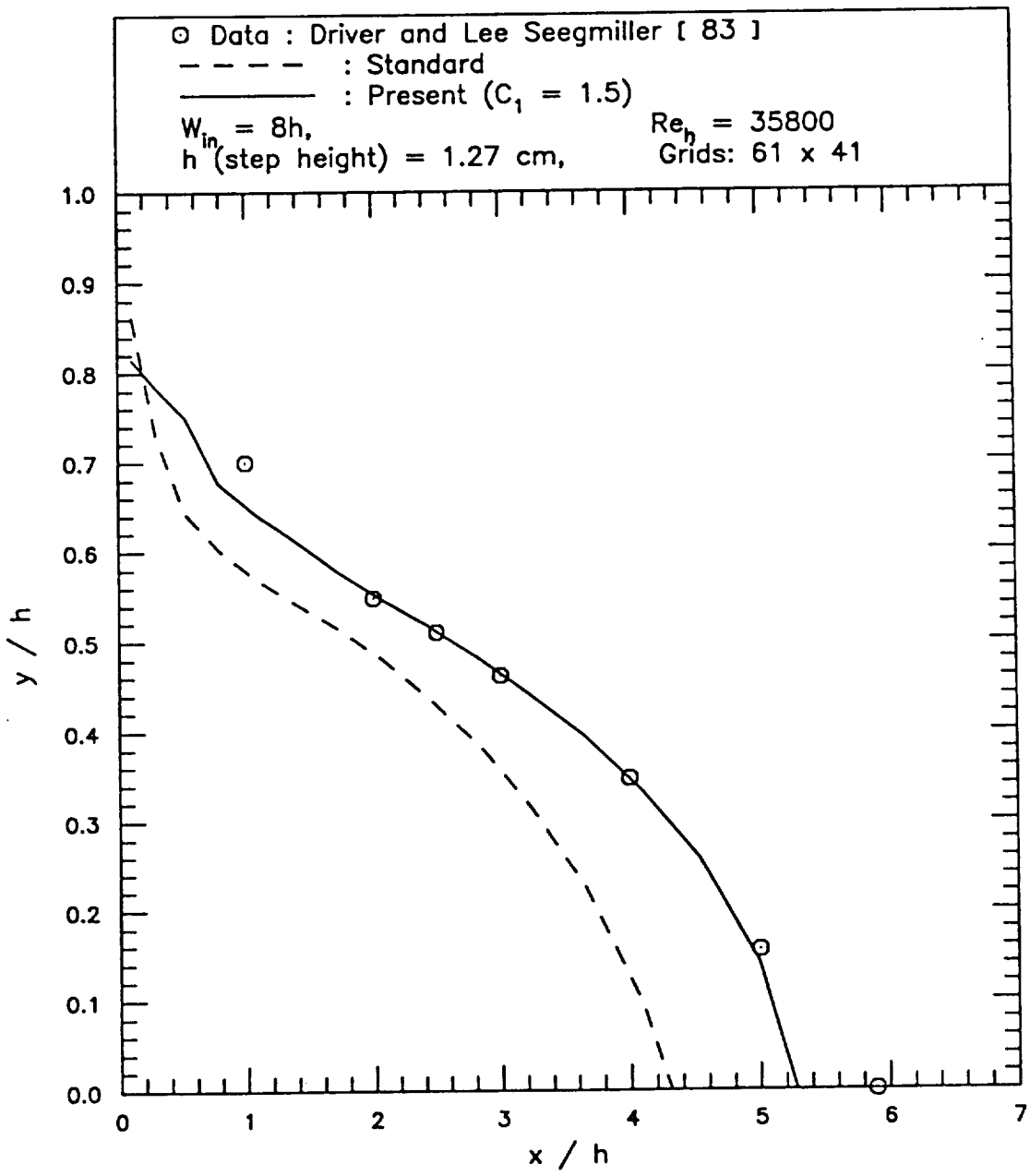

Figure 4 Locus of Flow Reversal in a Backward-Facing Step Flow

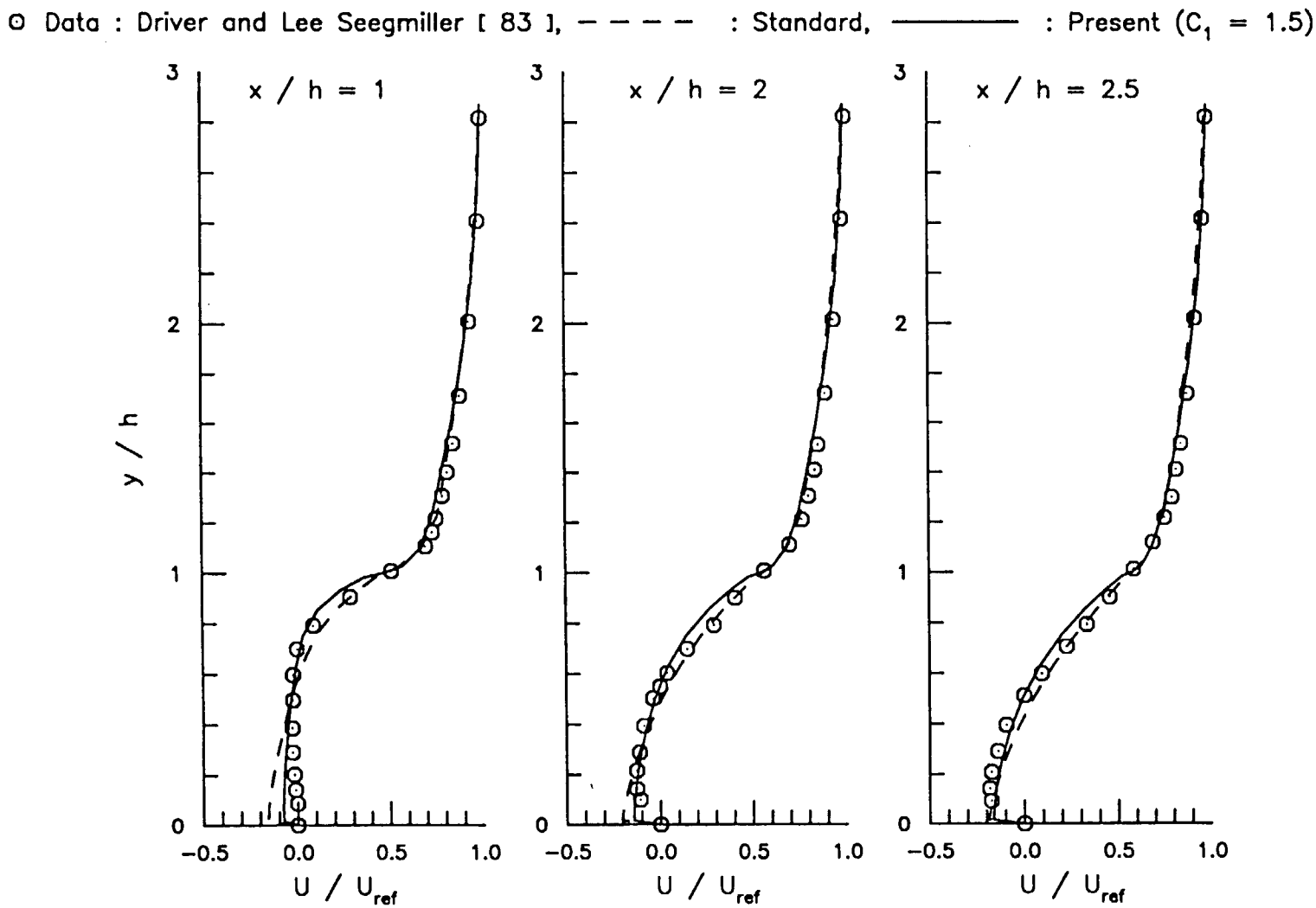

Figure 5 Streamwise Velocity Profiles in a Backward-Facing Step Flow (61 x 41 grids)

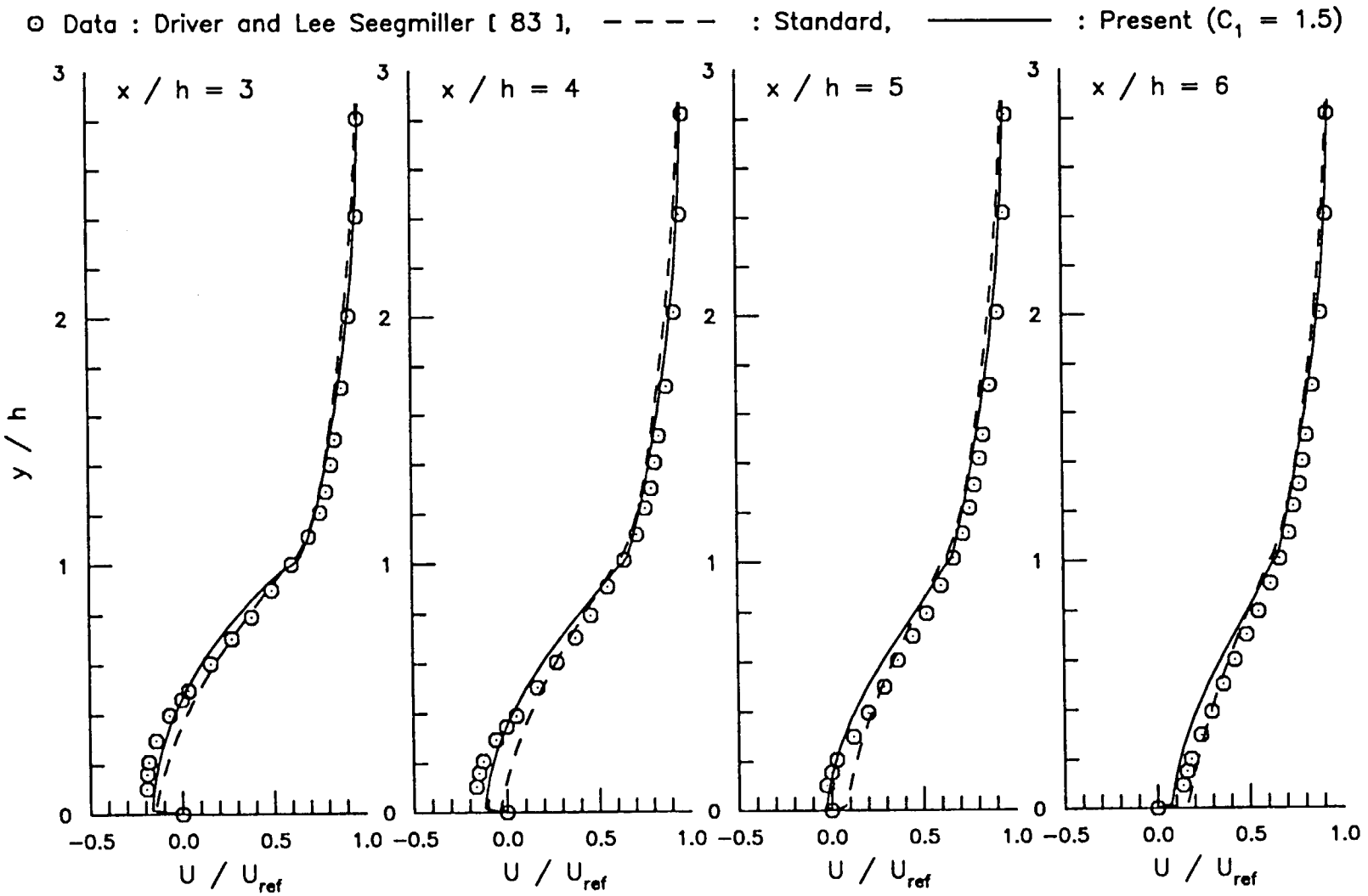

Figure 5 Continued

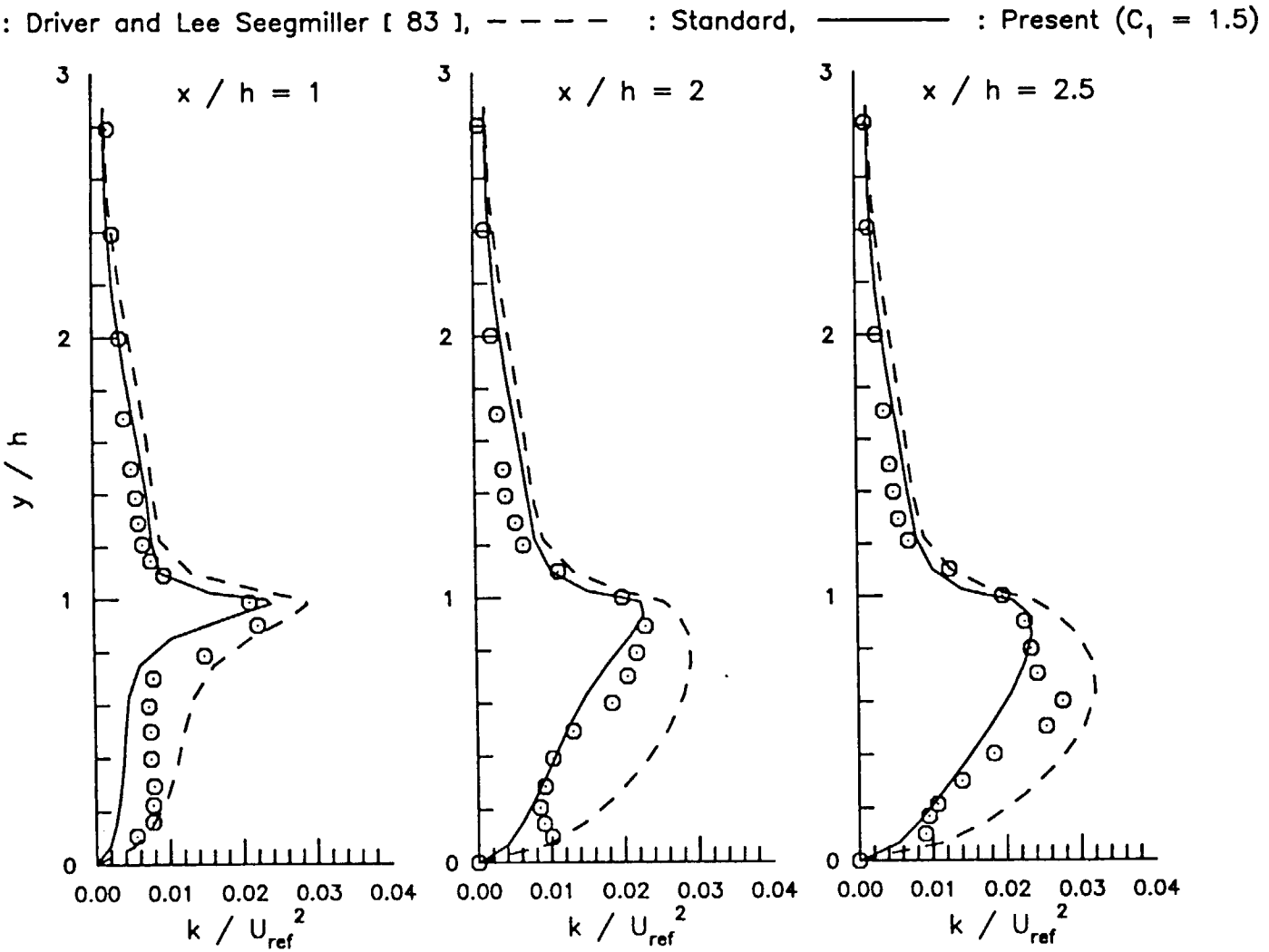

Figure 6 Turbulent Kinetic Energy Profiles in a Backward-Facing Step Flow (61 x 41 grids)

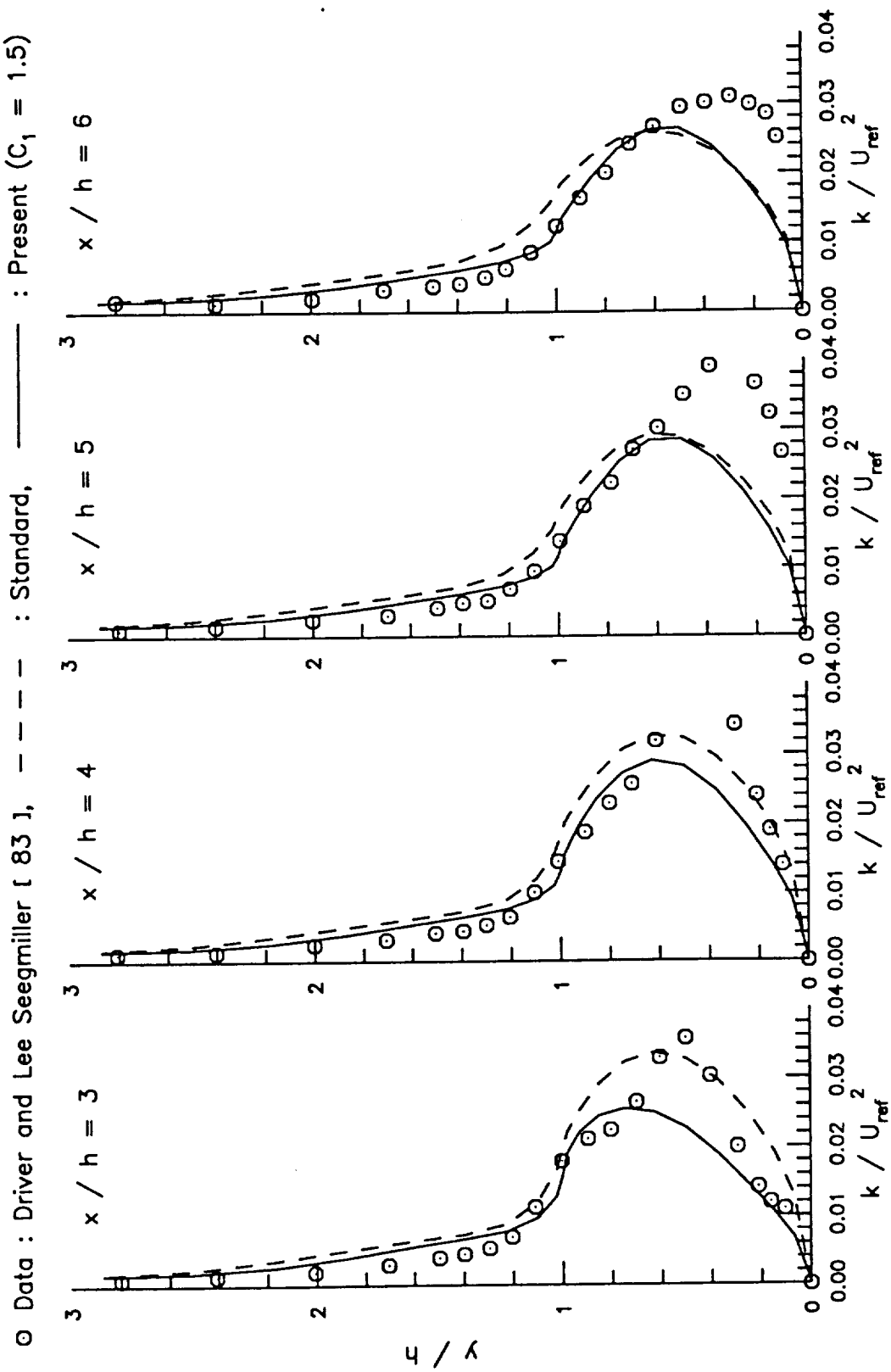

Figure 6 Continued

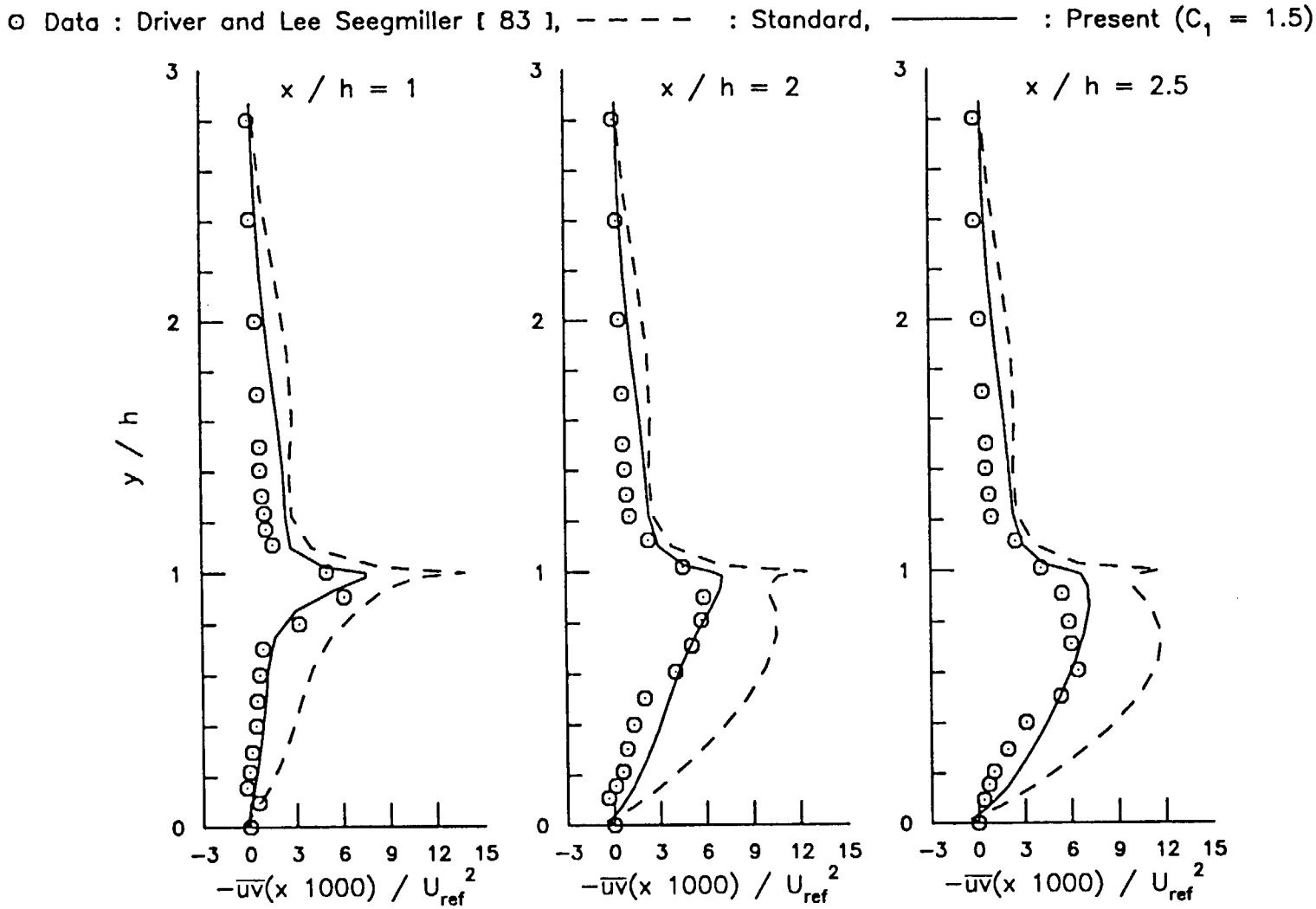

Figure 7 Reynolds Shear Stress $-\overline{uv}$ Profiles in a Backward-Facing Step Flow (61 x 41 grids)

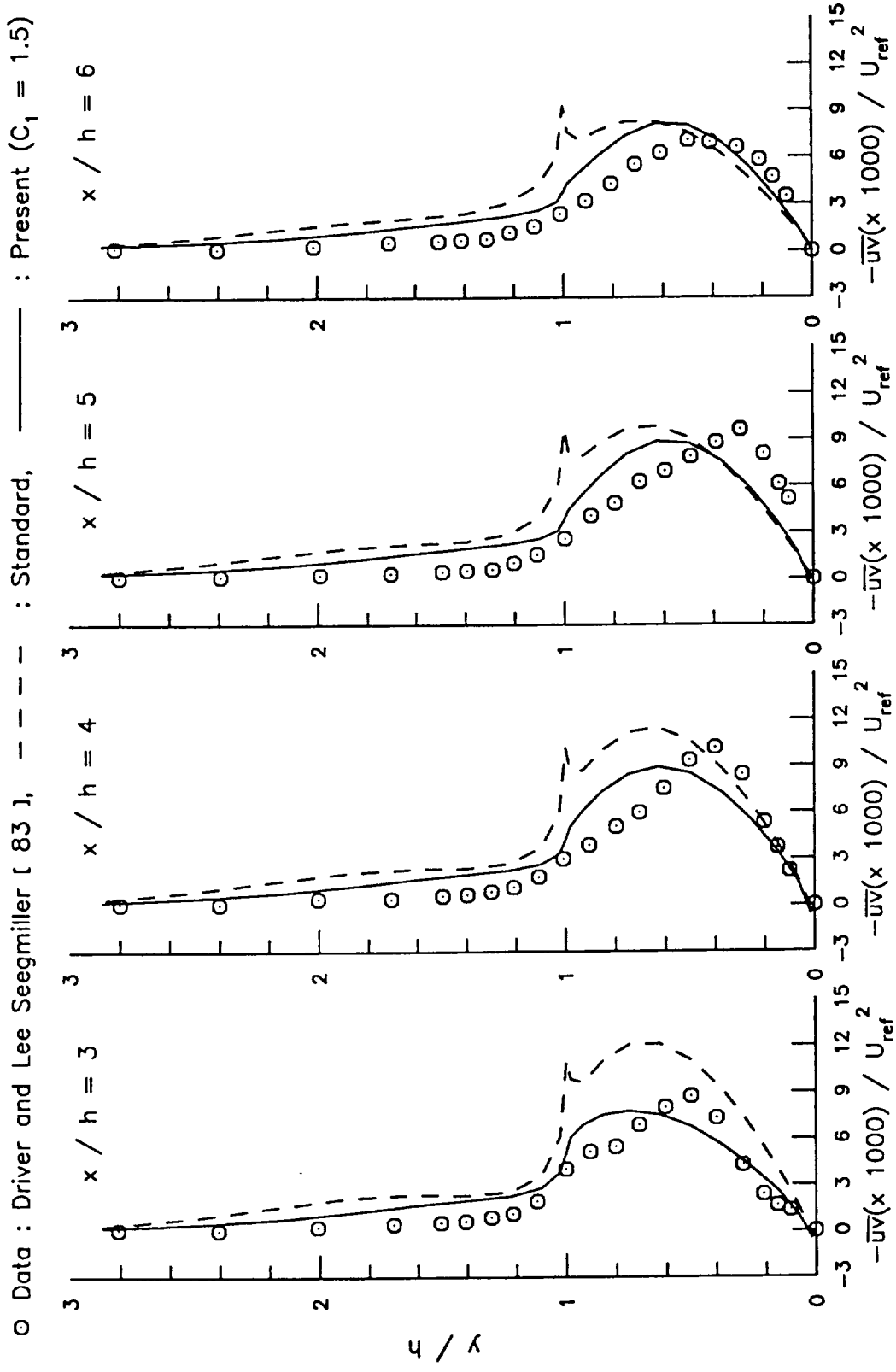

Figure 7 Continued

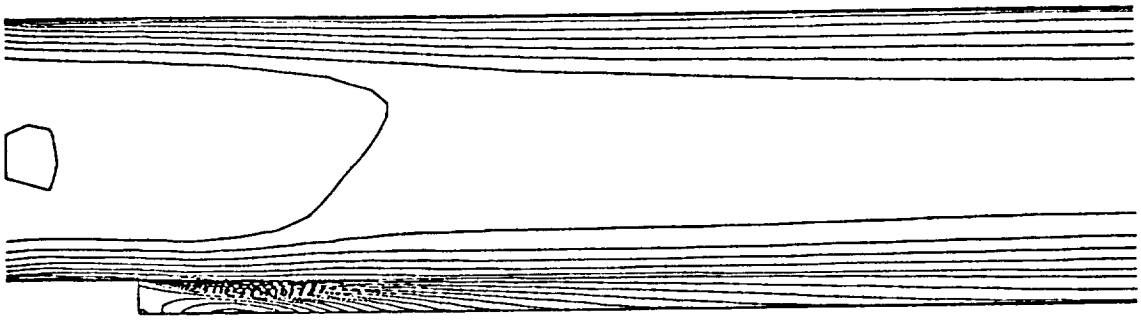

(a) present model

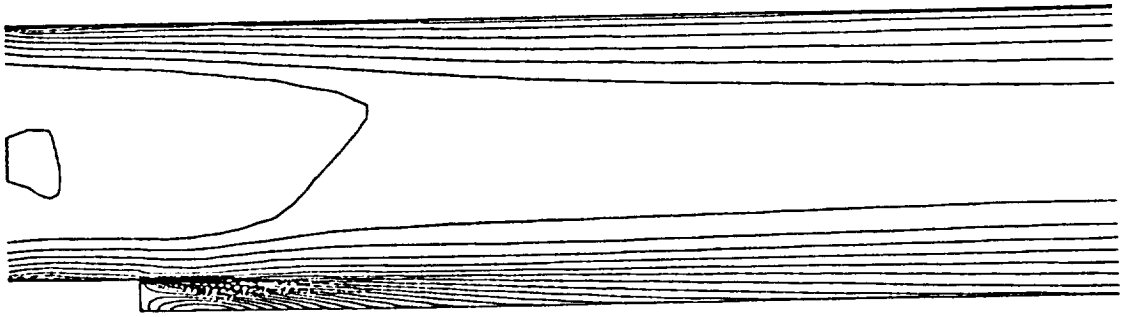

(b) standard k-ε model

Figure 8 Streamwise Velocity Contour in a Backward-Facing Step Flow (61 x 41 grids)

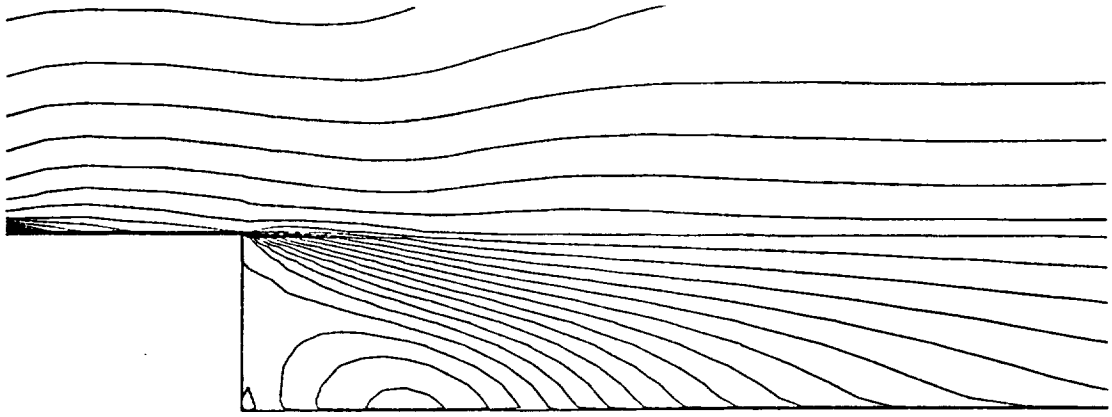

(a) present model

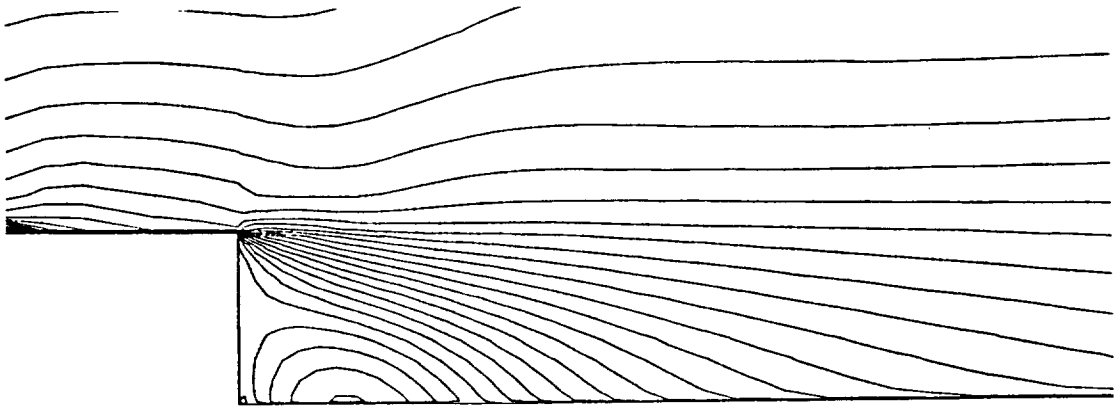

(b) standard k-ε model

Figure 9 Streamwise Velocity Contour near the Backward-Facing Step (close view)

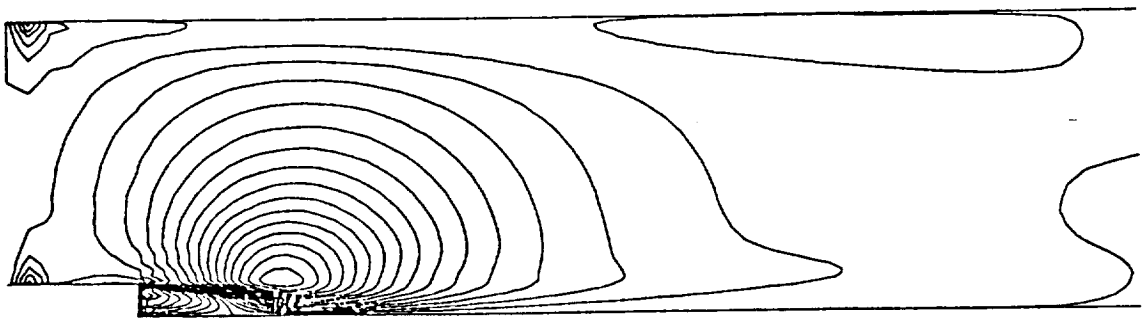

(a) present model

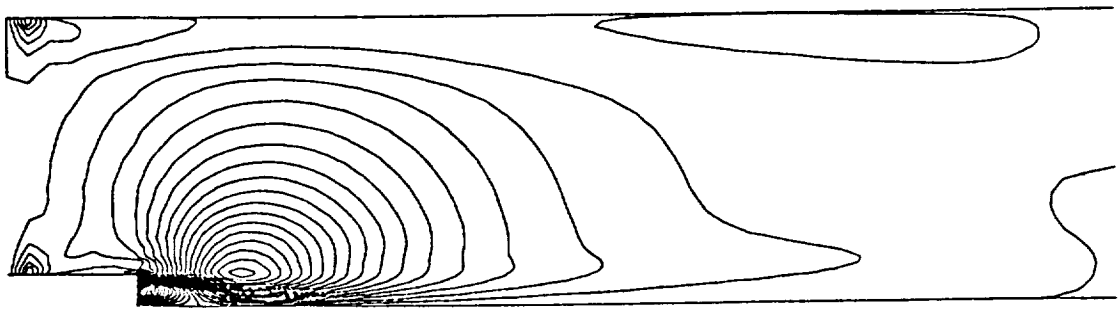

(b) standard k-ε model

Figure 10 Transverse Velocity Contour in a Backward-Facing Step Flow (61 x 41 grids)

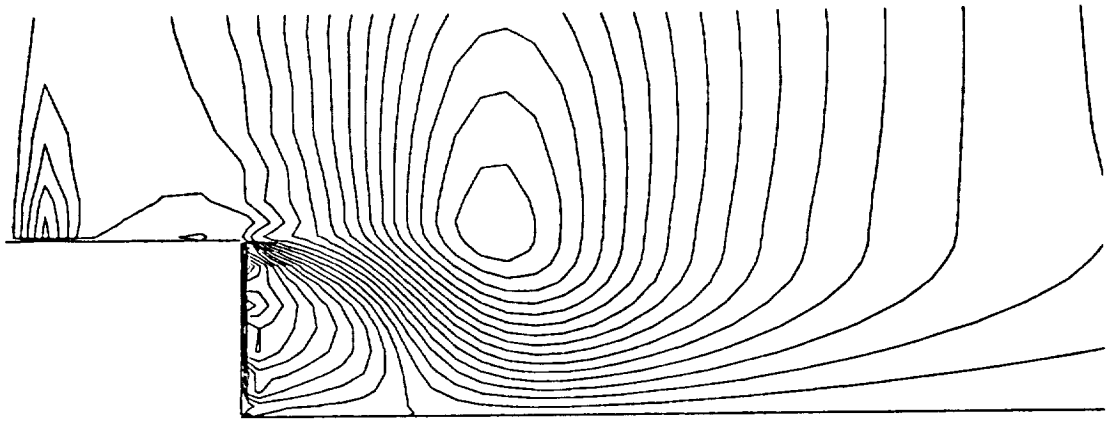

(a) present model

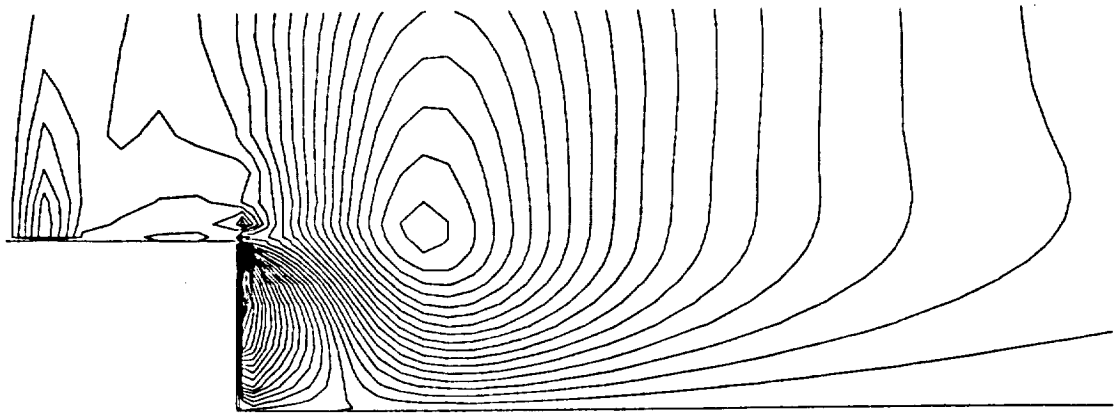

(b) standard k-ε model

Figure 11 Transverse Velocity Contour near the Backward-Facing Step (close view)

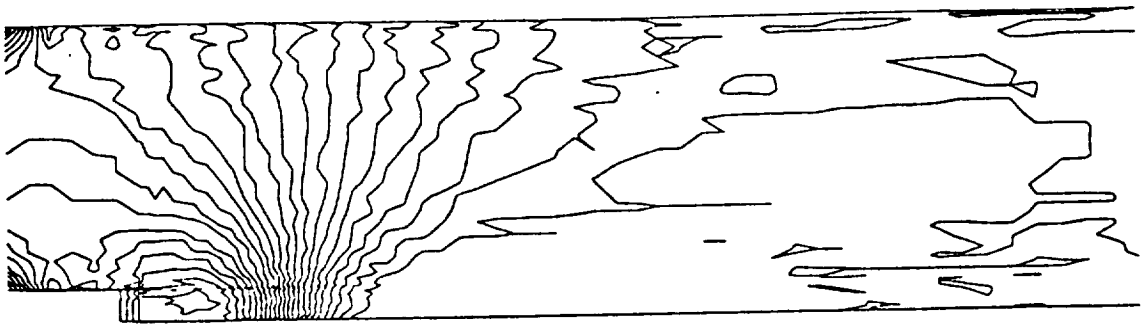

(a) present model

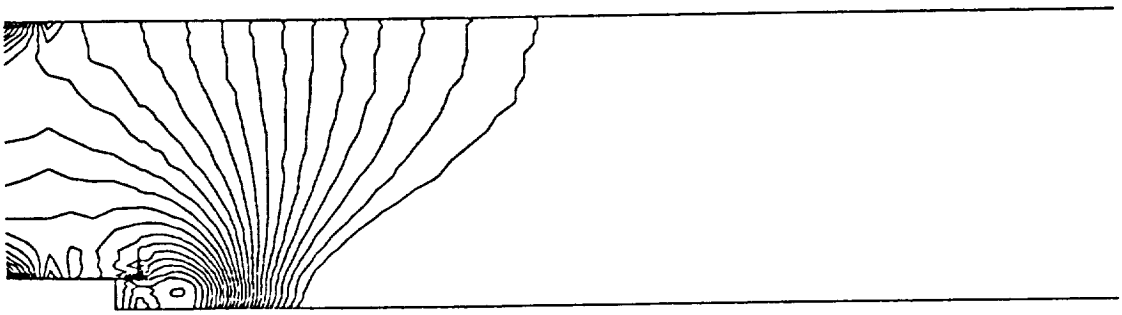

(b) standard k-ε model

Figure 12 Static Pressure Contour in a Backward-Facing Step Flow (61 x 41 grids)

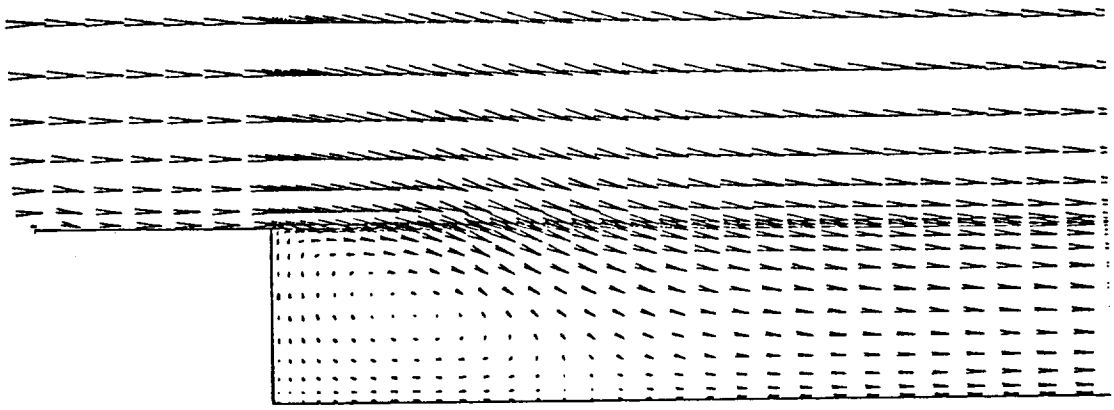

(a) present model

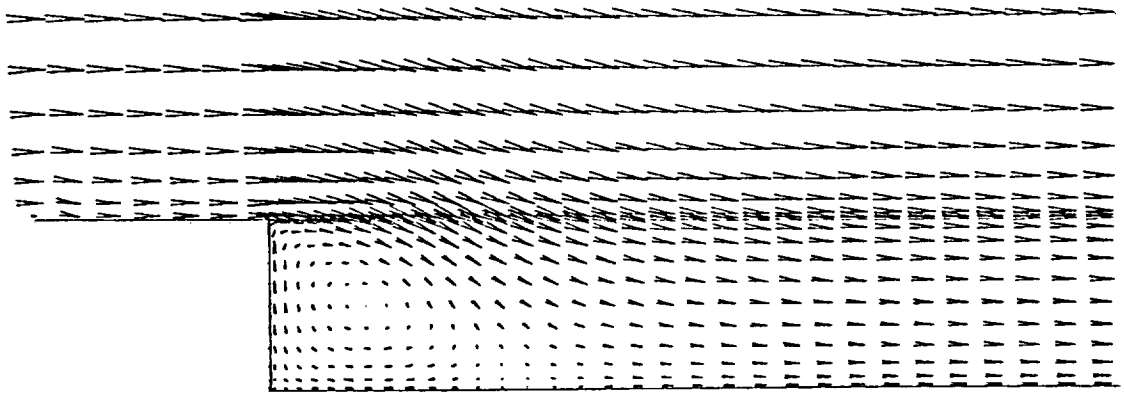

(b) standard k-ε model

Figure 13 Velocity Vectors in a Backward-Facing Step Flow (61 x 41 grids)

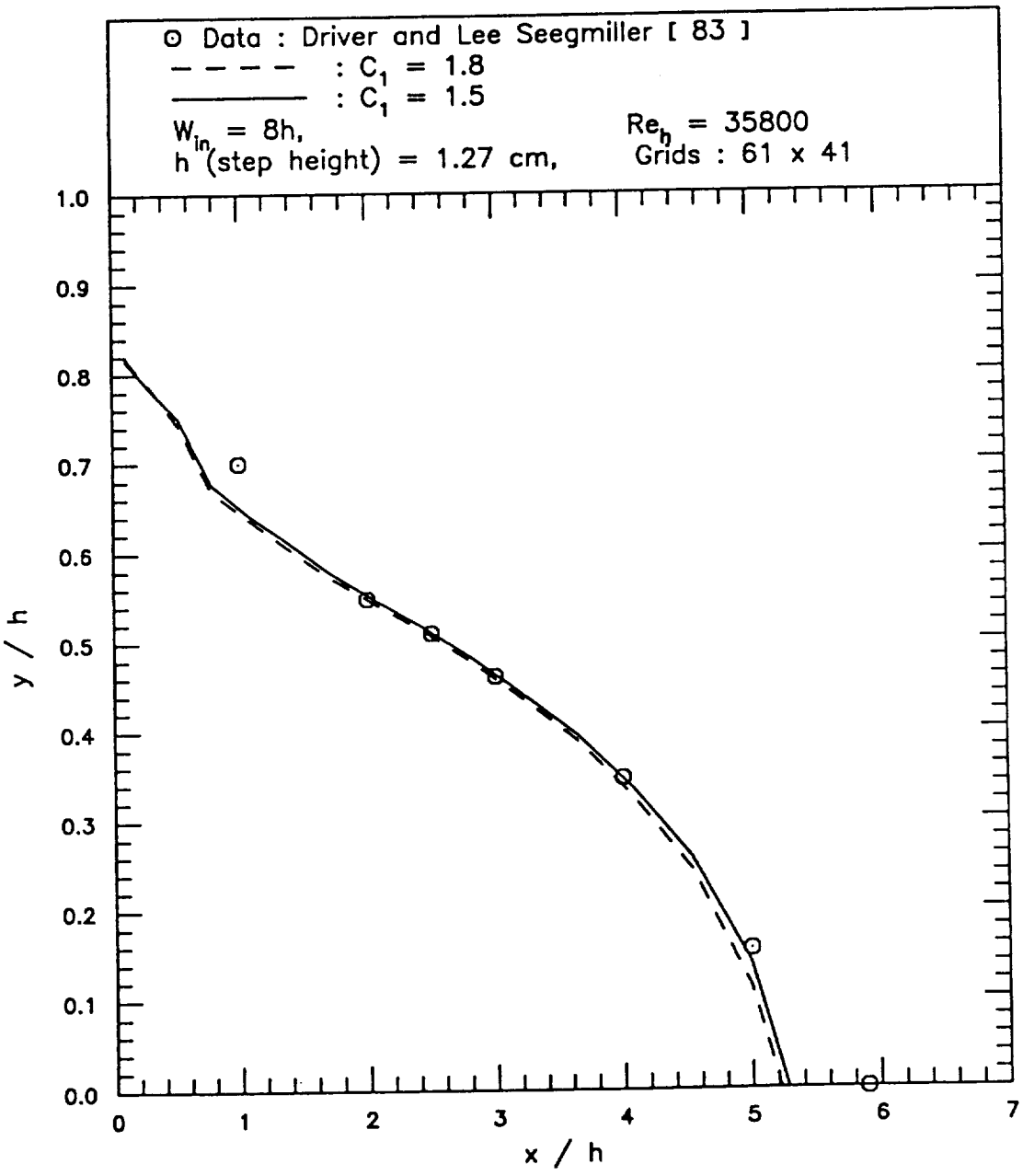

Figure 14 Locus of Flow Reversal in a Backward-Facing Step Flow with Different Modeling Constants

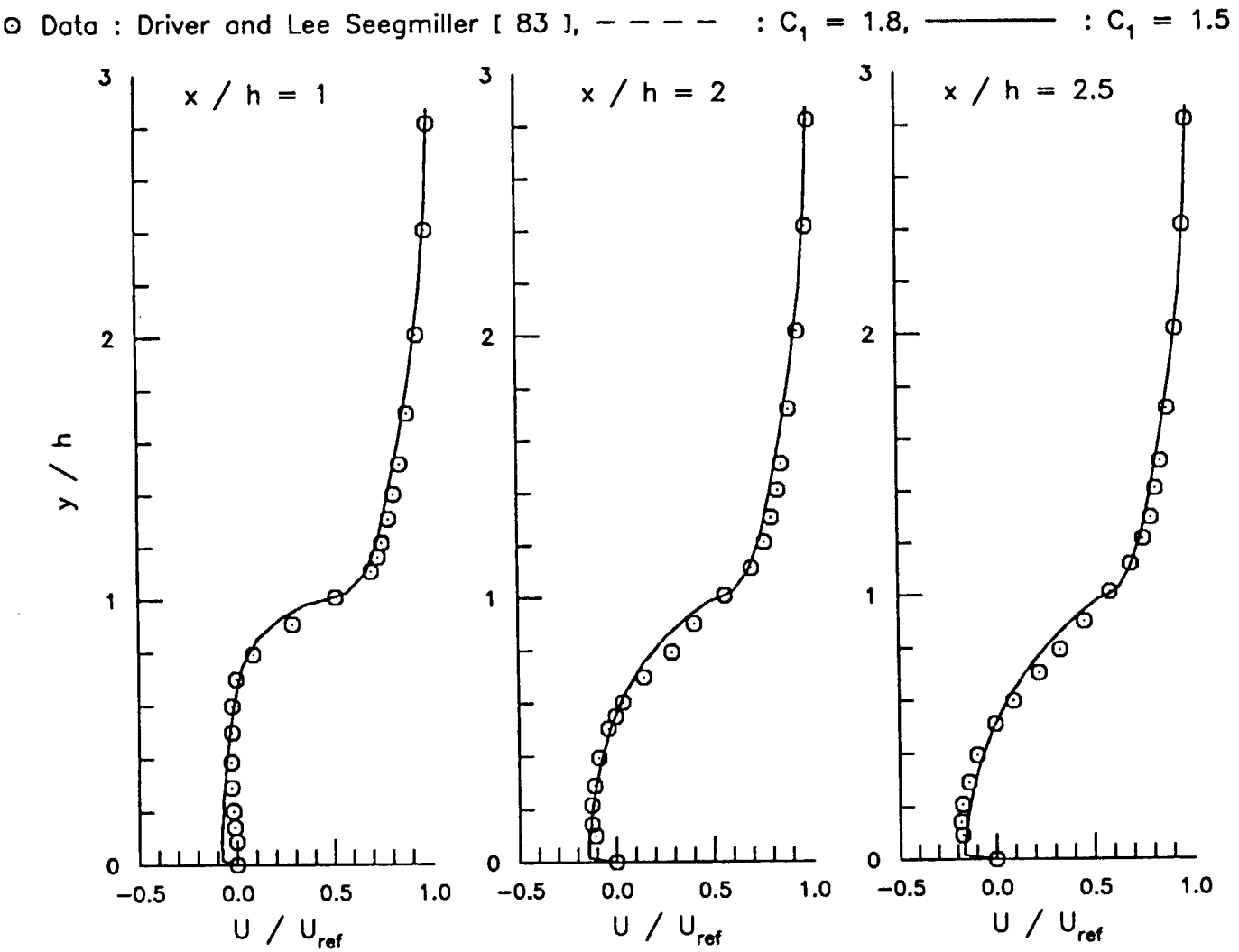

Figure 15 Streamwise Velocity Profiles in a Backward-Facing Step Flow with Different Modeling Constants

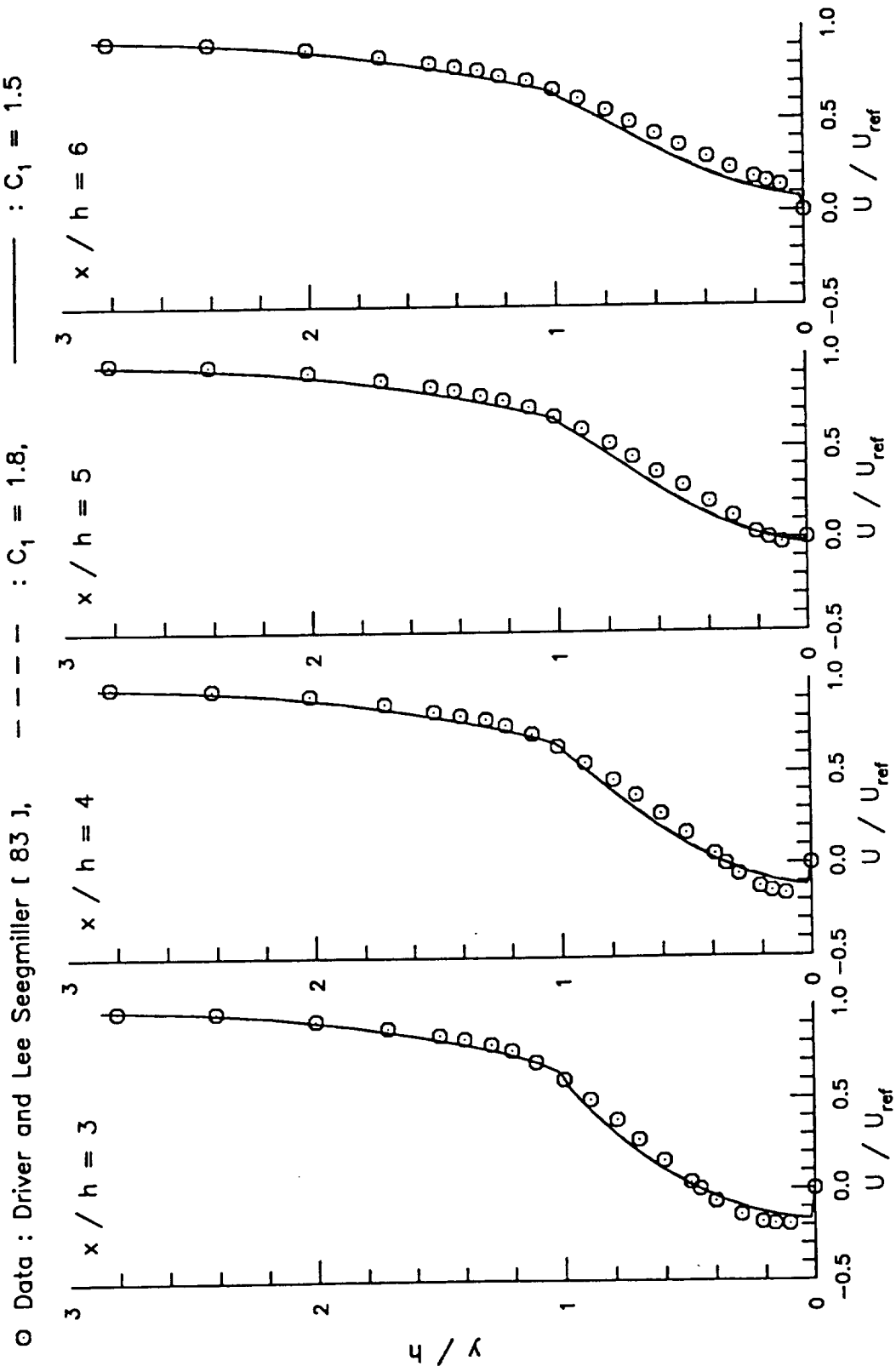

Figure 15 Continued

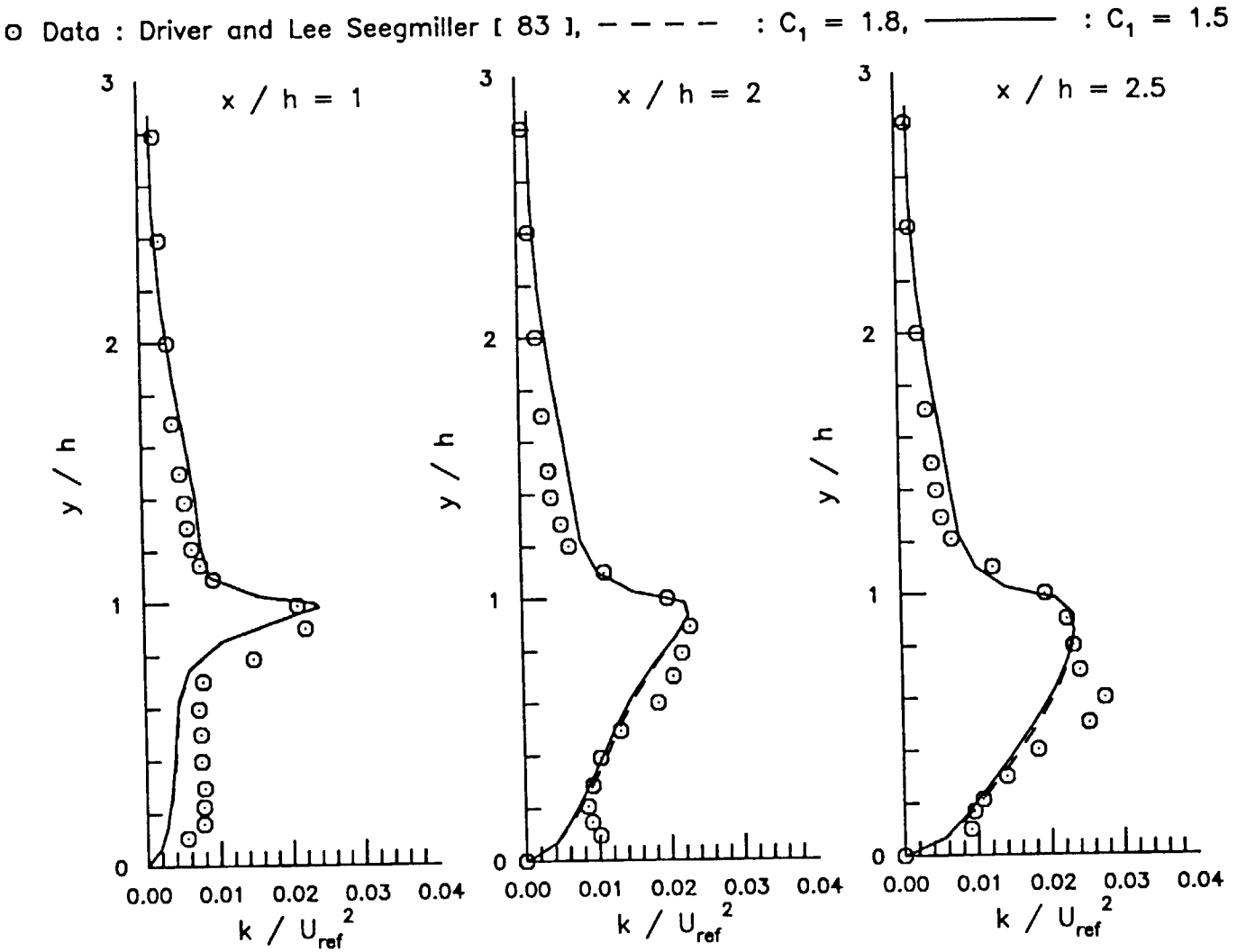

Figure 16 Turbulent Kinetic Energy Profiles in a Backward-Facing Step Flow with Different Modeling Constants

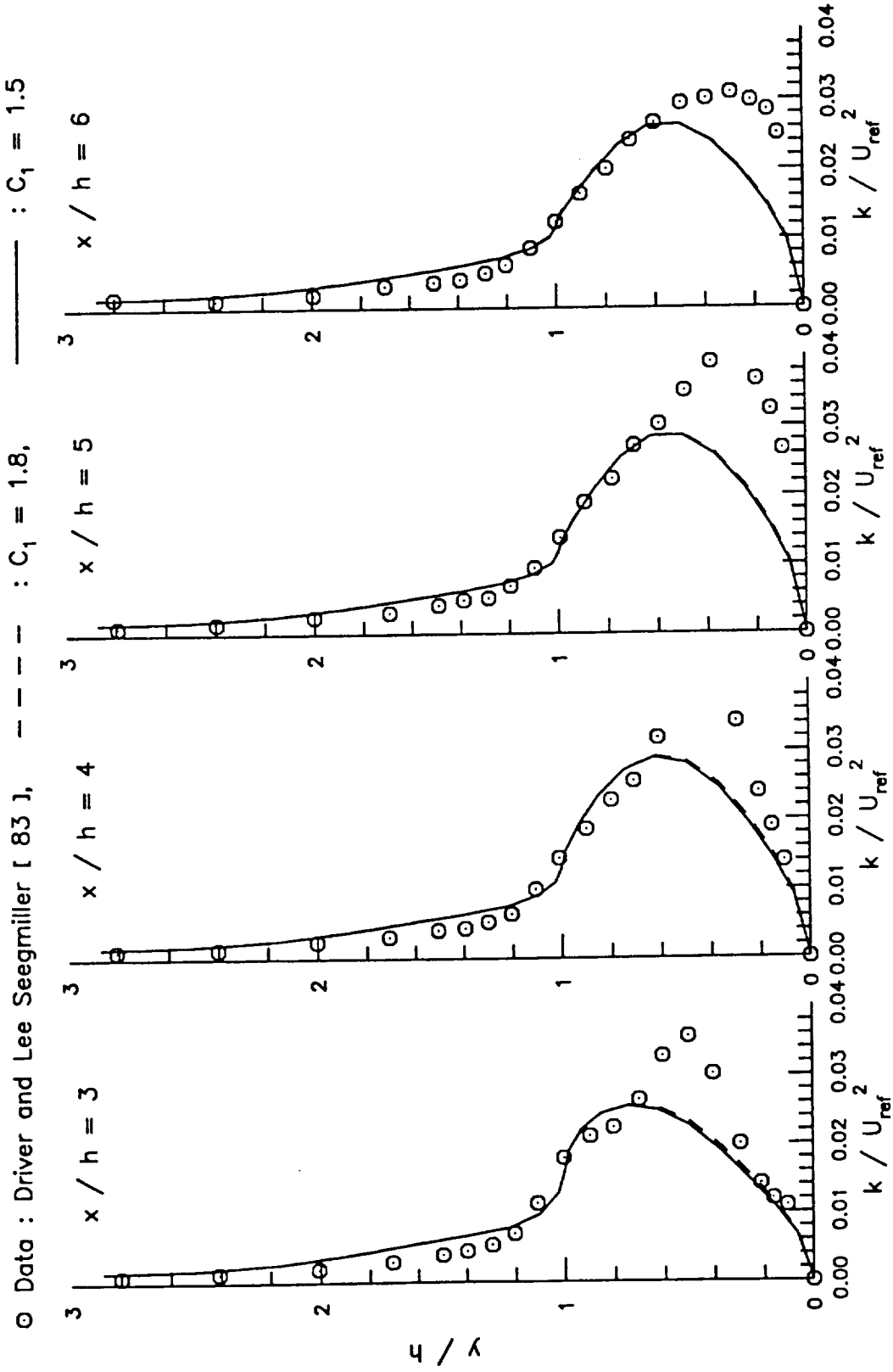

Figure 16 Continued

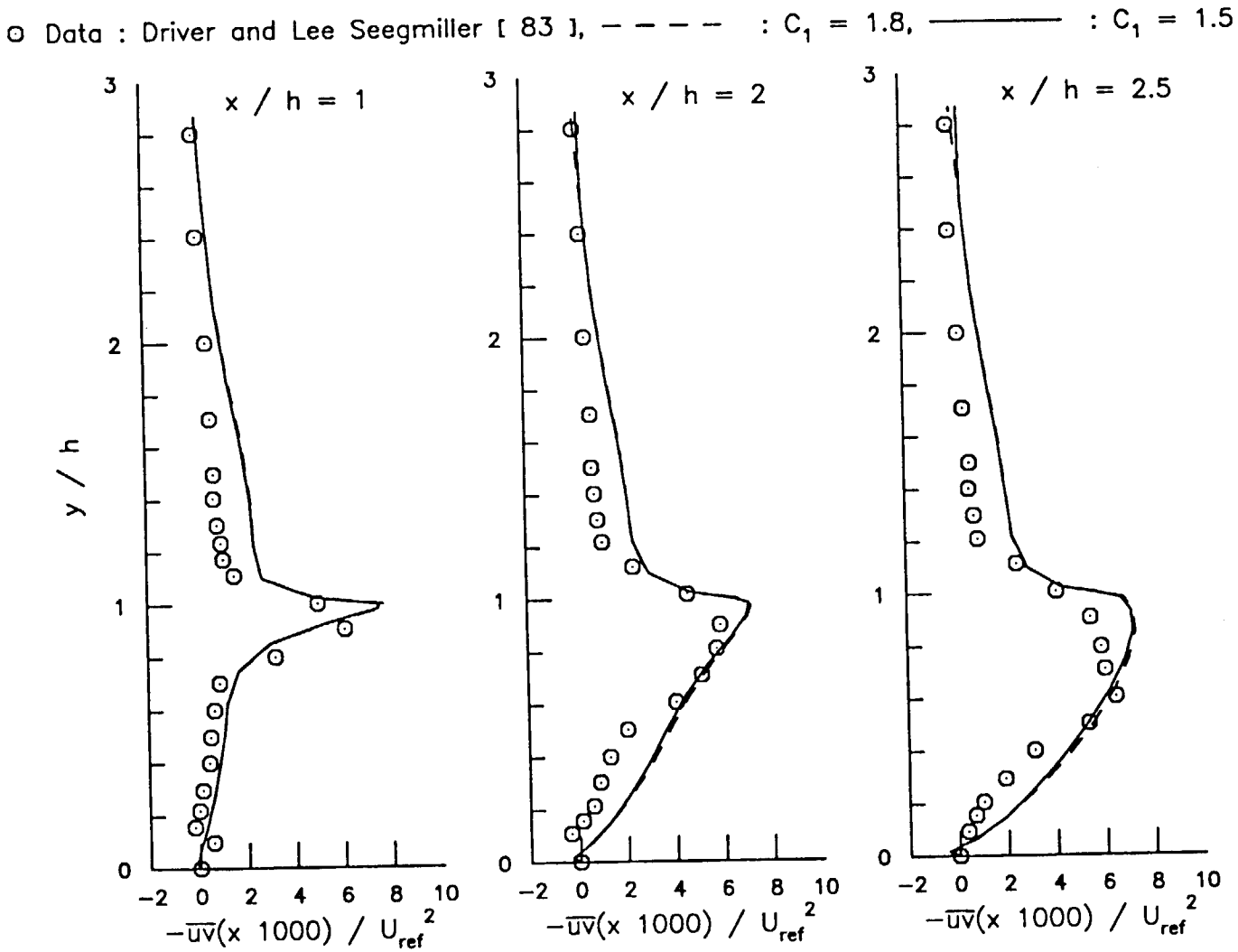

Figure 17 Reynolds Shear Stress -$\overline{uv}$ Profiles in a Backward-Facing Step Flow with Different Modeling Constants

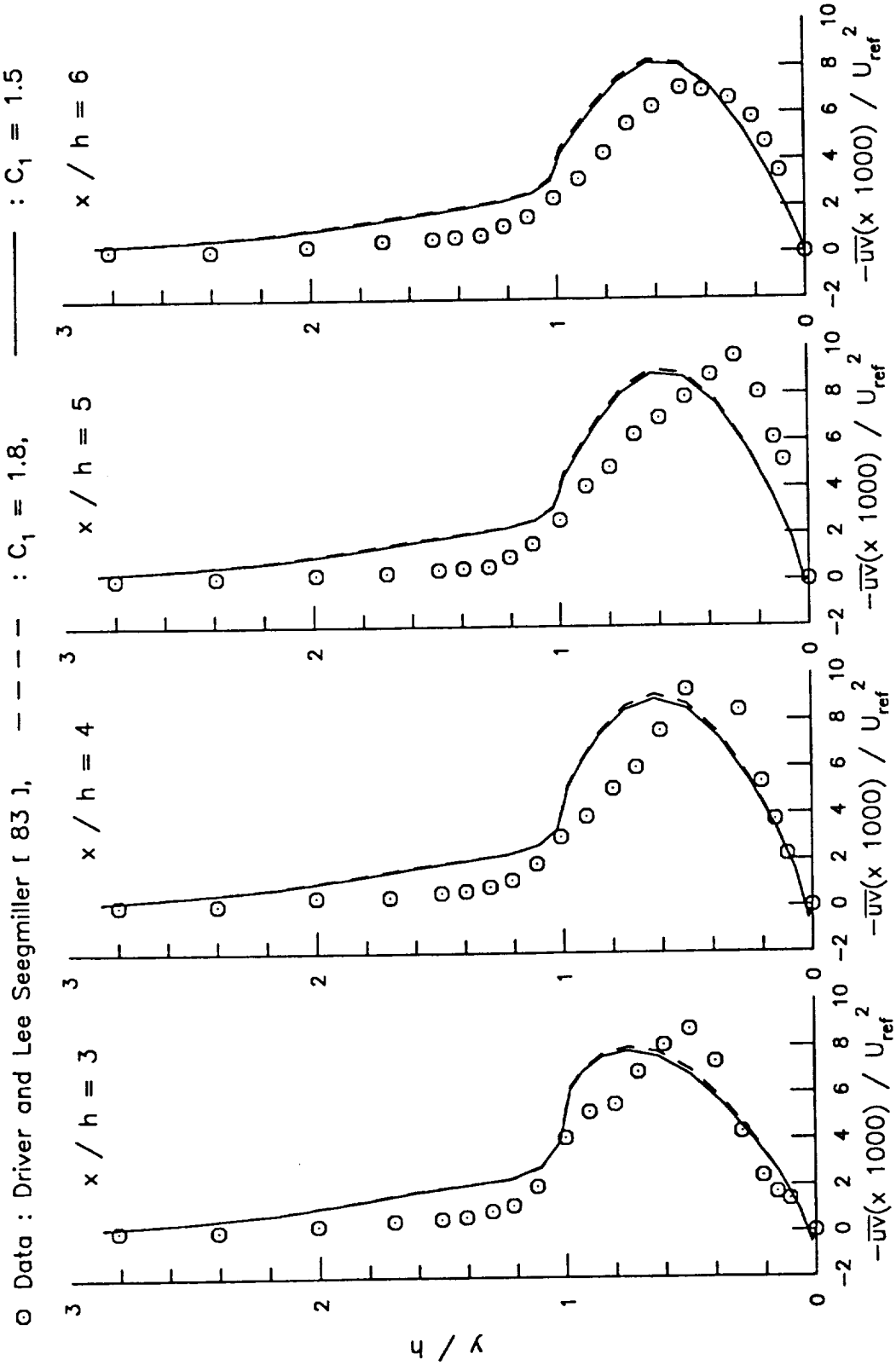

Figure 17 Continued

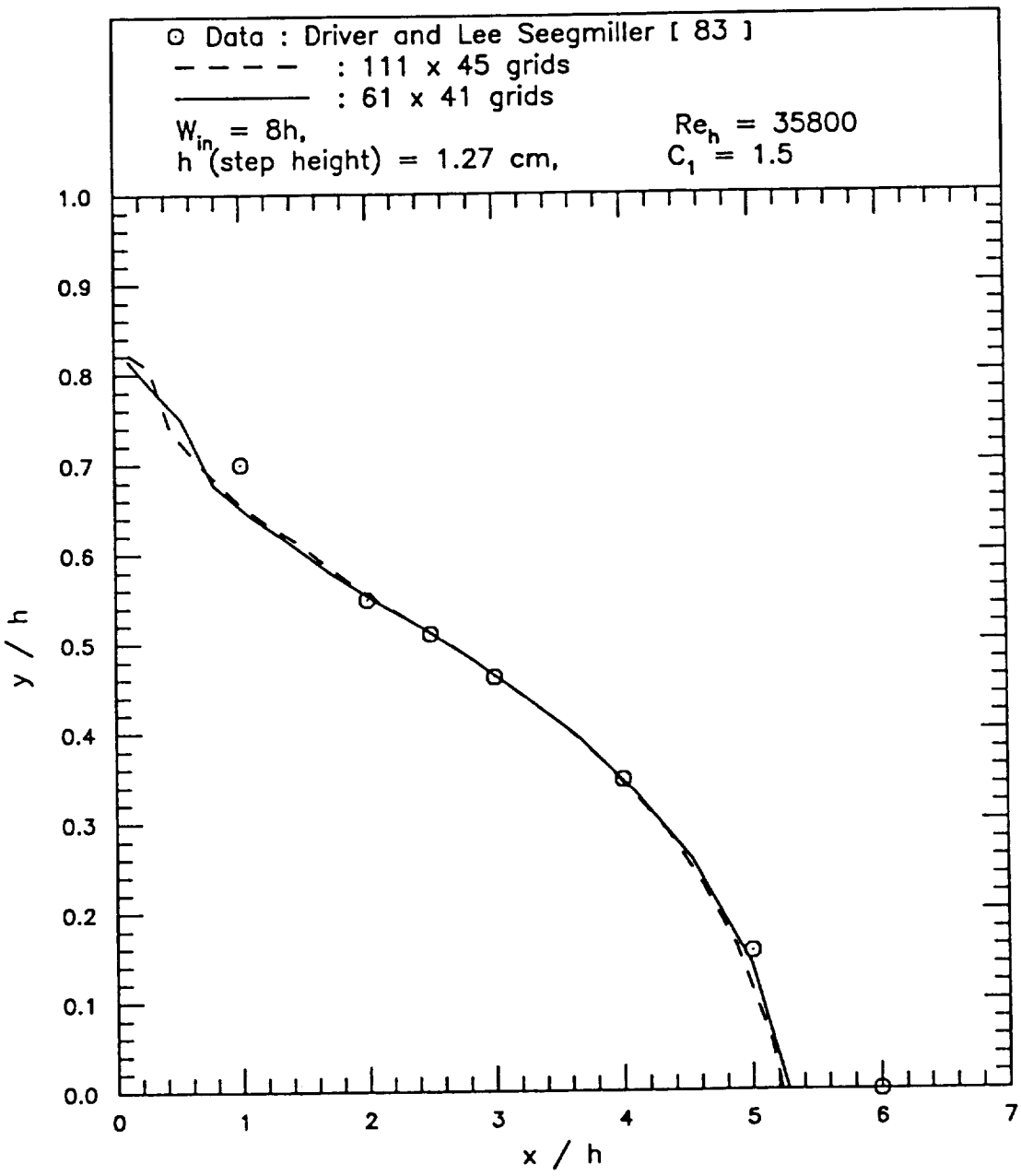

Figure 18 Locus of Flow Reversal in a Backward-Facing Step Flow with Different Grid Size

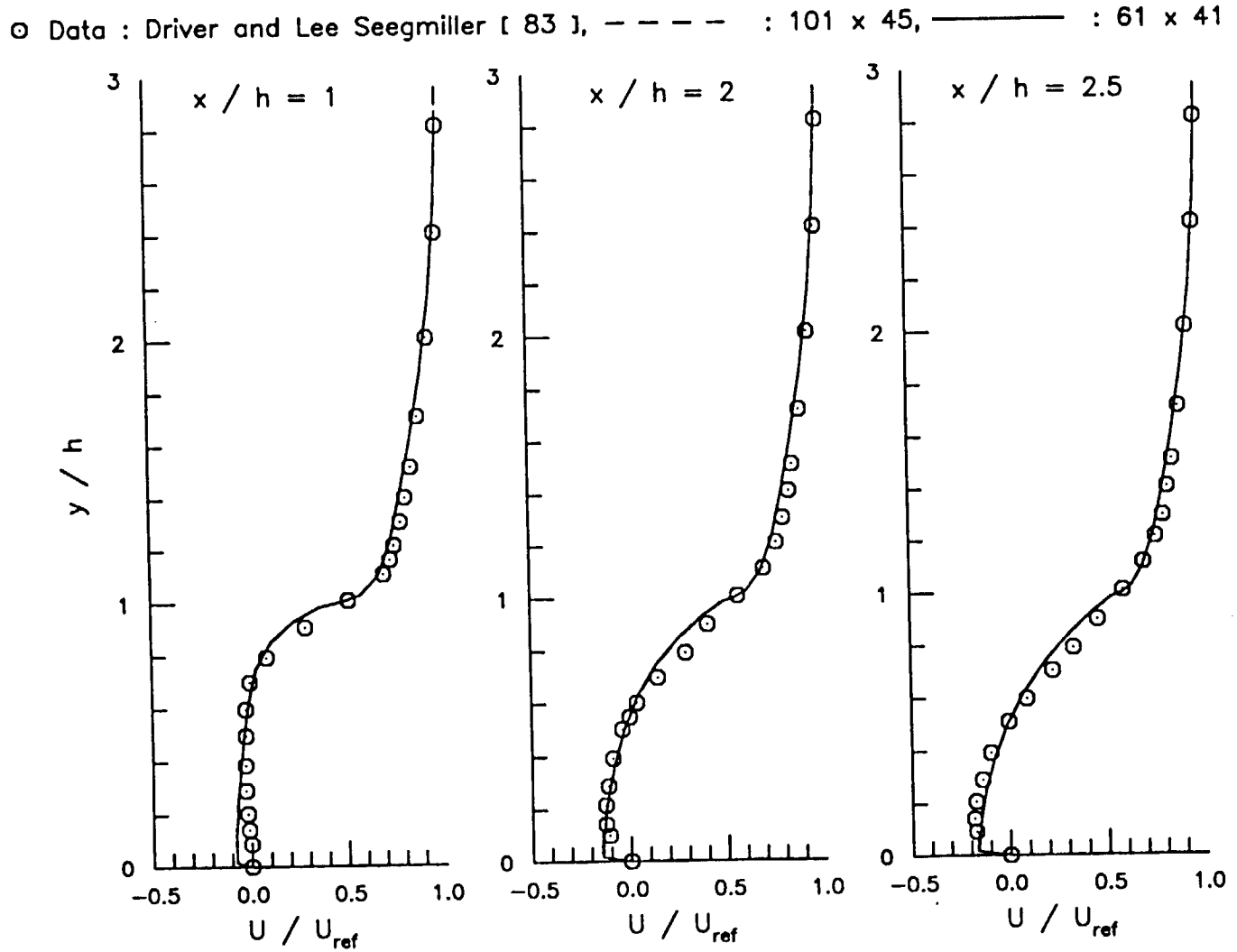

Figure 19 Streamwise Velocity Profiles in a Backward-Facing Step Flow with Different Grid Size

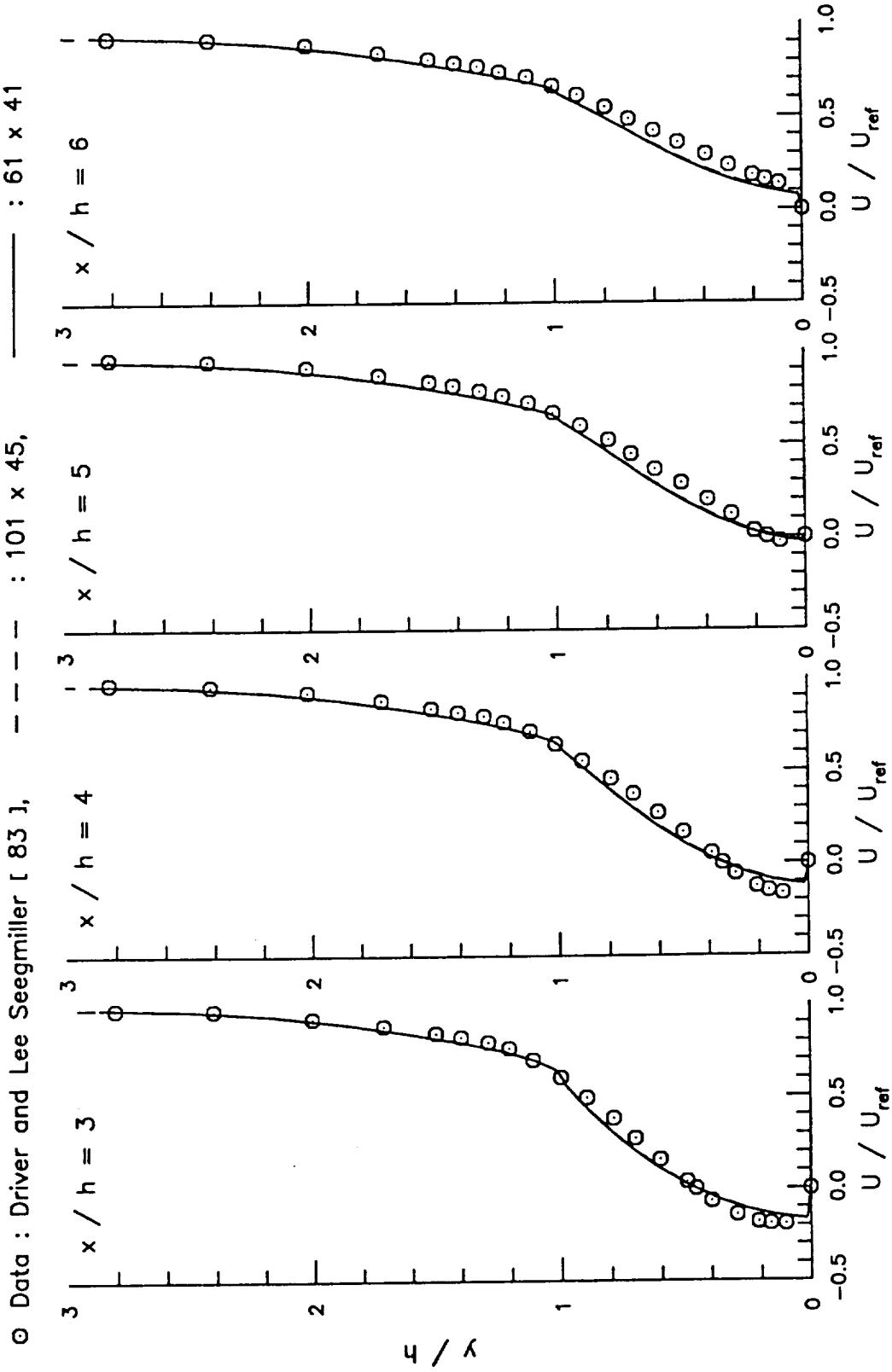

Figure 19 Continued

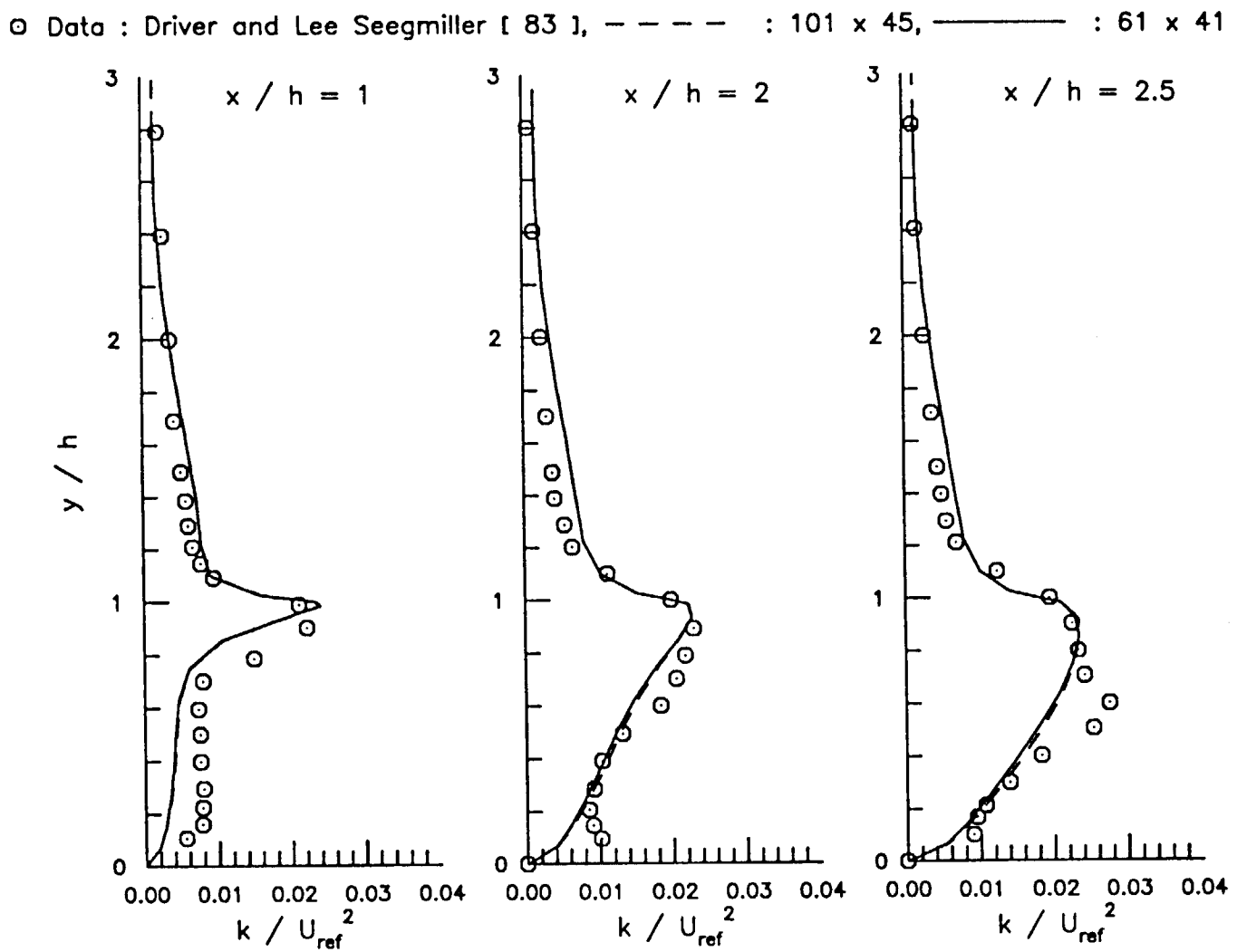

Figure 20 Turbulent Kinetic Energy Profiles in a Backward-Facing Step Flow with Different Grid Size

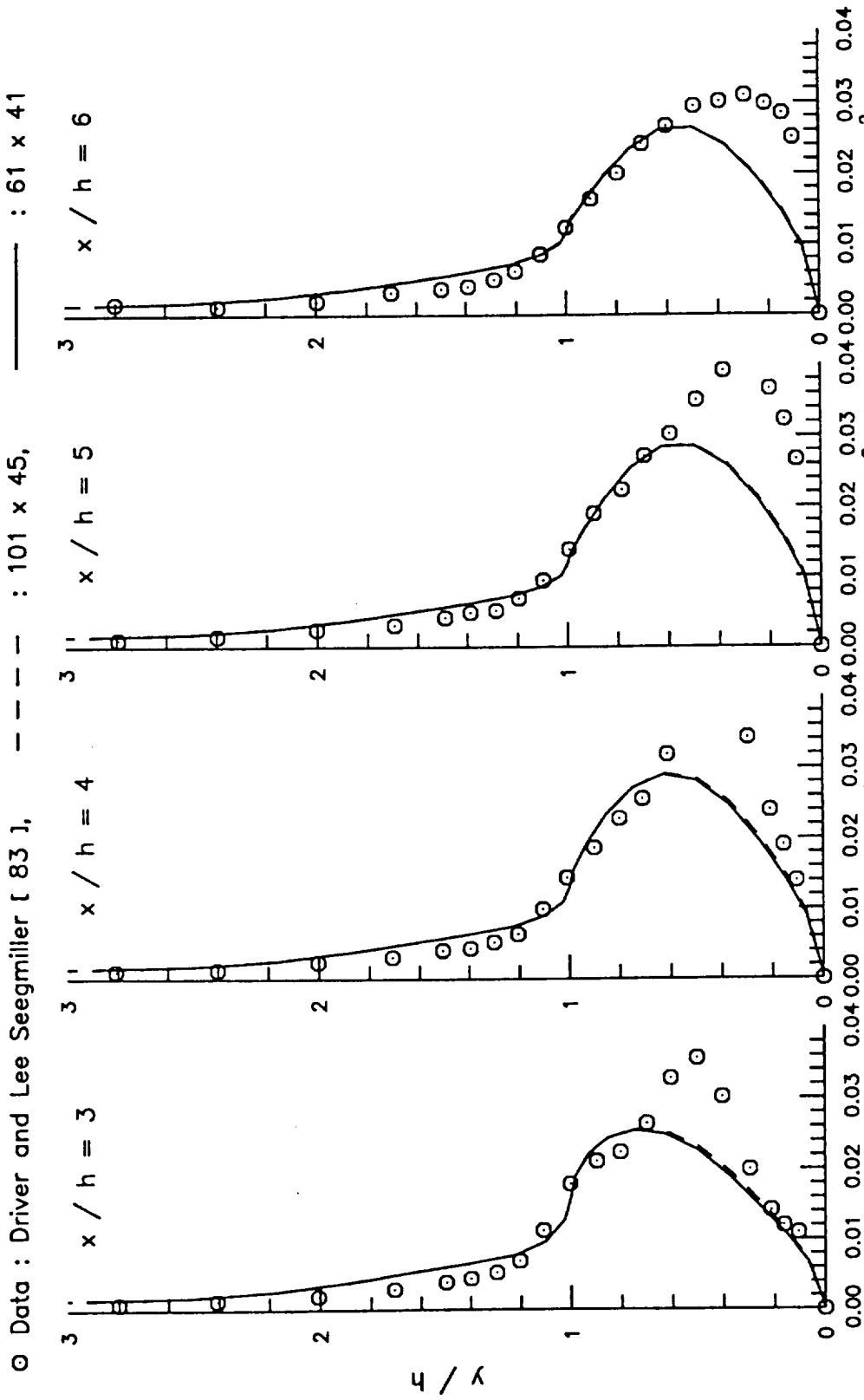

Figure 20 Continued

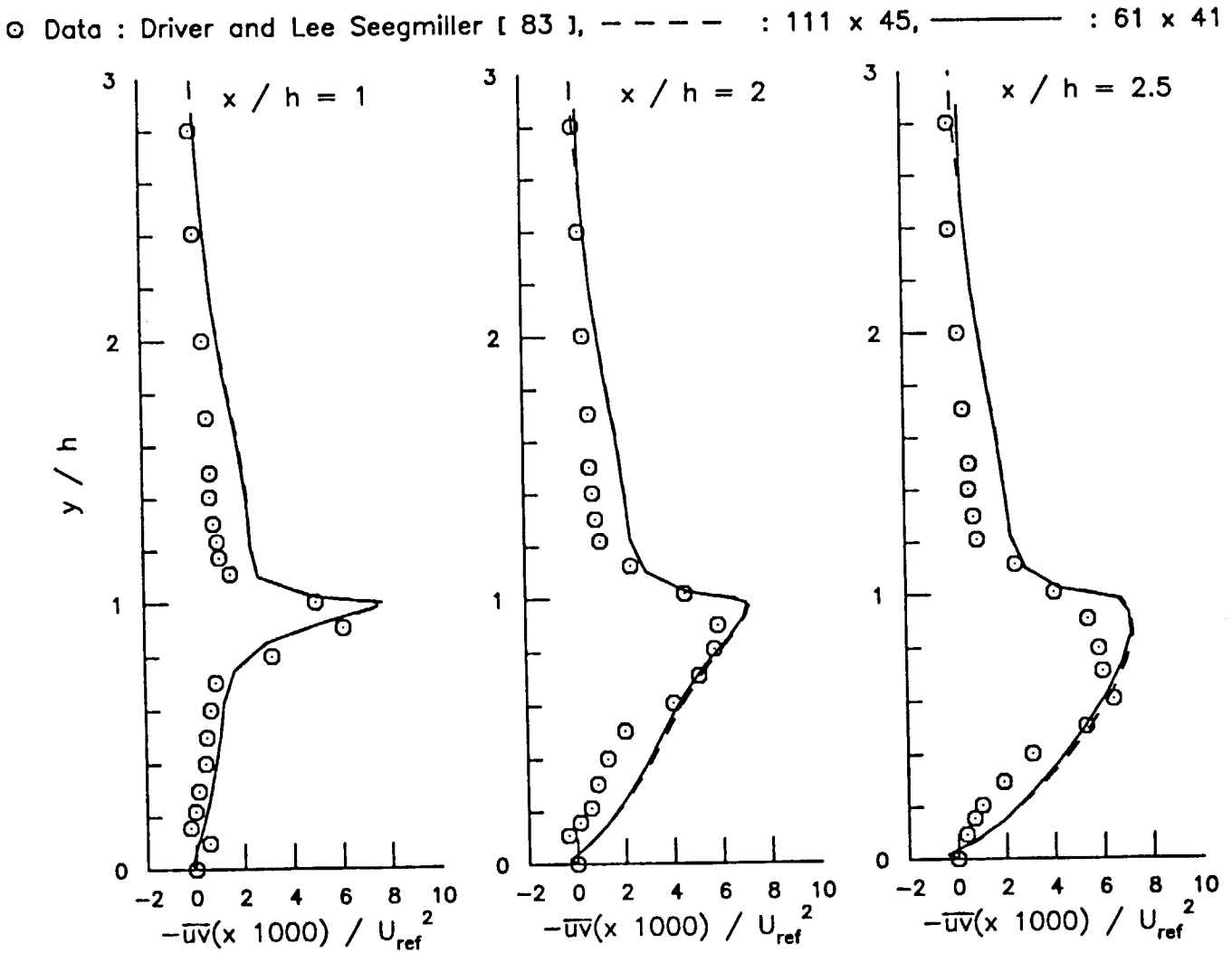

Figure 21 Reynolds Shear Stress $-\overline{uv}$ Profiles in a Backward-Facing Step Flow with Different Grid Size

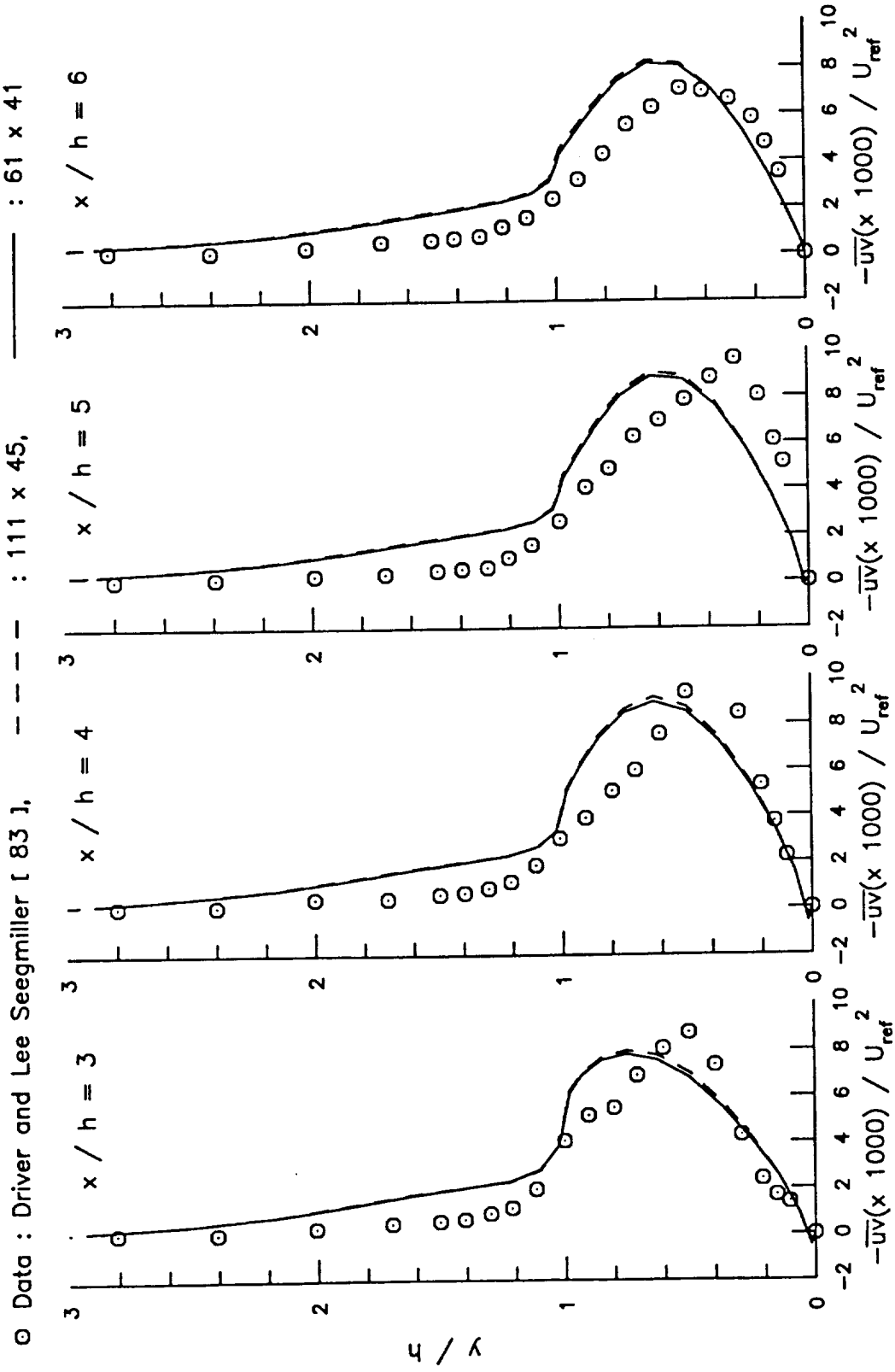

Figure 21 Continued

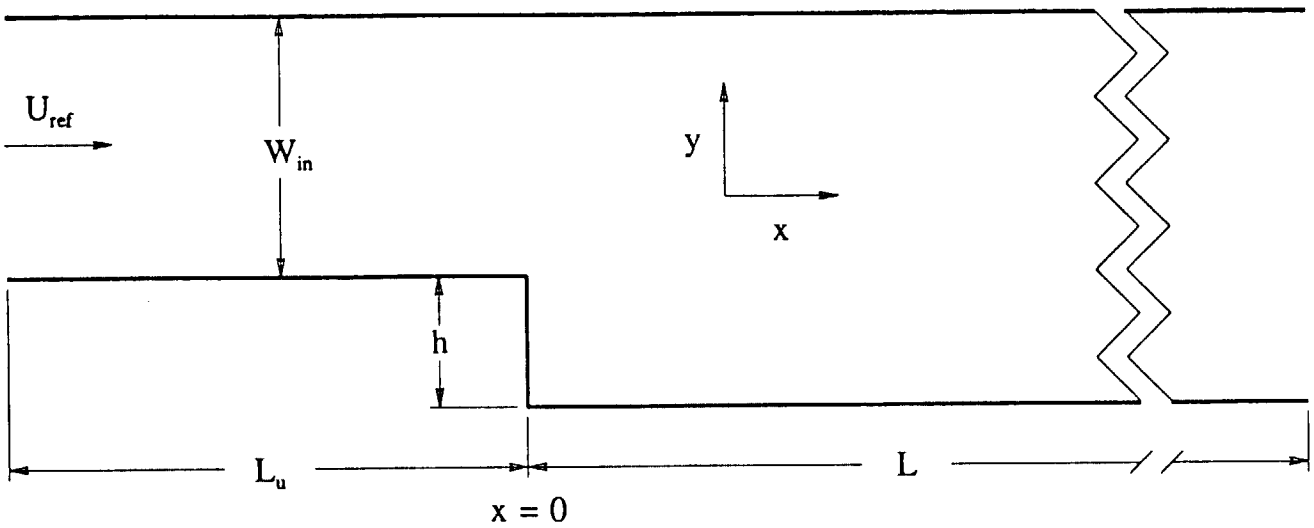

Tunnel Geometry

h= =3.81 cm
W_{in} = 2h
L = 30h
L_u = 4h
aspect ratio (B/h) = 16

Inlet Conditions

U_{ref} = 18.2 m/sec
Re_h = 45000

Figure 22 Backward-Facing Step Flow Configuration and Inlet Conditions [86]

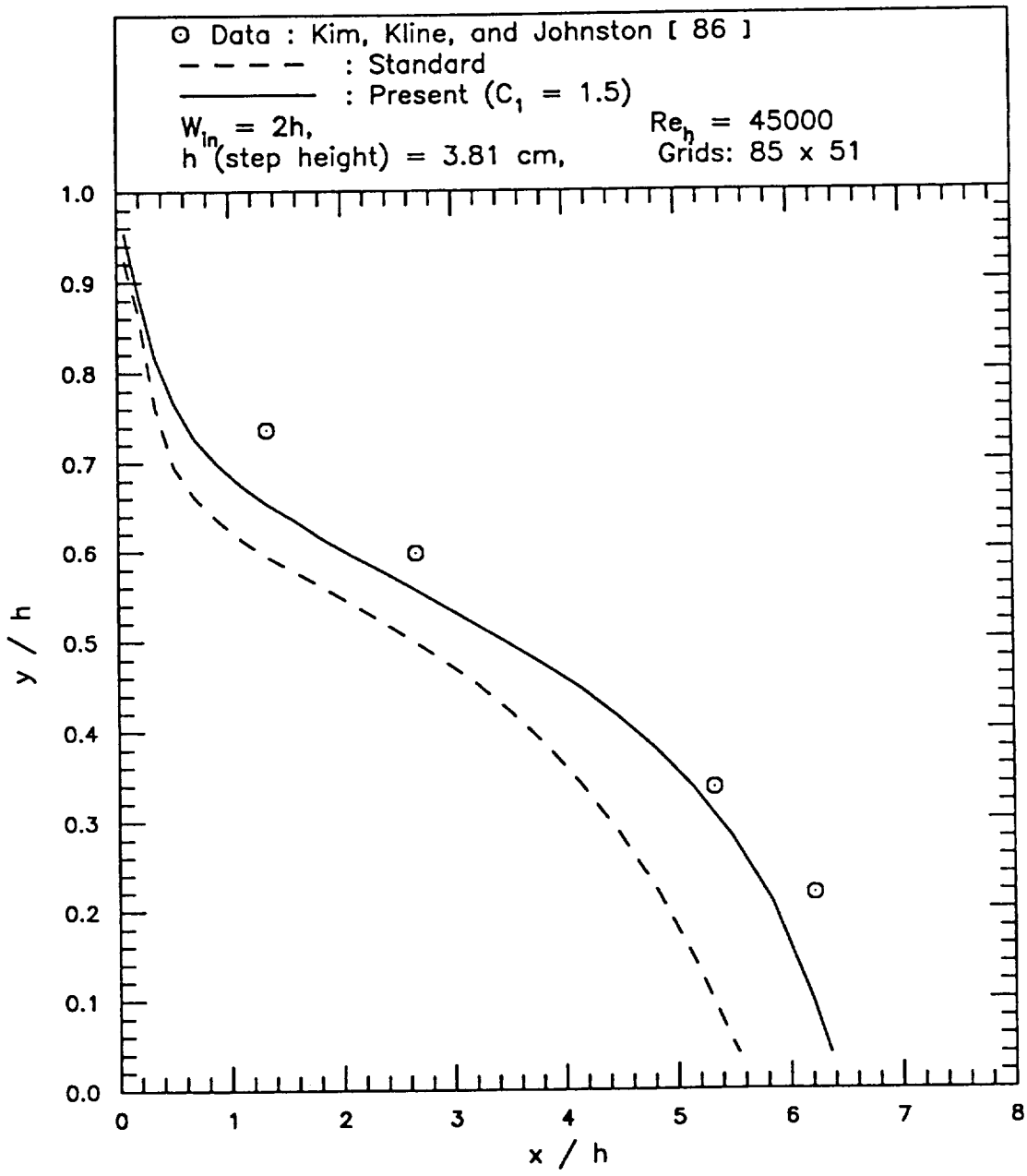

Figure 23 Locus of Flow Reversal in a Backward-Facing Flow (85 x 51 grids)

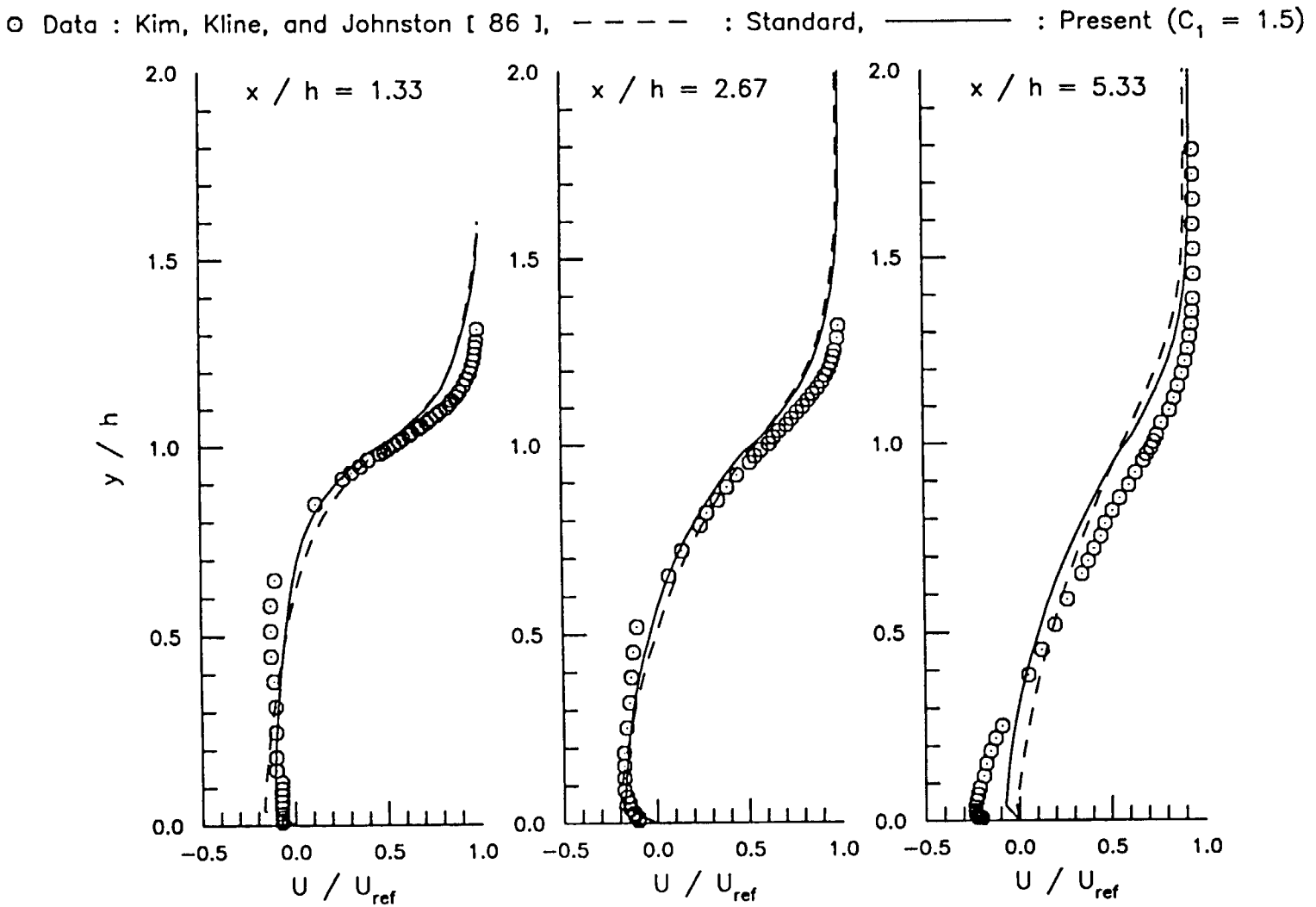

Figure 24 Streamwise Velocity Profiles in a Backward-Facing Step Flow (85 x 51 grids)

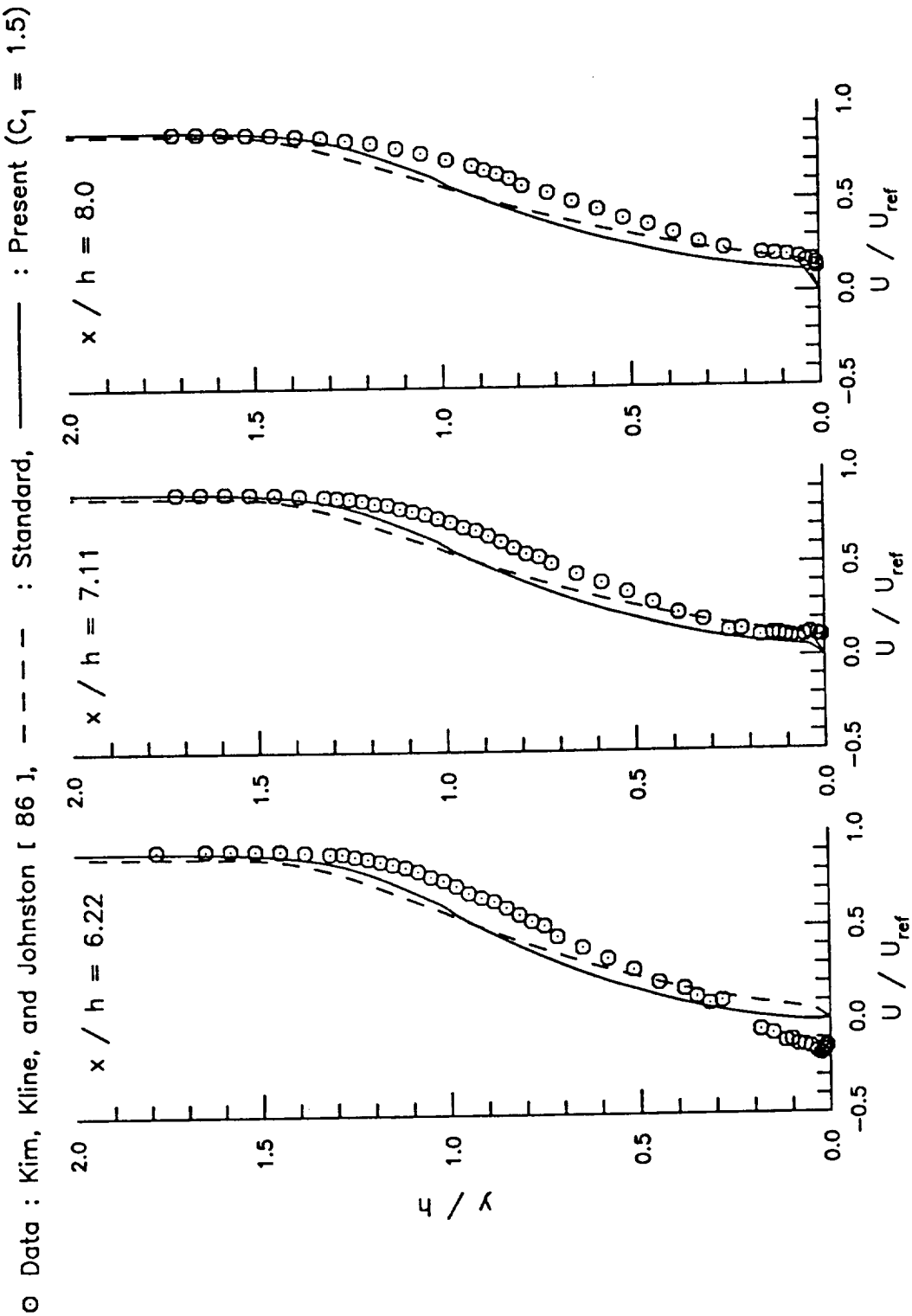

Figure 24 Continued

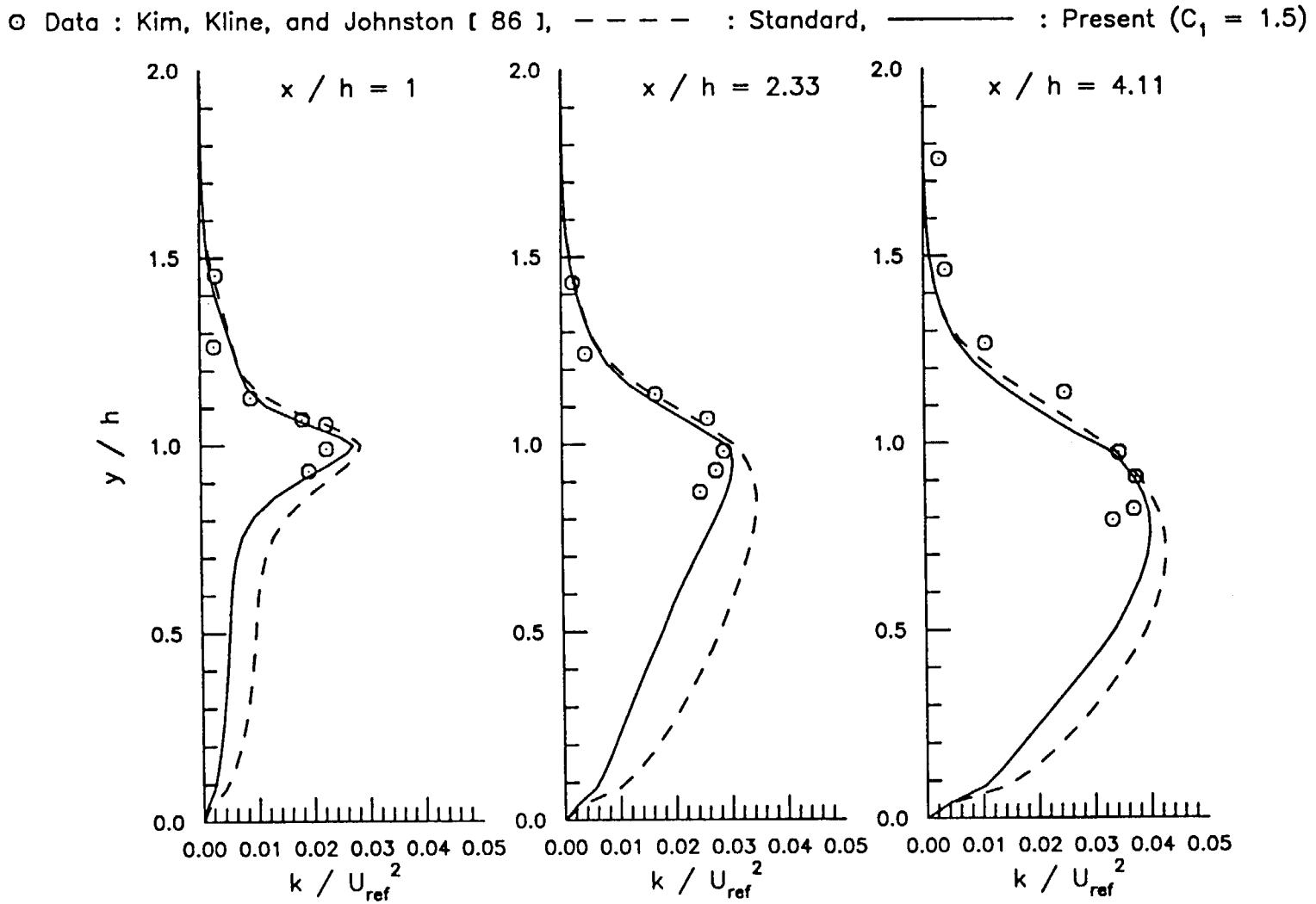

Figure 25 Turbulent Kinetic Energy Profiles in a Backward-Facing Step Flow (85 x 51 grids)

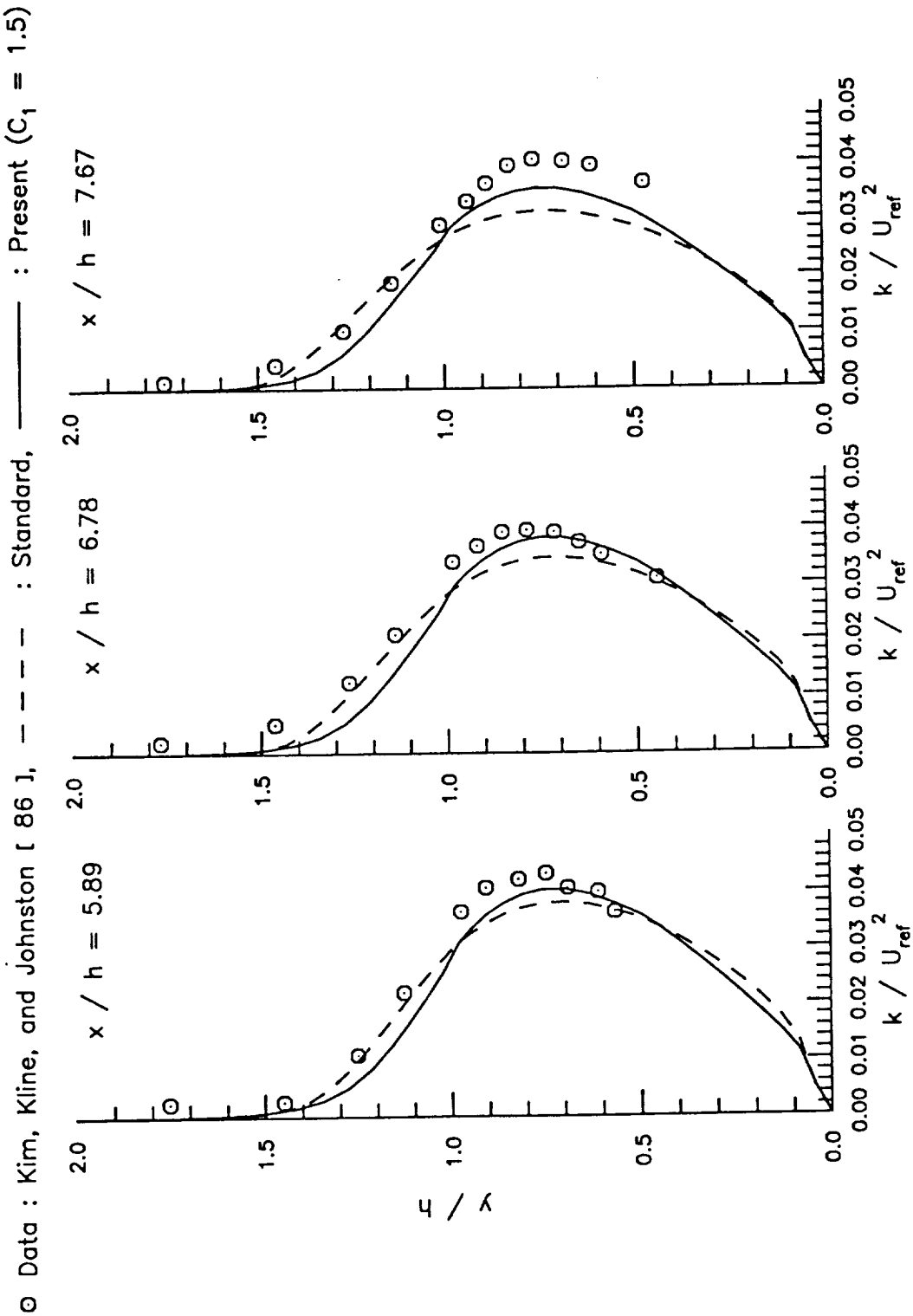

Figure 25 Continued

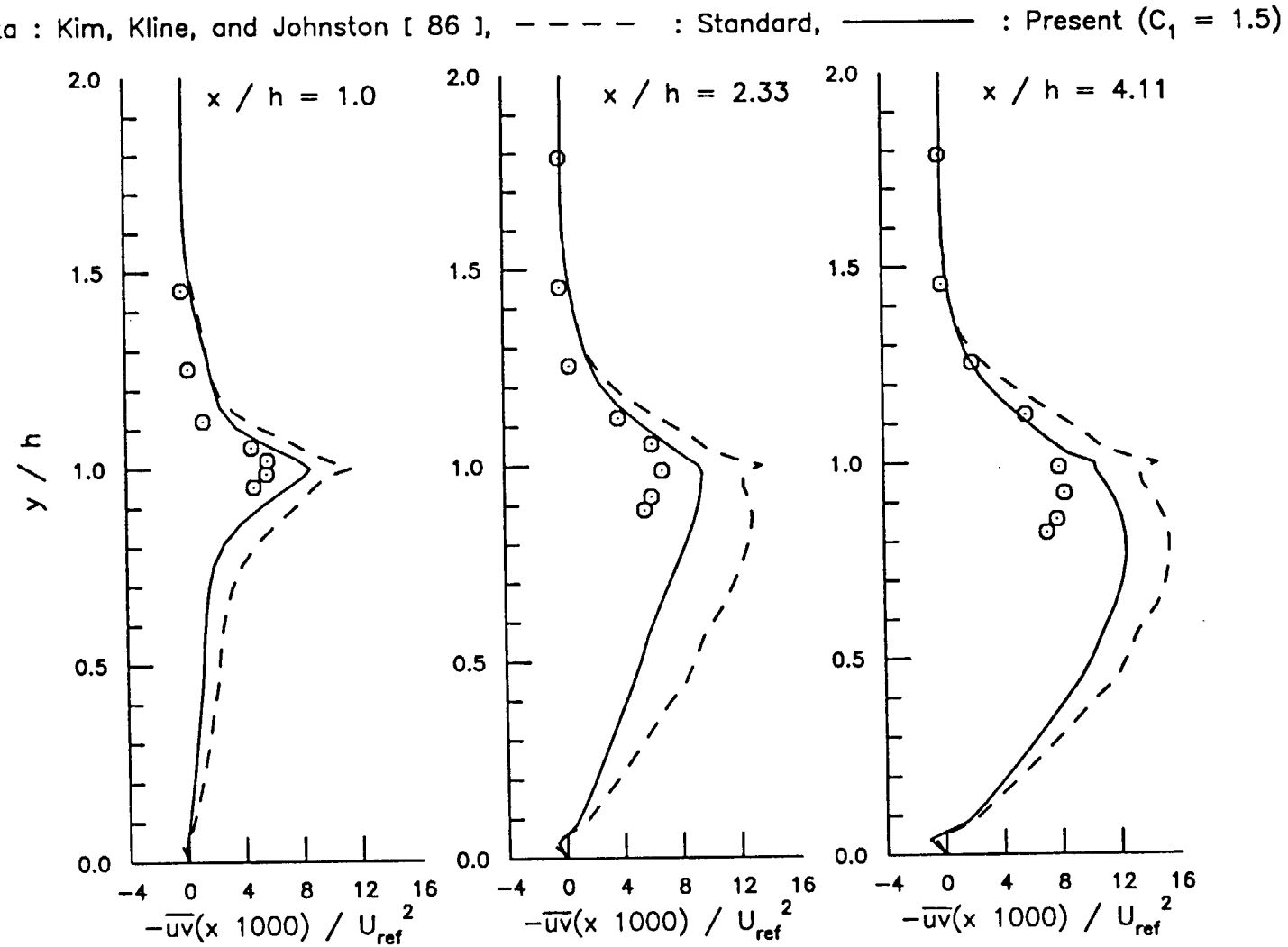

Figure 26 Reynolds Shear Stress -$\overline{uv}$ Profiles in a Backward-Facing Step Flow (85 x 51 grids)

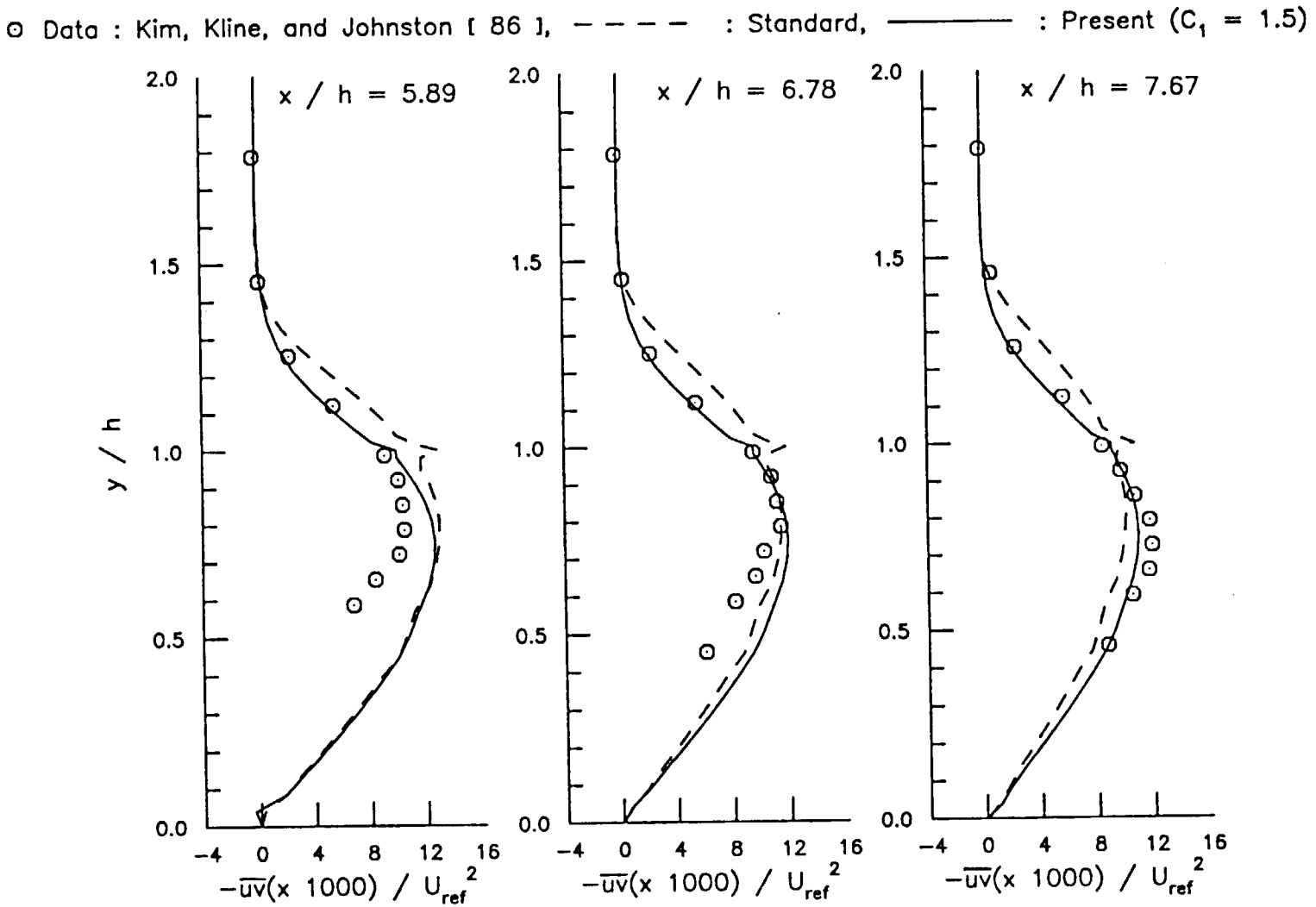

Figure 26 Continued

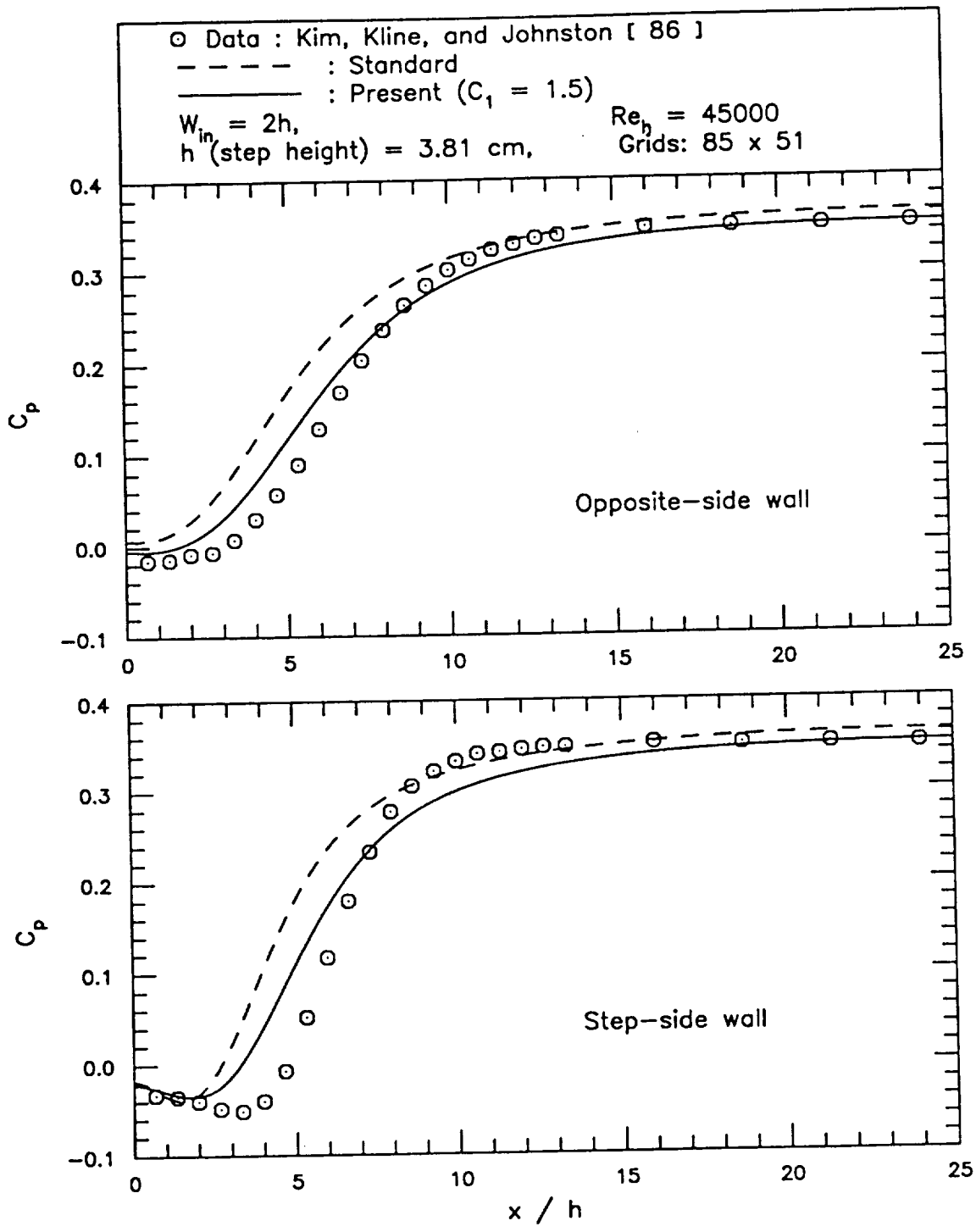

Figure 27 Static Pressure Coefficient Distributions along the Wall in a Backward-Facing Step Flow (85 x 51 grids)

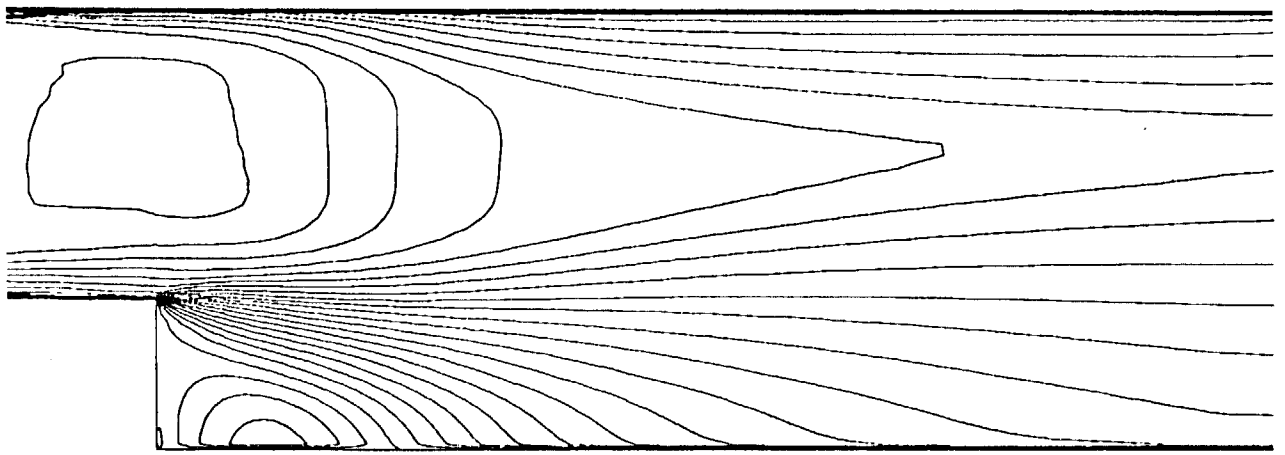

(a) present model

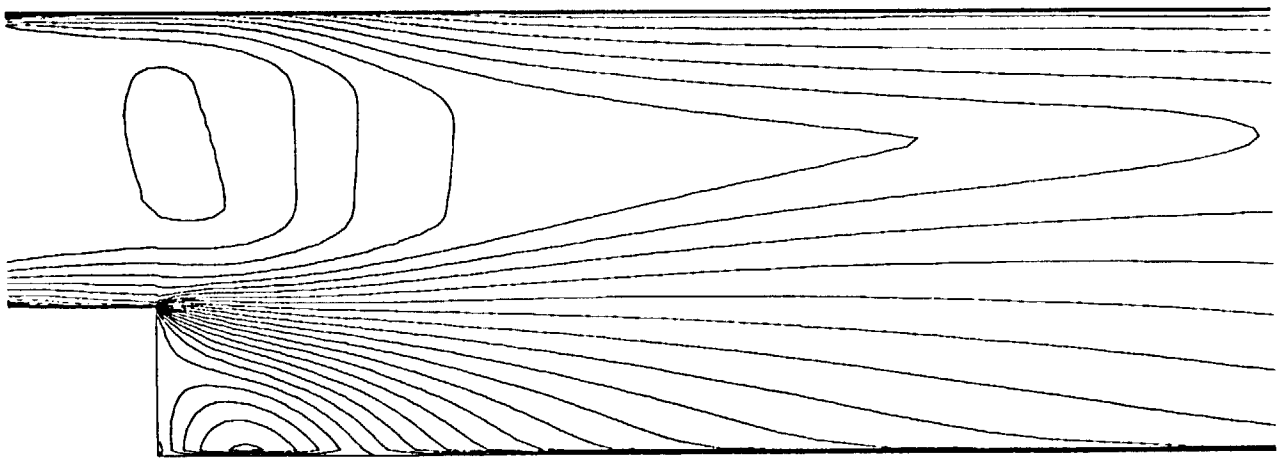

(b) standard k-ε model

Figure 28 Streamwise Velocity Contour in a Backward-Facing Step Flow [86] (85 x 51 grids)

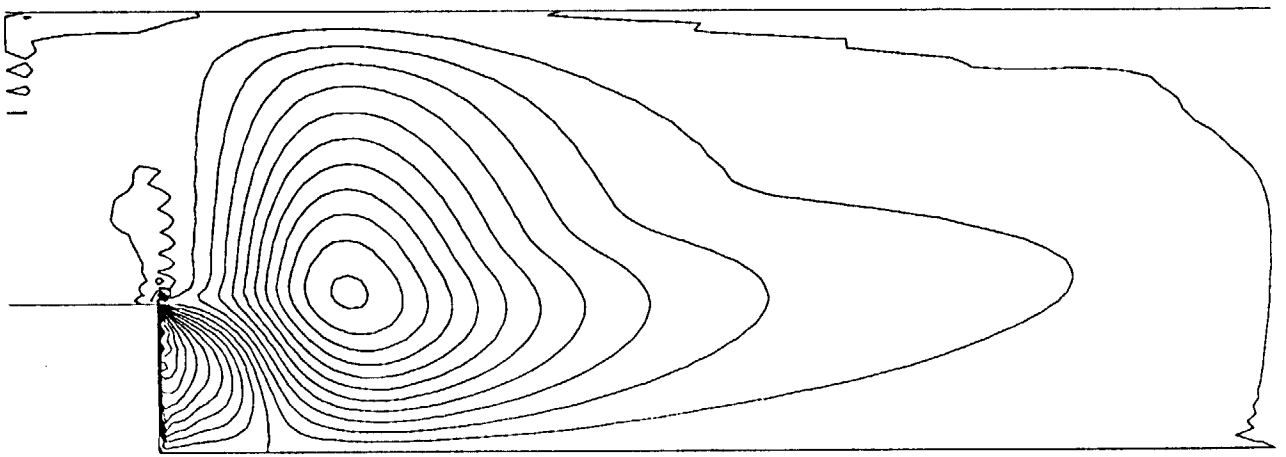

(a) present model

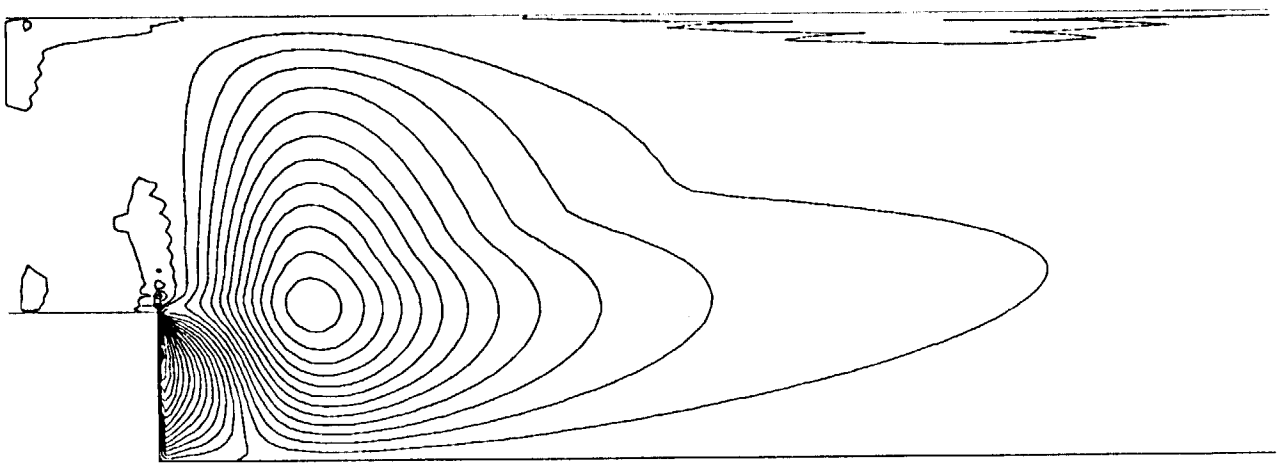

(b) standard k-ε model

Figure 29 Transverse Velocity Contour in a Backward-Facing Step Flow [86] (85 x 51 grids)

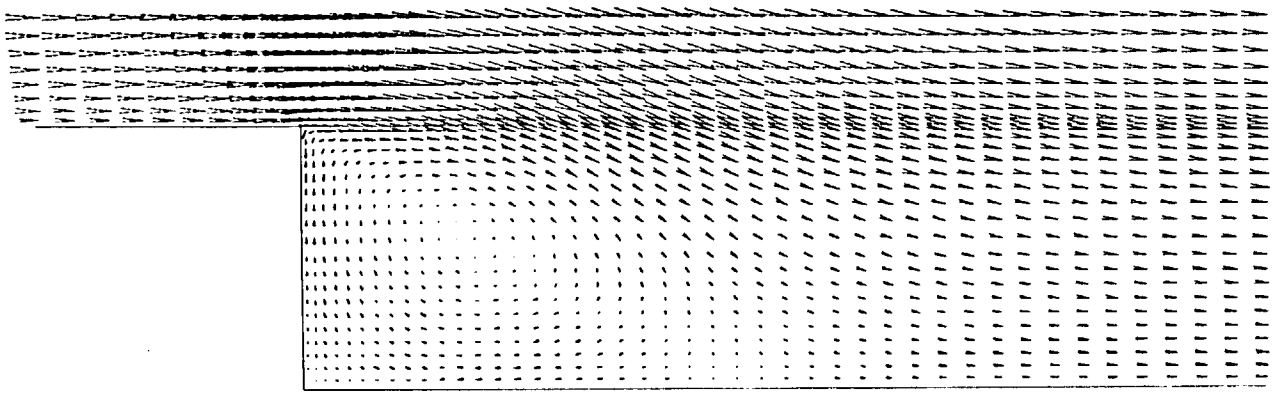

(a) present model

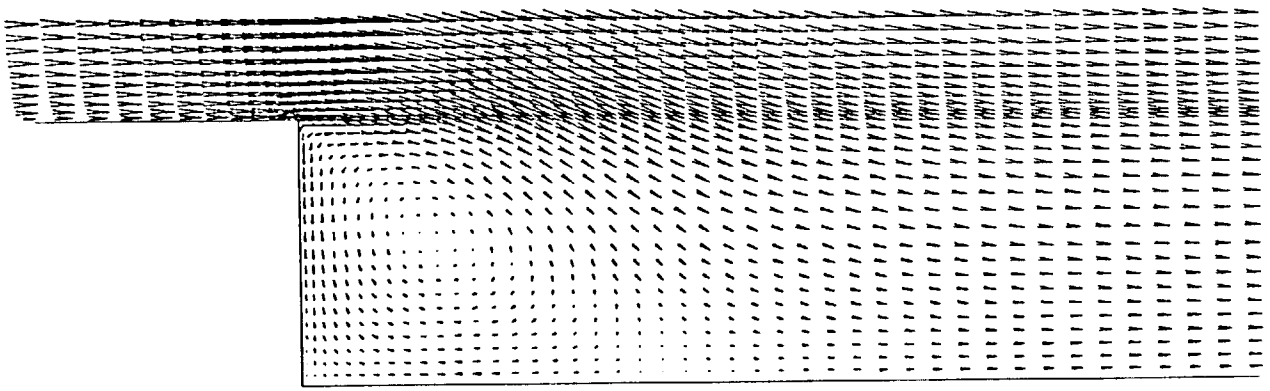

(b) standard k-ε model

Figure 30 Velocity Vectors in a Backward-Facing Step Flow [86] (85 x 51 grids)

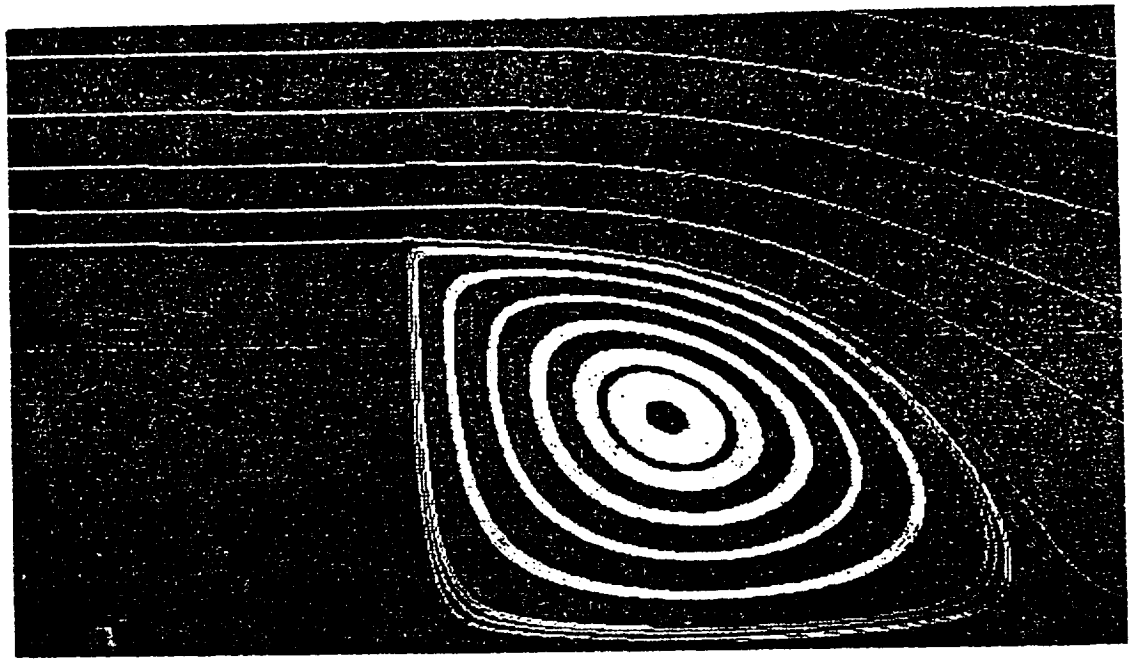

(a) present model

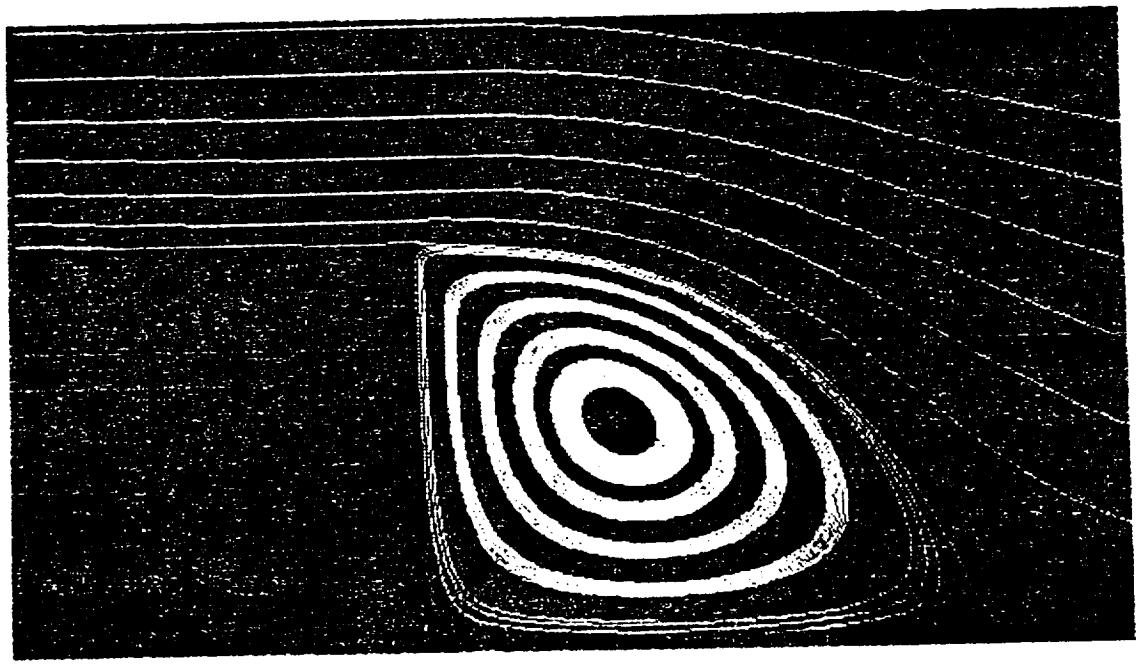

(b) standard k-ε model

Figure 31 Particle Traces in a Backward-Facing Step Flow (close view)

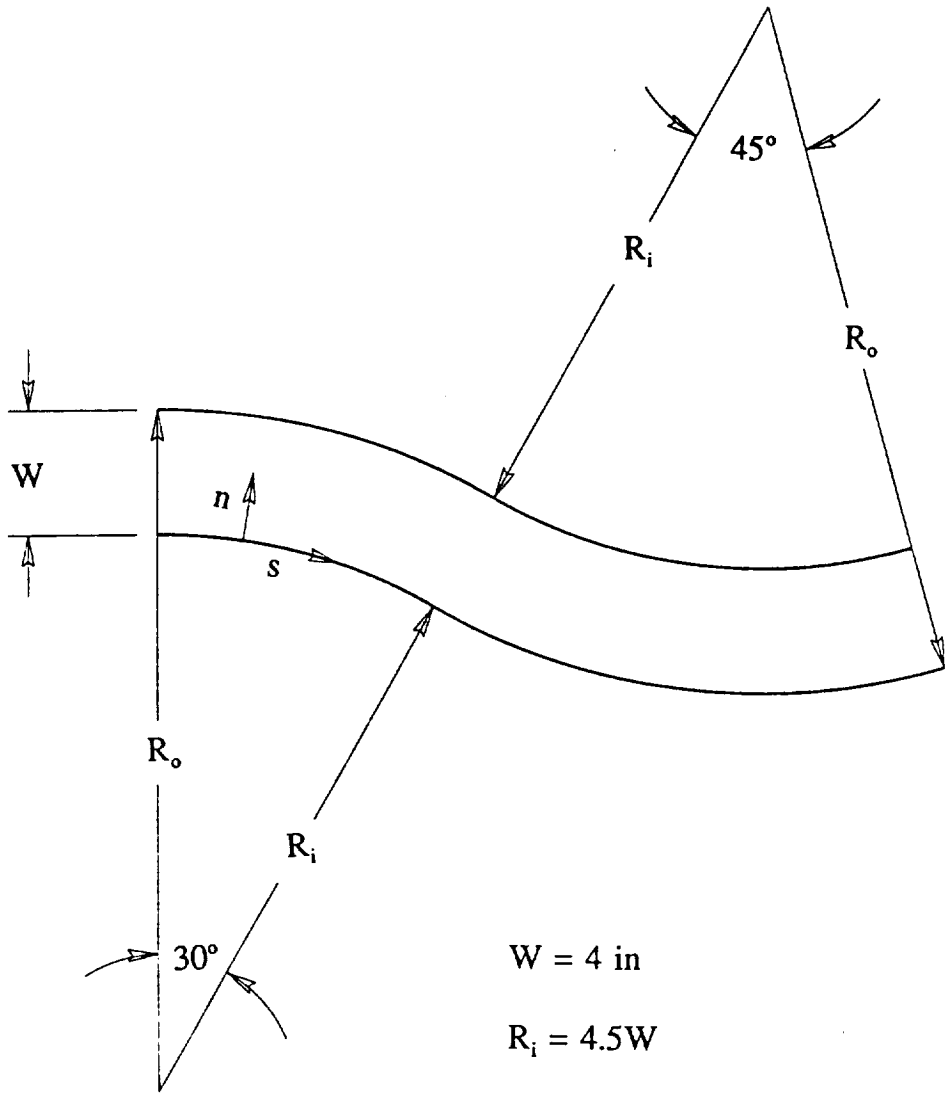

Figure 32 A 30°-45° S-Bend Duct Geometry and Inlet Conditions by L.A. Butz [23]

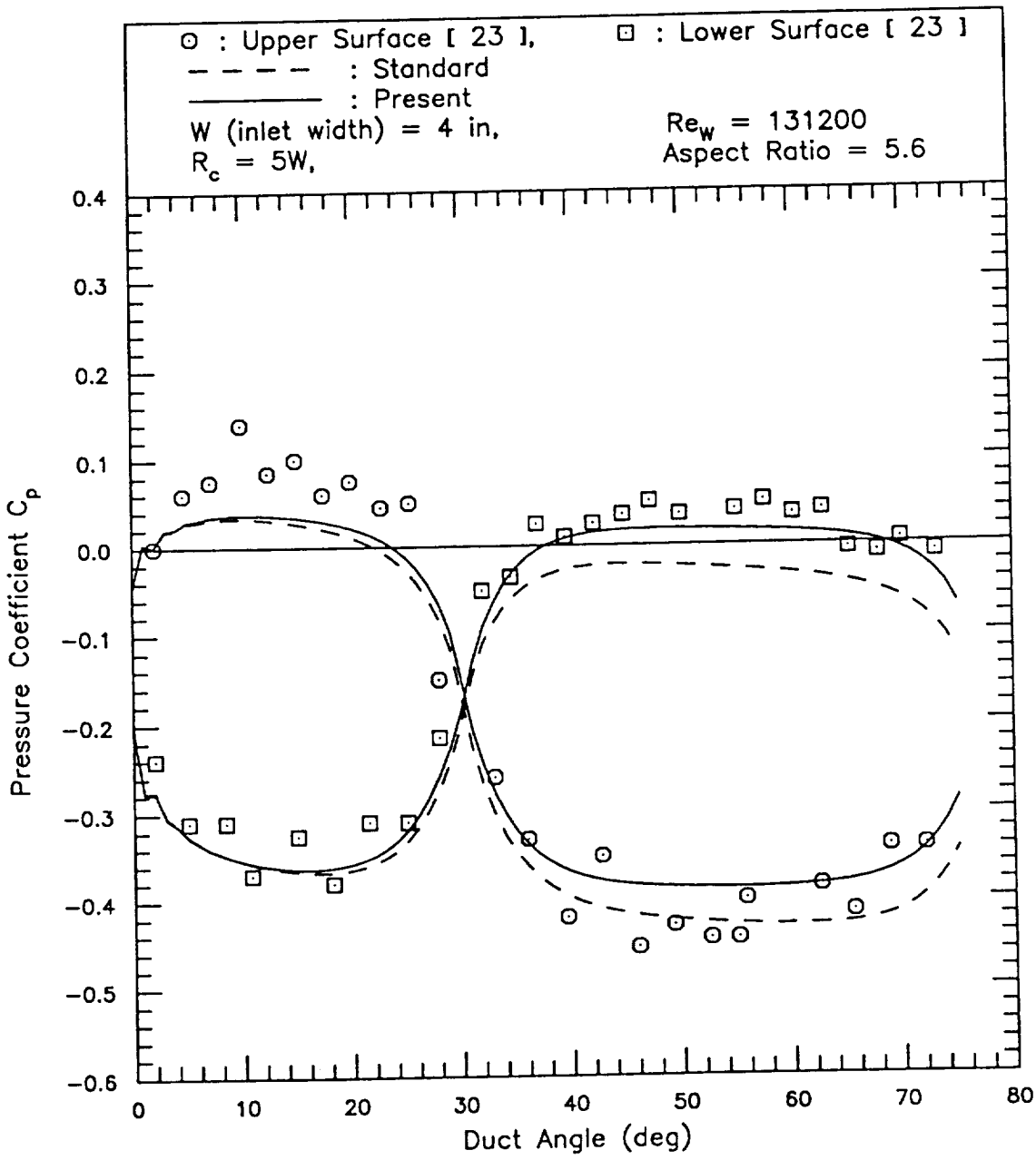

Figure 33 Static Pressure Coefficient Distribution for a 30°-45° S-Bend Duct (88 x 51 grids)

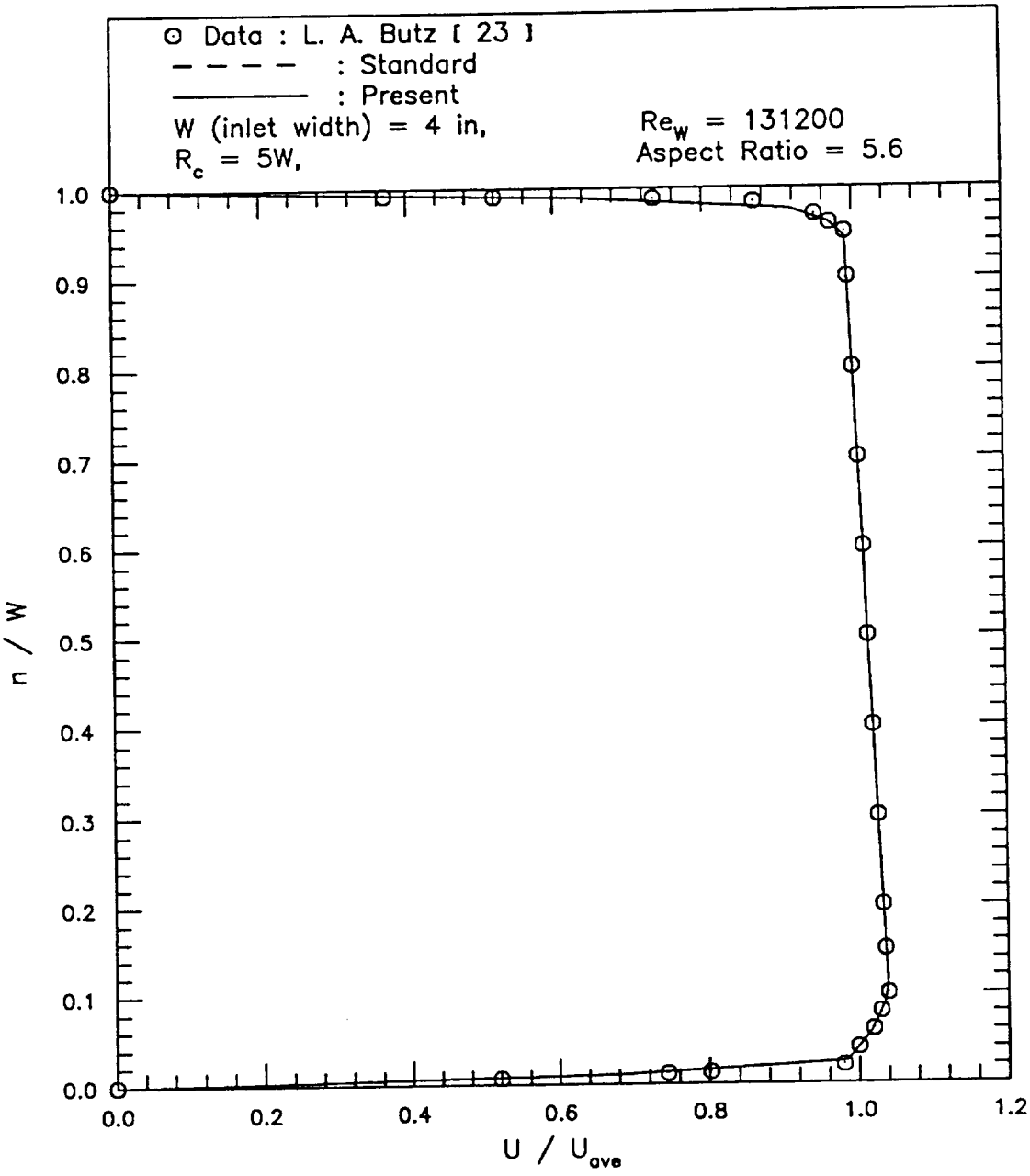

Figure 34 Longitudinal Velocity Profile at the Entrance Plane of a 30°-45° S-Bend Duct (88 x 51 grids)

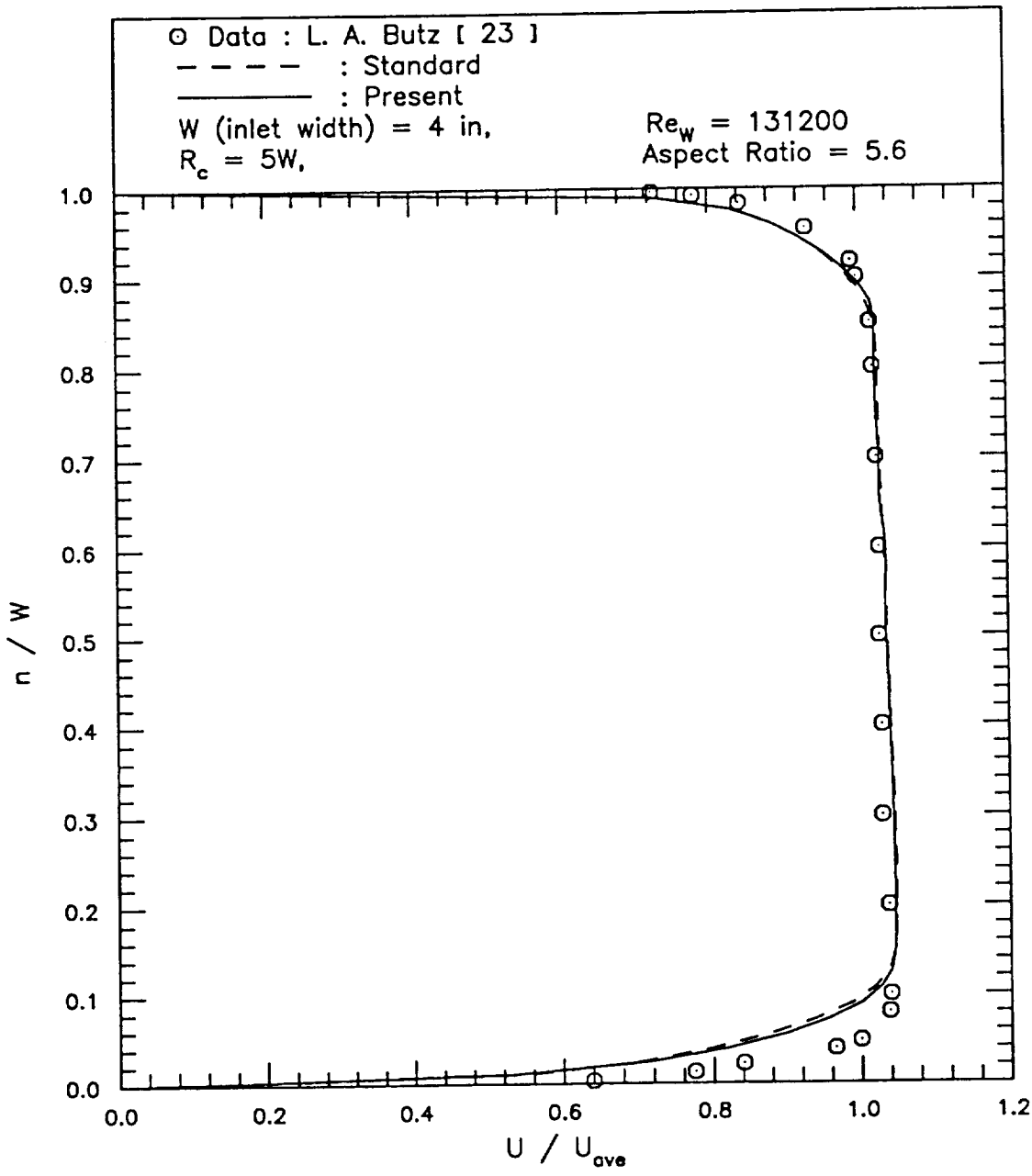

Figure 35 Longitudinal Velocity Profile at the Inflection Plane of a 30°-45° S-Bend Duct (88 x 51 grids)

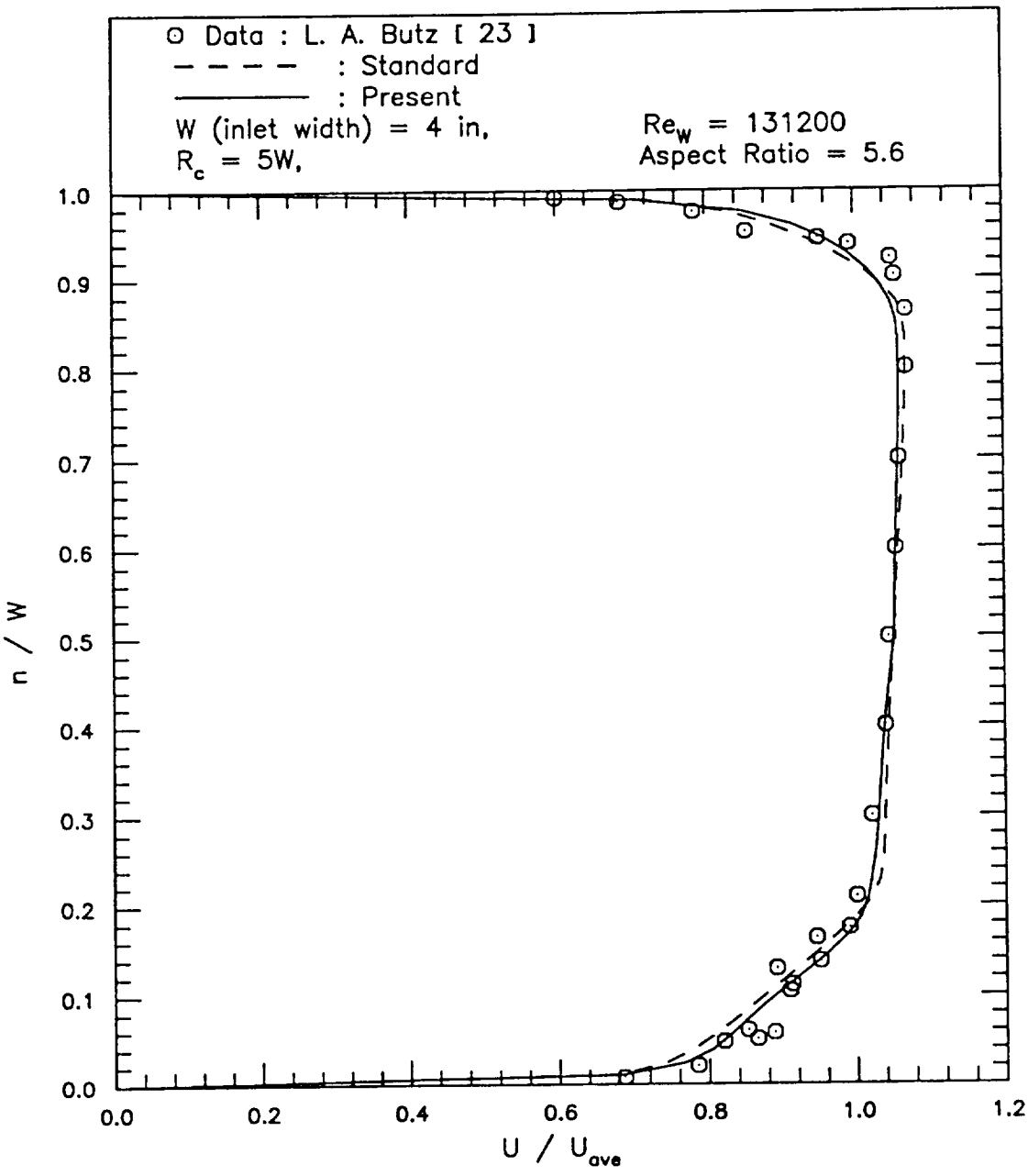

Figure 36 Longitudinal Velocity Profile at the Exit Plane of a 30°-45° S-Bend Duct (88 x 51 grids)

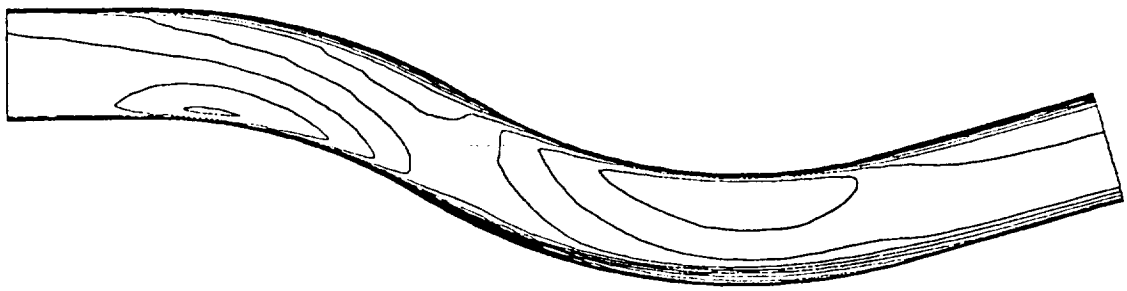

(a) present model

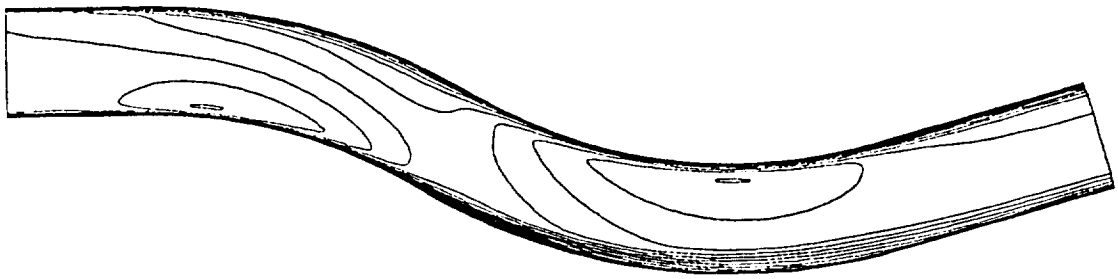

(b) standard k-ε model

Figure 37 X-Component Velocity Contour in a 30°-45° S-Duct (88 x 51 grids)

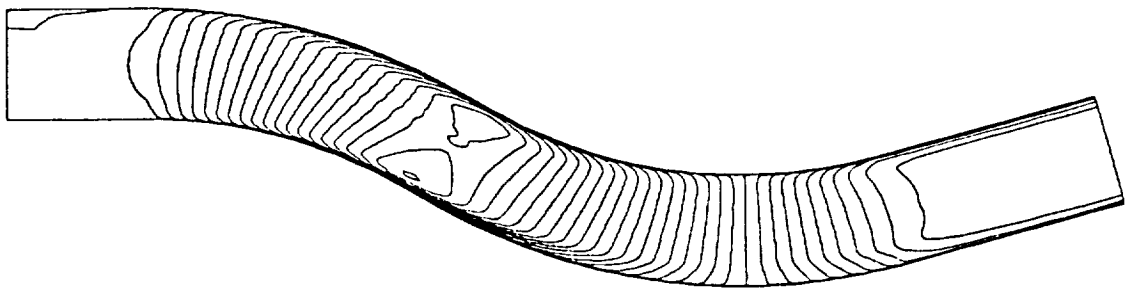

(a) present model

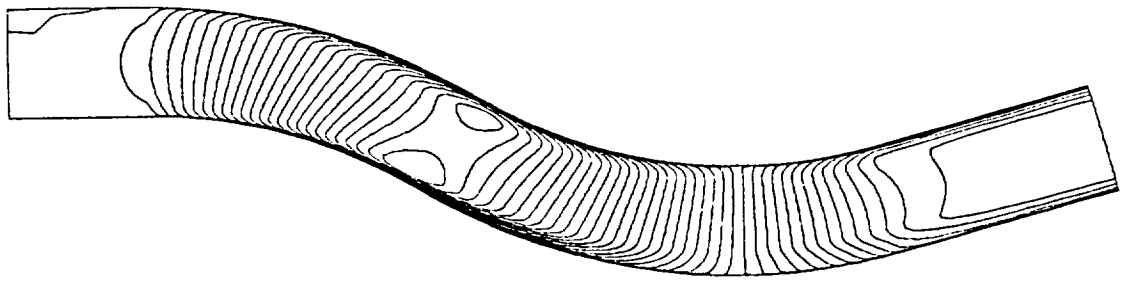

(b) standard k-ε model

Figure 38 Y-Component Velocity Contour in a 30°-45° S-Duct (88 x 51 grids)

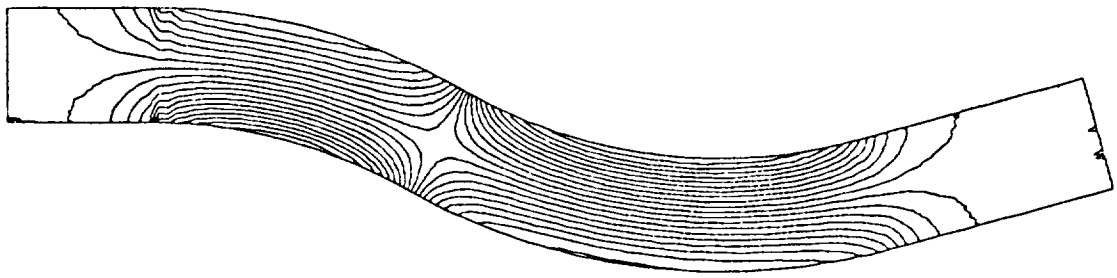

(a) present model

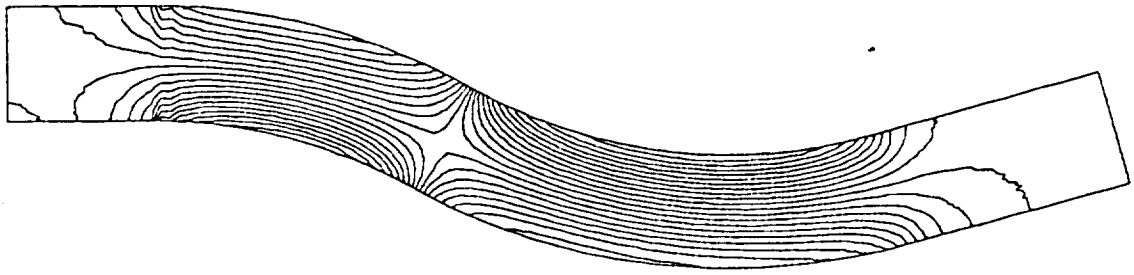

(b) standard k-ε model

Figure 39 Static Pressure Contour in a 30°-45° S-Duct (88 x 51 grids)

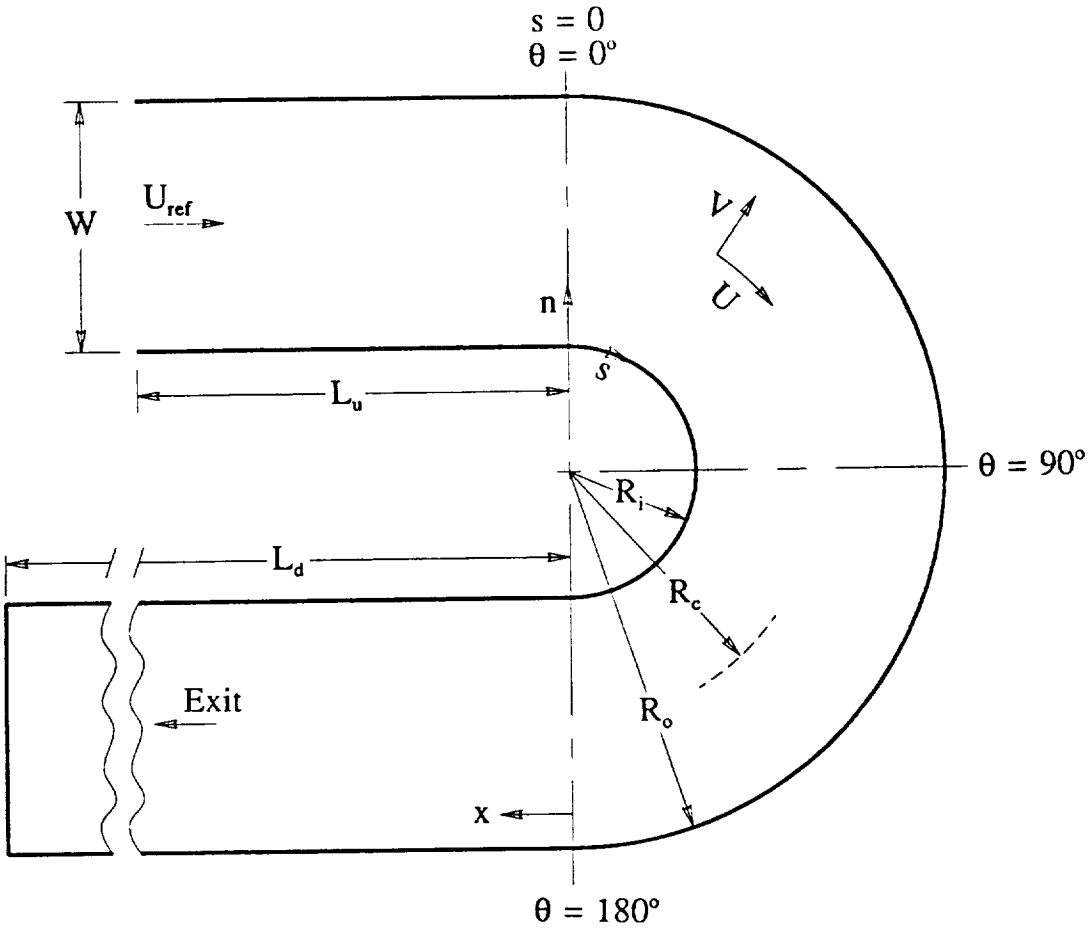

Test Section Geometry

W = 10 cm
R_i = 5 cm
R_c = 10 cm
R_o = 15 cm
L_u = 17.27 cm
L_d = 43.2 cm
aspect ratio = 10

Inlet Conditions

U_{ref} = 281.9 cm/sec
Re_W = 213000

Figure 40 The Geometrical Sketch and Inlet Conditions for a 180° Turn-Around Duct by Sandborn and Shin [87]

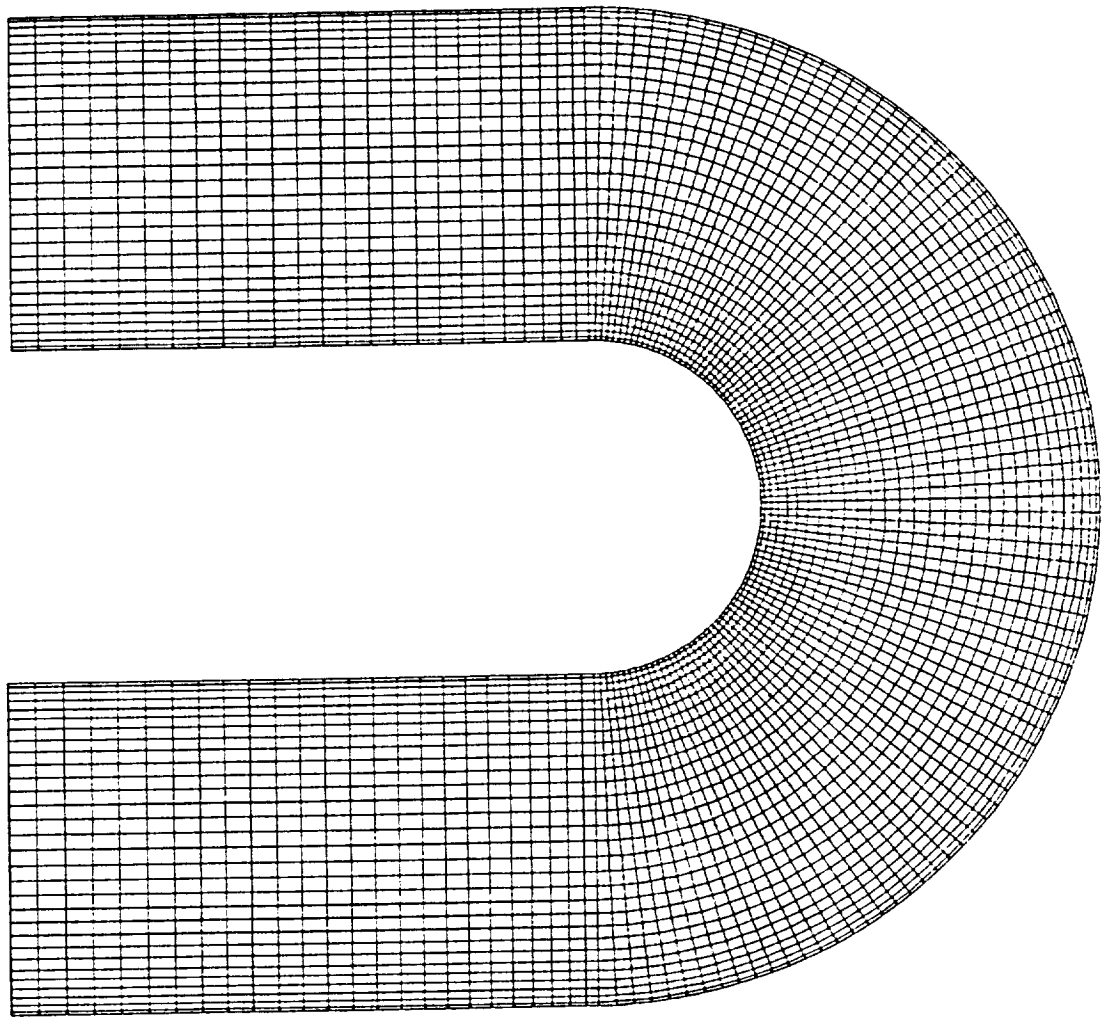

Figure 41 Grid System for a Two-Dimensional 180° Turn-Around Duct

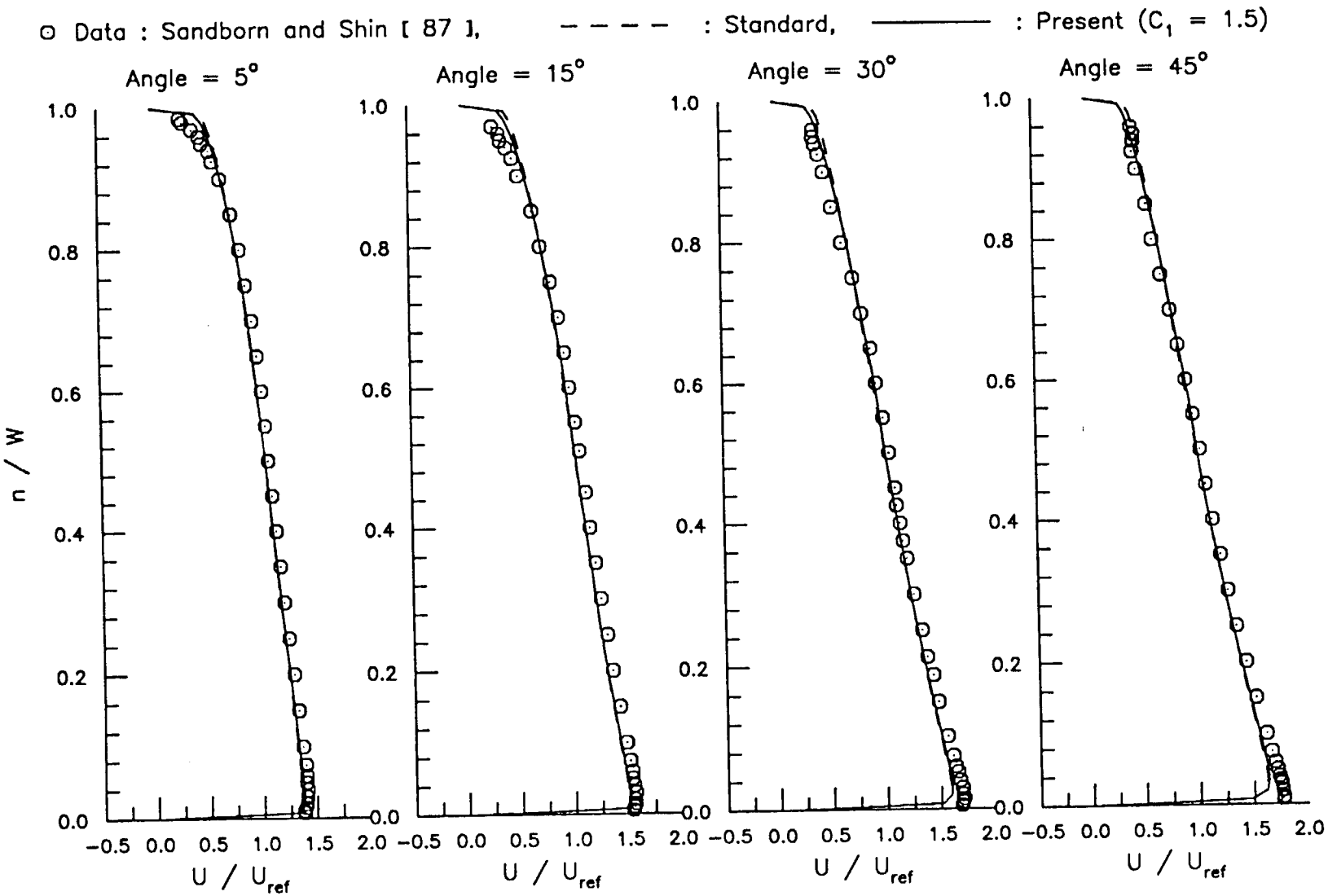

Figure 42 Longitudinal Velocity Profiles in a 180° Turn-Around Duct (141 x 41 grids)

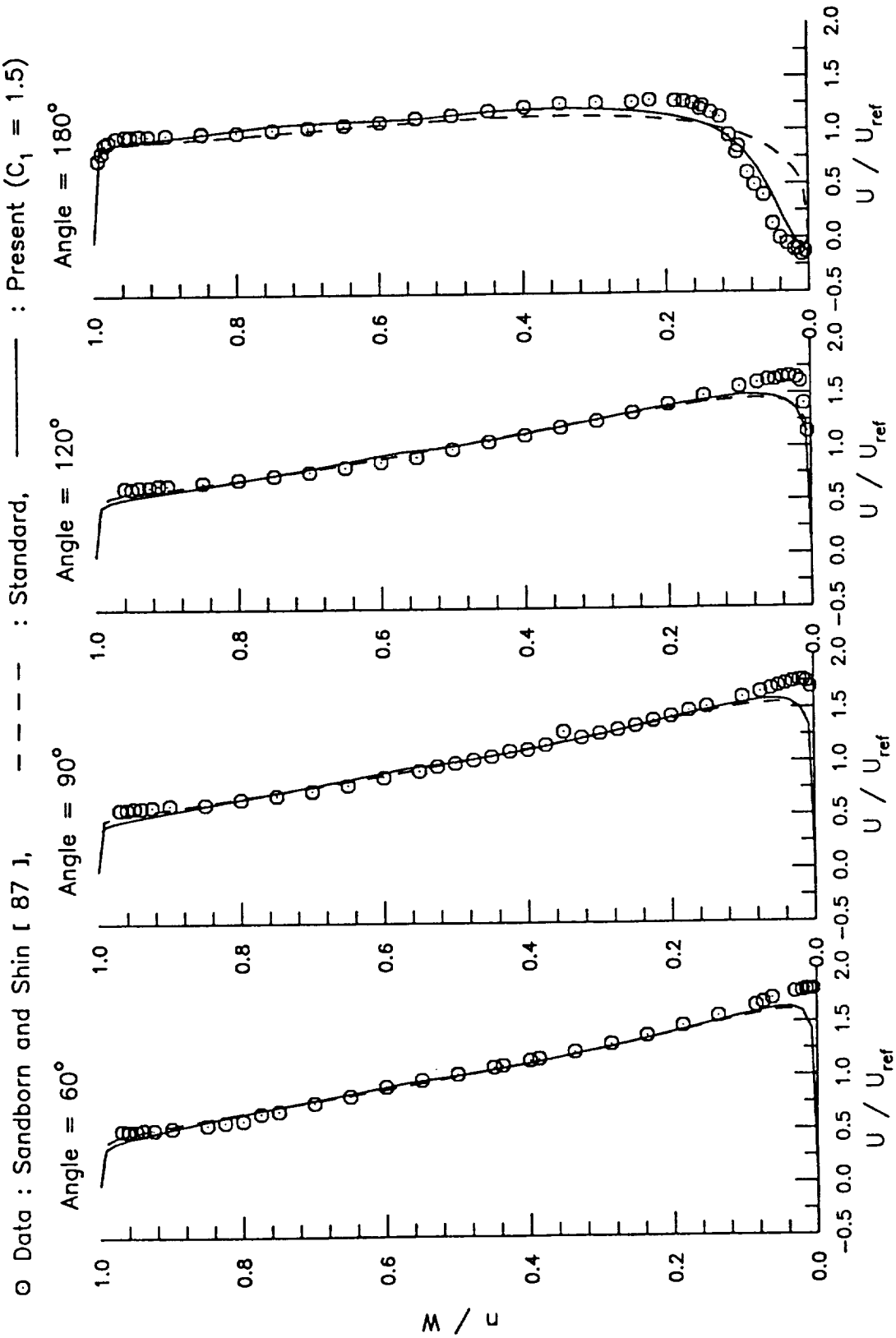

Figure 42 Continued

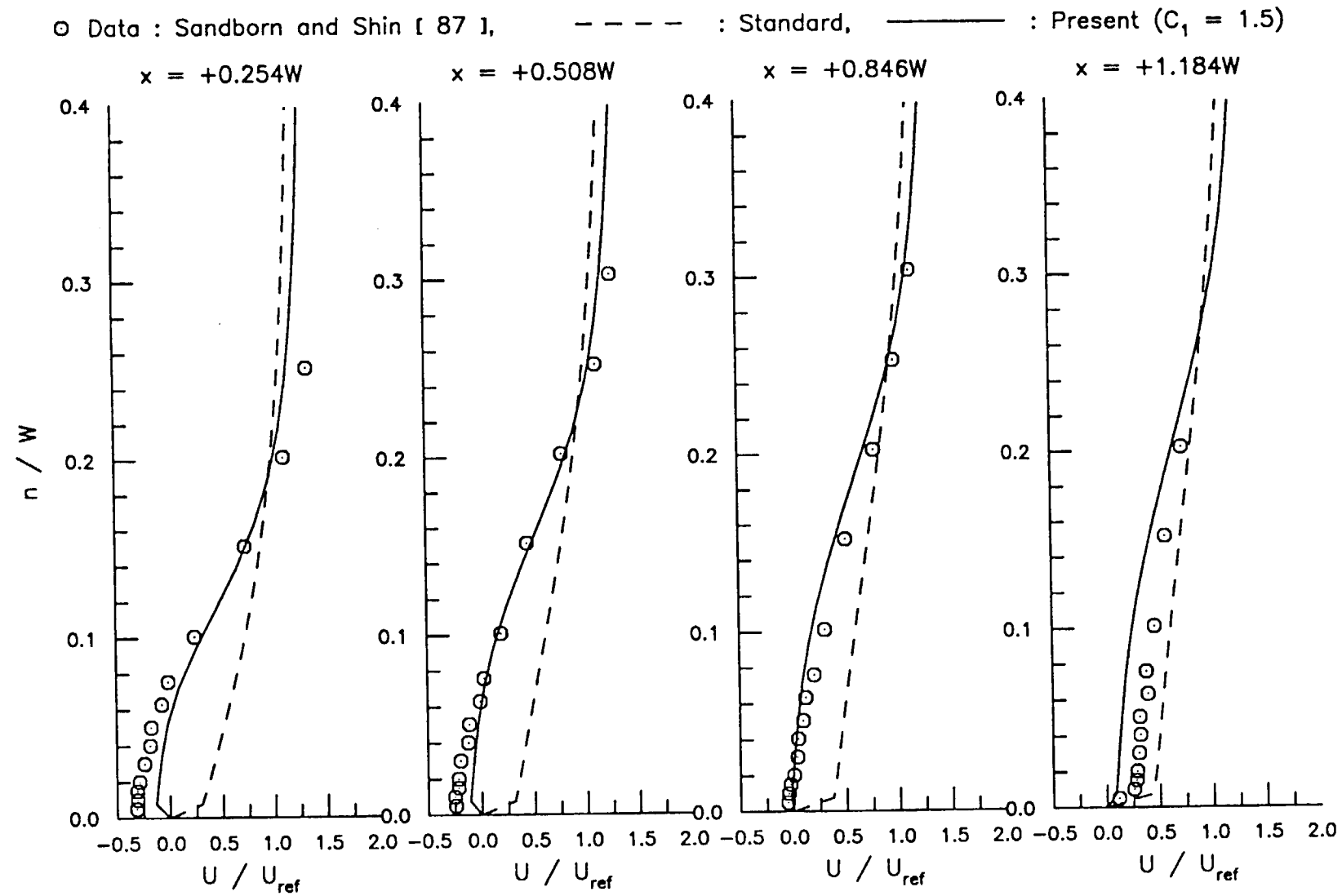

Figure 43 Longitudinal Velocity Profiles in the Separation Bubble Downstream of 180° Turn

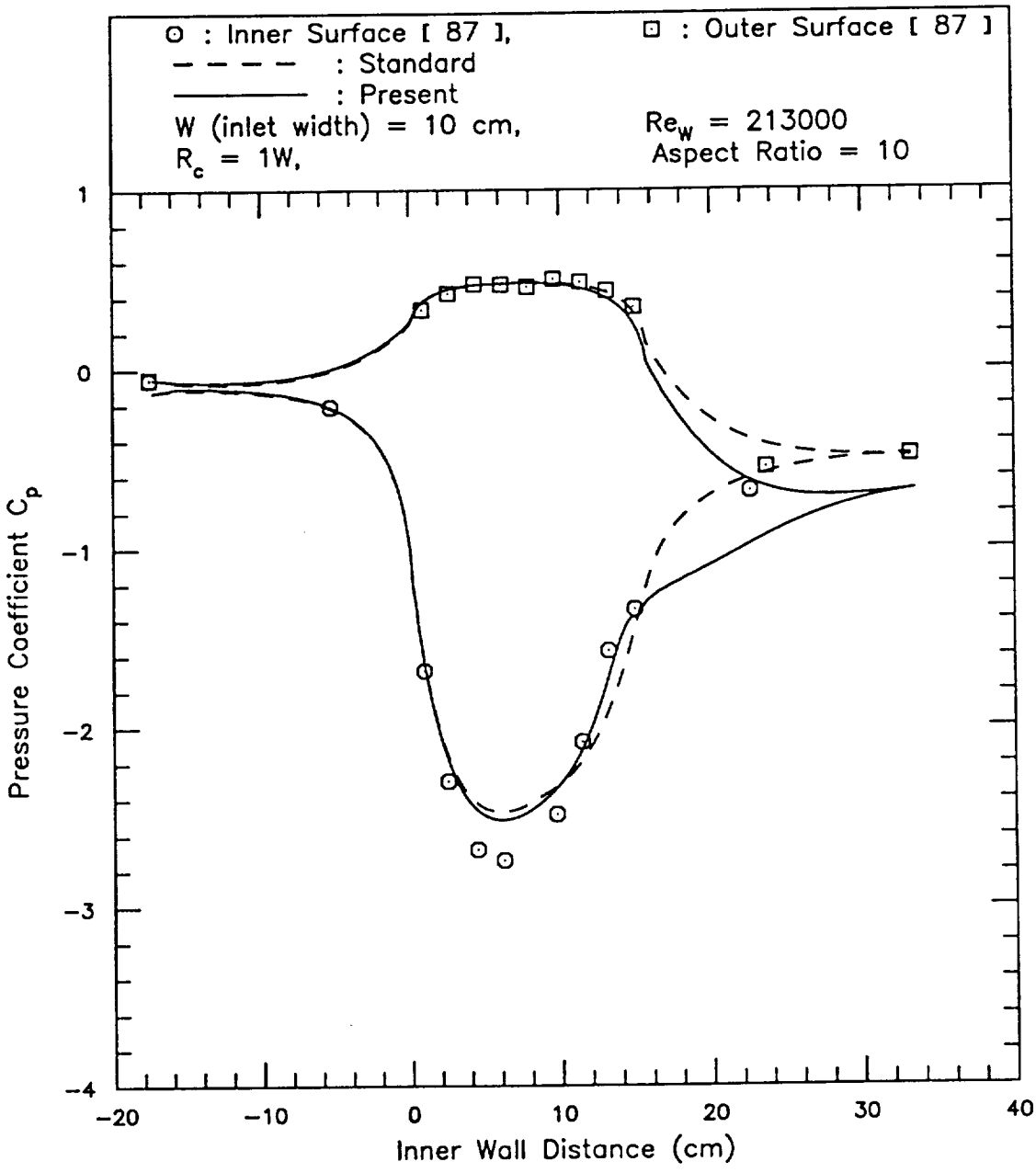

Figure 44 Wall Static Pressure Coefficient Distribution in a 180° Turn-Around Duct [87]

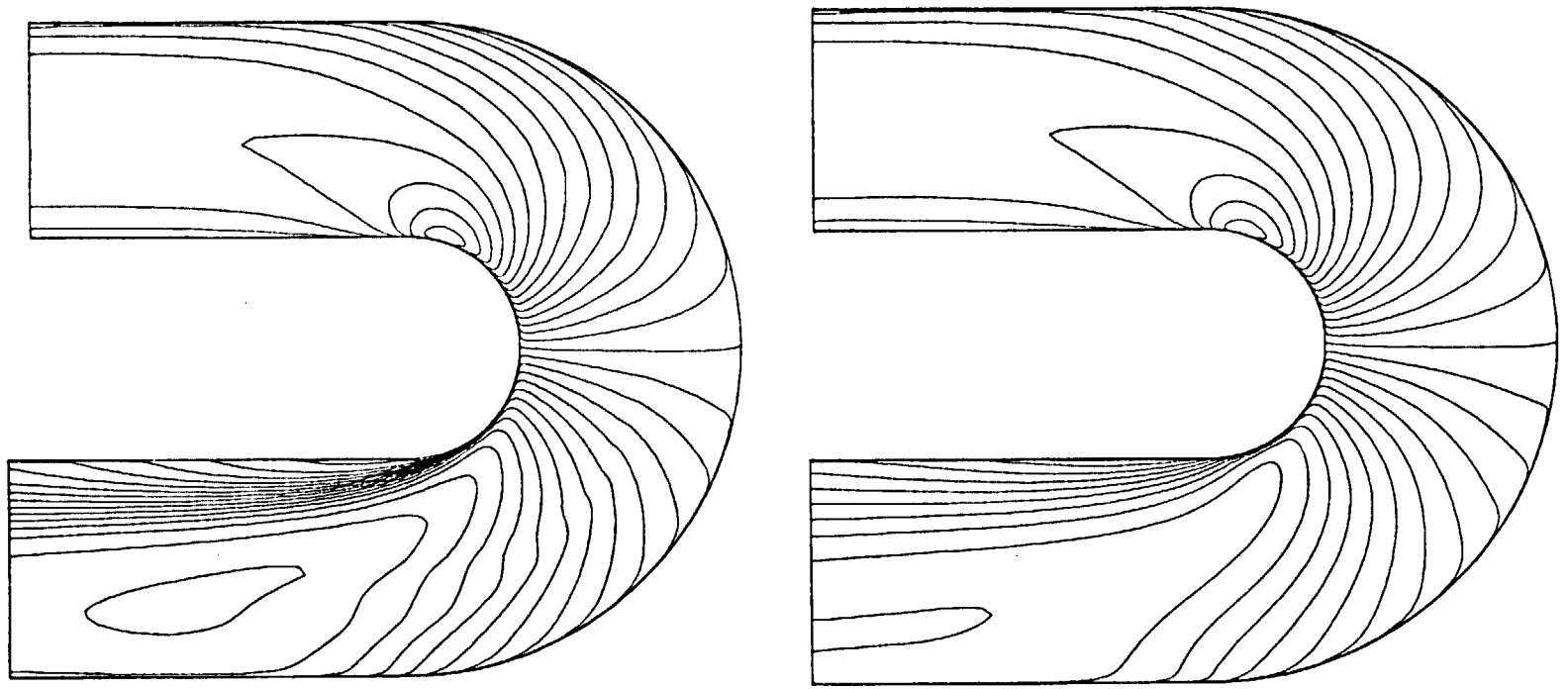

(a) present model

(b) standard k-ε model

Figure 45 X-Component Velocity Contour in a 180° Turn-Around Duct [87] (141 x 41 grids)

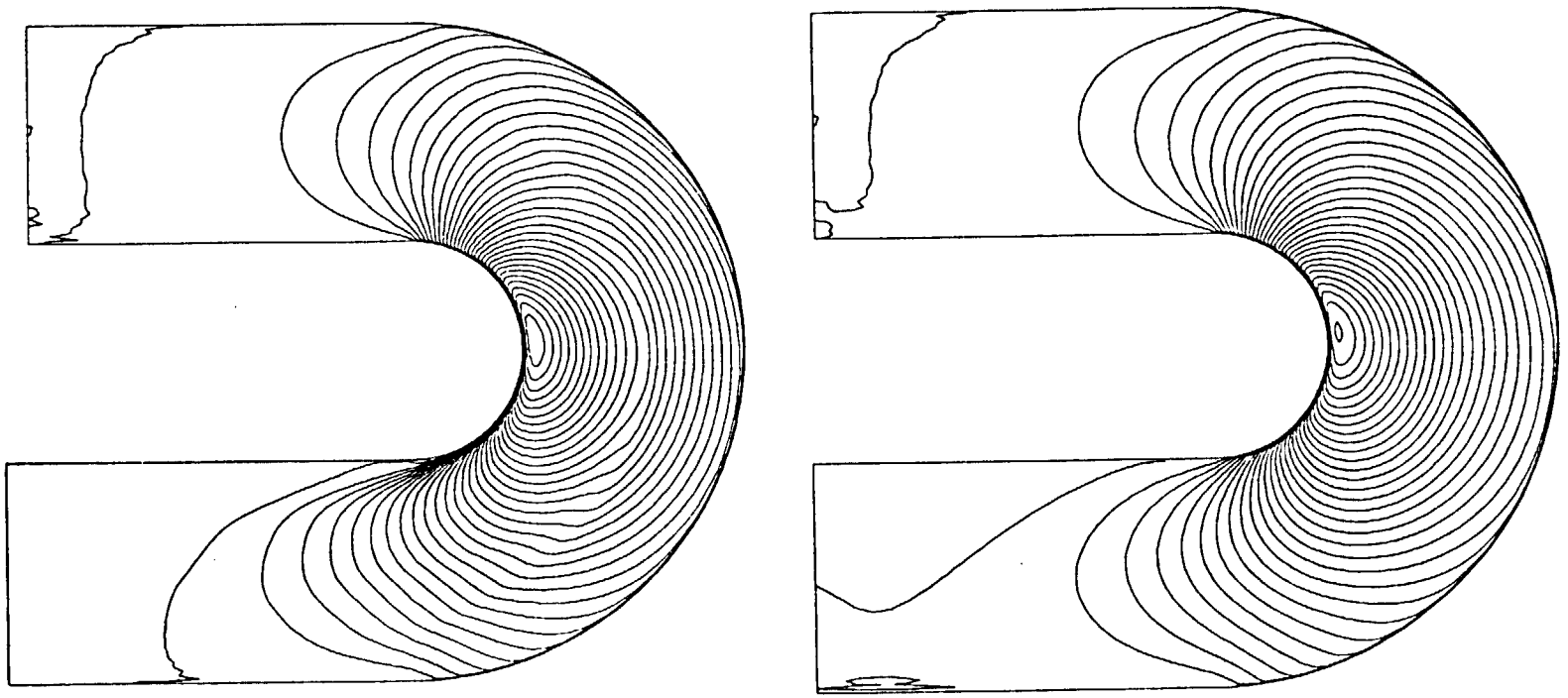

(a) present model

(b) standard k-ε model

Figure 46 Y-Component Velocity Contour in a 180° Turn-Around Duct [87] (141 x 41 grids)

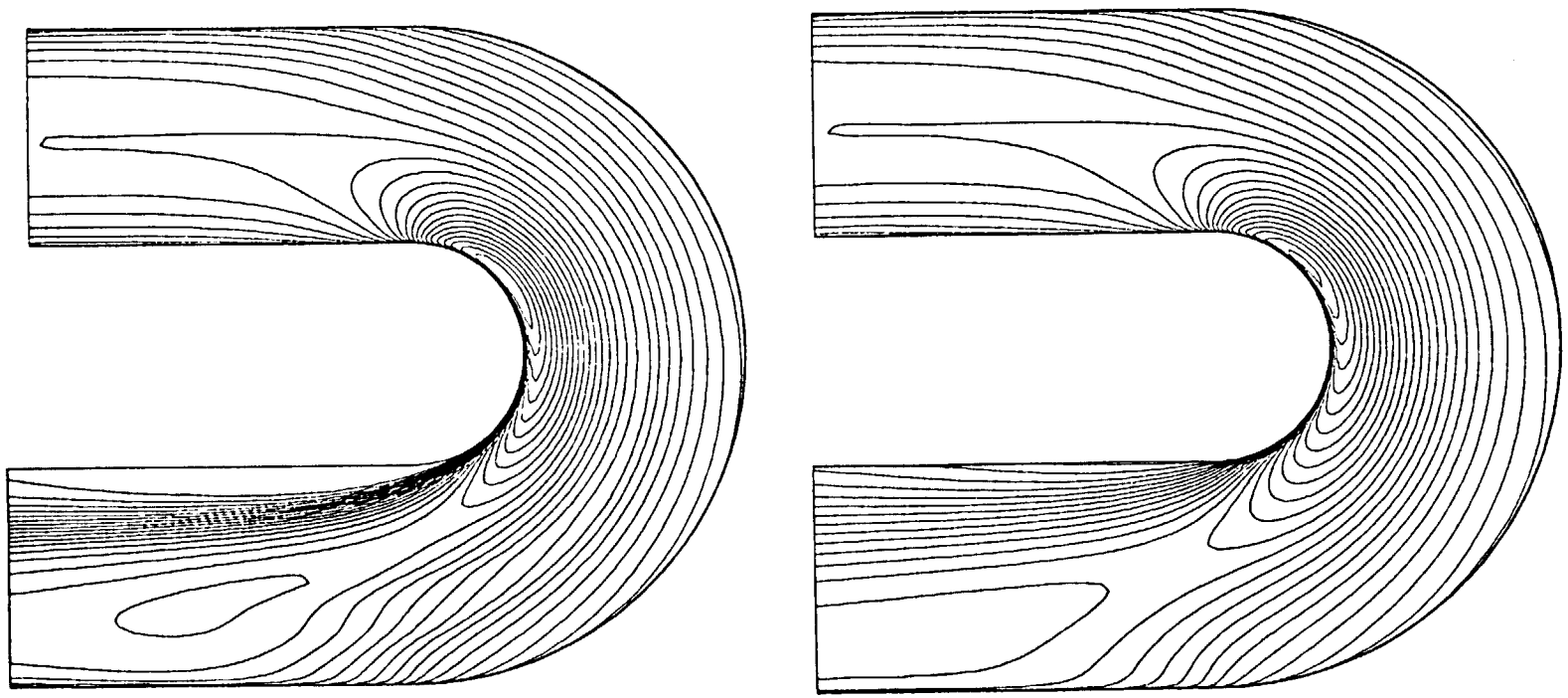

(a) present model

(b) standard k-ε model

Figure 47 Static Pressure Contour in a 180° Turn-Around Duct [87] (141 x 41 grids)

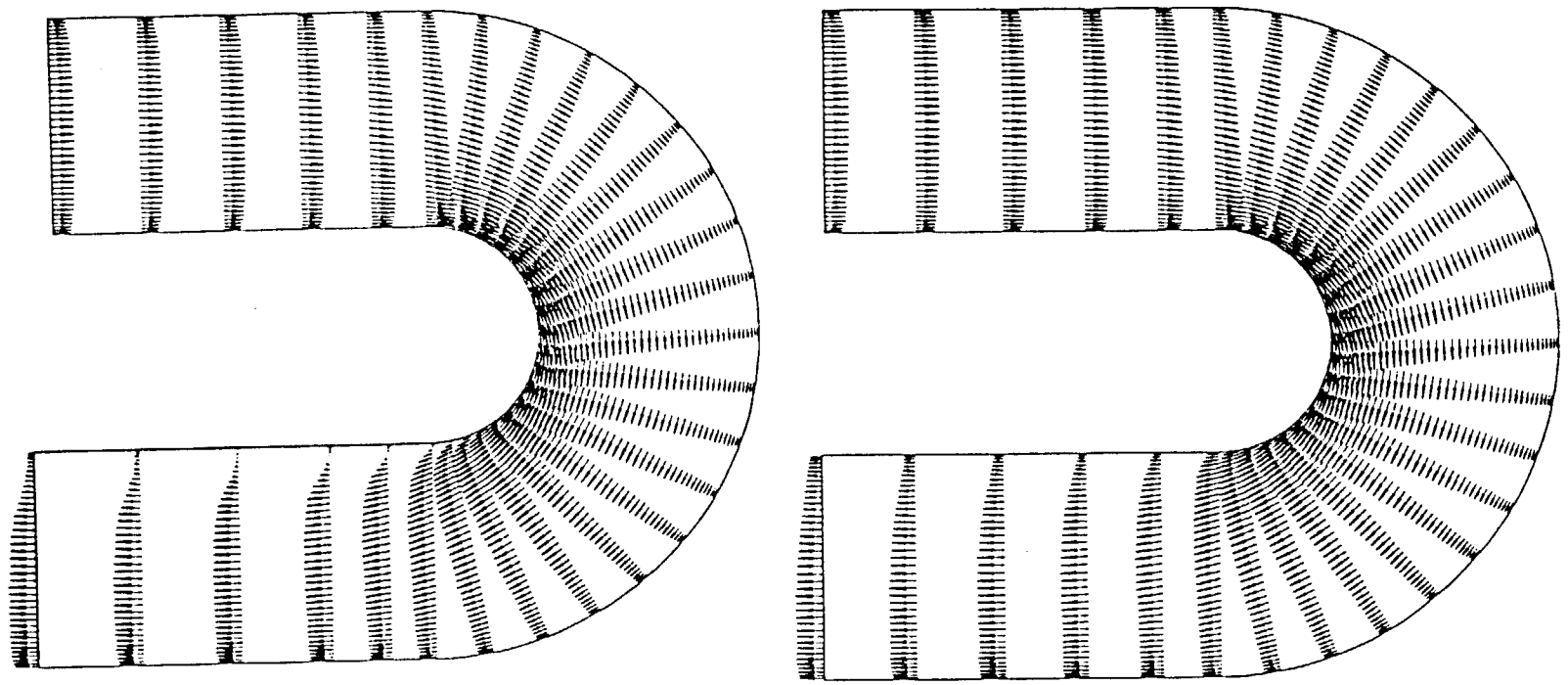

(a) present model

(b) standard k-ε model

Figure 48 Velocity Vectors in a 180° Turn-Around Duct [87] (141 x 41 grids)

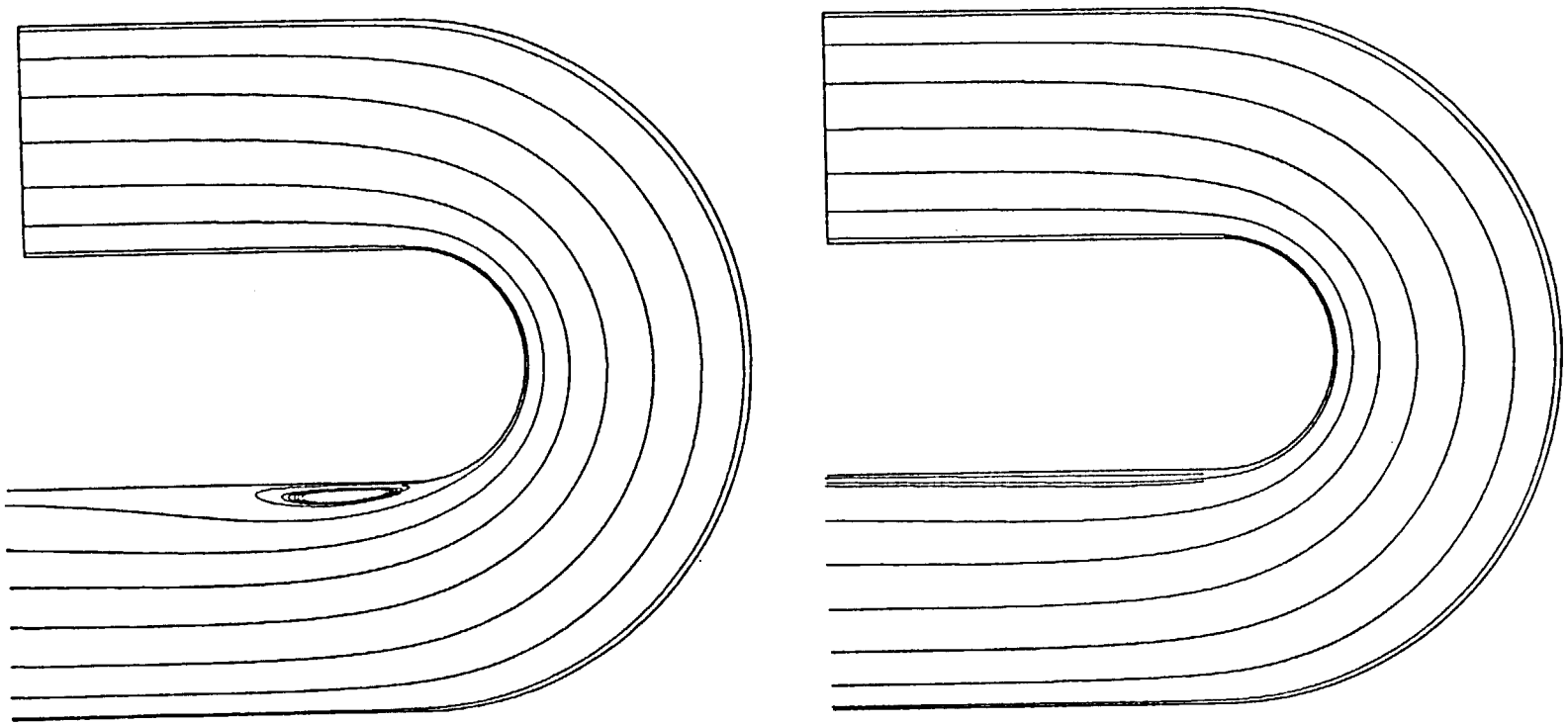

(a) present model

(b) standard k-ε model

Figure 49 Particle Traces in a 180° Turn-Around Duct [87] (141 x 41 grids)

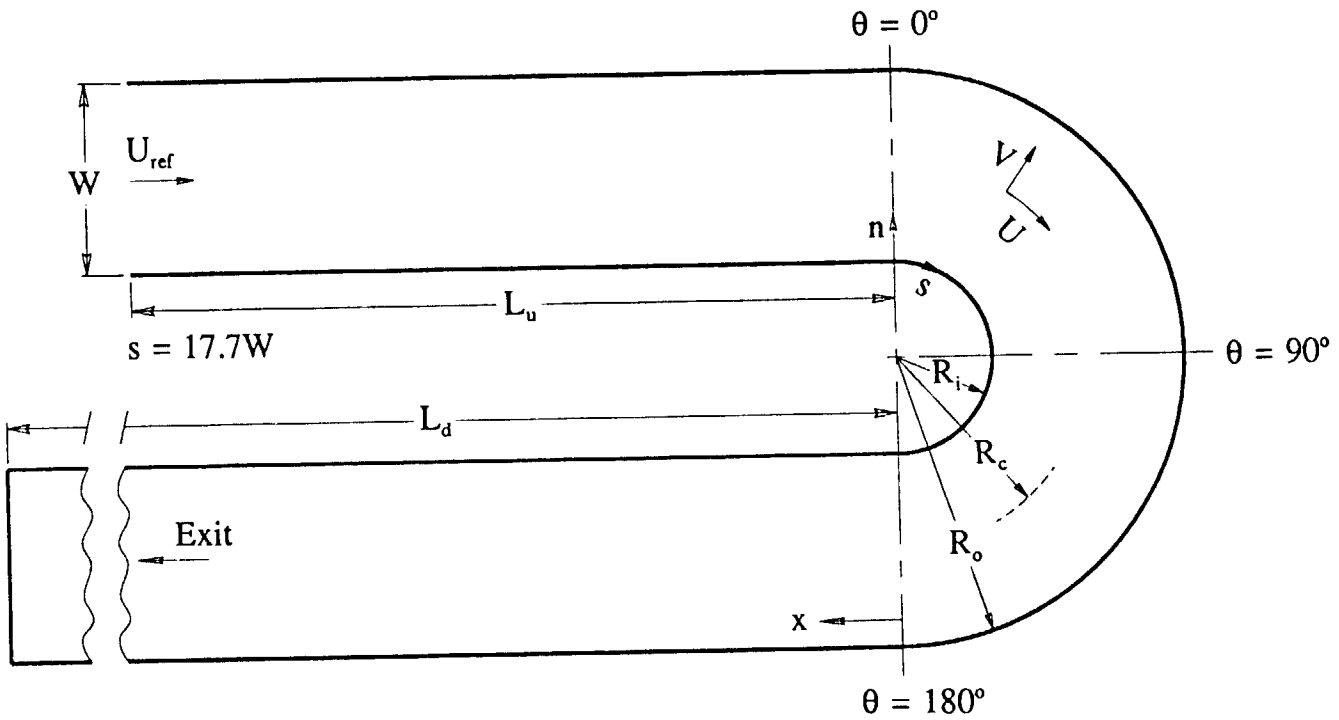

Test Section Geometry

W = 3.81 cm
R_i = 1.91 cm
R_o = 5.72 cm
L_u = 4W
L_d = 12W
aspect ratio = 10

Inlet Conditions

Uref = 32 m/sec
Re_W = 1000,000
M_{ref} = 0.1

Figure 50 The Configuration and Inlet Conditions for a 2-D U-Duct [88]

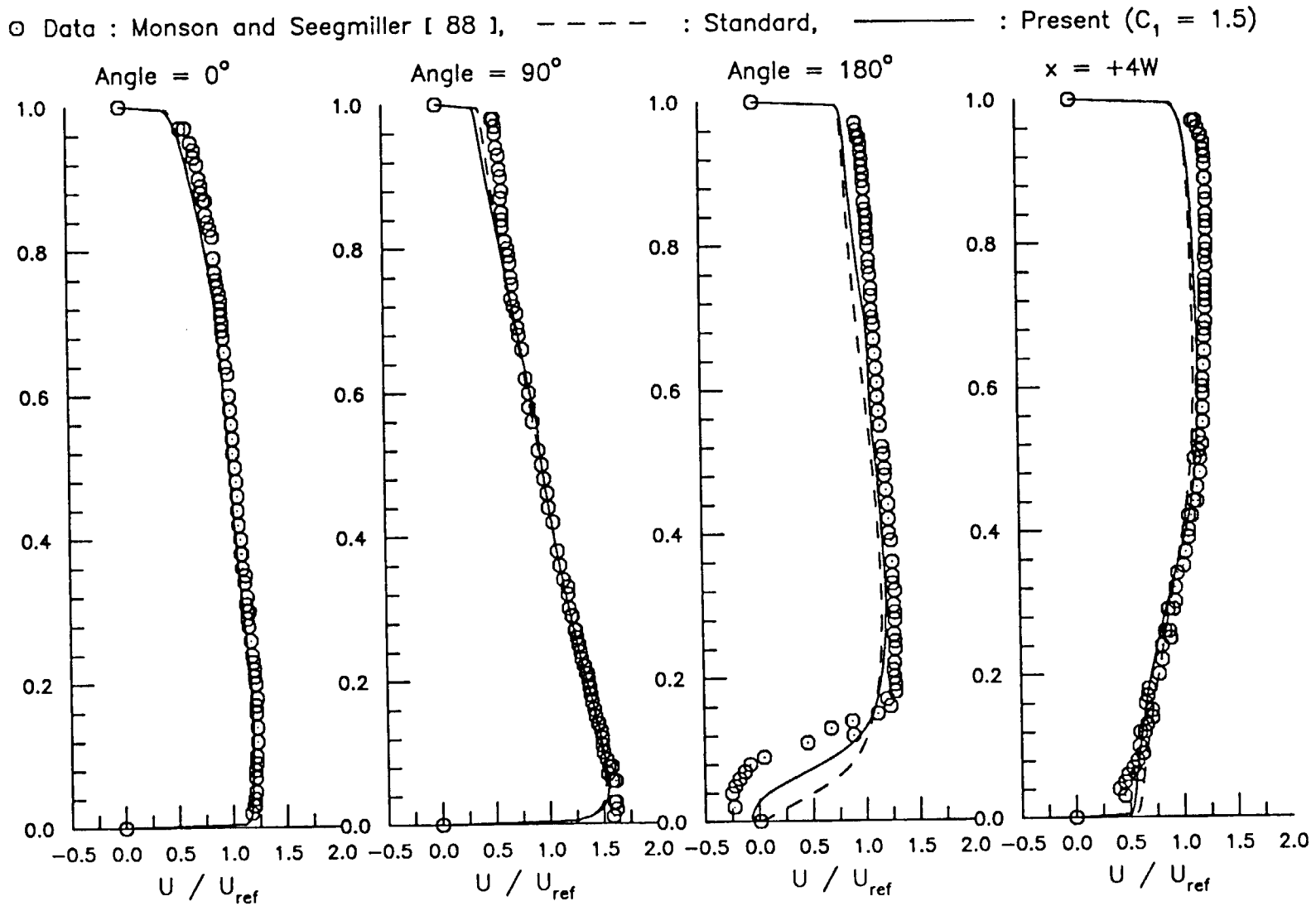

Figure 51 Longitudinal Velocity Profiles in a 2-D U-Duct (234 x 101 grids)

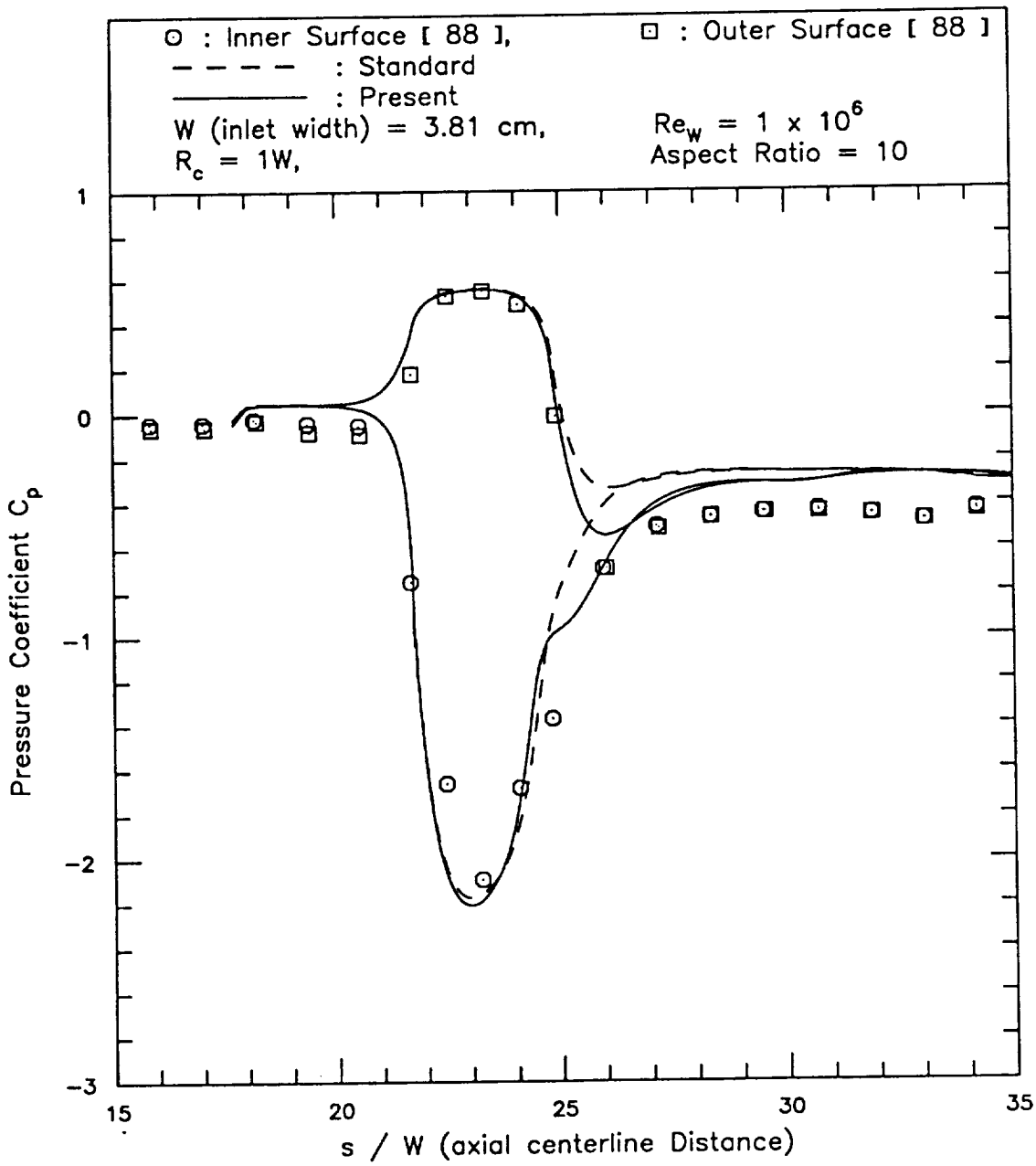

Figure 52 Wall Static Pressure Coefficient Distribution in a U-Duct (234 x 101 grids)

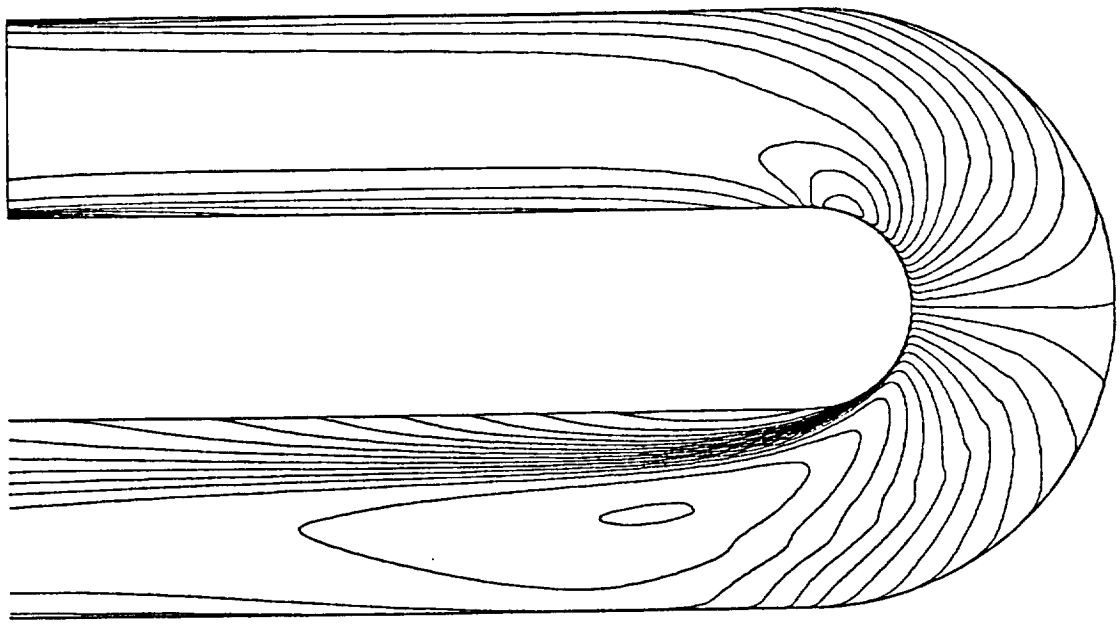

(a) present model

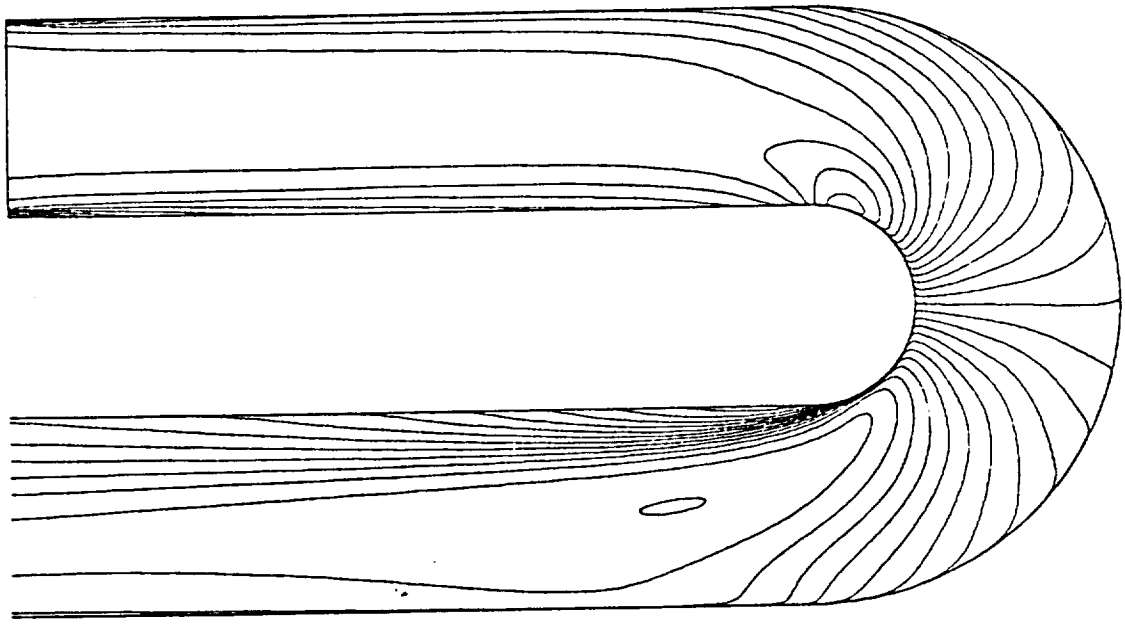

(b) standard k-ε model

Figure 53 X-Component Velocity Contour in a 2-D U-Duct [88]

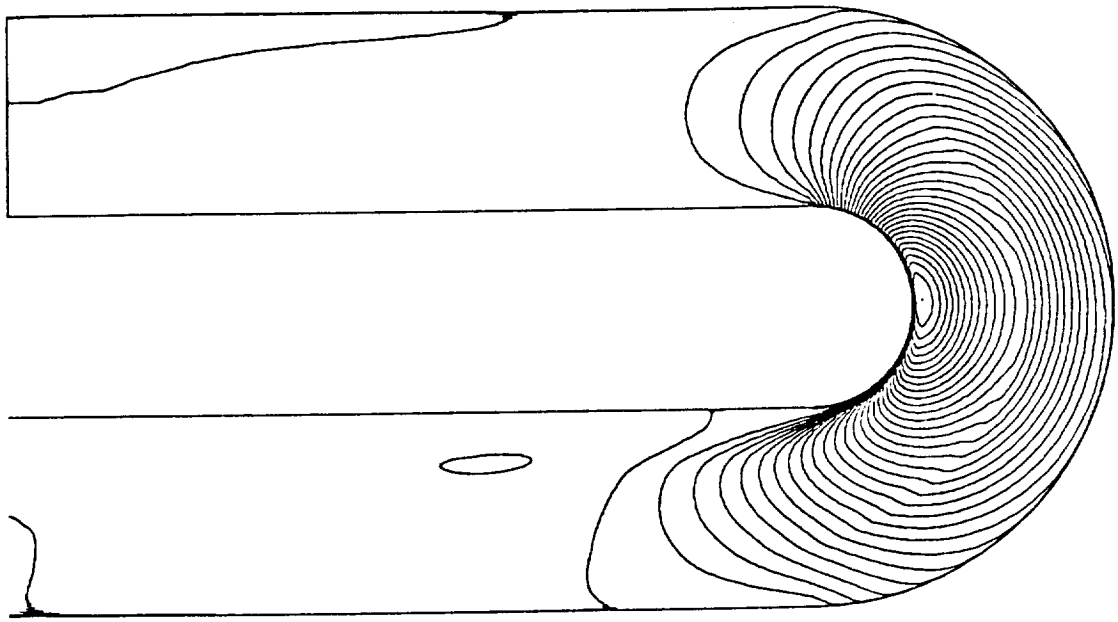

(a) present model

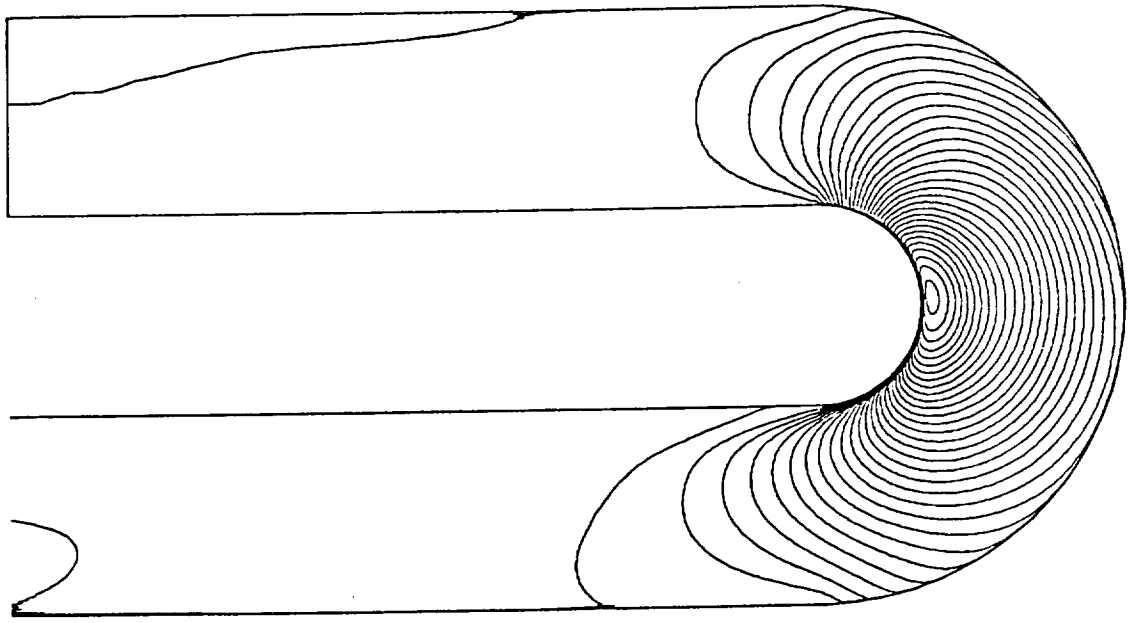

(b) standard k-ε model

Figure 54 Y-Component Velocity Contour in a 2-D U-Duct [88]

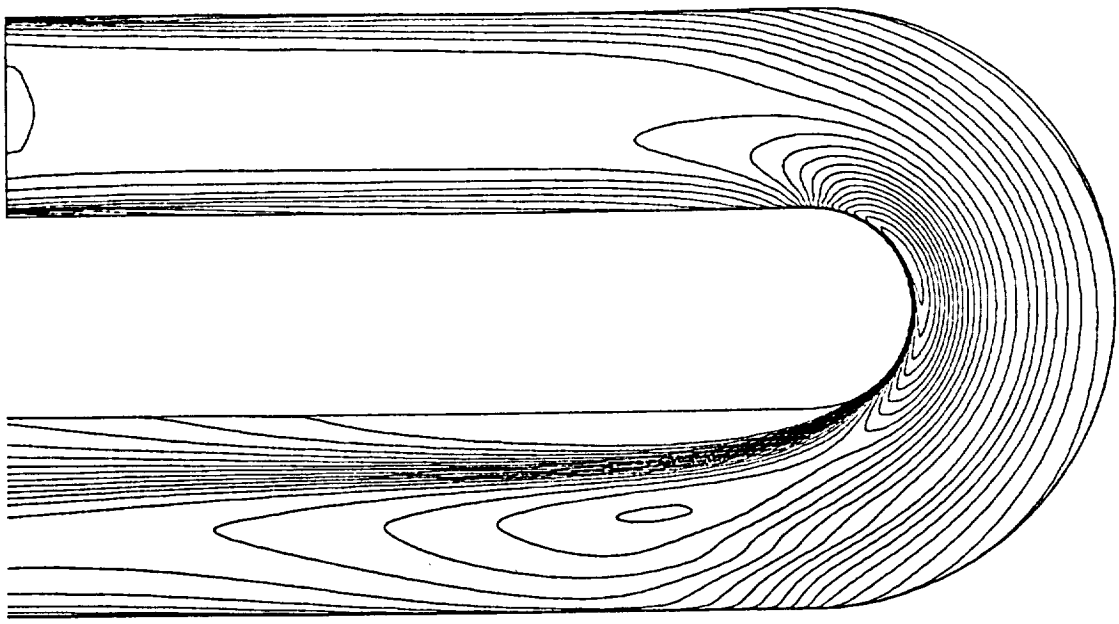

(a) present model

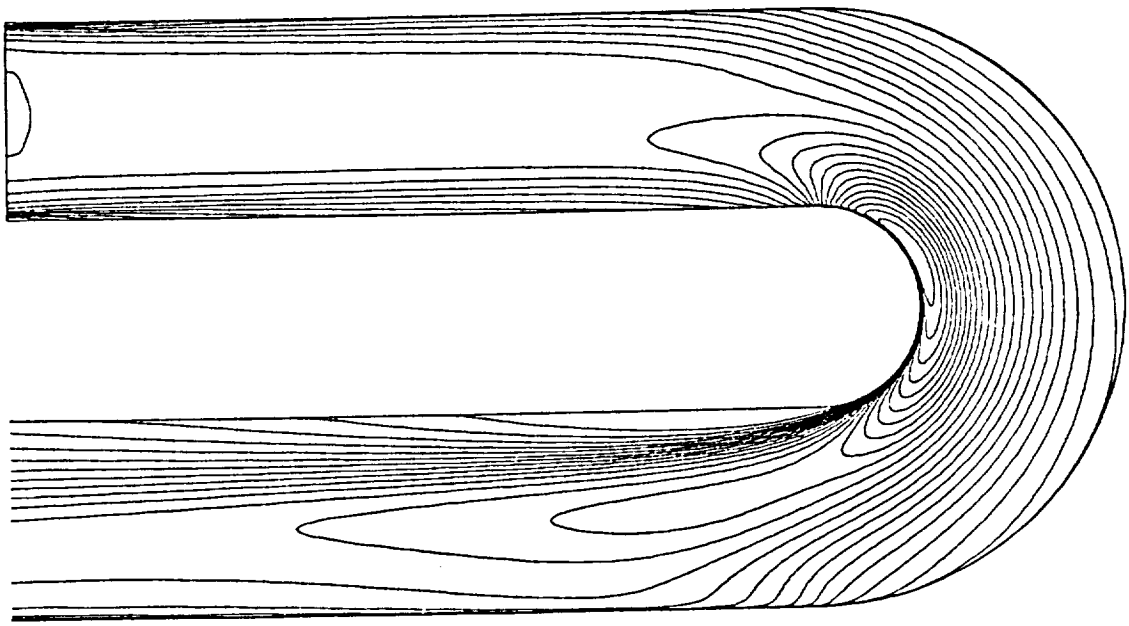

(b) standard k-ε model

Figure 55 Static Pressure Contour in a 2-D U-Duct [88]

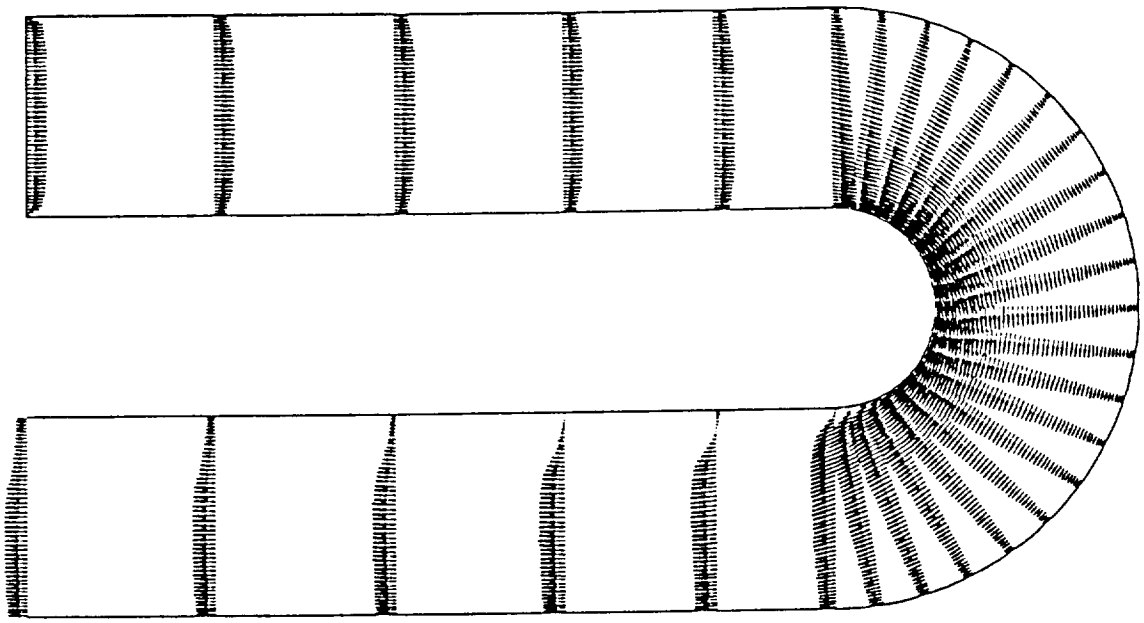

(a) present model

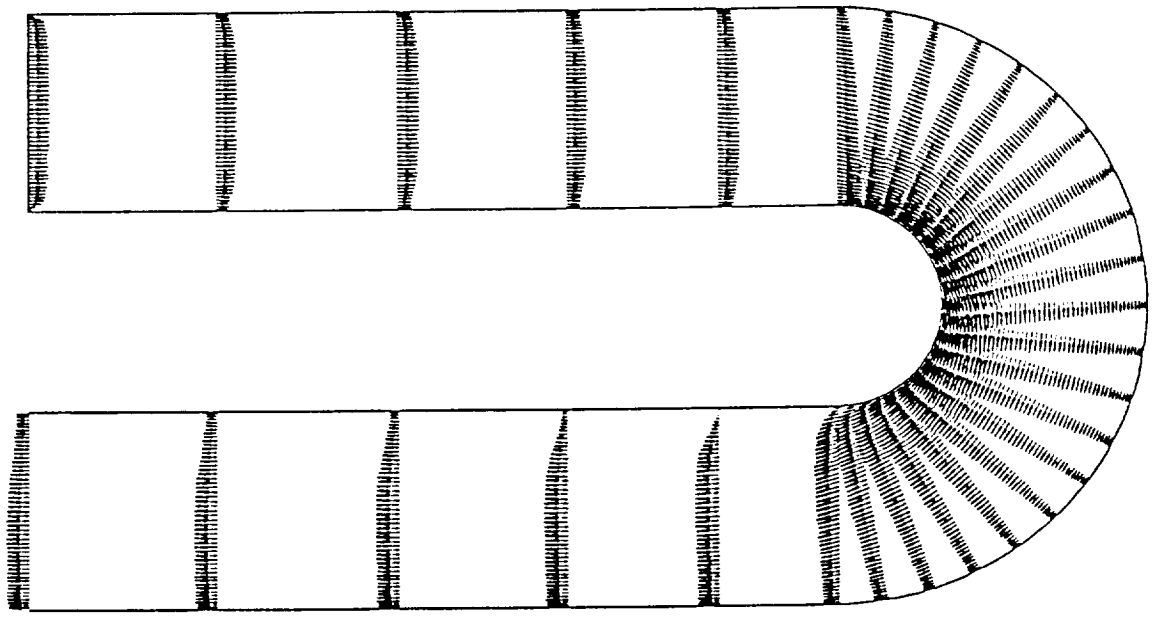

(b) standard k-ε model

Figure 56 Velocity Vectors in a 2-D U-Duct [88]

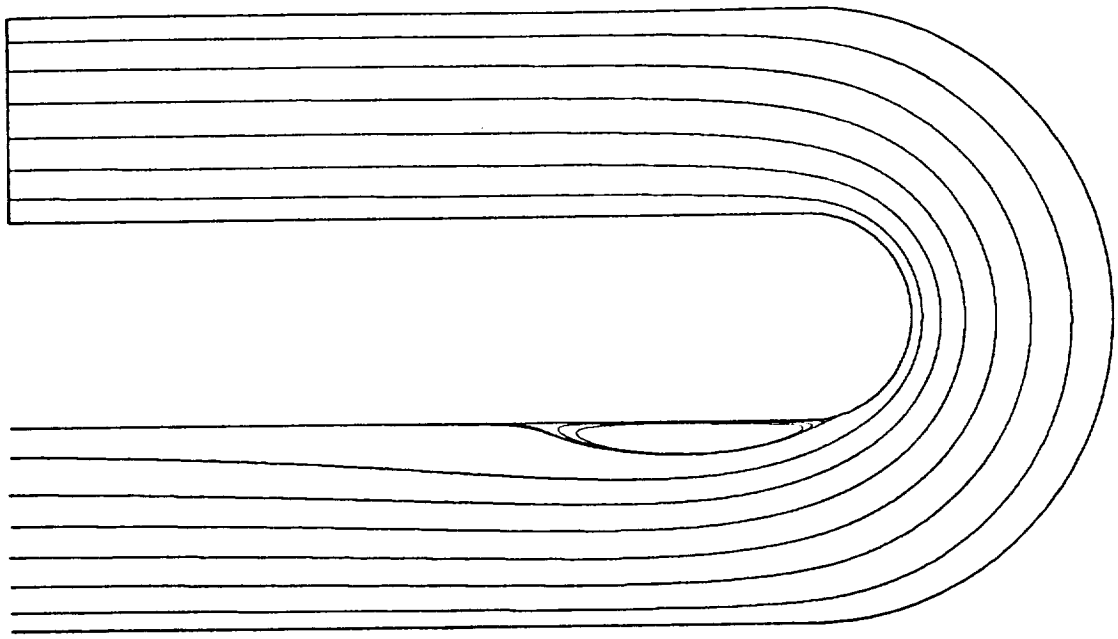

(a) present model

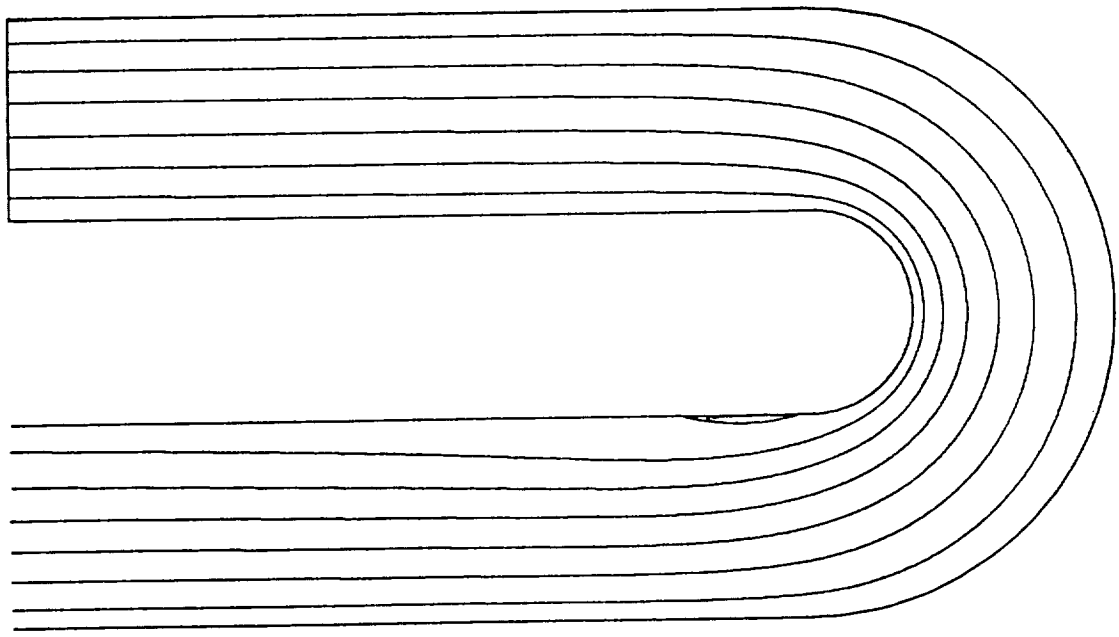

(b) standard k-ε model

Figure 57 Particle Traces in a 2-D U-Duct [88]

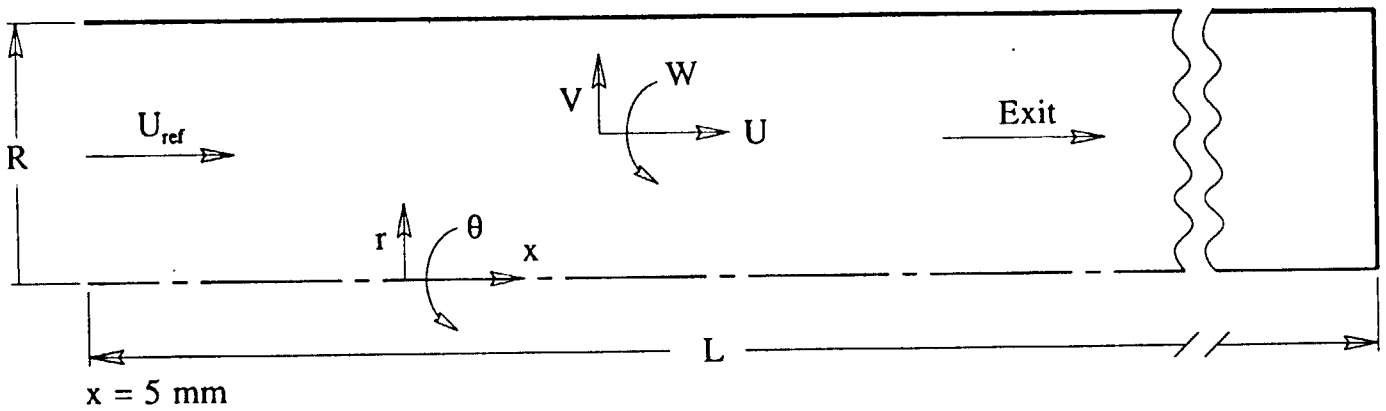

Test Section Geometry

R = 61 mm
L = 600 mm

Inlet Conditions

U_{ref} = 1 m/sec
Re_D = 8188
S (swirl no.) = 0.21

Figure 58 Illustrations of Test Section, Coordinate System, and Inlet Conditions for a Confined Swirling Jet [89]

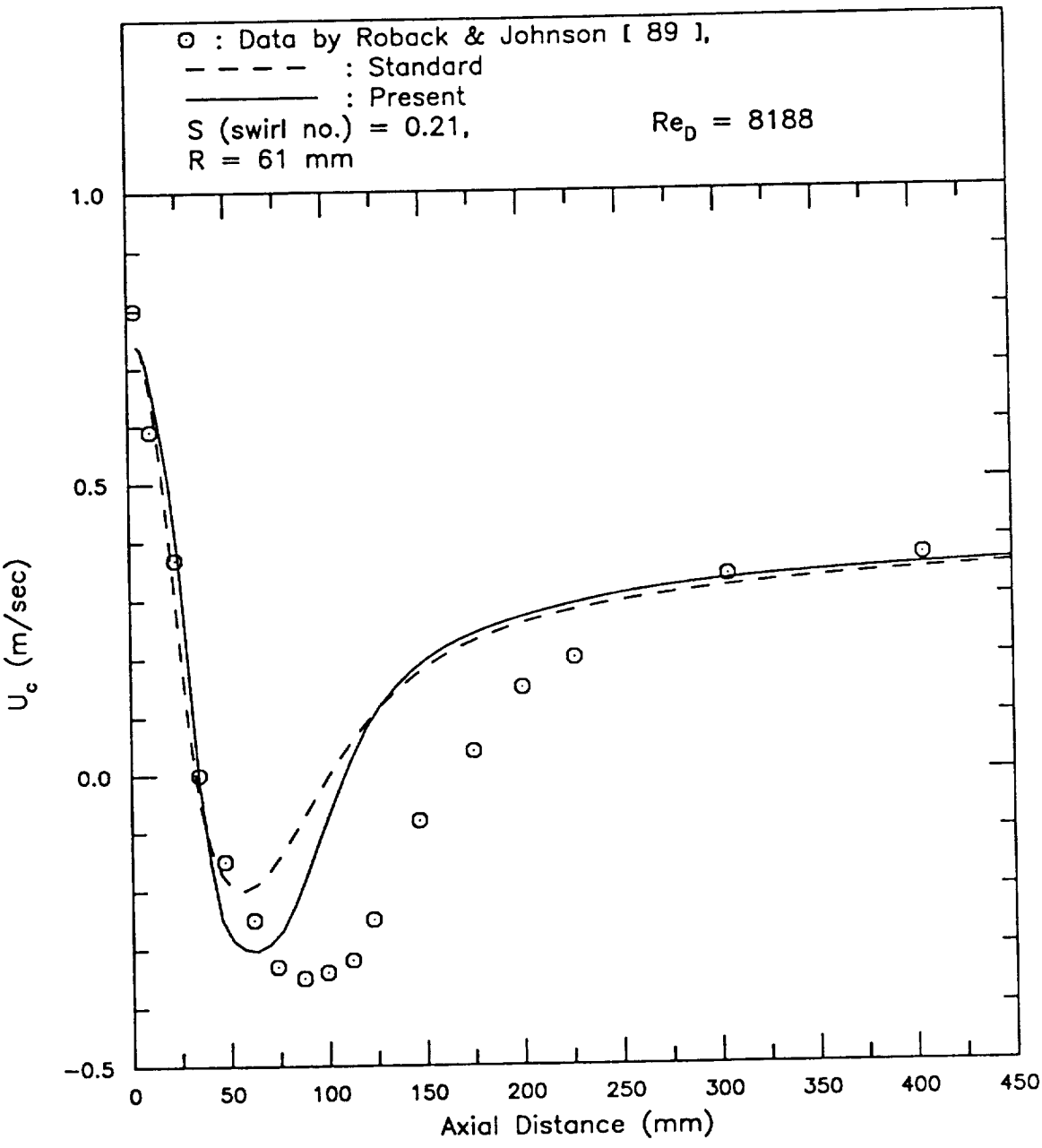

Figure 59 Mean Axial Velocity along the Centerline in a Confined Swirling Jet (151 x 45 grids)

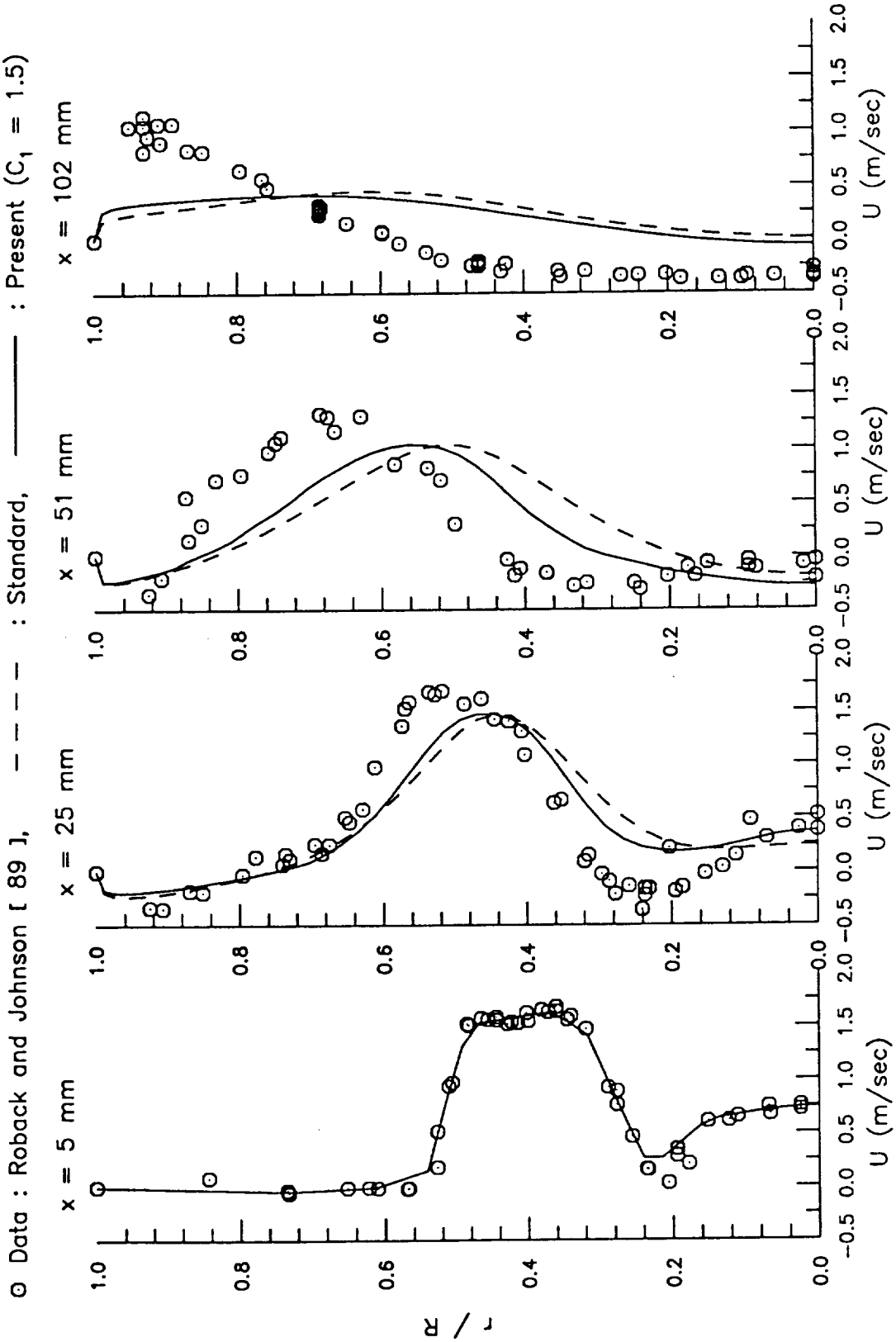

Figure 60 Mean Axial Velocity Profiles in a Confined Swirling Jet (151 x 45 grids)

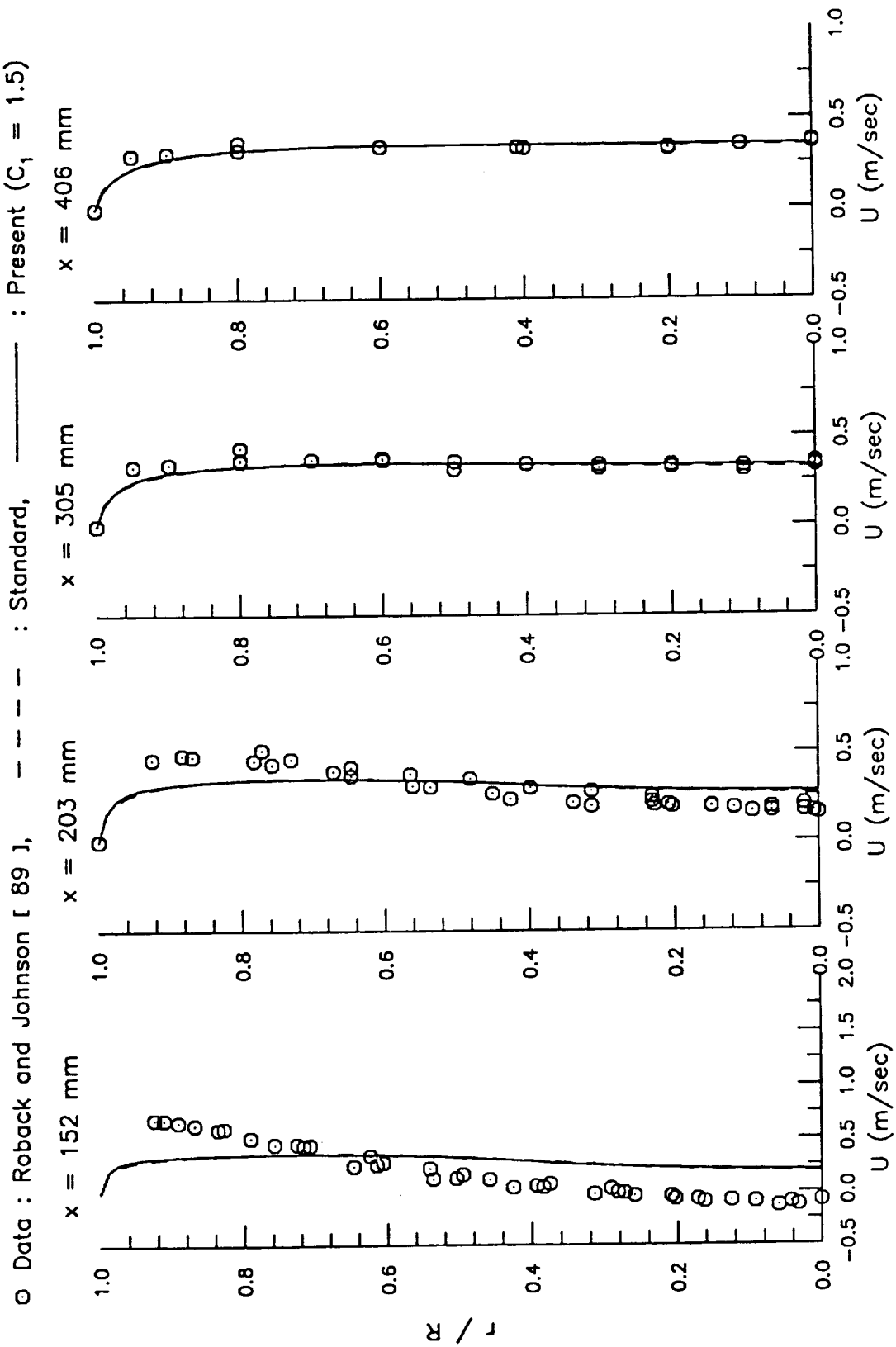

Figure 60 Continued

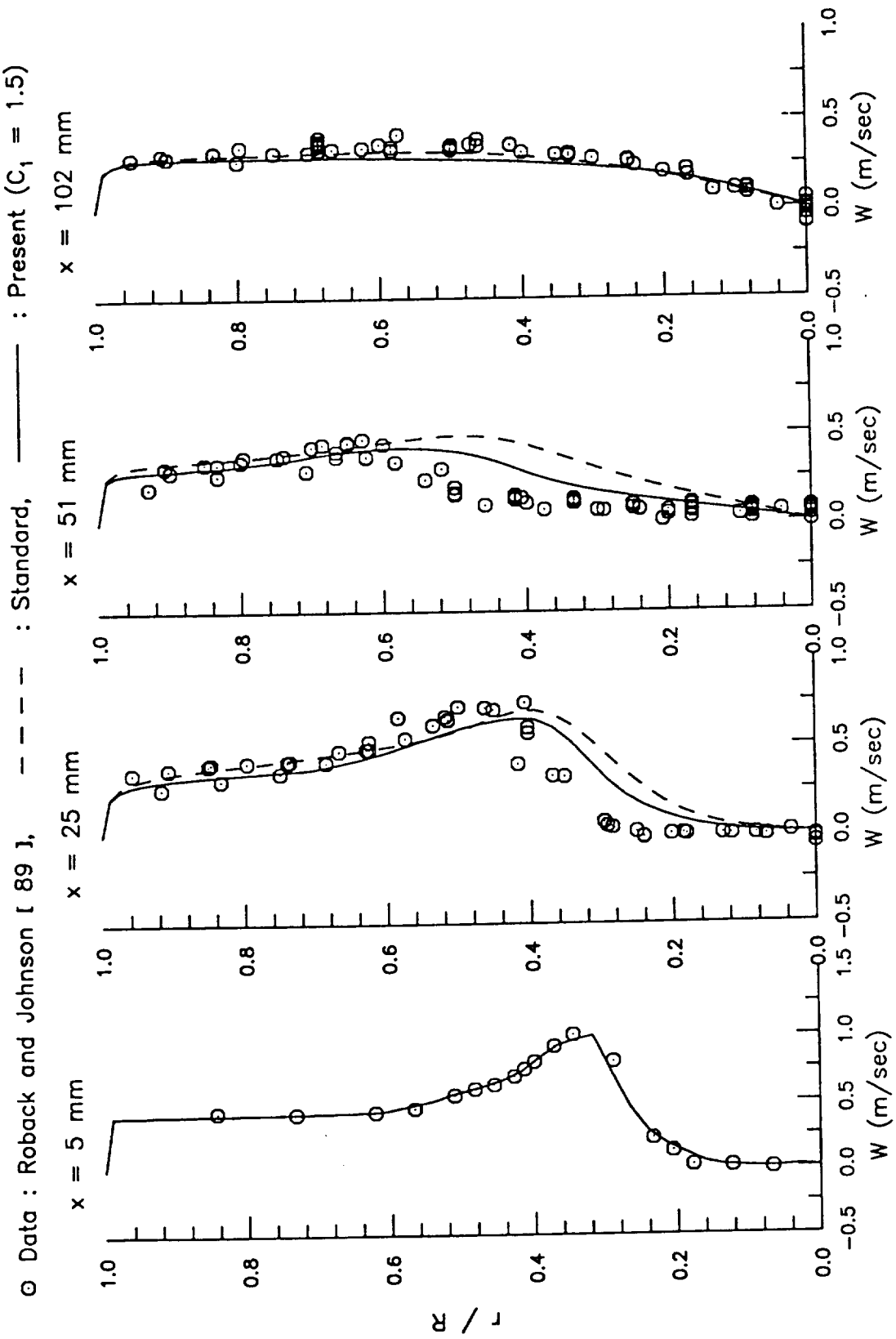

Figure 61 Mean Azimuthal Velocity Profiles in a Confined Swirling Jet (151 x 45 grids)

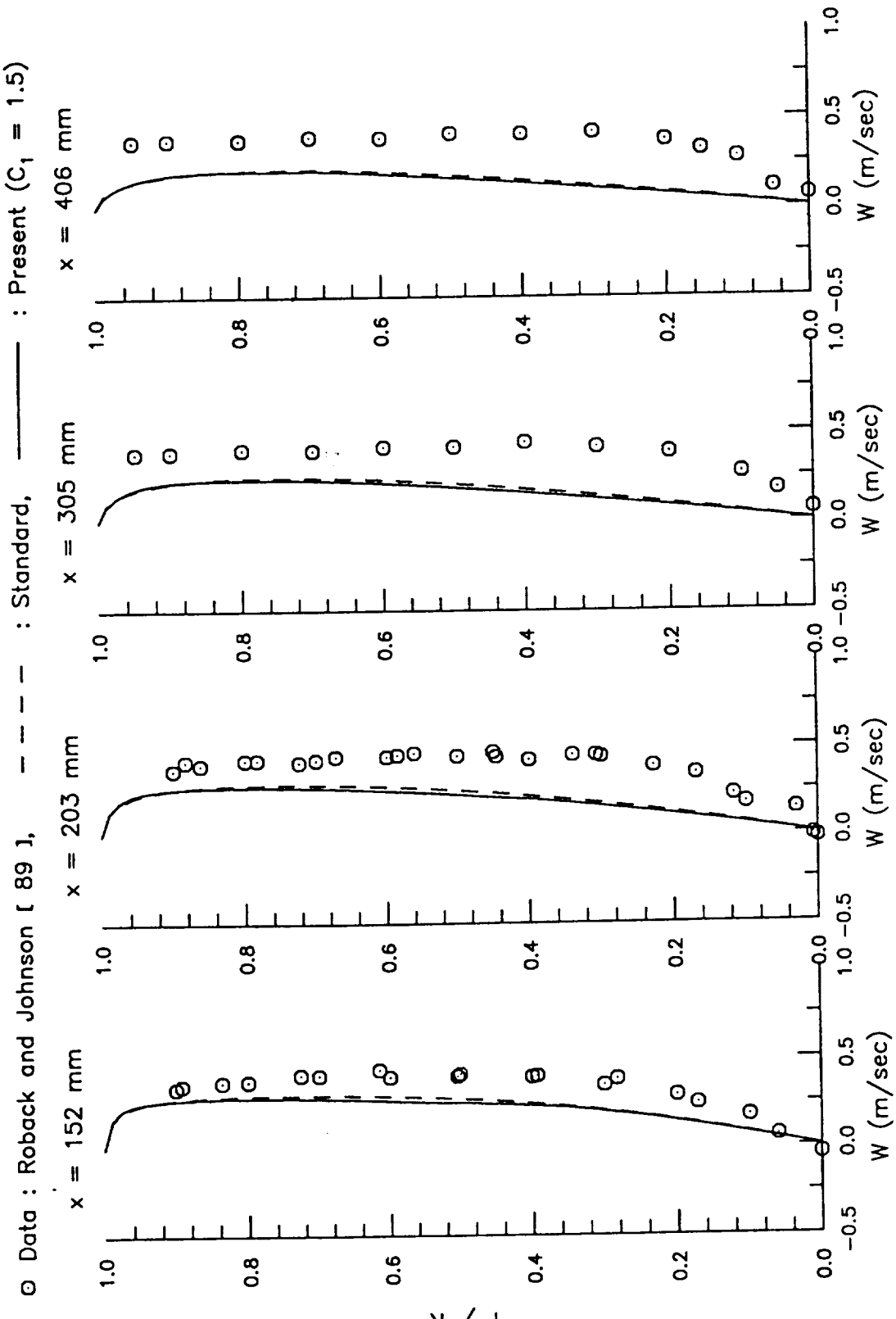

Figure 61 Continued

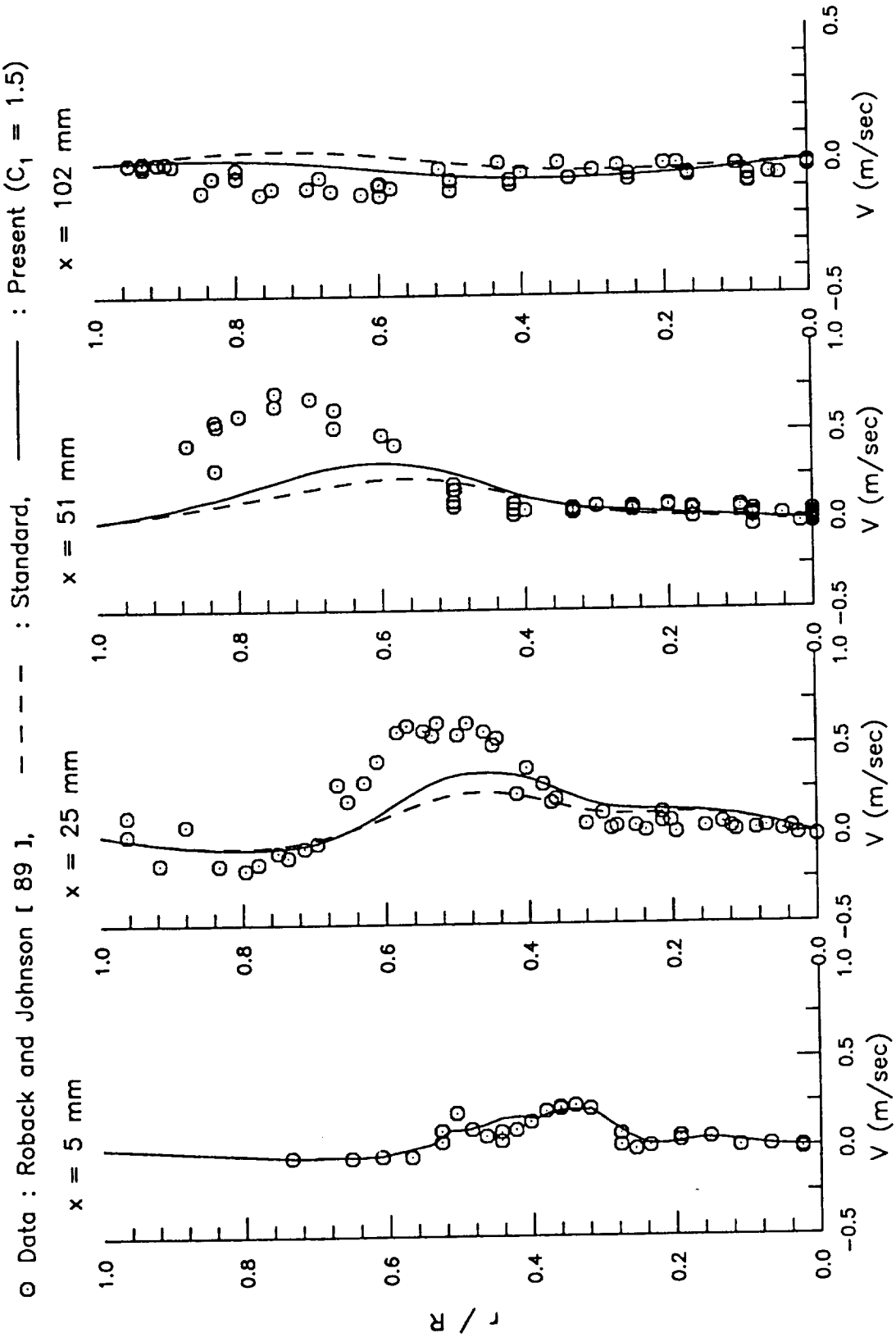

Figure 62 Mean Radial Velocity Profiles in a Confined Swirling Jet (151 x 45 grids)

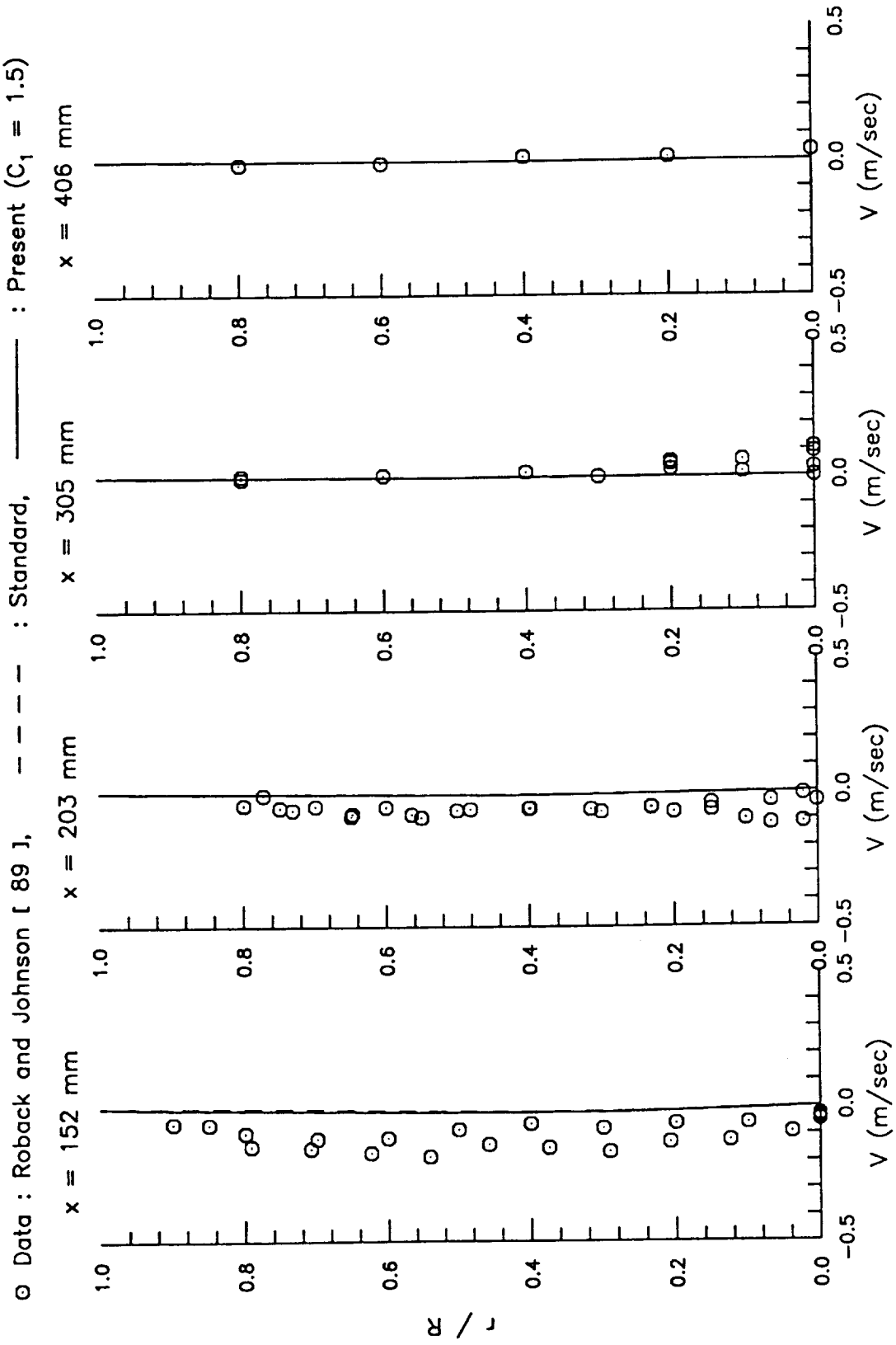

Figure 62 Continued

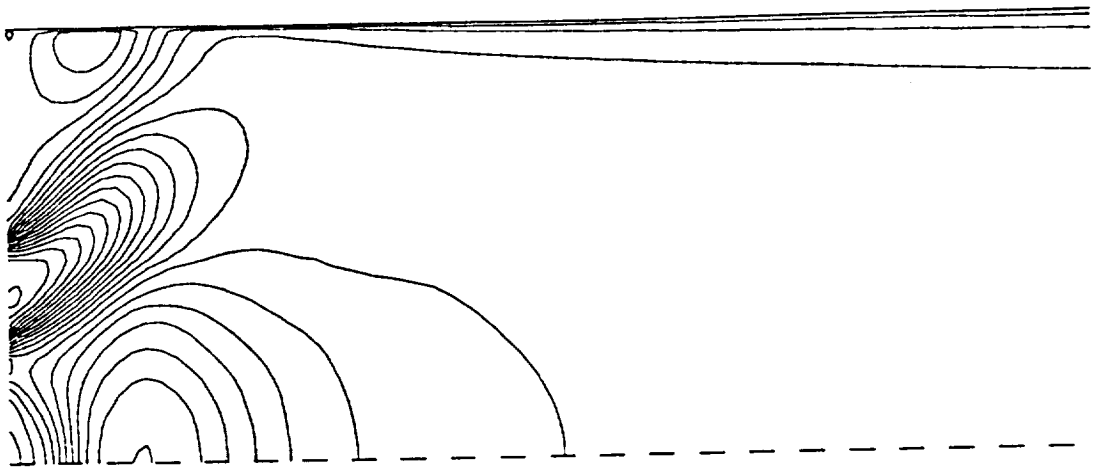

(a) present model

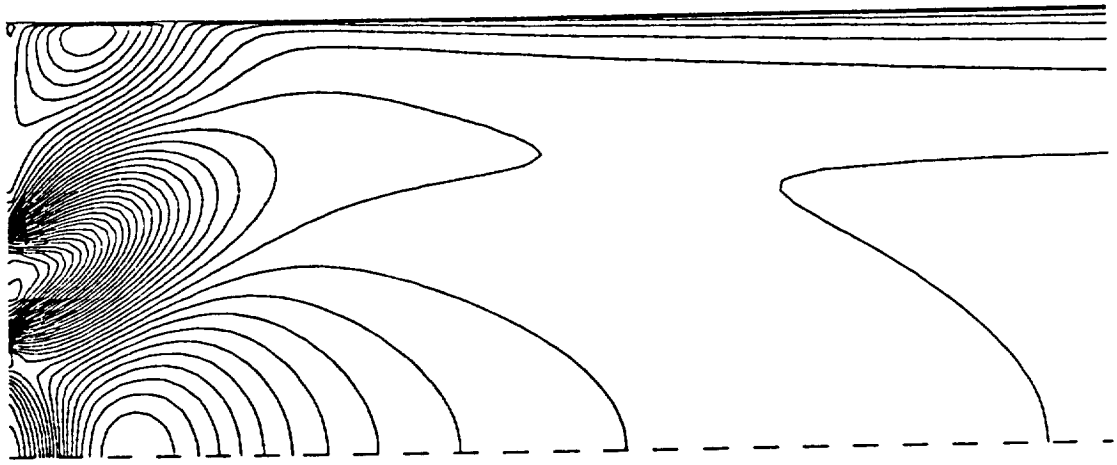

(b) standard k-ε model

Figure 63 Axial Velocity Contours in a Confined Swirling Jet [89]

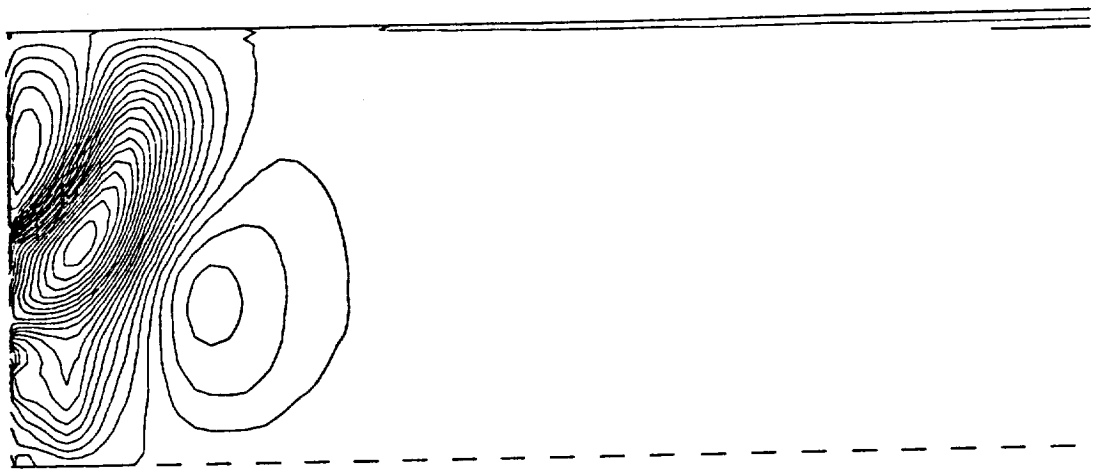

(a) present model

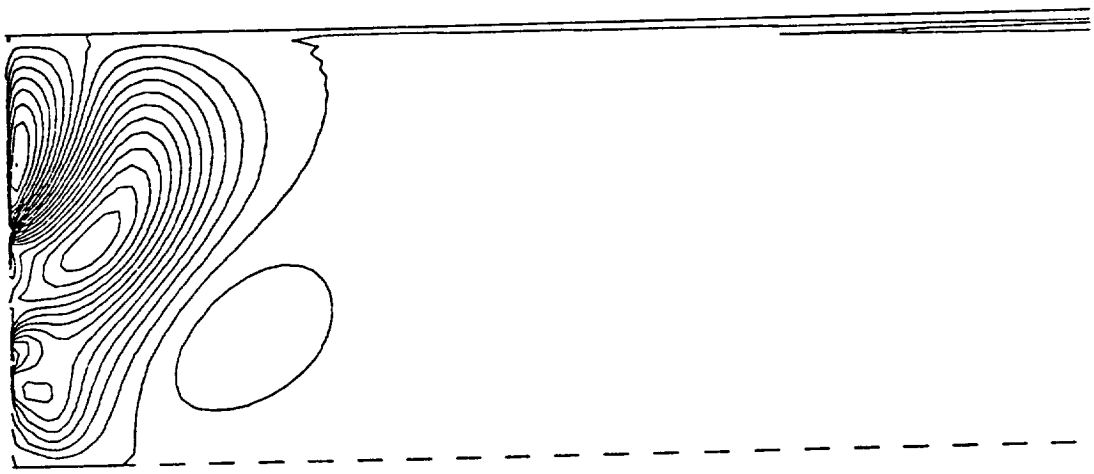

(b) standard k-ε model

Figure 64 Radial Velocity Contours in a Confined Swirling Jet [89]

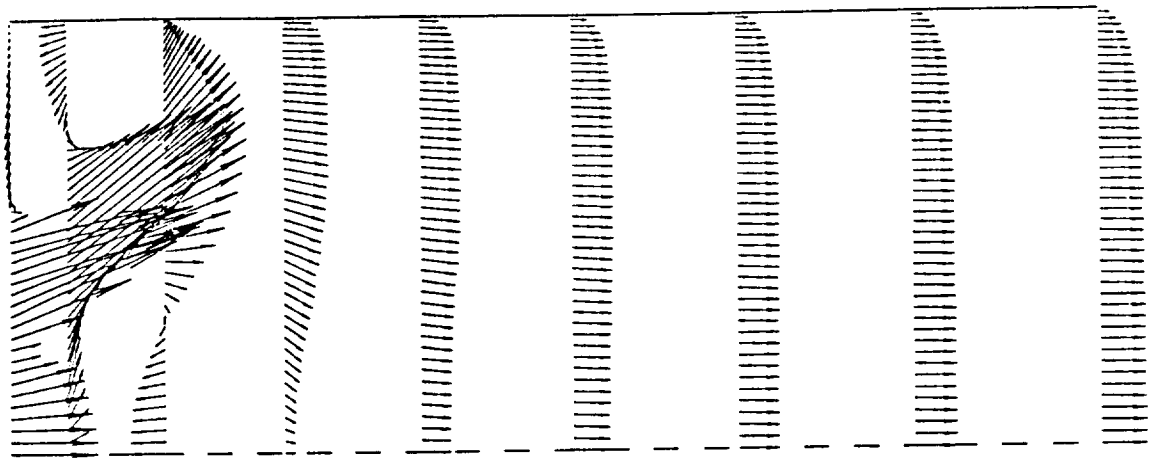

(a) present model

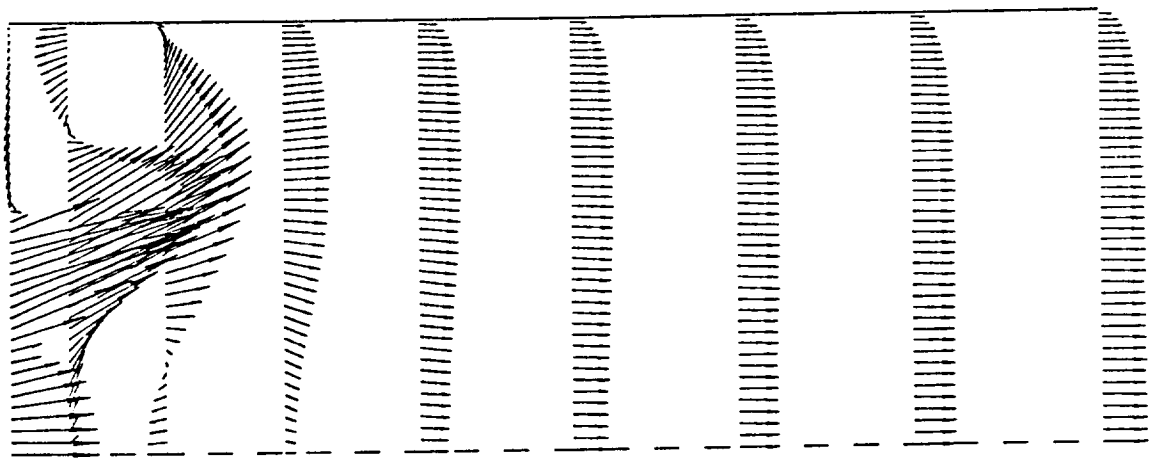

(b) standard k-ε model

Figure 65 Velocity Vectors in a Confined Swirling Jet [89]

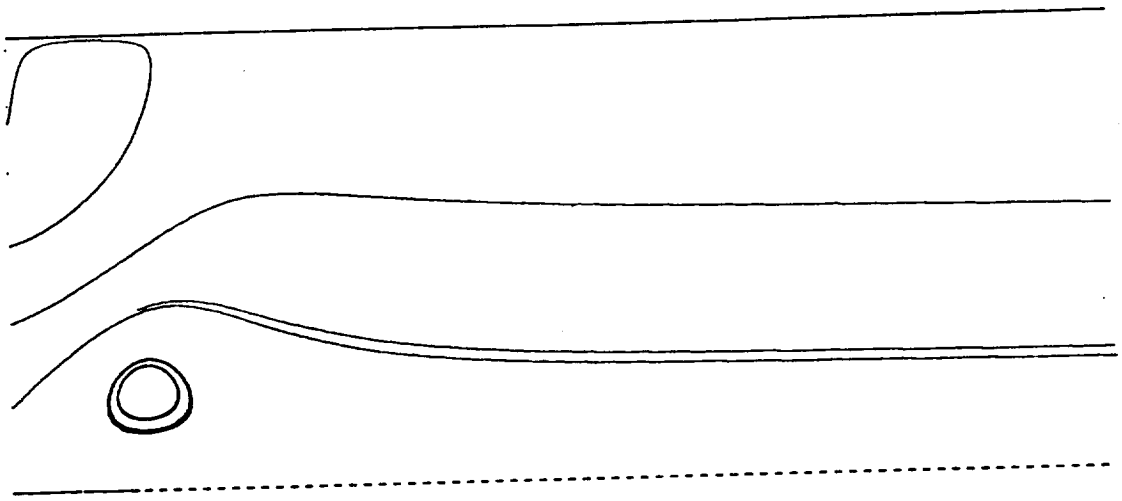

(a) present model

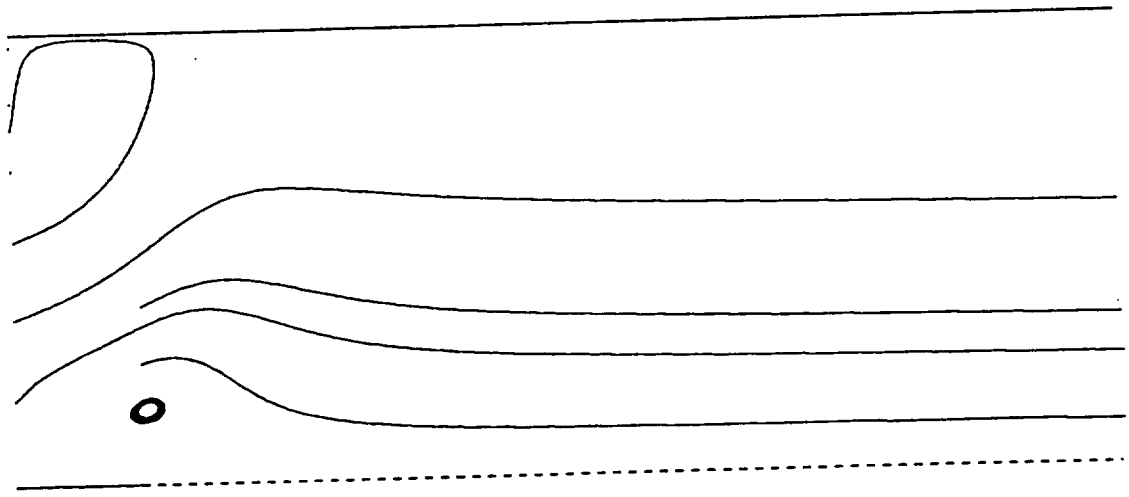

(b) standard k-ε model

Figure 66 Particles Traces in a Confined Swirling Jet [89]

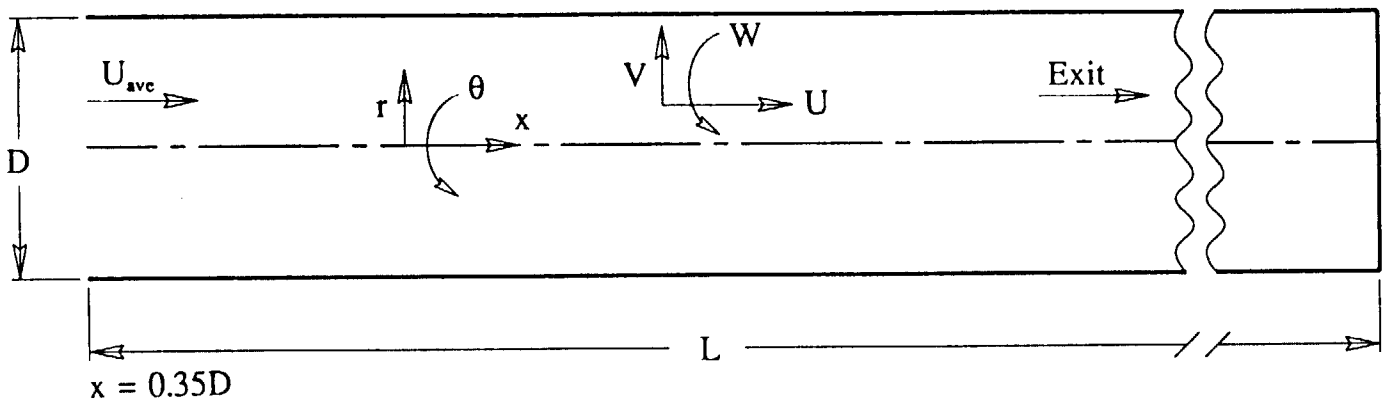

Test Section Geometry

D = 10 cm
L = 1600 cm

Inlet Conditions

U_{ave} = 440 cm/sec
Re_D = 30000
S (swirl no.) = 0.43

Figure 67 Schematics of the Test Section and the Inlet Conditions for a Confined Swirling Flow [90]

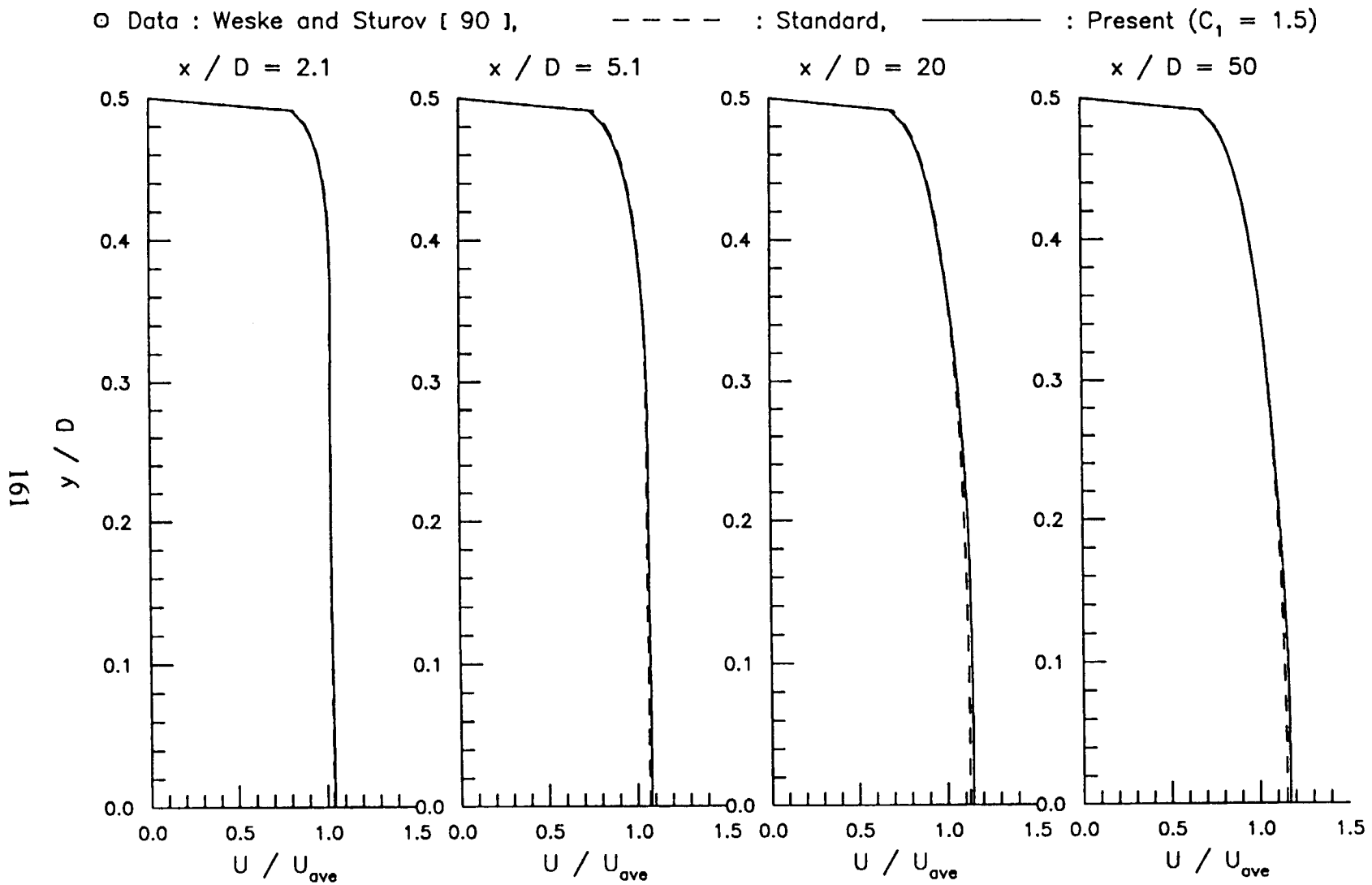

Figure 68 Axial Velocity Profiles in a Confined Swirling Flow (301 x 41 grids)

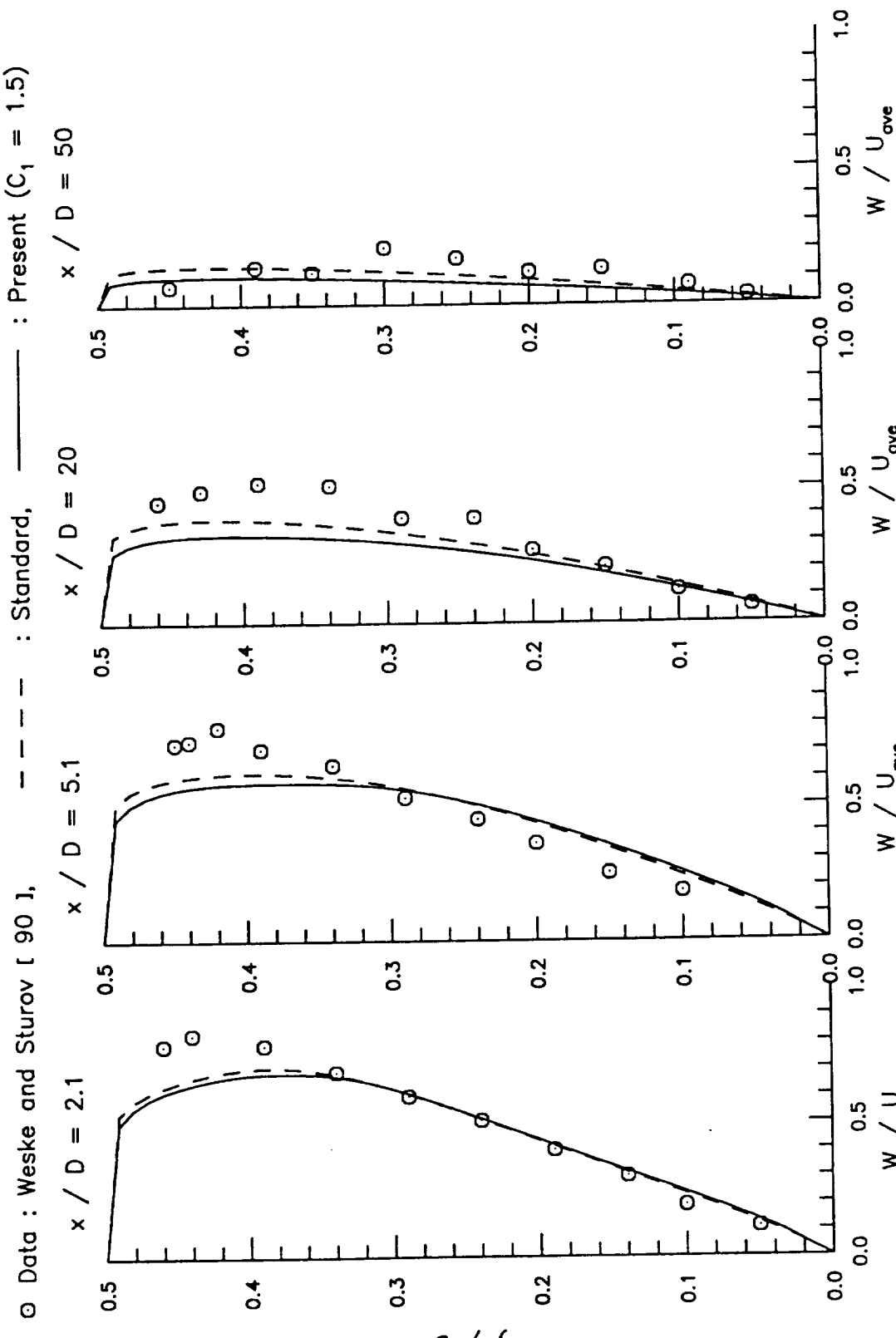

Figure 69 Circumferential Velocity Profiles in a Confined Swirling Flow (301 x 41 grids)

APPENDIX A

TABLES FOR REVIEW OF LITERATURE

TABLE A.1: SUMMARY OF DATA AVAILABLE IN SOME OF THE REFERENCES
(EXPERIMENTAL)

REFERENCE	GEOMETRY	CURVATURE	INLET REYNOLDS NUMBER	TURBU-LENT	LAM-INAR	INSTRUMENTS	MEASURED MEAN QUANTITIES	MEASURED TURBULENT QUANTITIES	REMARKS
Muck, Hoffmann, and Bradshaw [5]	convex surface	$\delta/R = 0.009$	$U_e\theta/\nu = 5000$	x		• pitot tube • hot wire	U, C_f, δ, θ	$\overline{u^2}$, $\overline{v^2}$, $\overline{w^2}$, $\overline{uv}$ ℓ_m, μ_t, k, τ_t, γ, $\overline{u^4}$, $\overline{u^3}$, $\overline{v^4}$, $\overline{v^3}$	• Inlet turbulence intensity ~ 0.1%. • The production and dissipation rates near the surface are roughly equal to the local equilibrium value. • The effect of curvature is suggested to be modeled in the Reynold-stress equation.
Hoffmann, Muck, and Bradshaw [6]	concave surface	$\delta/R = 0.01$-0.02	---	x		• pitot tube • hot wire	U, C_f, δ, u_τ	$\overline{u^2}$, $\overline{v^2}$, $\overline{w^2}$, $\overline{uv}$ $\overline{vw}$, $\overline{u^3}$, $\overline{v^3}$, $\overline{uv^2}$, $\overline{u^4}$, ℓ, μ_t, k, γ	• The apparent mixing length ℓ is greatly increased, and roughly proportional to the Richardson number. • The k and ε transport equations should contain coefficients depending explicitly on the ratio of length scale to streamline curvature.
Smits, Young, and Bradshaw [7]	curved duct	$W/R = 1$	2.6×10^5	x		• pitot tube • hot wire	U, V, δ, θ, C_p, C_f, u_τ	$\overline{u^2}$, $\overline{uv}$, $\overline{uw}$, $\overline{uv^2}$, $\overline{u^2v}$, τ_t	• The dissipation length scale is increased on the concave surface by an amount that increases with distance from the wall. • The pressure-strain term associated with the mean-velocity gradient decreases significantly when the generation term increases.
Castro and Bradshaw [8]	impinging plane jet with B.L. bleed	variable convex	---	x		• hot wire	U	$\overline{uv}$, shear-layer thickness, k, energy balance, triple products	• A stabilizing curvature occurs for the impinging jet. • In the curvature region: Reynolds stresses, triple products, and energy dissipation rate overshoot the plane-layers values. • The thin-shear-layer approximation is not valid because the extra rate of strain reaches its maximum value about 20% of main strain rate in a short region.
Meroney and Bradshaw [9]	concave, convex surfaces	$\delta/R = 0.01$-0.02	---	x		• stagnation tube • hot wire	U, p, θ, C_f	$\overline{uv}$, $\overline{u^2}$, $\overline{v^2}$	• On the convex surface: skin friction, turbulence intensities, and shear stress are reduced. • On the concave surface: skin friction, turbulent kinetic energy, and mixing are increased. • The law of the wall holds in a modified form on the concave surface.
Bansod and Bradshaw [10]	S-shaped ducts with circular cross section	$\frac{r}{R} = \frac{2}{9}, \frac{1}{7}$	5×10^5	x		• pitot tube • yaw meter	U, p, C_f, C_p, δ	---	• A small region of separation occurs near the bottom in the beginning of the second bend. • The flow is not quite symmetrical near the beginning of the second bend. • The boundary-layer thickness at the bottom of the end of the first bend increases rapidly, and fluids tend to migrate towards the top.

TABLE A.1: (continued)

REFERENCE	GEOMETRY	CURVATURE	INLET REYNOLDS NUMBER	TURBULENT	LAMINAR	INSTRUMENTS	MEASURED MEAN QUANTITIES	MEASURED TURBULENT QUANTITIES	REMARKS
Gillis and Johnston [11]	convex surface	$\delta/R = 0.05, 0.1$	$U_{pw}\theta/\nu = 3378$	x		• pitot tube • hot wire	U, δ, θ, C_f, St, u_τ	$\overline{uv}$, ℓ	• The law of the wall is valid for curved wall when $y^+ < 100$. • The outer-layer mixing length should be scaled on the width of the shear-stress layer. • Production and dissipation are small in the outer-layer region.
Hunt and Joubert [12]	curved ducts with rectangular cross section	$W_n/R = 0.01$	1.9×10^5	x		• total-head probe • hot wire	U, θ, δ	$\overline{uv}$, $\overline{vw}$, $\overline{uw}$, $\overline{u^2}$, $\overline{v^2}$, $\overline{w^2}$	• The flow in the core region does not follow the velocity defect and angular momentum defect hypothesis. • For flow with small curvature, the shear stress is dominant, while for flow with large curvature, the inertia is dominant.
Ramaprian and Shivaprasad [13]	curved ducts with rectangular cross section	$\delta/R = 0.01$	5×10^3	x		• total-head probe • hot wire	U, δ	ε, P_r, auto-correlation, auto-power spectra, cross-power spectra, amplitude of probability distribution, conditional correlation	• ε is measured based on Taylor's hypothesis. • Convex curvature suppresses the diffusion, and enforces k and τ_t towards high wave numbers. • The structure of large eddies is sensitive to wall curvature.
So and Mellor [14]	convex surface	$\delta/R = 0.09$	4.4×10^5	x		• total-head probe • hot wire	U, p, δ, u_τ	$\overline{uv}$, $\overline{u^2}$, $\overline{v^2}$, $\overline{w^2}$, P_r	• Curvature does not affect the flow near the wall • P_r/u_τ is similar to the flat plate data in the wall region.
So and Mellor [15]	concave surface	$\delta/R \cong 0.14$	1.4×10^6	x		• total-head probe • hot wire	U, p, δ, θ, u_τ, C_f	$\overline{uv}$, $\overline{u^2}$, $\overline{v^2}$, $\overline{w^2}$, $\overline{uv}$, $\overline{vw}$, k	• Mean velocity profiles agree with the law of the wall only in a small region very close to wall.
Tani [16]	concave surface	$\frac{W}{R} = \frac{1}{5}, \frac{3}{50}$	$2.3 \times 10^5 \sim 1.5 \times 10^6$	x		• pitot tube	U	---	• No answer to the determination of wave number of streamwise vorticities.
Agrawal, Talbot, and Gong [17]	180°-bend pipe	$r/R = 1/7, 1/20$	$150 \sim 1200$		x	• L.D.A.	U, V, W	---	• At downstream, maximum axial velocity occurs near the inner wall.
White [18]	coiled pipe	$r/R = \frac{1}{15} \sim \frac{1}{2050}$	$0.058 \sim 4.1 \times 10^4$	x	x	---	C_f	---	• For large disturbances, flow in curved pipe is more stable than in straight pipe.

TABLE A.1: (continued)

REFERENCE	GEOMETRY	CURVATURE	INLET REYNOLDS NUMBER	TURBULENT	LAMINAR	INSTRUMENTS	MEASURED MEAN QUANTITIES	MEASURED TURBULENT QUANTITIES	REMARKS
Taylor, Whitelaw, and Yianneskis [19]	S-shaped ducts with square cross-section	$\frac{D_H}{R} = \frac{1}{7}$	790, 4×10^4	x	x	• L.D.V.	U, V, p	$\overline{u^2}$, $\overline{v^2}$, $\overline{w^2}$, $\overline{uv}$	• In the first bend, secondary flows are larger in the laminar case than in the turbulent case. • At the exit of the second bend, a secondary flow is established in the opposite direction to that in the first bend.
Humphrey, Whitelaw, and Yee [20]	curved duct with square cross section	$\frac{W}{R_c} = \frac{10}{23}$	4×10^4	x		• L.D.A.	U, V	$\overline{uv}$, $\overline{u^2}$, $\overline{v^2}$	• Convex surface: low turbulence intensity, low level of anisotropy. • Concave surface: high turbulence intensity, high level of anisotropy.
Rowe [21]	180°-bend pipe, 45°/45° S-bend	$\frac{r}{R} = \frac{1}{12}$	2.36×10^5	x		• pitot tube • yaw meter • strain guage	P_o, yaw angle	---	• The second bend of a S-bend pipe is favorable to the generation of secondary flow.
Humphrey [22]	180°-bend with square cross section	---	---	x		• L.D.V.	U, V	---	• In the downstream straight duct, turbulence diffusion and redistribution force flow to "forget" the force imbalance acting on the flow in bend.
Butz [23]	30°/45° and 45°/45° S-bend duct; aspect ratio = 6	$\frac{W}{R_c} = \frac{1}{5}$	131200	x		• hot film anemometer • L.D.V. • static taps	U_θ, C_p	I (turbulence intensity)	• concave wall curvature accelerates the growth of boundary layer and rapid spread of the turbulence effects away from the wall • The convex curvature of the reverse turning after the concave curvature inhibits the growth of the boundary layer.
Brinich and Graham [24]	210° curved channels; aspect ratio = 6	$\frac{W}{R_c} = 0.0385$	5×10^4 ~ 1.6×10^5	x		• probe • oil-filled manometer	C_p, U_θ, C_f, St	---	• Wall-pressure coefficients were substantially the same at all three velocities. • Beginning at the curve section, there is a nearly constant pressure difference between the inner and outer channel walls of about 0.08 to 0.1 regardless of velocity.
Humphrey, Taylor, and Whitelaw [29]	90° bend duct; aspect ratio = 1	$\frac{W}{R_c} = \frac{10}{23}$	790	x		• L.D.A.	U_θ, V_θ, C_p, C_f	---	• The mean flow in the entrance of the bend has been significantly influenced by the downstream flow. • The secondary velocity increases from 15% bulk velocity in the 0° plane to 30% bulk velocity in the 90° plane.

TABLE A.2: SUMMARY OF DATA AVAILABLE IN SOME OF THE REFERENCES (THEORETICAL AND NUMERICAL)

REFERENCE	GEOMETRY	CURVATURE	INLET REYNOLDS NUMBER	TURBULENT	LAMINAR	TURBULENCE MODELLING	MODELLING CONSTANTS	PREDICTED PROPERTIES	REMARKS
Hunt and Joubert [12]	2-D curved duct	$W_n/R = 0.01$	1.9×10^5	x		algebraic	---	U, $\overline{uv}$, $\overline{u^2}$	• Navier-Stokes equations with Bradshaw's curvature model • Incompressible, steady.
Tani [16]	concave surface	$\frac{W}{R} = \frac{1}{5}, \frac{3}{50}$	$2.3 \sim 15 \times 10^5$		x	---	---	U, wave number	• Small disturbance theory. • Laminar instability is examined.
Agrawal, Talbot, and Gong [17]	180°-bend pipe	$\frac{r}{R} = \frac{1}{7} = \frac{1}{20}$	150 ~ 1200		x	---	---	U	• Based on Singh, and Yao and Berger theories. • Fail to predict the initial formation of the vortex-type inviscid core.
White [18]	coiled pipe	$r/R = 1/15 \sim 1/2050$	$0.058 \sim 4.1 \times 10^4$		x	---	---	C_f	• Analytically algebraic solutions.
Humphrey, Whitelaw, and Yee [20]	curved duct with square cross section	$\frac{W}{R_c} = \frac{10}{23}$	4×10^4	x		standard $k-\epsilon$	$C_\mu = 0.09$, $C_{\epsilon 1} = 1.47$, $C_{\epsilon 2} = 1.92$, $\sigma_k = 1$, $\sigma_\epsilon = 1.3$	U, W	• Semi-elliptical scheme is suggested for the flow with small Dean number. • Inlet conditions: U, W, k, ϵ are specified; V = 0. Outlet conditions: $\partial/\partial x = 0$.
Rowe [21]	180°-bend pipe; 45°/45° S-bend	$\frac{r}{R} = \frac{1}{12}$	2.36×10^5		x	---	---	U, V, W, P_o, yaw angle	• Base on inviscid theory (Squire and Winter) • Underpredict the onset of the secondary flow motion and overpredict the motion from 45° onwards.
Humphrey [22]	180°-bend with square cross section	---	---	x		standard $k-\epsilon$	$C_{\epsilon 1} = 1.47$, $C_{\epsilon 2} = 1.92$, $\sigma_k = 1$, $\sigma_\epsilon = 1.3$, $C_\mu = f(U, r, \partial U/\partial r)$	U, V	• Semi-elliptic, 3-D, incompressible, isothermal. • C_μ is modified to include streamline curvature and pressure strain contribution to turbulent diffusion. • Two finite difference schemes for convection terms in the momentum equations are used.
Singh [25]	curved pipe	$\frac{r}{R} \sim O(10^{-1})$	$O(10^3)$		x	---	---	U, V, W, p	• Incompressible, viscous with the method of matched asymptotic expansion. • The flowfield is divided into 1) a thin layer near the wall, and 2) an inviscid core.
Stewartson, Cebeci, and Chang [26]	coiled pipe	$D_e \gg 1$	---		x	---	---	U, V, W	• Series expansion method with presumably a jet setup directed towards the outer bend. • Calculation is terminated at the position of boundary-layer collision.
Van Dyke [27]	coiled pipe	---	---		x	---	---	friction ratio	• Series expansion method for the incompressible, viscous curved pipe flow. • Calculations are made up to 24 terms, and the curvature ratio is assumed to be zero near the wall.

TABLE A.2: (CONTINUED)

REFERENCE	GEOMETRY	CURVATURE	INLET REYNOLDS NUMBER	TURBULENT	LAMINAR	TURBULENCE MODELLING	MODELLING CONSTANTS	PREDICTED PROPERTIES	REMARKS
Humphrey [28]	45°- and 90°-bend pipes	$\frac{r}{R} = \frac{1}{50} \sim \frac{1}{2}$	154 ~ 2400		x	---	---	U, W, C_p	• Fully elliptic, 3-D, incompressible, isothermal. • Finite difference method with arbitrary curvilinear orthogonal coordinates, and implicit scheme. • Inlet conditions and exit boundary conditions are specified.
Humphrey, Taylor, and Whitelaw [29]	90°-bend duct; aspect ratio = 1	$\frac{W}{R_c} = \frac{1}{2.3}$	790		x	---	---	U_θ, V_θ, C_p, C_f	• The pressure-driven secondary flows are much larger than the stress-driven secondary flows. • Control volume with Gosman and Pun algorithm for "partially parabolic" Navier-Stokes equations.
Towne and Schum [34]	• 22.5°-22.5° circular S-duct • 22.5°-22.5° transition S-duct	$\frac{r}{R_c} = \frac{1}{14}$	48000	x		algebraic eddy viscosity	$A^+ = 26$, $\ell_\infty = 0.09$, $\kappa = 0.43$	U, P_t	• A small region of separated flow is tolerable in a streamwise marching technique with the "FLARE" approximation. • Two pairs of counter rotating vortices occur near the exit.
Towne and Hoffman [35]	• 30°-45° S-duct • diffuser	$\frac{W}{R_c} = \frac{1}{5}$	131200	x		algebraic eddy viscosity	$A^+ = 26$, $\ell_\infty = 0.09$, $\kappa = 0.43$	U, C_p	• Streamwise marching technique is used. • Pressure coefficients on the lower surface of the second bend are underpredicted.
Towne and Hoffman [36]	• 30°-45° S-duct • diffuser	$\frac{W}{R} = \frac{1}{5}$	131200	x		algebraic eddy viscosity	$A^+ = 26$, $\ell_\infty = 0.09$, $\kappa = 0.43$	U, C_p, $\overline{uv}$	• In the outer region, the turbulence model of Cebeci and Smith [38] is used. • In the inner region, the turbulence model of Cebeci and Smith, or McDonald and Caramata [39] is used.
Vakili, Wu, Hingst, and Towne [37]	30°-30° circular S-duct	$\frac{r}{R_c} = \frac{1}{5}$	1.76×10^6	x		algebraic eddy viscosity	$A^+ = 26$, $\ell_\infty = 0.09$, $\kappa = 0.43$	V, W, C_{pt}, p	• The computations underestimate the extent of the pressure distortion, due to simplifications made in the pressure field calculations.
Loeffler [41]	S-shaped diffuser	$\frac{W}{R_c} = \frac{4}{5}, \frac{2}{11.84}$	5.82×10^5	x		algebraic eddy viscosity	$A^+ = 26$, $\kappa = 0.4$, $P_r = 0.72$, $P_{rt} = 0.9$, $C_{cp} = 1.6$, $C_{KLEB} = 0.3$, $C_{WK} = 0.25$	U, V, W, p	• "Thin-layer" Navier-Stokes equation, Beam-warming implicit factorization scheme [42], and Baldwin-Lomax two-layer eddy viscosity model [40] are employed. • A large separation zone appears on the upper surface at the beginning of the second bend and extends to the exit plane.
Anderson [43]	• 2-D • streamline curvature and streamline divergence	---	---		x	mixing length hypothesis	$A^+ = 26$, $\kappa = 0.4$	U, p, C_p, C_f, $\overline{uv}$	• Navier-Stokes equations parabolized by the thin channel approximation. • The plane potential solution is obtained from Schwartz-Christoffel transformation. • This method is valid for the entry region, and fully developed region, except the leading edge region.

TABLE A.2: (CONTINUED)

REFERENCE	GEOMETRY	CURVATURE	INLET REYNOLDS NUMBER	TURBULENT	LAMINAR	TURBULENCE MODELLING	MODELLING CONSTANTS	PREDICTED PROPERTIES	REMARKS
Irwin and Smith [45]	• curved wall jets • curved free jets • curved boundary layer	small	---	x		modified algebraic stress equations	---	$\overline{uv}$, $\overline{u^2}$, $\overline{v^2}$, $\overline{w^2}$, k, ε	• Local isotropy, local equilibrium, $\partial p/\partial n$ is negligible. • $\overline{v^2}/\overline{u^2}$ is sensitive to curvature. • Streamline curvature has the major effect on the redistribution of energy and Reynolds stresses.
Gibson [47]	curved surface	small	---	x		ASM	$C_1 = 1.8$, $C_2 = 0.6$, $C_1' = 0.5$, $C_2' = 0.3$, $C_{\mu o} = 0.09$, $C_\mu = C_\mu(S,f)$, $f = \frac{k^{3/2} C_{\mu o}^{3/4}}{\varepsilon \kappa y}$, $S = \frac{U/r}{\partial U/\partial y}$	$\overline{u_i u_j}$	• The curvature effect is accounted for by adding an extra production term in each algebraic Reynolds stress equation. • An explicit form for the length-scale function is obtained to include the curvature effect. • Approximation procedure based on Rodi's approach, isotropic pressure strain term modelled by L.R.R. [46].
So [48]	curved surface	$\delta/R \sim O(1)$	---	x		ASM	$\beta = 0.6$	U, ℓ	• Local small-scale isotropy, local equilibrium, 2-D boundary-layer approximation. • The pressure-strain term and diffusion term in the Reynolds stress equation is modelled based on Rotta's proposal. • The velocity scale for the flow with curvature is $q = q_o \cdot f(R, \Omega, \frac{\partial U/\partial y}{(\partial U/\partial y)_o})$
Chang, Han, and Humphrey [50]	90°-bend with square cross section	---	---	x		standard k-ε	$C_\mu = 0.09$, $C_{\varepsilon 1} = 1.47$, $C_{\varepsilon 2} = 1.92$, $\sigma_k = 1$, $\sigma_\varepsilon = 1.3$	U, V	• 3-D, semi-elliptic, incompressible, isothermal. • "QUICK" and "HYBRID" schemes are tested. • k-ε model fail to calculate large-scale anisotropy in the flow.
Patankar, Pratap, and Spalding [51]	180°-bend pipe	$\frac{r}{R} = \frac{1}{24}$	2.36×10^5	x		standard k-ε	$C_{\varepsilon 1} = 1.47$, $C_{\varepsilon 2} = 1.92$, $C_\mu = 0.09$, $\sigma_k = 1.0$, $\sigma_\varepsilon = 1.3$	U_θ, f_c (friction factor)	• Parabolized scheme, the diffusion fluxes in the streamwise direction are neglected. • The agreement of predictions with the measured data for turbulent flow is less good than for laminar flow. • Turbulence modelling requires improvement probably in two ways: 1) solve Reynolds stress equations, 2) modified eddy viscosity.
Pratap and Spalding [52]	90°-bend duct; aspect ratio = 4	$W_{in}/R \simeq 0.48$	---	x		standard k-ε	(same as above)	U_θ, V	• 3-D partially parabolized scheme. • Secondary flow is underpredicted.

TABLE A.2: (CONTINUED)

REFERENCE	GEOMETRY	CURVATURE	INLET REYNOLDS NUMBER	TURBU-LENT	LAM-NAR	TURBULENCE MODELLING	MODELLING CONSTANTS	PREDICTED PROPERTIES	REMARKS
Murthy and Lakshminarayana [53]	103° curved duct (rectangular cross-section)	$\frac{D_H}{R} = \frac{1}{14}$	206	x		• standard k-ε • Baldwin-Lomax eddy viscosity	(same as above)	U, V, W, k, τ	• A space-marching scheme with a noniterative algorithm. • In 3-D flows, the k-ε model has better prediction than eddy viscosity model.
Pourahmadi and Humphrey [54]	curved channel (2-D)	$\frac{r}{R_c} > \frac{1}{40}$	1.5×10^5, 8.3×10^5	x		modifed k-ε	σ_ε : interpolated $C_\mu = 0.056[1-12.17Ri\pm O(Ri^2)]$ $\ell = k^{3/2}/\varepsilon\ (1 \pm \beta Ri)$ $\alpha = \frac{U}{r}\frac{\partial U}{\partial r}$, $\beta = O(10)$	U, V	• 2-D, incompressible, isothermal • Length scale is modified to include the effect of streamline curvature and pressure strain. • $\overline{u_i u_j}/k$ is assumed to be constant along streamline. • Near the wall, ε is modified to include curvature effect.
Santi [55]	180° curved duct	$\frac{W}{R_c} = 1$	1×10^6	x		• standard k-ε • extended k-ε	$F(\sqrt{C_\mu}) = C_\mu^{3/2} + a_1 C_\mu + a_2 C_\mu^{1/2} + a_3 = 0$	U_θ, p, k	• The calculated velocity and pressure profiles by the extended k-ε model [54] are virtually identical to the standard k-ε model. • An error was made in the extended model [54] in finding the root of $F(\sqrt{C_\mu})$ equation, and convergence difficulties are encountered.
Launder, Priddin, and Sharma [56]	• curved channel • spinning cylinder • spinning cones	---	---	x		modified k-ε	$C_\mu = 0.09\ \exp[-3.4/(1 + R_t/50)^2]$ $C_{\varepsilon 2} = 1.92[1-0.3\ \exp(-R_t^2)]$ $(1-C_c Ri_t)$ $C_{\varepsilon 3} = 2.0$, $C_c = 0.2$	U, V, τ_t, Nusselt number, Sherwood number	• R_t: turbulent Reynolds number = $k^2/\nu\varepsilon$. • Ri_t: turbulent Richardson number. • An extra term is added in the ε-equation with the modelling constant C_3. • The curvature correction is suggested to be made on the production term of the ε-equation instead of on the decay part (C_2).
Sharma [57]	• flow past a rotating cylinder	---	---	x		modified k-ε	(same as above)	V_θ, δ_θ	• One extra source was added to the k and ε equations due to the coordinate conversion. • It is suggested that a nonisotropic viscosity concept is required for a universal turbulence modelling.
Rodi and Scheurer [58]	curved surface	small	---	x		• standard k-ε • ASM • k-modified ε	$C_1 = 1.8$, $C_2 = 0.6$, $C_1' = 0.5$, $C_2' = 0.3$, $C_c = 0.25$, $C_{\mu o} = 0.09$, $C_\mu = C_\mu(S, f)$, $C_{\varepsilon 2} = C_{\varepsilon 2}^*(1 - C_c Ri_t)$	k, ε, $\overline{u_i u_j}$	• Launder, Priddin, and Sharma modify $C_{\varepsilon 2}$ to include curvature effect, while Hanjalic and Launder propose the extra rate of strain be excluded from the production term in ε-eq. • Reynolds stress is overpredicted by Gibson's ASM in the recovery region from the curved surface. • C_μ should be modified to capture the streamline curvature even at the region of zero wall curvature.

TABLE A.2: (CONTINUED)

REFERENCE	GEOMETRY	CURVATURE	INLET REYNOLDS NUMBER	TURBULENT	LAMINAR	TURBULENCE MODELLING	MODELLING CONSTANTS	PREDICTED PROPERTIES	REMARKS
Galmes and Lakshminarayana [59]	rotating duct, rotor blade	---	---	x		modified k-ε model coupled with ASM	C_1=1.5, C_2= 0.6, σ_k=1, σ_ε= 1.3, $C_{\varepsilon 1}$= 1.44, $C_{\varepsilon 2}$= 1.92, $C_{\varepsilon 3}$= 0.2	Reynolds stress tensor, eddy viscosity	• An extra term is added to the ε-equation to include the anisotropy that occurs near the wall. • An algebraic stress model is obtained based on these assumptions: 1) net transport of $\overline{u_i u_j}$ is proportional to the net transport of k. 2) pressure strain term is modelled to include the anisotropy. 3) dissipation term is modified to include the anisotropy that occurs at low Reynolds number.
Warfield and Lakshminarayana [60]	rotating channel	---	---	x		standard k-ε coupled with ASM	$C_\mu = f(\frac{P_r}{\varepsilon}, \Omega, \frac{k}{\varepsilon}, \frac{\delta U_i}{\delta x_j})$	U, u_τ	• Algebraic relations are obtained for Reynolds stresses based on Rodi's approach. • C_μ is a tensor, instead of a scalar, to include the turbulence anisotropy induced by rotation. • For 2-D rotating channel, $C_{\mu 1,max}$= 0.2, $C_{\mu 1,min}$= 0.025.
Naot and Rodi [62]	open channel	0	---	x		standard k-ε with ASM	$C_{\mu x} = f(y, L_\varepsilon, C_f)$ $C_{\mu y} = g(y, L_\varepsilon, C_f)$ $L_\varepsilon = \frac{C_\mu^{3/4} k^{3/2}}{\kappa \cdot \varepsilon}$	U, V, τ	• An isotropic eddy viscosity model will fail to predict the turbulence-driven secondary flow. • Algebraic relations are obtained for Reynolds stresses by neglecting the convection and diffusion terms.
Kim and Chung [63]	swirling jet	---	---	x		• standard k-ε coupled with ASM	$\nu_t = \frac{\alpha}{1 + \beta Ri} \frac{k^2}{\varepsilon}$ $\alpha = \phi_1 \phi_2$, $\beta = 4\phi_1^2 = 0.25$	U	• The modelling constant C_μ is modified to account for the extra straining effect of swirl. • For flows without recirculation, the shear stress $\overline{uv}$ has a negligible effect on the development of the flow field.
Wilcox and Chambers [65]	• flow over curved surface • flow past a cylinder • rotating channel	$\frac{\delta}{R} \ll 1$	• --- • R_{e_D} = 5x10^5 • R_{e_H} = (1~3)x10^4	x		ε-ω model	---	U, C_p, C_f, H, u_τ	• The turbulent mixing energy e is influenced by the streamline curvature and is not a scalar. • The turbulent dissipation rate ω is unaffected by the streamline curvature and is a scalar. • The velocity fluctuations normal to the wall v' are the dominant variable; the root-mean-square value of this component is an appropriate velocity scale.

TABLE A.2: (CONTINUED)

REFERENCE	GEOMETRY	CURVATURE	INLET REYNOLDS NUMBER	TURBU-LENT	LAM-NAR	TURBULENCE MODELLING	MODELLING CONSTANTS	PREDICTED PROPERTIES	REMARKS
Gibson and Rodi [66]	curved mixing layer	---	---	x		ε-RSM	---	U, $\overline{u_i u_j}$, L_ε, I_t, k	• Assumptions: isotropic, viscous diffusion is negligible; viscous dissipation of $\overline{u_i u_j}$ eq. is negligible. • Space marching scheme is used to solve the coupling equations of momentum, $\overline{u_i u_j}$ and ε. • RSM developed for plane flow can predict the effect of strong curvature without modification.
Hah and Lakshminarayana [67]	rotor blade (cascade)	---	---	x		• standard k-ε • ε-ASM • ε-RSM	---	U, V, W, $\overline{u_i u_j}$	• The source term in ε-eq., $C_{\varepsilon 1} \frac{\varepsilon}{k} P_r$, is a poor representation and inadequate for curved flow. • Different forms of source term in ε-eq. are tested. • The k-ε model with modified source term of ε-equation can predict the curvature effect very well, but ε-ASM or ε-RSM is required to predict the rotation effect.
Lilley [68]	swirling jet	---	---	x		• mixing length • k-kl model • Reynolds stress • algebraic stress	---	U, W	• The Richardson number and local swirl number play important roles in linking the rθ-shear with the rx-viscosity and the nonisotropy of the turbulent viscosity. • The factor accounts for the change in the length scale due to swirl and is analogous to the Monin-Oboukhov formula.

APPENDIX B

DERIVATION OF NEW FORMULATION FOR EDDY VISCOSITY IN CARTESIAN COORDINATES

The algebraic equation for the Reynolds stress $\overline{u_i u_j}$ in equation (3.17) is

$$\frac{\overline{u_i u_j}}{k} = \frac{\phi}{\varepsilon}\left[P_{ij} - \frac{2}{3}\delta_{ij} P_r \right] + \frac{2}{3}\delta_{ij} \tag{B.1}$$

where P_{ij} is the production rate of the Reynolds stress given by

$$P_{ij} = -\left[\overline{u_i u_k}\frac{\partial U_j}{\partial X_k} + \overline{u_j u_k}\frac{\partial U_i}{\partial X_k} \right] \tag{B.2}$$

and P_r is the production rate of the turbulent kinetic energy given by

$$P_r = -\overline{u_i u_k}\frac{\partial U_i}{\partial X_k} \tag{B.3}$$

For two-dimensional Cartesian (x,y) coordinates, the streamline direction (x) will be in accordance with the indices i, j and k equal to 1, while the indices i, j and k=2 represent the transverse direction (y). Therefore, the above equations can be written as

$$\frac{\overline{u^2}}{k} = \frac{\phi}{\varepsilon}\left[P_{11} - \frac{2}{3}P_r\right] + \frac{2}{3} \tag{B.4}$$

$$\frac{\overline{v^2}}{k} = \frac{\phi}{\varepsilon}\left[P_{22} - \frac{2}{3}P_r\right] + \frac{2}{3} \tag{B.5}$$

$$\frac{\overline{uv}}{k} = \frac{\phi}{\varepsilon}P_{12} \tag{B.6}$$

$$P_{11} = -2\left[\overline{u^2}\frac{\partial U}{\partial x} + \overline{uv}\frac{\partial U}{\partial y}\right] \tag{B.7}$$

$$P_{22} = -2\left[\overline{uv}\frac{\partial V}{\partial x} + \overline{v^2}\frac{\partial V}{\partial y}\right] \tag{B.8}$$

$$P_{12} = -\left[\overline{u^2}\frac{\partial V}{\partial x} + \overline{uv}\frac{\partial V}{\partial y} + \overline{uv}\frac{\partial U}{\partial x} + \overline{v^2}\frac{\partial U}{\partial y}\right] \tag{B.9}$$

$$P_r = -\left[\overline{u^2}\frac{\partial U}{\partial x} + \overline{uv}\frac{\partial U}{\partial y} + \overline{uv}\frac{\partial V}{\partial x} + \overline{v^2}\frac{\partial V}{\partial y}\right] \tag{B.10}$$

Following Bradshaw's observation [30]-[31], only the terms associated with $\partial U/\partial y$ and $\partial V/\partial x$ will be kept, and hence

$$P_{11} = -2\overline{uv}\frac{\partial U}{\partial y} \tag{B.11}$$

$$P_{22} = -2\overline{uv}\frac{\partial V}{\partial x} \tag{B.12}$$

$$P_{12} = -\left[\overline{u^2}\frac{\partial V}{\partial x} + \overline{v^2}\frac{\partial U}{\partial y}\right] \tag{B.13}$$

$$P_r = -\overline{uv}\left[\frac{\partial U}{\partial y} + \frac{\partial V}{\partial x}\right] \tag{B.14}$$

According to Bradshaw's analogy, the flux Richardson number R_f is the negative ratio of the turbulent kinetic energy production in the transverse direction to that in the streamwise direction, i.e.

$$R_f = \frac{-P_{22}}{P_{11}} = -\frac{(-2\overline{uv}\partial V/\partial x)}{(-2\overline{uv}\partial U/\partial y)} = \frac{-\partial V/\partial x}{\partial U/\partial y} \tag{B.15}$$

Combining equation (B.15) with equation (B.14), it yields

$$-\overline{uv}\frac{\partial U}{\partial y} = P_r\frac{1}{1-R_f} \tag{B.16}$$

$$-\overline{uv}\frac{\partial V}{\partial x} = -P_r\frac{R_f}{1-R_f} \tag{B.17}$$

Substituting equation (B.16) into equation (B.11) and equation (B.17) into equation (B.12) will give

From equations (B.4) and (B.18) as well as equations (B.5) and (B.19), it can

$$P_{11} = 2P_r \frac{1}{1 - R_f} \tag{B.18}$$

$$P_{22} = -2P_r \frac{R_f}{1 - R_f} \tag{B.19}$$

be shown that

$$\frac{\overline{u^2}}{k} = \frac{2}{3}\left[\phi \frac{P_r}{\varepsilon} \frac{2 + R_f}{1 - R_f} + 1 \right] \tag{B.20}$$

$$\frac{\overline{v^2}}{k} = -\frac{2}{3}\left[\phi \frac{P_r}{\varepsilon} \frac{1 + 2R_f}{1 - R_f} - 1 \right] \tag{B.21}$$

Equation (B.13) also can be rewritten as

$$P_{12} = -\left[\overline{u^2} \frac{\partial V}{\partial x} + \overline{v^2} \frac{\partial U}{\partial y} \right] = -\frac{\partial U}{\partial y} [-R_f \overline{u^2} + \overline{v^2}] \tag{B.22}$$

A new form for the equation of P_{12} can be obtained with the help of equation (B.20) and (B.21)

$$P_{12} = k \frac{\partial U}{\partial y} \frac{2}{3}\left[\phi \frac{P_r}{\varepsilon} \frac{R_f^2 + 4R_f + 1}{1 - R_f} - 1 + R_f \right] \tag{B.23}$$

According to equation (B.6), the algebraic equation for the Reynolds shear stress can then be obtained by incorporating with equation (B.23) as

$$-\overline{uv} = \frac{k^2}{\varepsilon}\frac{\partial U}{\partial y}\frac{2}{3}\phi\left[1 - R_f - \phi\frac{P_r}{\varepsilon}\frac{R_f^2 + 4R_f + 1}{1 - R_f}\right] \qquad \text{(B.24)}$$

APPENDIX C

DERIVATION OF NEW FORMULATION FOR EDDY VISCOSITY IN STREAMLINE COORDINATES

Following Rodi's [61] step, the algebraic equation for the Reynolds stress $\overline{u_i u_j}$ is obtained as

$$\frac{\overline{u_i u_j}}{k} = \frac{\phi}{\varepsilon}\left[P_{ij} - \frac{2}{3}\delta_{ij} P_r \right] + \frac{2}{3}\delta_{ij} \tag{C.1}$$

where P_{ij}, the production rate of the Reynolds stress is

$$P_{ij} = -\left[\overline{u_i u_k}\frac{\partial U_j}{\partial X_k} + \overline{u_j u_k}\frac{\partial U_i}{\partial X_k} \right] \tag{C.2}$$

and P_r, the production rate of the turbulent kinetic energy is

$$P_r = -\overline{u_i u_k}\frac{\partial U_i}{\partial X_k} \tag{C.3}$$

With the selection of a two-dimensional streamline (s,n) coordinates, the streamwise direction (s) will be aligned with the indices i, j and k equal 1, while the indices i, j and k equal to 2 represent the normal direction (n). Therefore, the above equations can be expressed as

$$\frac{\overline{u^2}}{k} = \frac{\phi}{\varepsilon}\left[P_{11} - \frac{2}{3}P_r\right] + \frac{2}{3} \tag{C.4}$$

$$\frac{\overline{v^2}}{k} = \frac{\phi}{\varepsilon}\left[P_{22} - \frac{2}{3}P_r\right] + \frac{2}{3} \tag{C.5}$$

$$\frac{\overline{uv}}{k} = \frac{\phi}{\varepsilon}P_{12} \tag{C.6}$$

$$P_{11} = -2\overline{u^2}\left(\frac{\partial U}{\partial s} + \frac{V}{R}\right) - 2\overline{uv}\left[\left(1 + \frac{n}{R}\right)\frac{\partial U}{\partial n} + \frac{U}{R}\right] \tag{C.7}$$

$$P_{22} = -2\overline{uv}\left(\frac{\partial V}{\partial s} - 2\frac{U}{R}\right) - 2\overline{v^2}\left(1 + \frac{n}{R}\right)\frac{\partial V}{\partial n} \tag{C.8}$$

$$P_{12} = -\overline{u^2}\left(\frac{\partial V}{\partial s} - 2\frac{U}{R}\right) - \overline{v^2}\left[\left(1 + \frac{n}{R}\right)\frac{\partial U}{\partial n} - \frac{U}{R} + 2\frac{U}{R}\right] \tag{C.9}$$

$$\begin{aligned} P_r = &-\overline{u^2}\left(\frac{\partial U}{\partial s} + \frac{V}{R}\right) - \overline{v^2}\left(1 + \frac{n}{R}\right)\frac{\partial V}{\partial n} \\ &-\overline{uv}\left[\left(1 + \frac{n}{R}\right)\frac{\partial U}{\partial n} + \frac{\partial V}{\partial s} - \frac{U}{R}\right] \end{aligned} \tag{C.10}$$

where R is the radius of surface curvature and n is the normal distance away from the wall.

Since the dominant extra rate of strain is U/R, only those term coupled with U/R and the main strain $\partial U/\partial n$ will be remained, and hence

$$P_{11} = -2\overline{uv}\left[\left(1 + \frac{n}{R}\right)\frac{\partial U}{\partial n} + \frac{U}{R}\right] \tag{C.11}$$

$$P_{22} = 4\overline{uv}\frac{U}{R} \tag{C.12}$$

$$P_{12} = 2\overline{u^2}\frac{U}{R} - \overline{v^2}\left[\left(1 + \frac{n}{R}\right)\frac{\partial U}{\partial n} + \frac{U}{R}\right] \tag{C.13}$$

$$P_r = -\overline{uv}\left[\left(1 + \frac{n}{R}\right)\frac{\partial U}{\partial n} - \frac{U}{R}\right] \tag{C.14}$$

According to Bradshaw's analogy [30]-[31], the flux Richardson number R_f is the negative ratio of turbulent energy in the normal direction to that in the shear direction, i.e.

$$R_f = \frac{-P_{22}}{P_{11}} = \frac{-4\overline{uv}\frac{U}{R}}{-2\overline{uv}\left[\left(1 + \frac{n}{R}\right)\frac{\partial U}{\partial n} + \frac{U}{R}\right]} = \frac{2\frac{U}{R}}{\left(1 + \frac{n}{R}\right)\frac{\partial U}{\partial n} + \frac{U}{R}} \tag{C.15}$$

Combining equations (C.14) and (C.15) will yield

$$-\overline{uv}\left[\left(1 + \frac{n}{R}\right)\frac{\partial U}{\partial n} + \frac{U}{R}\right] = P_r\frac{1}{1 - R_f} \tag{C.16}$$

$$-2\overline{uv}\frac{U}{R} = P_r\frac{R_f}{1-R_f} \tag{C.17}$$

The above equations show that equations (C.11) and (C.12) can be expressed as

$$P_{11} = 2P_r\frac{1}{1-R_f} \tag{C.18}$$

$$P_{22} = -2P_r\frac{R_f}{1-R_f} \tag{C.19}$$

Substituting equation (C.18) into equation (C.4) and equation (C.19) into equation (C.5) will obtain

$$\frac{\overline{u^2}}{k} = \frac{2}{3}\left[\phi\frac{P_r}{\varepsilon}\frac{2+R_f}{1-R_f}+1\right] \tag{C.20}$$

$$\frac{\overline{v^2}}{k} = -\frac{2}{3}\left[\phi\frac{P_r}{\varepsilon}\frac{1+2R_f}{1-R_f}-1\right] \tag{C.21}$$

Since the equation (C.13) can be rewritten as

$$P_{12} = \left[\left(1+\frac{n}{R}\right)\frac{\partial U}{\partial n}+\frac{U}{R}\right](R_f\overline{u^2}-\overline{v^2}) \tag{C.22}$$

a new expression for P_{12} can be deduced with the aid of equations (C.20) and (C.21), which is

$$P_{12} = k\frac{2}{3}\left[\left(1+\frac{n}{R}\right)\frac{\partial U}{\partial n}+\frac{U}{R}\right]\left[\phi\frac{P_r}{\varepsilon}\frac{R_f^2+4R_f+1}{1-R_f}-1+R_f\right] \qquad (C.23)$$

By putting equation (C.23) into equation (C.6), an algebraic equation for the Reynolds shear stress can be resolved as

$$-\overline{uv} = \frac{k^2}{\varepsilon}\frac{2\phi}{3}\left[\left(1+\frac{n}{R}\right)\frac{\partial U}{\partial n}+\frac{U}{R}\right]\left[1-R_f-\phi\frac{P_r}{\varepsilon}\frac{R_f^2+4R_f+1}{1-R_f}\right] \qquad (C.24)$$

The Boussinesq's eddy-viscosity reveals that

$$-\rho\overline{uv} = \mu_t\left[\left(1+\frac{n}{R}\right)\frac{\partial U}{\partial n}+\frac{U}{R}\right] \qquad (C.25)$$

so that we can obtain eddy viscosity μ_t as

$$\mu_t = \rho\frac{k^2}{\varepsilon}\frac{2\phi}{3}\left[1-R_f-\phi\frac{P_r}{\varepsilon}\frac{R_f^2+4R_f+1}{1-R_f}\right] \qquad (C.26)$$

APPENDIX D

DERIVATION OF NEW FORMULATION FOR EDDY VISCOSITY WITH TRANSVERSE CURVATURE EFFECT

With the adoption of the cylindrical coordinates, the coordinate axis, mean and fluctuating velocity components can be expressed in the tensor notation as $X_i = [x, r, \theta]$, $U_i = [U, V, W]$, and $u_i = [u, v, w]$. According to Ref. [84] and Ref. [85], the transport equations of Reynolds stresses $\overline{u_i u_j}$ and turbulent kinetic energy k can be expressed as follows:

$$U_k \frac{\partial \overline{u^2}}{\partial X_k} = -2\overline{u u_k} \frac{\partial U}{\partial X_K} + Ps_{11} + D_{11} - \varepsilon_{11} \tag{D.1}$$

$$U_k \frac{\partial \overline{v^2}}{\partial X_k} - 2\frac{W}{r}\overline{vw} = -2\left(\overline{v u_k} \frac{\partial V}{\partial X_k} - \frac{W}{r}\overline{vw} \right) + Ps_{22} + D_{22} - \varepsilon_{22} \tag{D.2}$$

$$U_k \frac{\partial \overline{w^2}}{\partial X_k} + 2\frac{W}{r}\overline{vw} = -2\left(\overline{w u_k} \frac{\partial W}{\partial X_k} + \frac{V}{r}\overline{w^2} \right) + Ps_{33} + D_{33} - \varepsilon_{33} \tag{D.3}$$

$$U_k \frac{\partial \overline{uv}}{\partial X_k} - \frac{W}{r}\overline{uw} = -\left(\overline{vu_k} \frac{\partial U}{\partial X_k} + \overline{uu_k} \frac{\partial V}{\partial X_K} - \frac{W}{r}\overline{uw} \right) + Ps_{12} + D_{12} - \varepsilon_{12} \quad \text{(D.4)}$$

$$U_k \frac{\partial \overline{uw}}{\partial X_k} + \frac{W}{r}\overline{uv} = -\left(\overline{wu_k} \frac{\partial U}{\partial X_k} + \overline{uu_k} \frac{\partial W}{\partial X_K} - \frac{V}{r}\overline{uw} \right) + Ps_{13} + D_{13} - \varepsilon_{13} \quad \text{(D.5)}$$

$$U_k \frac{\partial \overline{vw}}{\partial X_k} + \frac{W}{r}(\overline{v^2} - \overline{w^2}) = -\left[\overline{wu_k} \frac{\partial V}{\partial X_k} + \overline{vu_k} \frac{\partial W}{\partial X_K} + \frac{V}{r}\overline{vw} - \frac{W}{r}\overline{w^2} \right] + Ps_{23} + D_{23} - \varepsilon_{23} \quad \text{(D.6)}$$

$$U_k \frac{\partial k}{\partial X_k} = -\left(\overline{u_i u_k} \frac{\partial U_i}{\partial X_k} - \frac{W}{r}\overline{vw} + \frac{V}{r}\overline{w^2} \right) + P_k + D_k - \varepsilon \quad \text{(D.7)}$$

where subscripts i and k are the tensor indices, $\partial X_k = [\partial x, \partial r, r\partial\theta]$, and Ps_{ij}, D_{ij}, and ε_{ij} are the pressure-strain, diffusion, and dissipation of Reynolds stresses, respectively; while P_k, D_k, and ε are the pressure-strain, diffusion, and dissipation of the turbulent kinetic energy.

Therefore the production terms of Reynolds stresses and turbulent kinetic energy can be written as

$$P_{22} = P_{rr} = -2\left[\overline{uv}\frac{\partial V}{\partial x} + \overline{v^2}\frac{\partial V}{\partial r} + \overline{vw}\left(\frac{\partial V}{r\partial\theta} - 2\frac{W}{r}\right)\right] \tag{D.9}$$

$$P_{33} = P_{\theta\theta} = -2\left[\overline{uw}\frac{\partial W}{\partial x} + \overline{vw}\frac{\partial W}{\partial r} + \overline{w^2}\frac{\partial W}{r\partial\theta} + \frac{V}{r}\overline{w^2} + \frac{W}{r}\overline{vw}\right] \tag{D.10}$$

$$\begin{aligned} P_{12} = P_{xr} = &-\overline{uv}\frac{\partial U}{\partial x} - \overline{v^2}\frac{\partial U}{\partial r} - \overline{vw}\frac{\partial U}{r\partial\theta} - \overline{u^2}\frac{\partial V}{\partial x} \\ &- \overline{uv}\frac{\partial V}{\partial r} - \overline{uw}\frac{\partial V}{r\partial\theta} + 2\overline{uw}\frac{W}{r} \end{aligned} \tag{D.11}$$

$$\begin{aligned} P_{13} = P_{x\theta} = &-\overline{u^2}\frac{\partial W}{\partial x} - \overline{w^2}\frac{\partial U}{r\partial\theta} - \overline{uv}\left(\frac{\partial W}{\partial r} + \frac{W}{r}\right) \\ &- \overline{uw}\left(\frac{\partial U}{\partial x} + \frac{\partial W}{r\partial\theta} + \frac{V}{r}\right) - \overline{vw}\frac{\partial U}{\partial r} \end{aligned} \tag{D.12}$$

$$\begin{aligned} P_{23} = P_{r\theta} = &-\overline{v^2}\left(\frac{\partial W}{\partial r} + \frac{W}{r}\right) - \overline{w^2}\left(\frac{\partial V}{r\partial\theta} - 2\frac{W}{r}\right) - \overline{uv}\frac{\partial W}{\partial x} \\ &- \overline{uw}\frac{\partial V}{\partial x} - \overline{vw}\left(\frac{\partial V}{\partial r} + \frac{\partial W}{r\partial\theta} + \frac{V}{r}\right) \end{aligned} \tag{D.13}$$

$$\begin{aligned} P_r = &-\overline{u^2}\frac{\partial U}{\partial x} - \overline{v^2}\frac{\partial V}{\partial r} - \overline{w^2}\left(\frac{\partial W}{r\partial\theta} + \frac{V}{r}\right) - \overline{uv}\left(\frac{\partial U}{\partial r} + \frac{\partial V}{\partial x}\right) \\ &- \overline{uw}\left(\frac{\partial U}{r\partial\theta} + \frac{\partial W}{\partial x}\right) - \overline{vw}\left(\frac{\partial V}{r\partial\theta} + \frac{\partial W}{\partial r} - \frac{W}{r}\right) \end{aligned} \tag{D.14}$$

with the assumption of weak swirl, axisymmetric and slender shear layer, which means $W/r \ll \partial W/\partial r$, $\partial/\partial\theta \approx 0$, and $\partial/\partial r \gg \partial/\partial x$, equations (D.8)-(D.14) can be simplified as

$$P_{11} = P_{xx} = -2\overline{uv}\frac{\partial U}{\partial r} \tag{D.15}$$

$$P_{22} = P_{rr} = 4\overline{vw}\frac{W}{r} \tag{D.16}$$

$$P_{33} = P_{\theta\theta} = -2\overline{vw}\frac{\partial W}{\partial r} - 2\overline{vw}\frac{W}{r} \tag{D.17}$$

$$P_{12} = P_{xr} = -\overline{v^2}\frac{\partial U}{\partial r} \tag{D.18}$$

$$P_{13} = P_{x\theta} = -\overline{vw}\frac{\partial U}{\partial r} \tag{D.19}$$

$$P_{23} = P_{r\theta} = -\overline{v^2}\frac{\partial W}{\partial r} \tag{D.20}$$

$$P_r = -\overline{uv}\frac{\partial U}{\partial r} - \overline{vw}\frac{\partial W}{\partial r} + \overline{vw}\frac{W}{r} \tag{D.21}$$

The flux Richardson number R_f of three-dimensional flows is defined by Bradshaw [30] as

$$R_f = -\left[\frac{\text{extra } \overline{v^2} \text{ production}}{\text{sum of } \overline{u^2} \text{ and } \overline{w^2} \text{ production}}\right] = \frac{-P_{22}}{P_{11} + P_{33}}$$

$$= \frac{2\overline{vw}\dfrac{W}{r}}{\overline{uv}\dfrac{\partial U}{\partial r} + \overline{vw}\dfrac{\partial W}{\partial r} + \overline{vw}\dfrac{W}{r}} \tag{D.22}$$

From equations (D.21) and (D.22), the production of turbulent kinetic energy can be derived as

$$P_r = -2\overline{vw}\,\frac{W}{r}\,\frac{1 - R_f}{R_f} \tag{D.23}$$

and so a new expression for P_{22} can be obtained as

$$P_{22} = -2P_r\,\frac{R_f}{1 - R_f} \tag{D.24}$$

According to equation (3.17), which is

$$\frac{\overline{u_i u_j}}{k} = \frac{\phi}{\varepsilon}\left[P_{ij} - \frac{2}{3}\delta_{ij}P_r\right] + \frac{2}{3}\delta_{ij} \tag{D.25}$$

an expression for the shear stresses $\overline{uv}$ and $\overline{v^2}$ can be denoted as

$$\frac{\overline{uv}}{k} = \frac{\phi}{\varepsilon}P_{12} \tag{D.26}$$

$$\frac{\overline{v^2}}{k} = \frac{\phi}{\varepsilon}\left[P_{22} - \frac{2}{3}P_r\right] + \frac{2}{3} \tag{D.27}$$

Substituting equations (D.23) and (D.24) into equation (D.27) will yield

$$\overline{v^2} = \frac{2}{3}k\left[1 - \phi\,\frac{P_r}{\varepsilon}\,\frac{1 + 2R_f}{1 - R_f}\right] \tag{D.28}$$

With the aid of equation (D.28), equation (D.18) can be rewritten as

$$P_{12} = -\frac{2}{3}k\left[1 - \phi\frac{P_r}{\varepsilon}\frac{1+2R_f}{1-R_f}\right]\frac{\partial U}{\partial r} \tag{D.29}$$

Therefore, the Reynolds shear stress $\overline{uv}$ can be obtained from equations (D.26) and (D.29), which is

$$\overline{uv} = -\frac{k^2}{\varepsilon}\frac{2\phi}{3}\left[1 - \phi\frac{P_r}{\varepsilon}\frac{1+2R_f}{1-R_f}\right]\frac{\partial U}{\partial r} \tag{D.30}$$

and also the eddy viscosity could be shown as

$$\mu_t = \rho\frac{k^2}{\varepsilon}\frac{2\phi}{3}\left[1 - \phi\frac{P_r}{\varepsilon}\frac{1+2R_f}{1-R_f}\right] \tag{D.31}$$

The final step is to further simplify the expression of the flux Richardson number R_f. Due to the assumption of weak swirl, i.e. $W/r \ll \partial W/\partial r$, equation (D.22) becomes

$$R_f \approx \frac{2\overline{vw}\dfrac{W}{r}}{\overline{uv}\dfrac{\partial U}{\partial r} + \overline{vw}\dfrac{\partial W}{\partial r}} \tag{D.32}$$

From equation (D.25), it can be seen that

$$\frac{\overline{uv}}{\overline{vw}} = \frac{P_{12}}{P_{23}} \tag{D.33}$$

Substituting equations (D.18) and (D.20) into the above equation will evolve the following expression

$$\frac{\overline{uv}}{\overline{vw}} = \frac{\partial U / \partial r}{\partial W / \partial r} \tag{D.34}$$

Hence, the flux Richardson number R_f can be derived from equations (D.32) and (D.34), which is

$$R_f = \frac{2\dfrac{W}{r}\dfrac{\partial W}{\partial r}}{\left(\dfrac{\partial U}{\partial r}\right)^2 + \left(\dfrac{\partial W}{\partial r}\right)^2} \tag{D.35}$$